HAL
open science

In situ synchrotron X-ray scattering of SiGe NWs : growth, strain and bending

Tao Zhou

To cite this version:

Tao Zhou. In situ synchrotron X-ray scattering of SiGe NWs : growth, strain and bending. Physics [physics]. Université Grenoble Alpes, 2015. English. NNT : 2015GREAY084 . tel-01686408

HAL Id: tel-01686408

https://theses.hal.science/tel-01686408

Submitted on 17 Jan 2018

HAL is a multi-disciplinary open access archive for the deposit and dissemination of scientific research documents, whether they are published or not. The documents may come from teaching and research institutions in France or abroad, or from public or private research centers.

L'archive ouverte pluridisciplinaire **HAL**, est destinée au dépôt et à la diffusion de documents scientifiques de niveau recherche, publiés ou non, émanant des établissements d'enseignement et de recherche français ou étrangers, des laboratoires publics ou privés.

UNIVERSITÉ GRENOBLE ALPES

THÈSE

Pour obtenir le grade de

DOCTEUR DE L'UNIVERSITÉ GRENOBLE ALPES

Spécialité : **Physique**

Arrêté ministériel : 3 Novembre 2014

Présentée par

Tao ZHOU

Thèse dirigée par **Gilles RENAUD**

préparée au sein du **CEA-Grenoble/INAC/SP2M/NRS**
dans **l'École Doctorale de Physique de Grenoble**

In Situ Synchrotron X-ray Scattering of SiGe NWs : Growth, Strain and Bending

Thèse soutenue publiquement le **7 Décembre 2015**,
devant le jury composé de :

M. Daniel Bouchier
Directeur de recherche, IEF Orsay, Président
M. Pierre Müller
Professeur, Université Aix Marseille, Rapporteur
M. Yves Garreau
Professeur, Université Paris-Diderot, LMPQ, Rapporteur
M. Vincent Favre Nicolin
Docteur, CEA-Grenoble, SP2M, Examinateur
M. Tobias Schülli
Docteur, Responsable de la ligne ID01, ESRF, Examinateur
M. Roberto Felici
Docteur, Responsable de la ligne ID03, ESRF, Invité
SPIN-CNR, Roma, c/o Department DICII, University of Tor Vergata
M. Gilles Renaud
Docteur, CEA-Grenoble, SP2M, Directeur de thèse

INTRODUCTION

Nanoscale one-dimensional materials have stimulated great interest in the past decade thanks to their unique physical, electrical, optical and mechanical properties relative to their bulk counterparts. Among them, Si nanowires (NWs) are of particular interest due to their (1) being formed by the second most abundant element on Earth (2) high stability and non-toxicity (3) mature synthesis techniques and (4) direct compatibility with the booming microelectronics industry. Typically, Si NWs are grown with Chemical Vapor Deposition (CVD) via the Vapor-Liquid-Solid (VLS) mechanism, during which the NWs gradually emerge from the substrate as a result of preferential decompositions of the precursor gas on the liquid catalyst alloy droplets. Although discovered more than half a century ago (1964, R. S. Wagner and W. C. Ellis), many aspects of the VLS growth are still not well understood, since most experimental information was extracted from *ex situ* investigations, *i.e.* only when the growth process was terminated and after the sample was removed from its initial environment. *In situ* electron microscopy (EM) is, up to now, the major technique employed in both the qualitative and the quantitative studies of the growth mechanics. However, it usually requires laborious sample preparations and has a field of view that is limited to only a small area of the sample surface. Grazing Incidence Small Angle X-ray Scattering (GISAXS) and Grazing Incidence X-ray Diffraction (GIXD) complement the existing literature as they provide statistically averaged information on a much larger scale (~mm^2). GISAXS reveals morphological information (size, spacing, faceting of the NWs) similar to EM while GIXD offers, in addition, an unparalleled view of the structural properties such as strain, stress and atomic composition. To our knowledge, no *in situ* X-ray studies have been reported for the growth of SiGe NWs, mainly due to the difficulties

of attaching a growth apparatus to a functioning X-ray machine. In our case, this is achieved by adding a CVD injector to the existing Ultra High Vacuum (UHV) chamber on the BM32 beamline at the European Synchrotron Radiation Facility (ESRF). Additional efforts have been made to further exploit the upgraded equipment to study the physical and mechanical properties of SiGe NWs.

This manuscript mainly centers on our current state of NW growth as well as our results on three different subjects, namely, the *in situ* growth of Si and Ge NWs, the strain evolution in Si-Ge core-shell NWs and the *in situ* bending of Si NWs. In fact, if it wasn't too unorthodox a choice, I would give each chapter a very different title, which coincidentally (or not) reflects my path as an ordinary Ph.D. student.

Chapter 1 - Motivate. X-ray and nanowires are the two key components in this thesis work, but I have to admit that my motivation lies mainly in the former. I love everything about X-ray, which is why in addition to the basics of the several techniques essential to this work, a brief introduction to the history and characteristics of (synchrotron) X-rays is also included in this chapter.

Chapter 2 - Struggle. Chapter 2 is actually a literature review on the growth and characterization of Si and Ge nanowires. Instead of citing directly the results from other groups, I chose to present each time some *ex situ* Scanning Electron Microscopy (SEM) images on the NWs grown with our setup, followed by established explanations in the literature with regard to our observations. As a matter of fact, we struggled for a long time to find the optimal growth conditions appropriate to our new setup, only to reproduce what was very well understood in the literature.

Chapter 3 - Apply. The objective of this study is to apply our own expertise (X-ray techniques) to the problem. Despite knowing that most of the experimental aspects have already been covered by Electron Microscopy studies, we have performed a

comprehensive *in situ* follow-up on the simple NW growth, in hope of finding something that would complement the existing results (which we did eventually) and to demonstrate the viability of our techniques.

Chapter 4 - Excel. The next step is to further explore our specialties, to do what we excel at. X-ray is extremely sensitive to the changes in lattice parameters. This, combined with the knowledge of compound composition acquired with anomalous scattering techniques, allowed us to calculate the strain evolution during the formation and the annealing of the Si-core/Ge-shell heterostructure NWs.

Chapter 5 - Innovate. The final chapter is all about innovations. If we are not smart enough to invent a new X-ray technique, maybe we can find ourselves a unique problem to solve. It all started when we suddenly decided to stop rotating the sample when we were supposed to. Instead of growing a homogenous all-around Ge shell, atomic Ge was deposited on only one side of Si NWs, which led to the bending of the NWs. A new measuring technique (Stationary Method) was devised to follow in real time the bending process while the exact shape of the bent NWs was deduced by comparing the experimental data with results from an also original simulation. Finally, a theoretical model was built which allowed us to quantify the amount of misfit stress and surface stress that contributed to the bending.

[This Page Intentionally Left Blank]

ACKNOWLEDGEMENTS

Immeasurable appreciation and deepest gratitude for the help and support are extended to the following people who in one way or another have contributed to making this study possible.

My highest, most respectful gratitude goes to my mentor Dr. Gilles Renaud, Head of the BM32 beamline at the ESRF who, by kindly accepting me as an intern years ago, introduced me to the vast world of synchrotron radiation. Positive and enthusiastic even at the toughest times, Gilles is a quick-witted and knowledgeable person from whom there is always much to learn.

It is a genuine pleasure to express my deep sense of thanks and gratitude to Dr. Odile Robach for her keen interest in every stage of my research, for the most inspiring discussions and timely suggestions. I am also extremely thankful to my fellow colleague Dr. Fabien Jean for the exchange of ideas both inside and outside work, as well as to Dr. Nils Blanc and Dr. Valentina Cantelli whose selfless contribution had made this project possible.

I owe a deep sense of gratitude (and apology) to Dr. Laurent Vila, a brilliant research scientist at the CEA, for his kindness, enthusiasm and dynamism during our collaboration, despite a fruitless result. I would also like to thank our collaborators Dr. Laetitia Vincent and Dr. Charles Renard from IEF Orsay, for the countless instructive discussions over the years.

None of the experimental work would have been completed without the technical assistance of Olivier Geaymond, Olivier Ulrich, Dr. Frederic Boudaa and Dr. Harald Muller. There are just as much, if not more, to learn from them than from the others. I am also hugely indebted to Dr. Christina Revenant whose early guidance and advice proved invaluable in saving me from mis-steps.

I thank profusely all the jury members, Dr. Pierre Muller, Dr. Yves Garreau, Dr. Daniel Bouchier, Dr. Vincent Favre Nicolin, Dr. Tobias Schulli and Dr. Roberto Felici for taking the time to read the manuscript and to participate in the defense of this thesis.

Finally, I would like to thank all the other people I have had the privilege of working with (or bothering) over the course of this study. Francois Rieutord, Jean-Sebastien Micha, Joel Eymery, Denis Buttard, Pascal Gentile from CEA-Grenoble, Maurizio De-Santis, Johann Coraux, Aude Bailly, Marie-Claire Saint-Lager, Stéphan Arnaud from Institut Neel, Helena Isern, Thomas Dufrane, Jakub Drnec, Stelian Pintea, Willem Onderwaater, and Francesco Carla from the ID03 beamline of the ESRF, Gilbert Chahine from the ID01 beamline of the ESRF, Alesssandro Coati from the SIXS beamline of Soleil, Dr. Marie-Ingrid Richard from IM2NP Marseille, Frederic Leroy and Georges Sitja from CINaM Marseille, Geoffroy Prevot from INSP Paris, Guillaume Saint-Girons from ECL Lyon and Sebastien Linas from ILM Lyon.

ABSTRACT

This work summarizes the progress made on the BM32 beamline at the ESRF over the past 4 years since the launch of the CVD project, which was aimed at studying the *in situ* growth of SiGe nanowires, using synchrotron X-ray scattering techniques.

Results on the growth of Si and Ge NWs are first presented. The NWs length, size, spacing, facet morphology and their tapering angle are determined in real time with X-ray techniques. Special attention was paid to the very early stage of growth where changes in the shape of the AuSi liquid droplet were clearly observed. We also found clues indicating the presence of a metastable AuGe phase at the catalyst-substrate interface, the formation of which may be crucial to the sub-eutectic growth of Ge NWs.

Strain relaxation in Si-Ge core-shell NWs is presented next. The composition and strain were determined *in situ* as a function of the Ge overgrowth amount and of the annealing time, using anomalous X-ray scattering techniques. Their dependence on the NW size and on the shell growth temperature was also studied.

Finally, results on the *in situ* bending of as-grown NWs are shown. The bending was induced by depositing a second material on one side of the NWs. The strain and stress were determined by a combination of Bragg peak tracking, intensity simulation plus fitting and classic elasticity calculations. The bending induced by Ge deposition at 220°C is found to be mainly driven by the misfit stress, which scales almost linearly with Ge film thickness. On the other hand, the bending induced by Ge deposition at RT is found to be mainly driven by the surface stress, which evolves gradually from tensile to compressive for larger Ge thickness. A new technique was also devised which makes it possible to follow qualitatively the bending process. The NWs were seen dancing back and forth with increasing amount of deposition as revealed by real time stationary measurements with a 2D detector.

[This Page Intentionally Left Blank]

TABLE OF CONTENTS

1. CHARACTERIZATION TECHNIQUES 1

1.1. EXPERIMENTAL SETUP 1
1.1.1. SYNCHROTRON RADIATION 1
1.1.2. BEAMLINE BM32 4
1.2. CHARACTERIZATION TECHNIQUES 10
1.2.1. WHY X-RAY? 10
1.2.2. WHY GRAZING INCIDENCE? 12
1.2.3. (GRAZING INCIDENCE) X-RAY DIFFRACTION 17
1.2.4. (GRAZING INCIDENCE) MULTIWAVELENGTH ANOMALOUS DIFFRACTION 24
1.2.5. (GRAZING INCIDENCE) SMALL ANGLE X-RAY SCATTERING 30
1.2.6. OTHER TECHNIQUES 37

2. UHV-CVD GROWTH OF SI/GE NWS 41

2.1. VLS GROWTH AND UHV-CVD 41
2.1.1. NANOWIRES IN A NUTSHELL 41
2.1.2. VLS AND VSS 43
2.1.3. METAL CATALYST 44
2.1.4. CVD, MBE AND UHV-CVD GROWN NWS 47
2.1.5. SIZE EFFECT 49
2.2. NW GROWTH AT BM32 51
2.2.1. SI NWS 51
2.2.2. GE NWS 57
2.2.3. GE/SI RADIAL NW HETEROSTRUCTURES 64
2.2.4. GE/SI AXIAL NW HETEROSTRUCTURES 65
2.2.5. SI/GE AXIAL NW HETEROSTRUCTURES 69
2.2.6. GROWTH WITH COLLOIDAL GOLD 70
2.2.7. GROWTH WITH PATTERNED SUBSTRATES 73
2.3. CONCLUSION 75

3. IN SITU GROWTH STUDY OF SI/GE NWS 83

3.1. EXPERIMENTAL SETUP 83
3.2. SI NWS 84
3.2.1. SI NWS AS SEEN BY GIXD 84
3.2.2. SI NWS AS SEEN BY GISAXS 98
3.2.3. DISCUSSION 107
3.3. GE NWS 108
3.3.1. GE NWS AS SEEN BY GIXD 108
3.3.2. GE NWS AS SEEN BY GISAXS 117
3.3.3. DISCUSSION 119

4. STRAIN IN CORE-SHELL NWS 121

4.1. CVD GE ON SI NWS 122
4.1.1. GENERAL IN SITU MEASUREMENTS 122
4.1.2. STRAIN ANALYSIS BY ANOMALOUS SCATTERING 131
4.1.3. EFFECT OF POST-GROWTH ANNEALING 134
4.1.4. EFFECT OF NW SIZE 138
4.1.5. EFFECT OF GE GROWTH TEMPERATURE 140
4.2. MBE GE ON SI NWS 141
4.3. DISCUSSION 144

5. IN SITU NANOWIRE BENDING 149

5.1. EXPERIMENTAL SETUP 151
5.2. GE ON SI NWS AT 220°C 152
5.2.1. STRAIN: PEAK SHIFT 152
5.2.2. CURVATURE: INTEGRATED INTENSITIES 159
5.2.3. STRESS: CURVATURE 161
5.3. GE ON SI NWS AT RT 164
5.3.1. THE STATIONARY METHOD 164
5.3.2. STRAIN AND STRESS 166
5.4. AU ON SI NWS AT RT 168
5.4.1. AU ON SI NWS AT RT 168
5.4.2. SIDEWALL CONFIGURATION 171
5.4.3. SIZE EFFECT 173
5.5. DISCUSSION 175
5.5.1. THE DISPLACED BRAGG METHOD 175
5.5.2. GE/SI NWS AT 220°C 176
5.5.3. GE/SI NWS AT RT 179
5.5.4. AU/SI NWS AT RT 179

6. CONCLUSION AND OUTLOOK 183

APPENDIX I. WORKING WITH 2D DETECTORS AND PYROD I-1

APPENDIX II. ON CLASSICAL BEAM THEORY II-1

APPENDIX III. SAMPLE PREPARATIONS III-1

APPENDIX IV. LIST OF SAMPLES CONCERNED IN THIS WORK IV-1

1. CHARACTERIZATION TECHNIQUES

X-rays have long established themself as an invaluable and irreplaceable tool for studying the structure of matter. Even since their discovery in 1895 by Wilhelm Conrad Röntgen, tremendous progress has been made, not only to improve the sources that produce X-rays, but also to develop new and more powerful techniques that exploit them. The former has led to the construction of synchrotrons all over the world to generate X-rays far more intense and versatile than those produced by conventional laboratory sources. The latter is better understood by looking at the numerous experimental endstations built around the synchrotrons, called beamlines. Each of them makes use of one or more ways by which X-rays interact with matter, scattering, absorption, refraction, magnetic interaction, etc. in fields as diverse as physics, chemistry, biology, geoscience and paleontology.

The first part of this chapter consists of a brief introduction to synchrotron radiation. It is followed by a detailed presentation of the BM32 beamline at the European Synchrotron Radiation Facility, where all the X-ray measurements concerned in this dissertation were carried out. As for the second part, each section is devoted to providing basic knowledge of one of the characterization techniques that were used over the course of this work.

1.1. Experimental Setup

1.1.1. SYNCHROTRON RADIATION

Significant breakthrough was made in applications of X-rays soon after their discovery, especially in the field of medical analysis. Meanwhile, little improvement had been made to the source. The Coolidge tube, developed by William David Coolidge in 1912 as a successor to Röntgen's cathode ray tube, remained the standard X-ray source

for many decades before being replaced by the so-called rotating anode generators in the 1960s which allow for better heat dissipation, and hence higher power. When electrons (or other charged particles) moving at relativistic speeds are forced by magnetic fields to follow curved trajectories, they emit electromagnetic radiation tangentially to their path, known as synchrotron radiation. Theoretical considerations of synchrotron radiation can be traced back to the end of the 19th century, when Alfred-Marie Liénard (1898) and Emil Wiechert (1900) worked out independently the expression for the radiated power of a relativistic particle undergoing centripetal acceleration in a circular trajectory. Experimental (visual) confirmation, however, had to wait until 1947 when a *bright arc of light* was observed, mostly unexpectedly, through an unshielded area at General Electric's 70 MeV facility. Initially viewed as an unwanted phenomenon since it is responsible for the major energy loss in high energy particle accelerators, synchrotron radiation (wavelength of peak radiation ~300Å at the time) soon established itself as a viable source for spectroscopy experiments in the ultraviolet.

The 1st generation of synchrotron radiation facilities operated parasitically on existing accelerators designed for particle physics studies. Consequently, the output of the radiation was limited by the low energy and low (electron) beam current of the host experiments. Dedicated sources (2nd generation) were later built as a result of the surging demand for synchrotron radiation for the research in physics and in biology, with some being transformed directly from 1st generation facilities by means of upgrade.

$$\text{Brilliance}=\frac{\text{Photons/second}}{(\text{mrad}^2)(\text{mm}^2)(0.1\%\text{BW})} \qquad (1\text{-}1)$$

A key factor that determines the overall quality of an X-ray source is its brilliance, which is given by the number of photons emitted per second (flux) divided by

the solid angle of the radiation cone (angular divergence), the size of the source beam (source area) and the relative energy bandwidth (spectral distribution).

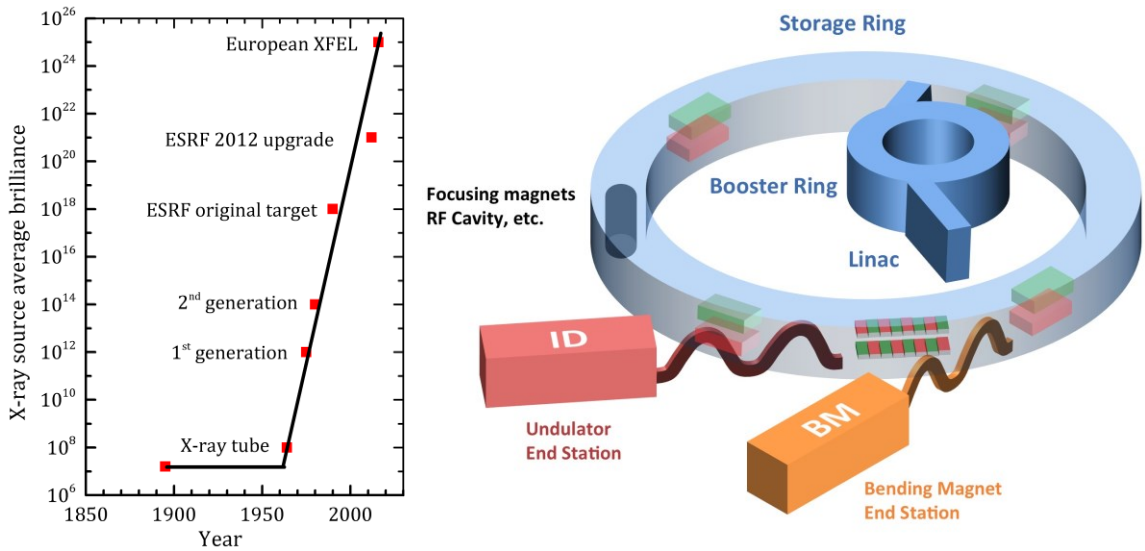

Figure 1-1: (Left) the average brilliance of X-ray sources. (Right) schematic of a 3rd generation synchrotron.

X-ray beams generated by a 2nd generation synchrotron are about a millions times more brilliant than those generated by a rotating anode. In other words, an hour of experiment at a synchrotron will otherwise take one century to complete in the home laboratory! The 3rd generation synchrotrons further extended the gap by another factor of million through the introduction of wigglers or undulators, collectively known as the insertion devices. An insertion device can be viewed as a periodic magnetic structure that forces the electron to emit radiation multiple times by undergoing oscillations. In the case of an undulator, the period of the magnets is chosen in a way that the radiation emitted by a given electron from one oscillation is in phase with those from the others. The resulted coherent condition is the main driver behind the high intrinsic brilliance and monochromaticity (with harmonics) of the undulator radiation. It was later theorized that

not only the radiation from a single electron is coherent, but that the radiation from different electrons can be rendered coherent as well, either by self-seeding or by Self Amplified Stimulated Emission (SASE). The instrument that emanates from these concepts is called a free electron laser (4th generation light source), which boasts a peak brilliance so high that few samples can withstand one single shot before being vaporized by the laser pulse. Its latest addition, the European X-ray Free Electron Laser, to be commissioned in 2016, is expected to achieve a peak brilliance of around 5×10^{33}, some 10 orders of magnitude higher than the peak brilliance delivered by a normal undulator, as our pursuit for a more brilliant and more coherent X-ray source continues.

1.1.2. BEAMLINE BM32

Situated in Grenoble France, the European Synchrotron Radiation Facility (ESRF) is the world's third largest 3rd generation synchrotron. (Figure 1-1 right) The electrons, produced by a cathode electron gun, are first accelerated by the linear accelerator (LINAC) until their energy reaches ~ 200 MeV (99.9997% speed of light). They are then injected into the booster ring to receive a second energy bump to up to 6 GeV (99.9999996% speed of light), at which point they are transferred to the storage ring for user experiments. The 844.4 meters long (circumference) circular storage ring is in fact a polygon consisting of 32 straight and 32 curved sections in alternating order. In each of the 32 straight sections is hosted a variety of devices such as the RF cavities to help the electrons regain the energy loss due to synchrotron radiation, the focusing magnets (quadrupoles, sextupoles, etc.), and of course the undulators which serve as the main source of X-ray at a 3rd generation synchrotron. The electrons exiting one straight section are redirected into the next by a 0.85T (or 0.40T) bending magnet (curved section). Synchrotron radiation emitted during this process can also be harnessed. At the ESRF, the endstations that utilize bending magnet radiation are labeled BM, to be distinguished

from those labeled ID which utilize radiation generated by insertion devices. In the following paragraphs, the general properties of bending magnet radiation as well as X-ray beam characteristics of the BM32 beamline shall be discussed.

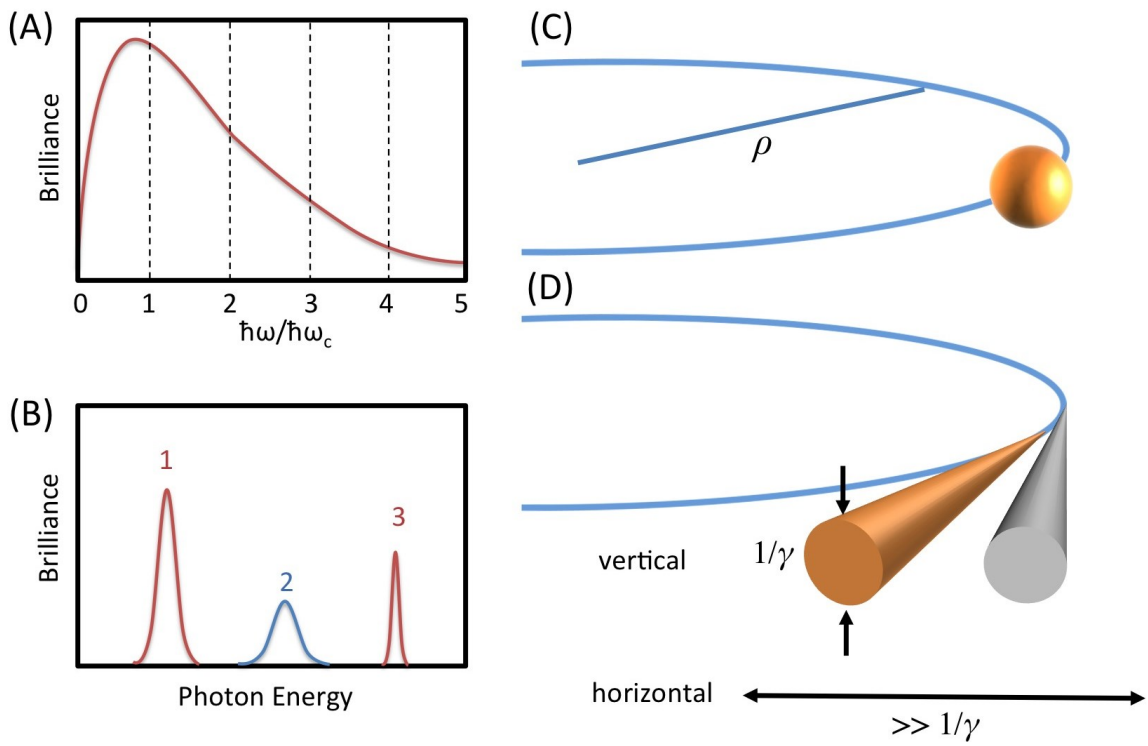

Figure 1-2: Schematics of the spectral distribution of (A) bending magnet radiation compared to that of (B) undulator radiation. Schematics of radiation emitted by (C) a non-relativistic and (D) a relativistic charged particle moving in a circular trajectory of radius ρ.

The spectral distribution of the radiation from a bending magnet (Figure 1-2A) is distinctly different from that from an undulator (Figure 1-2B). The latter is quasi-monochromatic, with a typical bandwidth of ~1% and a tunable fundamental wavelength (energy) whereas the former is a continuous function which extends from the X-ray to far infrared. A key parameter of bending magnet radiation is the characteristic energy which divides the spectrum into two parts of equal (50% each) radiated power. It also marks the

approximate location of the energy (frequency) beyond which the spectrum starts to fall off rather quickly. The characteristic energy is a function of both the electron energy $\mathcal{E}_e$ and the field strength of the bending magnet B. At BM32, it is calculated to be 20.6 keV which makes the beamline ideal for researches in the field of condensed matter physics.

$$\hbar\omega_c[\text{keV}] = 0.665\mathcal{E}_e^2[\text{GeV}] \cdot B[\text{T}] = 0.665 \times 6.04^2 \times 0.85 = 20.6\ [\text{keV}] \qquad (1\text{-}2)$$

To understand the angular collimation of synchrotron radiation, we first consider the case of a non-relativistic charged particle. Its emitted pattern (Figure 1-2C), known as cyclotron radiation, is similar to that of an oscillating dipole with its maximum intensity in the direction perpendicular to the centripetal acceleration. In the case of a relativistic particle, this pattern is compressed into a narrow cone, the instantaneous direction of which is tangential to the circulating orbit. As can be inferred from Figure 1-2D, the nominal angular divergence of the bending magnet radiation in the vertical plane is the natural opening angle of the cone, and is equal to the inverse of the Lorentz factor:

$$\gamma^{-1} = m_e c^2/\mathcal{E}_e = 0.511[\text{MeV}]/6[\text{GeV}] \sim 0.08[\text{milli-radian}] \qquad (1\text{-}3)$$

Where m_e is the rest mass of an electron and $\mathcal{E}_e$ is the electron energy inside the storage ring. The actual angular divergence decreases for increasing energies, and equals ~1.5 times the nominal value when working at $\hbar\omega = \hbar\omega_c$. In the horizontal plane, the angular divergence is much larger as the electron radiates continuously while circulating along its orbit.

In most cases the emitted radiation does not meet the requirements to be used directly, instead, it has to first go through a series of optical devices put together in the optics hutch. Although the number of devices and the principles they operate upon (reflection, diffraction, interference and absorption) may vary significantly between

beamlines, their objective is the same, to prepare a well collimated, focused and (very often) monochromatic beam optimized for each experiment. To do so, the large fan of radiation is first collected through a pair of slits, positioned at the entrance of the optics hutch, 23.84m from the source of radiation (bending magnet). The horizontal slit is widely opened to 23.84mm (= 1mrad) to accept as many X-ray photons as possible while still maintaining a minimum level of collimation for grazing incidence experiments (incidence angle ~ 2mrad). Before considering the opening of the vertical slit, we need to first understand the role of the first mirror. The 1.1m long Ir coated single crystal Si mirror is actually a high energy cut-off filter which absorbs incoming photons above its critical angle (*c.f.* Chapter 1.2.2). For a given material, the product of X-ray photon energy $\hbar\omega$ and the corresponding critical angle θ_c is almost constant (Figure 1-3C).

$$\hbar\omega[\text{keV}] \cdot \theta_c[\text{mrad}] \sim C \qquad (1\text{-}4)$$

For Si, we have $C \sim 32$. If we now simply set the inclination angle of the first mirror to, for instance $\theta = 1.6$ mrad, then only photons with energy lower than $\hbar\omega_{lim}$ = 20keV are allowed to pass through. This is crucial for experiments with a monochromatic beam of for example 11keV, as it will help filter out the higher harmonics (22keV, 33keV, *etc.*) for the double crystal monochromator. Ideally we would like to apply this filter to all incoming photons in the vertical plane, since this is the plane where the x-ray is best (naturally) collimated. This however requires the opening of the vertical slit to be no less than two times the natural opening angle, which equals 3.81mm (0.08mrad at 23.84m) under our previous assumption. Moreover, to fully accommodate the incoming beam (Figure 1-3B), the product of the usable length of the first mirror (L) and its inclination angle (θ) should also be larger than 3.81mm. At $\theta = 1.6$ mrad, this requires the mirror to be at least 2.38m long which is both expensive and impractical. The conundrum

is solved by the Ir coating at the mirror surface that increases the product in equation (1-4) to $C \sim 87$. Consequently, for the same energy $\hbar\omega_{lim}$, the inclination angle of the mirror can be set to 2.7 times larger which in turn implies that the length of the mirror can be made 2.7 times smaller (L = 1.1m at BM32)!

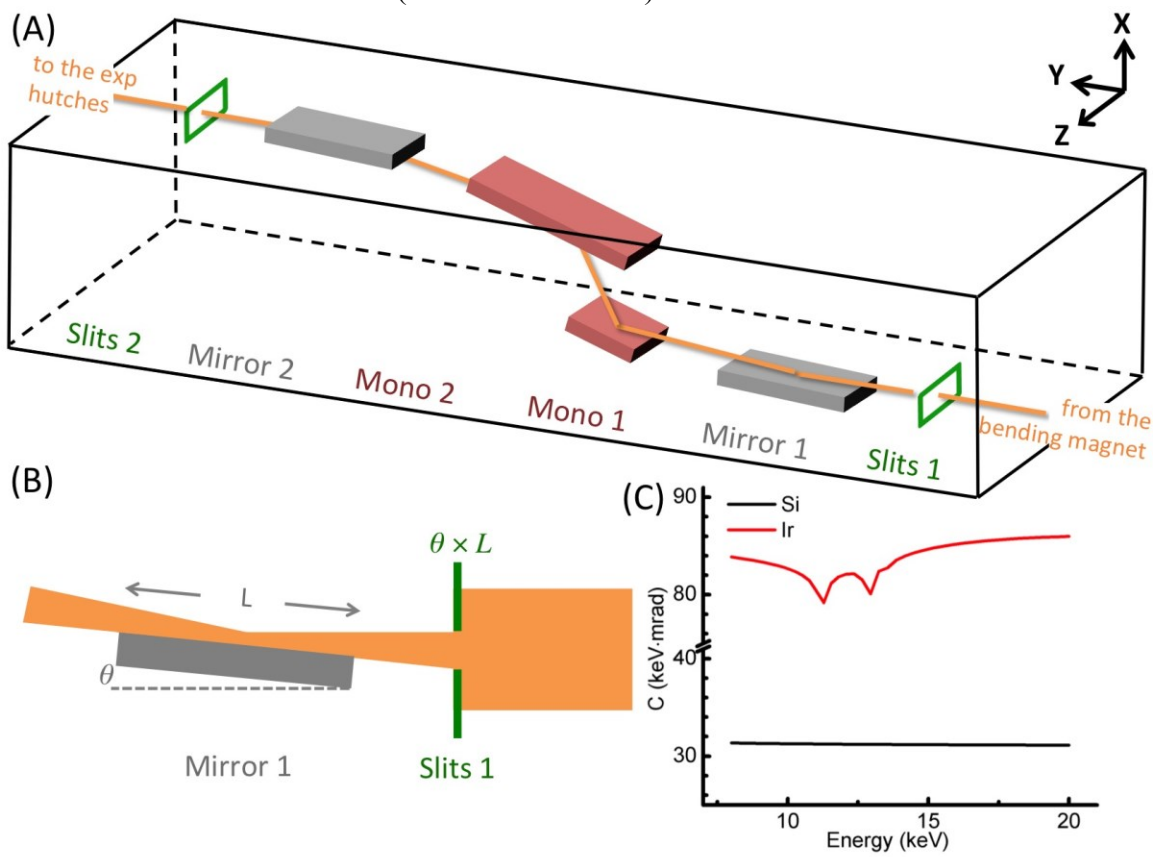

Figure 1-3: (A) Schematics of the optical devices in the optics hutch of BM32. (B) Schematic view in the vertical plane of the entrance slit and the first mirror. (C) Line plot of the product of the photon energy and the critical angle of Si and Ir for energies between 8keV and 20keV.

With the opening of both entrance slits in mind, we can now estimate the peak flux at the exit of the optics hutch for a monochromatic beam (energy dispersion = 0.1% BW) with the following equation:

$$\frac{\text{Photons}}{\text{second}\cdot(0.1\%\text{BW})}=1.33\times10^{13}\,\mathcal{E}_e^2[\text{GeV}]\,I[\text{A}]\,(\Theta_v\cdot\Theta_h)\left[\text{mrad}^2\right]x^2\,K_{2/3}^2(x/2) \quad (1\text{-}5)$$

where I = 0.2A is electron current in the storage ring, $\Theta_v = 0.08$mrad Θ_h=1mrad are the effective angular acceptance of the vertical and horizontal entrance slits respectively, $x = \omega/\omega_c$ and $K_{2/3}(x/2)$ is the modified Bessel function of second kind. Assuming a uniform distribution of photon density in both directions, we obtain 1.11×10^{13} photons/sec/(0.1%BW) for $\hbar\omega = \hbar\omega_c = 20.6$ keV. In practice, the majority of the measurements in this work were carried out in the vicinity of E = 11 keV in order to exploit the Ge K edge (*c.f.* Chapter 1.2.4), in which case the peak flux is slightly reduced to 1.06×10^{13}. The x-ray beam is subsequently rendered monochromatic by the Si(111) double crystal monochromator which applies the Bragg's law (*c.f.* Chapter 1.2.3) to pick out photons with the required wavelength. Considering a monochromator with an energy resolution of 1.5×10^{-4} (0.015%BW), the peak flux of the monochromatic beam is hence 6.9×10^{11}. The second crystal of the monochromator (mono 2) is also slightly curved in order to focus the beam in the horizontal plane. The focusing in the vertical plane is achieved by the second mirror, which in addition positions the x-ray beam back in the horizontal plane (parallel to the Y direction, Figure 1-3A). The beam is focused in a way that an exact copy of the source image is recreated at the sample stage. There is no point in further reducing the beam size as it will inevitably increase the beam divergence (degraded collimation) as stated by Liouville's theorem. The beam size at the sample stage is thus determined by the size of the electron beam in the storage ring, which is 183μm (horizontally) by 30μm (vertically) at the ESRF. In practice, the final size is always slightly larger, mainly because of thermal deformation of the optical devices, despite them being constantly cooled by water.

1.2. Characterization techniques

1.2.1. WHY X-RAY?

The physics society acknowledges the importance of the discovery of X-rays by awarding Röntgen the first ever Nobel Prize for Physics. In 1914 Max von Laue, and just one year later Sir William Henry Bragg together with his son William Laurence Bragg each received a Nobel Prize for their pioneering work that gave birth to X-ray crystallography. To date, a total of 15 Nobel Prizes have been honored to discoveries made in the field of X-rays. One can't help but wonder, what makes X-rays so special?

[Short Wavelength] It is no longer a mystery that X-rays, like any other electromagnetic radiation, exhibit both wave and particle properties at the same time (wave-particle duality). X-rays have a wavelength of around 1Å, making them ideal for resolving atomic and molecular structures which share a comparable characteristic length, either via diffraction (Bragg's law) or via direct imaging (Rayleigh's criterion).

[Ideal Energy] As a particle, an X-ray photon possesses a typical energy of 0.12-120 keV, which covers the binding energy of most elements, from C K edge (0.284keV) to U K edge (115.606keV). A photoelectric event takes place when an X-ray photon is absorbed by the material, ejecting a core electron in the process. The resulting absorption spectra (absorption coefficient versus photon energy) contain information on the local structure and electronic states of the subject, the analysis of which lies at the heart of most X-ray absorption spectroscopy techniques (*e.g.*, EXAFS, XANES). Alternatively, the emitted photoelectron can be studied. This gives rise to a bunch of techniques collectively known as X-ray photoemission spectroscopy (*e.g.*, XPS, ARPES), whose main focus is to resolve the electronic structure and chemical state of the given material.

[Strong Penetration] X-rays are known for their penetration ability, especially those with higher energies (12-120keV) otherwise known as hard X-rays. The advantages

are twofold. First of all, high penetration means little requirement on sample thickness, as opposed to the delicate sample preparation for, for example Transmission Electron Microscopes. This is one of the two reasons (the other one being the short wavelength) behind the popularity of X-ray imaging techniques such as radiography and tomography. Secondly, high penetration also implies little interaction, which is why X-ray is generally considered as a non-destructive method for the study of solid state physiques.

[Tunable Polarization] Synchrotron sources naturally produce X-rays which are linearly polarized in the horizontal plane (viewed from within the orbital plane), with possibilities of introducing circular and elliptical polarizations at the optics stage. The high degree of polarization and versatile nature of synchrotron X-rays make them the perfect tool for the study of magnetic properties in the subject material.

Below is a list of some commonly used techniques that can be found on a synchrotron beamline, classified by the interaction of X-rays with matter on which the techniques are based.

Interaction	**Techniques**	**Short Wavelength**	**Ideal Energy**	**Strong Penetration**	**Tunable Polarization**
Scattering	X-ray Diffraction	☑	☒	☐	☒
	Small Angle Scattering	☑	☒	☐	☒
	Resonant Scattering	☑	☑	☐	☒
	Coherent Diffraction Imaging	☑	☒	☐	☒
Absorption	Absorption Spectroscopy	☒	☑	☐	☐
	X-ray Dichroism	☒	☑	☐	☑
	Emission Spectroscopy	☒	☑	☐	☒
	Absorption Contrast Imaging	☑	☒	☑	☒
Refraction	Phase Contrast Imaging	☑	☒	☑	☒

Table 1-1: A list of some commonly used techniques that can be found on a synchrotron beamline. ☑ stands for if a property, *e.g.* short wavelength, is fundamental to the application of the technique. ☒ stands for not required ☐stands for optional.

1.2.2. WHY GRAZING INCIDENCE?

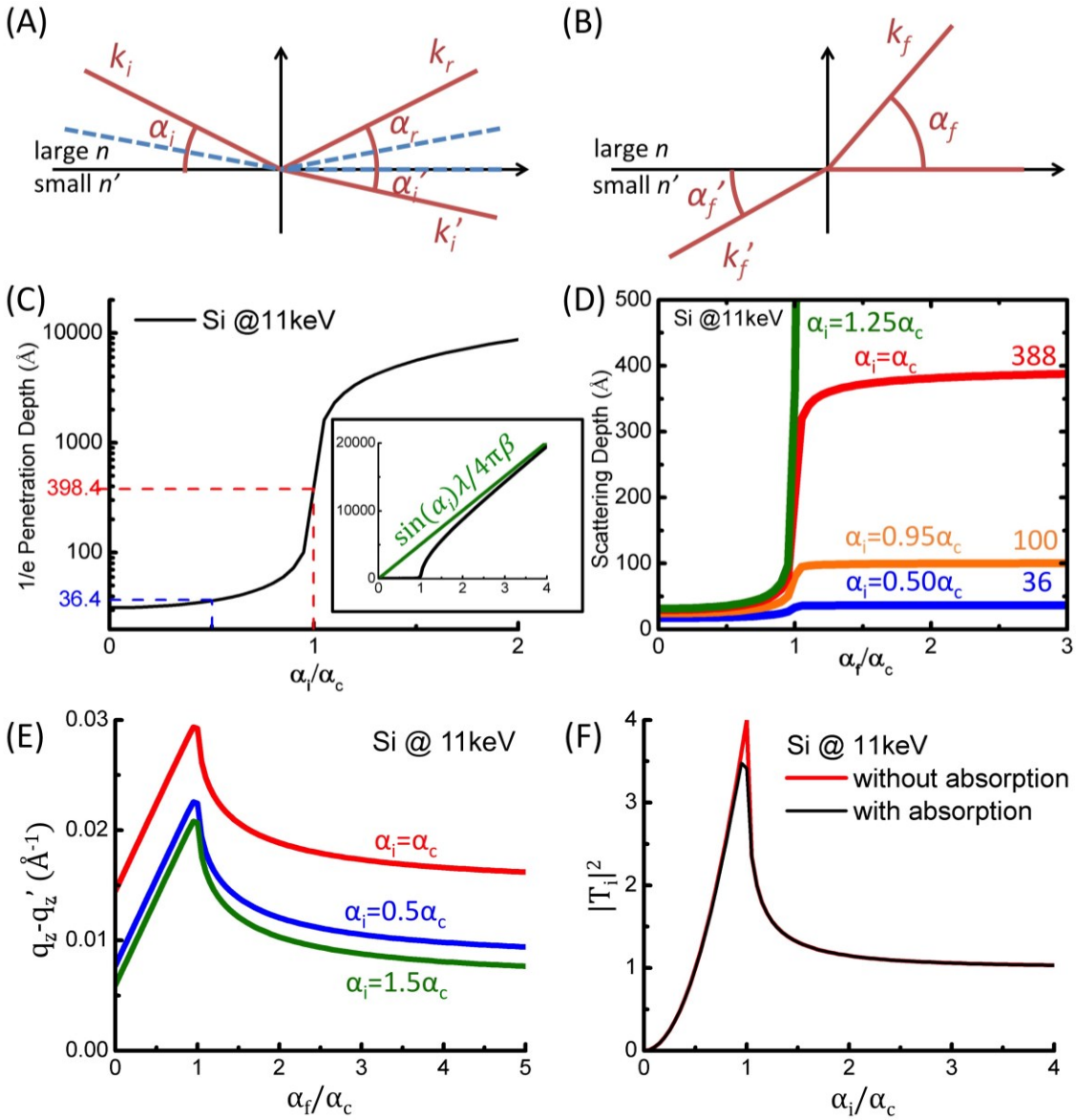

Figure 1-4: (A) Schematics of the reflection and refraction of a plane wave propagating from an optically denser medium to a less dense one. (B) The refraction of the out-going wave using the reciprocity theorem. (C) The penetration depth (in log scale) in the case of Si for 11keV x-ray. (inset) the same plot with linear scale shows that the penetration depth tends to $\sin(\alpha_i)\,\lambda/4\pi\beta$ for large incident angles. (D) The effective scattering depth as a function of the exit angle for various values of incident angle. (E) The difference between the out-of-plane component of the momentum transfer in the vacuum and in the sample as a function of the exit angle for various values of incident angle. (F) Absolute square of the incoming transmittance as a function of the incident angle.

(red solid lines, Figure 1-4A) When an electromagnetic wave travels from a medium with a larger refractive index *n* to one with a smaller index *n'* at incident angle α_i, part of wave is reflected back at $\alpha_r = \alpha_i$, the rest continues to propagate inside the second medium following a slightly deviated trajectory. In terms of Snell's law, this is written as

$$\frac{\cos\alpha_i}{\cos\alpha_i'} = \frac{n'}{n} \qquad (1\text{-}6)$$

Since $n > n'$, the refraction angle α_i' is always smaller than the incident angle α_i. (blue dashed lines, Figure 1-4A) Intuitively if we start to reduce α_i, it will come to a point $\alpha_i = \alpha_c$ where α_i' becomes 0. α_c is called the critical angle below which the incident wave appears to be completely reflected. For visible lights, the phenomenon is known as total internal reflection, and is commonly observed when light is projected from a transparent material (water *n*=1.333, glass *n*=1.46) into vacuum (*n*=1) or air (*n*=1.000293). In the case of X-ray, a similar event occurs when the beam is impinged from vacuum (*n*=1) onto any surface at sub-critical angle, as all materials turn out to have a refractive index (slightly) smaller than unity. The phenomenon is called total external reflection with the term external referring to the fact that the reflection now takes place in the vacuum and thus outside of the given material. We shall ignore absorption at the current stage and present the expression of the refractive index *n* as follows

$$n = 1 - \delta = 1 - 2.701 \times 10^{-6}(Z/A)\,\rho[\mathrm{g/cm^3}]\lambda^2[\mathrm{Å}^2] \qquad (1\text{-}7)$$

Z is the atomic number (14 for Si), *A* is the atomic mass (28.085 for Si) and ρ is the mass density (2.329 for Si). Exchanging *n* with 1 and α_i' with 0 in Equation (1-6)

$$\cos\alpha_c = n' = 1 - \delta \qquad (1\text{-}8)$$

δ is extremely small, of the order of 10^{-6} or 10^{-5} (4.034×10^{-6} for Si at 11keV). This allows the above equation to be further reduced to $\alpha_c = \sqrt{2\delta}$, with typical value of α_c of the order of several mrad (0.163° for Si at 11keV). In reality, besides being refracted, the x-ray is also being gradually attenuated whilst travelling in the material. The refractive index should thus be extended to a complex number to take into account the absorption process.

$$n = 1 - \delta + i\beta \qquad (1\text{-}9)$$

Since both α_i and α_i' are small, Equation (1-6) can be rewritten as

$$\alpha_i^2 = \alpha_i'^2 + 2\delta - 2i\beta = \alpha_i'^2 + \alpha_c^2 - 2i\beta \qquad (1\text{-}10)$$

β is also small and varies from 10^{-8} to 10^{-5}, depending on the material (5.068×10^{-8} for Si at 11keV). Solving the above equation, we obtain

$$\begin{aligned} \alpha_i' &= \mathrm{Re}(\alpha_i') + i\,\mathrm{Im}(\alpha_i') \\ \mathrm{Re}(\alpha_i') &= \left(\sqrt{(\alpha_i^2 - \alpha_c^2)^2 + 4\beta^2} + (\alpha_i^2 - \alpha_c^2)\right)^{1/2}/\sqrt{2} \\ \mathrm{Im}(\alpha_i') &= \left(\sqrt{(\alpha_i^2 - \alpha_c^2)^2 + 4\beta^2} + (\alpha_c^2 - \alpha_i^2)\right)^{1/2}/\sqrt{2} \end{aligned} \qquad (1\text{-}11)$$

The classical description of the refracted wave writes (ignoring the electric field)

$$\exp(-ik_i'\alpha_i' z) = \exp(-ik_i' Re(\alpha_i')z)\exp(k_i'\mathrm{Im}(\alpha_i')z) \qquad (\text{for } Z < 0) \qquad (1\text{-}12)$$

The second term describes an exponential decay of the wave amplitude as it propagates further into the material. For $\alpha_i > \alpha_c$, $\mathrm{Im}(\alpha_i')$ is small, and tends to $\beta/\sin\alpha_i$, which is common for a linear absorption process (Figure 1-4C inset). For $\alpha_i < \alpha_c$, the imaginary part becomes more prominent, resulting in a sharper dampening of the wave amplitude. The direct implication is that the refracted wave, called evanescent, is now confined to just a few hundreds Angstroms below the surface (Figure

1-4C). In other words, only the region close to the surface is probed by impinging x-rays at angles below the critical angle. The enhanced surface sensitivity is one of the two reasons as to why almost all x-ray surface science experiments are conducted under grazing incidence.

To quantitatively evaluate the surface sensitivity, we shall introduce the classic $1/e$ penetration depth, which is defined as the depth at which point the intensity falls to $1/e$ (or $1/2e$ when it comes to the amplitude) of its original value at the surface. From Equation (1-12), immediately we have

$$\Lambda_i = \frac{1}{2k_i' \mathrm{Im}(\alpha_i')} \tag{1-13}$$

For a complete scattering process, the contribution from the out-going wave (the one that is measured by the detector) should also be taken into consideration. The analysis is made simple by the use of the reciprocity theorem which allows us to proceed the analysis in a similar manner as we did with the incoming wave.

$$\begin{gathered} \alpha_f' = \mathrm{Re}(\alpha_f') + i\,\mathrm{Im}(\alpha_f') \\ \mathrm{Re}(\alpha_f') = (\sqrt{(\alpha_f^2 - \alpha_c^2)^2 + 4\beta^2} + (\alpha_f^2 - \alpha_c^2))^{1/2}/\sqrt{2} \\ \mathrm{Im}(\alpha_f') = (\sqrt{(\alpha_f^2 - \alpha_c^2)^2 + 4\beta^2} + (\alpha_c^2 - \alpha_f^2))^{1/2}/\sqrt{2} \\ \Lambda_f = \frac{1}{2k_f' \mathrm{Im}(\alpha_f')} \end{gathered} \tag{1-14}$$

The effective scattering depth is given by

$$\frac{1}{\Lambda} = \frac{1}{\Lambda_i} + \frac{1}{\Lambda_f} \tag{1-15}$$

It can be inferred from the above equation that Λ is dominated by the smaller of the pair Λ_i, Λ_f, which is why the effective scattering depth is always small (*i.e.* always surface sensitive) regardless of the exit angle (out-of-plane detector angle) in a grazing

incidence experiment. Figure 1-4D shows such dependence as a function of the exit angle for various values of incident angle. At $\alpha_i = \alpha_c/2$ and at 11keV, X-rays merely penetrate into 3.6nm of Si, which is equal to 11.5 monolayers along the [111] direction.

Before moving on to the second advantage of grazing incidence experiments, let us take a last look at Equations (1-11) and (1-14). We have previously established that the imaginary part of the refraction angle is associated with the absorption process as the wave propagates inside the material. The real part is in fact useful for calculating the out-of-plane component of the momentum transfer q_z' (*c.f.* next section) inside the sample which, for reason of simplicity, is often replaced by its counterpart in vacuum q_z.

$$q'_{z,\text{sample}} = k(\sin(\text{Re}(\alpha'_i) + \sin(\text{Re}(\alpha'_f))$$
$$q_{z,\text{vacuum}} = k(\sin(\alpha_i) + \sin(\alpha_f) \qquad (1\text{-}16)$$

Figure 1-4E shows the offset between the two values as a function of exit angle for various incident angles. The offset is at its largest for $\alpha_i = \alpha_c$. For a given α_i, the offset is peaked at $\alpha_f = \alpha_c$ then gradually decreases with increasing exit angle. This offset is the main reason why the same out-of-plane Bragg peak of the Si substrate (with refraction) is separated from that of the Si nanowires (without refraction) in a case presented in chapter 5, and should be corrected for most quantitative analysis.

When the incident wave arrives at the surface, its power is distributed between the reflected wave and the refracted (or evanescent) wave. The fraction of the incident power that goes to each part is given by the reflectance R and transmittance T_i, respectively, and can be calculated with Fresnel's equations

$$\text{R} = \frac{\alpha_i - \alpha'_i}{\alpha_i + \alpha'_i}, \qquad T_i = \frac{2\alpha_i}{\alpha_i + \alpha'_i} \qquad (1\text{-}17)$$

$\text{R} + T_i = 1$, as is dictated by the conservation of energy. Let us first ignore absorption for the sake of simplicity by setting β to 0. For $\alpha_i < \alpha_c$, the real part of α'_i

becomes 0 and hence $|R| = 1$. This indicates that all incoming x-rays are reflected back from the surface, which coincides with our previous conclusion of total external reflection below the critical angle. At $\alpha_i = \alpha_c$, we have $\alpha_i' = 0$ and as a result $T_i = 2$. This is an intriguing feature as it implies a two-fold increase in the evanescent amplitude and a four-fold increase in the evanescent intensity! The enhanced signal at critical angle is the second reason for working under grazing incidence. Figure 1-4F shows $|T_i|^2$ as a function of the α_i, with and without taking absorption into account. Note that the overall intensity of the scattering process is at the same time affected by the transmittance of the outgoing wave, which also amounts to 4 for $\alpha_f = \alpha_c$. However, one can rarely benefit from the enhanced $|T_f|^2$ since α_f is seldom fixed in surface diffraction experiments.

1.2.3. (GRAZING INCIDENCE) X-RAY DIFFRACTION

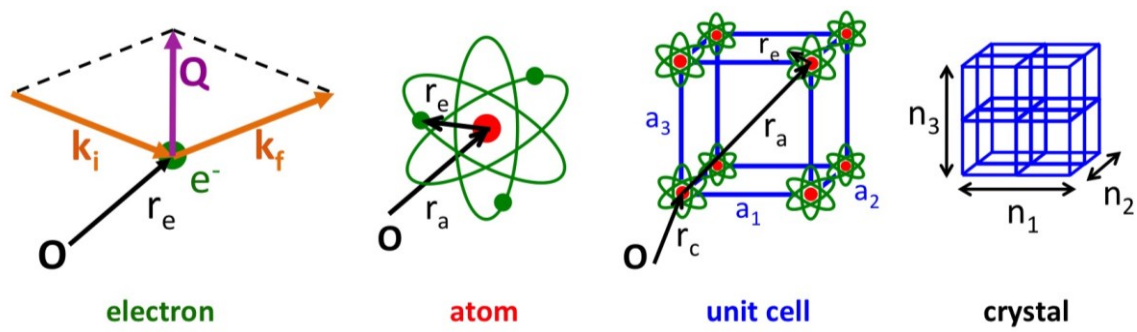

Figure 1-5: Schematics of an incoming wave with wave vector $\mathbf{k_i}$ scattered by an electron at $\mathbf{r_e}$ and definition of the real space vectors used in equations (1-18) to (1-26).

Before we dwell on the classical interpretation (as opposed to derivation with quantum mechanics) of X-ray diffraction by crystalline materials, we need to first introduce the three conditions that help reduce significantly the complexity of the problem, namely, elastic scattering, the Fraunhofer limit, and kinematical approximation. (Figure 1-5) Let us neglect polarization and consider simply an incident wave with amplitude E_0, being scattered by an electron at $\mathbf{r_e}$. The outgoing wave is viewed by an

observer (detector) placed at a distance $\mathbf{R_0}$ from the scattering center. The Fraunhofer limit, also called the far-field limit, requires that the distance R_0 to be sufficiently large. This allows us to treat both the incoming and outgoing X-rays as plane waves, with their amplitude being related by

$$E_1 \exp(-i\mathbf{k_f} \cdot \mathbf{r_e}) = E_0 \frac{r_0}{R_0} \exp(-i\mathbf{k_i} \cdot \mathbf{r_e}) \qquad (1\text{-}18)$$

where $r_0 = e^2/mc^2 = 2.82 \times 10^{-15}$m is the classical radius of electron, also known as the Thomson scattering length. $\mathbf{k_i}$ and $\mathbf{k_f}$ are the wave vectors for the incoming and outgoing wave, respectively. Thomson scattering is essentially elastic (to be distinguished from for example Compton scattering where $|\mathbf{k_i}| > |\mathbf{k_f}|$), in which case we shall have $|\mathbf{k_i}| = |\mathbf{k_f}| = |\mathbf{k}| = 2\pi/\lambda$. Rearranging Equation (1-18) we obtain

$$E_1 = E_0 \frac{r_0}{R_0} \exp(i\mathbf{q} \cdot \mathbf{r_e}) \qquad (1\text{-}19)$$

The momentum transfer $\mathbf{q} = \mathbf{k_f} - \mathbf{k_i}$ (in units Å^{-1}) is a convenient term when addressing elastic X-ray scattering problems. It follows that to calculate the scattering amplitude from an atom at $\mathbf{r_a}$, it suffices to sum up the contribution of all the orbiting electrons. In a classical way, this is achieved by performing an integration of the electron density distribution function $\rho(\mathbf{r_e})$

$$E_2 = E_0 \frac{r_0}{R_0} \int \rho(\mathbf{r_e}) \exp(i\mathbf{q} \cdot (\mathbf{r_a} + \mathbf{r_e}))\, \mathrm{d}\mathbf{r_e} = E_0 \frac{r_0}{R_0} f^0(q) \exp(i\mathbf{q} \cdot \mathbf{r_a}) \qquad (1\text{-}20)$$

$$f^0(q) = \int \rho(\mathbf{r_e}) \exp(i\mathbf{q} \cdot \mathbf{r_e})\, \mathrm{d}\mathbf{r_e} \qquad (1\text{-}21)$$

Note that $f^0(q)$, called the atomic form factor, is nothing but the Fourier transform of the electron density of the given atom. It is sometimes referred to as the atomic scattering factor as it reflects how strong an individual atom scatters the X-ray photons. In the limit that $q \to 0$, all the electrons scatter in phase and we have

$f^0(q=0)=Z$ which is the number of electrons in the atom and at infinity we have $f^0(q\to\infty)=0$. More strictly speaking, the atomic scattering factor is a complex number which deviates considerably from $f^0(q)$ for energies close to some discrete values known as the absorption edges. The complete description of the atomic scattering factor should thus be amended to

$$f(q,\hbar\omega)=f^0(q)+f'(\hbar\omega)+if''(\hbar\omega) \tag{1-22}$$

The analysis of the energy dependent dispersive corrections f',f'' is the essence of anomalous scattering techniques and shall be discussed in details in the next section.

The next logical step would be to calculate the scattering amplitude of a unit cell placed at $\mathbf{r_c}$, by adding up the contribution of all the atoms it contains, each positioned at $\mathbf{r_c}+\mathbf{r_{a,j}}$ with regard to the origin

$$E_3=E_0\frac{r_0}{R_0}\sum_{j=1}^{N_c}f_j^0(q)\exp(i\mathbf{q}\cdot(\mathbf{r_c}+\mathbf{r_{a,j}}))=E_0\frac{r_0}{R_0}F(\mathbf{q})\exp(i\mathbf{q}\cdot\mathbf{r_c}) \tag{1-23}$$

$$F(\mathbf{q})=\sum_{j=1}^{N_c}f_j^0(q)\exp(i\mathbf{q}\cdot\mathbf{r_{a,j}}) \tag{1-24}$$

Instead of remaining firmly at $\mathbf{r_{a,j}}$, the atoms constantly vibrate around their average positions. A Debye-Waller factor is thus appended to the structure factor $F(\mathbf{q})$ to take into account the attenuation caused by these thermal motions.

$$F(\mathbf{q})=\sum_{j=1}^{N_c}f_j^0(q)\exp(-B_j(q/4\pi)^2)\exp(i\mathbf{q}\cdot\mathbf{r_{a,j}}) \tag{1-25}$$

For isotropic vibrations the B-factor is given by $B_j=(8\pi^2/3)\langle u_j^2\rangle$, $\langle u_j^2\rangle$ being the root mean square displacement of atom j from its average position. In most cases, the higher the temperature gets, the more significant the attenuation becomes due to increasing displacements.

A crystalline material, by definition, can be constructed by repeating its unit cell in the directions given by the primitive translation vectors. For the sake of simplicity, let us consider the unit cell to be block shaped (Figure 1-5), with primitive vectors $\mathbf{a_1}$, $\mathbf{a_2}$ and $\mathbf{a_3}$. Under the kinematical approximation (*i.e.*, ignoring multiple scattering events), the final scattering amplitude is simply the geometric sum over all the cells inside the crystal

$$\begin{aligned} E_4 &= E_0 \frac{r_0}{R_0} F(\mathbf{q}) \sum_{n_1=0}^{N_1-1} \sum_{n_2=0}^{N_2-1} \sum_{n_3=0}^{N_2-1} \exp(i\mathbf{q}\cdot(n_1\mathbf{a_1} + n_2\mathbf{a_2} + n_3\mathbf{a_3})) \\ &= E_0 \frac{r_0}{R_0} F(\mathbf{q})\, S_{N_1}(\mathbf{q}\cdot\mathbf{a_1})\, S_{N_2}(\mathbf{q}\cdot\mathbf{a_2})\, S_{N_3}(\mathbf{q}\cdot\mathbf{a_3}) \end{aligned} \tag{1-26}$$

where $S_{N_j}(\mathbf{q}\cdot\mathbf{a_j})$ is called the N-slit interference function

$$S_{N_j}(\mathbf{q}\cdot\mathbf{a_j}) = \sum_{n_j=0}^{N_j-1} \exp(i\mathbf{q}\cdot n_j\mathbf{a_j}) = \frac{1-\exp(i\mathbf{q}\cdot N_j\mathbf{a_j})}{1-\exp(i\mathbf{q}\cdot\mathbf{a_j})} \tag{1-27}$$

$$\left|S_{N_j}(\mathbf{q}\cdot\mathbf{a_j})\right|^2 = \frac{\sin^2(\frac{1}{2}\mathbf{q}\cdot N_j\mathbf{a_j})}{\sin^2(\frac{1}{2}\mathbf{q}\cdot\mathbf{a_j})} \tag{1-28}$$

The intensity of the scattered wave is the absolute square of E_4, and equals to

$$I(\mathbf{q}) = E_0^2 \frac{r_0^2}{R_0^2} |F(\mathbf{q})|^2 |S(\mathbf{q})|^2 \tag{1-29}$$

$$|S(\mathbf{q})|^2 = \left|S_{N_1}(\mathbf{q}\cdot\mathbf{a_1})\right|^2 \left|S_{N_2}(\mathbf{q}\cdot\mathbf{a_2})\right|^2 \left|S_{N_3}(\mathbf{q}\cdot\mathbf{a_3})\right|^2 \tag{1-30}$$

For large N_j, $\left|S_{N_j}(\mathbf{q}\cdot\mathbf{a_j})\right|^2$ yields small values everywhere except for $\mathbf{q}\cdot\mathbf{a_j} = 2\pi m$ ($m \in \mathbb{Z}$), at which point it tends to N_j^2. As a result, the diffracted intensity of the crystal is a three-dimensional Dirac δ-function which peaks at $\mathbf{q}$ values that meet simultaneously the following conditions.

$$\mathbf{q}\cdot\mathbf{a_1} = 2\pi h, \qquad \mathbf{q}\cdot\mathbf{a_2} = 2\pi k, \qquad \mathbf{q}\cdot\mathbf{a_3} = 2\pi l \tag{1-31}$$

The integers h, k and l are called Miller indices. Equation (1-31) is known as the Laue conditions and is fulfilled for all vectors $\mathbf{q} = h\mathbf{b_1} + k\mathbf{b_2} + l\mathbf{b_3}$, with

$$\mathbf{b_1} = 2\pi \frac{\mathbf{a_2} \times \mathbf{a_3}}{\mathbf{a_1} \cdot \mathbf{a_2} \times \mathbf{a_3}}$$
$$\mathbf{b_2} = 2\pi \frac{\mathbf{a_3} \times \mathbf{a_1}}{\mathbf{a_2} \cdot \mathbf{a_3} \times \mathbf{a_1}} \qquad (1\text{-}32)$$
$$\mathbf{b_3} = 2\pi \frac{\mathbf{a_1} \times \mathbf{a_2}}{\mathbf{a_3} \cdot \mathbf{a_1} \times \mathbf{a_2}}$$

We call the space spanned by vectors $\mathbf{b_1}$, $\mathbf{b_2}$ and $\mathbf{b_3}$ the reciprocal space. A linear combination of the aforementioned vectors generates a periodic set of points in the reciprocal space, collectively known as the reciprocal lattice. The reciprocal lattice plays a fundamental role in the studies of periodic structures, more particularly so when it comes to diffraction experiments. For instance, Bragg's law was first proposed after the discovery that solid crystals can produce regular patterns of reflected X-rays. It was later understood that the bright spots observed are the result of constructive interference between waves scattered by parallel lattice planes with interplanar distance d.

$$2d sin\theta = n\lambda \qquad (1\text{-}33)$$

n is a positive integer and θ is the scattering angle. Although not so intuitive, Bragg's law Eq. (1-33) is in fact equivalent to the Laue conditions Eq. (1-31). A demonstration of such equivalence is shown in Figure 1-6A. If, at some point, the momentum transfer $\mathbf{q} = \mathbf{k_f} - \mathbf{k_i}$ is aligned with a vector in the reciprocal lattice so that $\mathbf{q} = h\mathbf{b_1} + k\mathbf{b_2} + l\mathbf{b_3}$, a bright spot (Bragg reflection) will be observed. The normal of the plane sets that contribute to the constructive interference is given by the direction of the vector and their interplanar distance is given by the reciprocal of the vector length $d = 2\pi/|\mathbf{q}|$.

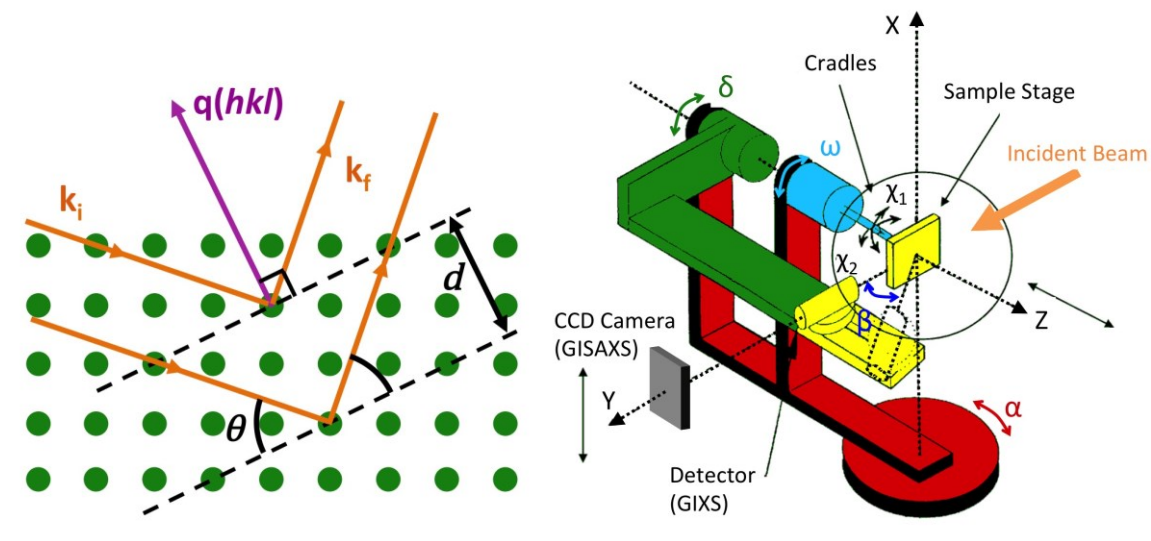

Figure 1-6 : Schematic illustration of (A) the equivalence between Bragg's law and the Laue conditions in coplanar diffraction geometry and (B) a Z-axis diffractometer.

We now take a second look at Equation (1-30), the scattered intensity at points satisfying the Laue conditions is

$$I(hkl) = E_0^2 \frac{r_0^2}{R_0^2} |F(hkl)|^2 N_1^2 N_2^2 N_3^2 \qquad (1\text{-}34)$$

The arrangement of these points (*hkl*) is directly related to the symmetry, orientation and period of the unit cell while their relative intensities (dominated by the term $|F(hkl)|^2$) are indicative of the atom positions inside the unit cell, making X-ray diffraction the perfect tool for resolving atomic structures.

One problem that hinders the practical application of Equation (1-34) for structure resolution is the non-Dirac nature of the peaks. In reality, instead of having zero intensity at positions other than those satisfying the Laue conditions, each peak has a finite breadth, which then depends primarily on three factors, the choice of the optic elements (Darwin width), the calibration of the beam (coherence length) and the crystalline quality (average domain size, strain and defects). The theoretical peak

intensity $I(hkl)$ is hence impossible to evaluate unless measured behind an infinitely small slit centered at the exact position. A more realistic approach is thus introduced. The measurement of the integrated intensity $I_{int}(hkl)$ involves scanning through a 3D volume in the reciprocal space that encompasses the broadened peak. The out-of-plane acceptance, in most cases, is given by the opening of the slits situated in front of the detector while sufficient in-plane acceptance is ensured by simply rotating the sample around its surface normal. The latter is known as a rocking scan. It is worth mentioning that the rocking scan is not the only way for integrating intensities, the same can be very well achieved by scanning along other arbitrary paths in the sample plane. In the event that either acceptance falls short of accommodating the entire peak, multiple measurements should be carried out instead.

For a Z-axis diffractometer (Figure 1-6B) such as the one in operation at BM32, the rocking scan is achieved by the ω rotation. α is the incident angle. δ, β are the in plane and out-of-plane exit angle, respectively. The motors χ_1, χ_2 are reserved for sample alignment. The sample is mounted vertically to avoid the suppressed polarization factor in the orbit plane. The theoretical estimation of the complete integrated intensity is thus

$$I_{int}(\mathbf{q}) = E_0^2 \frac{r_0^2}{\omega_0} \frac{\lambda^3}{V_u} \frac{1}{L} |F(\mathbf{q})|^2 \iiint |S(\mathbf{q})|^2 \, dhdkdl \qquad (1\text{-}35)$$

where ω_0 is the rotation speed, V_u is the volume of the unit cell. $L = \sin\delta \cos\alpha \cos\beta$ is the Lorentzian factor that substitutes integration in the angular space with that in the reciprocal space. $|F(\mathbf{q})|$ is assumed constant in the integration intervals.

We recall that the structure factor $F(\mathbf{q})$ is nothing but the Fourier transform of the electron density of the unit cell. Unfortunately structure resolution by simple inverse Fourier transform cannot be applied since only the amplitude $|F(\mathbf{q})|$ is preserved in the integrated intensity $I_{int}(\mathbf{q})$ whereas information on the phase is lost in the process. The

latter is known as the phase problem in crystallography and shall be discussed further in the next section. Very often, a model of the unit cell is created instead. The theoretical $|F(\mathbf{q})|$ of the model cell is computed and compared to the experimental data. Slight adjustments are carried out after each iteration until a good match is found, at which point the model cell can be considered as a good approximation to the real unit cell structure.

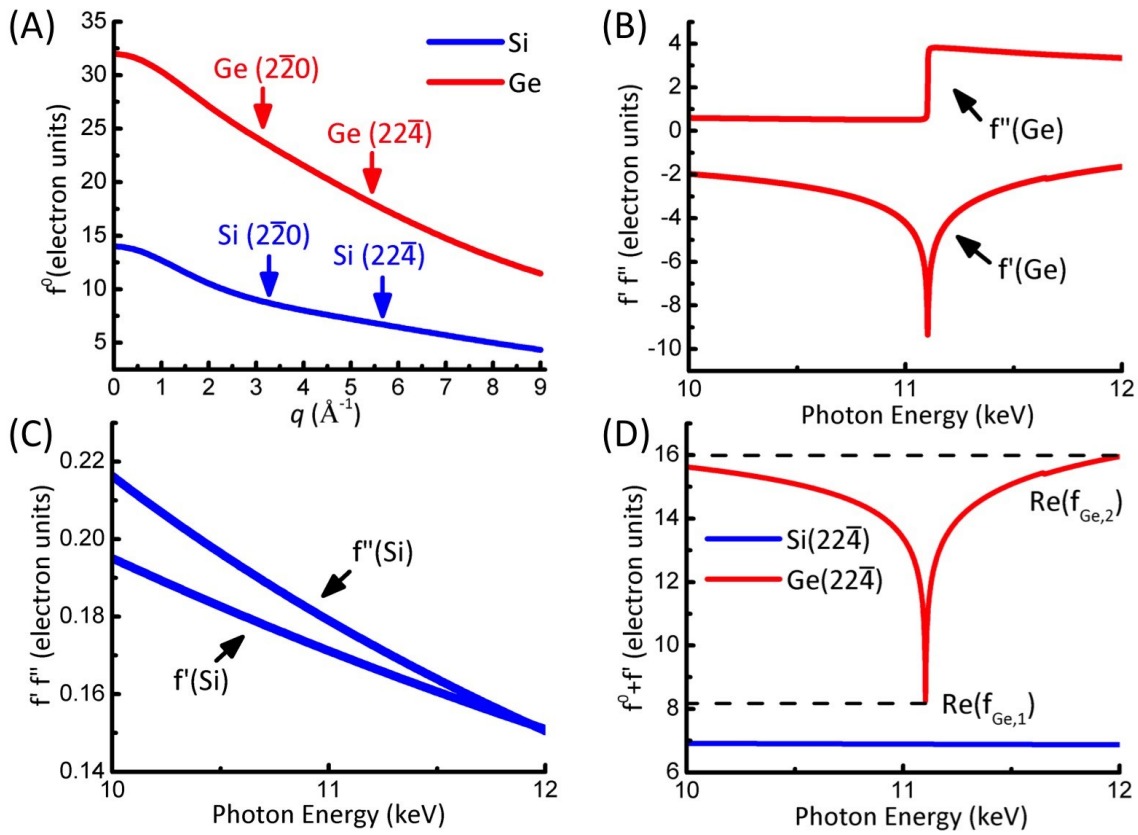

Figure 1-7: (A) The momentum dependence of f^0 of Si and Ge atoms for q ranging from 0 to 9Å^{-1}, the reflections are calculated for photon energy equals to 11keV. The energy dependence of the dispersion corrections of (B) Ge and (C) Si atoms for photon energy between 10 and 12 keV. (D) The real part of the atomic form factor of Si and Ge at q=5.67Å^{-1} (22$\bar{4}$ reflection at 11keV) for photon energy ranging from 10 to 12 keV.

1.2.4. (GRAZING INCIDENCE) MULTIWAVELENGTH ANOMALOUS DIFFRACTION

We have previously stated that the scattering length of an atom, known as the atomic scattering factor, is a complex number composed of two parts, the Thomson term

f^0 and the dispersion corrections f', f''. The Thomson term $f^0(q)$ describes pure scattering of the X-ray photons by the electrons, and is as a result independent of the incoming photon energy. Heavier elements in general contribute more to the scattering (*i.e.* larger $f^0(q)$) as they possess a larger number of atomic electrons. Figure 1-7(A) shows the momentum dependence of $f^0(q)$ of Si and Ge atoms for the accessible q range in our experiments. The values are calculated using the tabulated parameters listed in the International Tables of Crystallography. It can be seen that $f^0(q)$ gradually decreases for increasing q as different electrons in the atom start to scatter out of phase.

In addition to being scattered, X-ray photons can also be absorbed by the atoms in a process known as the photoelectric absorption. The response of a bound electron to the incoming photon is substantially altered for photon energies close to its corresponding binding energy. The resulted modification of the scattering length is taken into account by the dispersion corrections $f'(\hbar\omega), f''(\hbar\omega)$. The dispersion corrections are hence energy dependent, and take on extremal values at discrete energy levels known as the absorption edges. Figure 1-7B and Figure 1-7C show the theoretical values of the dispersion corrections of Ge and Si for energies between 10 and 12keV, respectively. The values are obtained using the Cromer-Liberman Tables. It can be inferred from the figures that while $f'(\mathrm{Ge})$ manifests a significant drop (from -2 to -10) close to its K edge (11103eV), the change in $f'(\mathrm{Si})$ remains negligible (less than 0.02). At q = 5.67Å^{-1} for instance, this translates into a 50% drop in the real part of the Ge atomic scattering factor for photon energy equals to its K edge compared to the values away from the edge, while that of Si can be considered constant (Figure 1-7D). The technique that exploits this huge variation in the scattering factor of an atom near and away from its absorption edges is called anomalous scattering (a.k.a. resonant scattering). The element (*e.g.* Ge in this case) of which the atomic scattering factor varies significantly in the given energy

range is called an anomalous element; the element (*e.g.* Si in this case) of which the atomic scattering factor stays relatively invariant is called a non-anomalous element.

A straightforward application of anomalous scattering is its chemical sensitivity over classic x-ray scattering. Let us consider a homogenous material A_xN_{1-x} composed of two elements, the anomalous element (A) and the non-anomalous element (N). The structure factor of each element is the Fourier transform of its atomic scattering factor, which includes contributions from the atomic form factor and the dispersion corrections.

$$F_N(\mathbf{q}) = \sum (f_N^0 + f_N' + if_N'')\, \mathrm{e}^{i\mathbf{q}\cdot\mathbf{r}} = F_N^0 + F_N' + iF_N'' = |F_N|\mathrm{e}^{i\varphi_N} \qquad (1\text{-}36)$$

$$F_A(\mathbf{q},\hbar\omega) = \sum \left(f_A^0 (1 + \frac{f_A'}{f_A^0} + \frac{if_A''}{f_A^0}) \right) \mathrm{e}^{i\mathbf{q}\cdot\mathbf{r}} = |F_A^0|(1 + \frac{f_A'}{f_A^0} + i\frac{f_A''}{f_A^0})\mathrm{e}^{i\varphi_A} \qquad (1\text{-}37)$$

The scattered intensity from this material is proportional to the square of the sum of the structure factors.

$$I(\mathbf{q},\hbar\omega) \propto |F_N(\mathbf{q}) + F_A(\mathbf{q},\hbar\omega)|^2 = \left| |F_N|\mathrm{e}^{i(\varphi_N - \varphi_A)} + |F_A^0|(1 + \frac{f_A'}{f_A^0} + i\frac{f_A''}{f_A^0}) \right|^2 \qquad (1\text{-}38)$$

which, after further development, becomes

$$\begin{aligned} I(\mathbf{q},\hbar\omega) \propto\ & |F_N|^2 + |F_A^0|^2 [\left(1 + \frac{f_A'}{f_A^0}\right)^2 + (\frac{f_A''}{f_A^0})^2] \\ & + 2|F_N F_A^0|(1 + \frac{f_A'}{f_A^0})\cos(\varphi_N - \varphi_A) + 2|F_N F_A^0|\frac{f_A''}{f_A^0}\sin(\varphi_N - \varphi_A) \end{aligned} \qquad (1\text{-}39)$$

Note that there are only three unknowns in the above equations, F_N, F_A^0 and $\varphi_N - \varphi_A$, which means that it suffices to measure $I(\mathbf{q},\hbar\omega)$ at three different energies to determine their exact value. In practice however, it is advised to collect data points at at least ten (sometimes over twenty) energies in order to improve the accuracy of the results. The composition of the anomalous element *x* in an disordered material can then be estimated using the following formula

$$\frac{F_N}{F_A^0} = \frac{(1-x)f_N}{xf_A^0} \qquad (1\text{-}40)$$

The procedure described above is known as MAD, short for Multiwavelength Anomalous Diffraction. In the case of homogenous compounds, it converts the intensity contrast between measurements at different energies into knowledge of the chemical composition x of the anomalous element. It is obvious from Equation (1-39) that in order to increase the sensitivity of the technique, the values of the two variables f_A', f_A'' should be as scattered as possible. This requires one of the measurements to be carried out preferably very close to the absorption edge and one far away from it. Alternatively, one could enhance the sensitivity by reducing $f_A^0(\mathbf{q})$ found in the denominator, which is why most anomalous experiments are performed at large q reflections (*c.f.* Figure 1-7A).

It can also be inferred from Equation (1-39) that the result of the technique relies heavily on the accurate knowledge of the dispersion corrections. Theoretical estimation of $f', f''$for isolated atoms only yields smooth line-shapes (red lines, Figure 1-8A) and fails in reproducing the wiggling features near the absorption edge (black lines, Figure 1-8A) which are related to the chemical environment of the atoms. The dispersion corrections should thus be calibrated experimentally. Direct measurement of f' is possible, for instance by measuring the real part of the refractive index $1-\delta$ of the material. However, it is often a lot easier to first determine f'' instead, as it is closely related to the linear absorption coefficient μ,

$$\mu = \sum_j \rho_{at,j}\sigma_{a,j} = 2r_0\lambda \sum_j \rho_{at,j} f_j'' \qquad (1\text{-}41)$$

Here, ρ_{at} is the number density, σ_a is called the absorption cross-section, r_0 is the classic electron radius and λ is the wavelength of the X-ray. The sum runs over all

the elements present in the material. It follows that μ can be obtained simply by measuring the transmitted intensity I_{trans} or the fluorescence intensity I_{fluo}.

$$\mu \propto -\log(I_{trans}/I_0) \quad , \quad \mu \propto I_{fluo}/I_0 \tag{1-42}$$

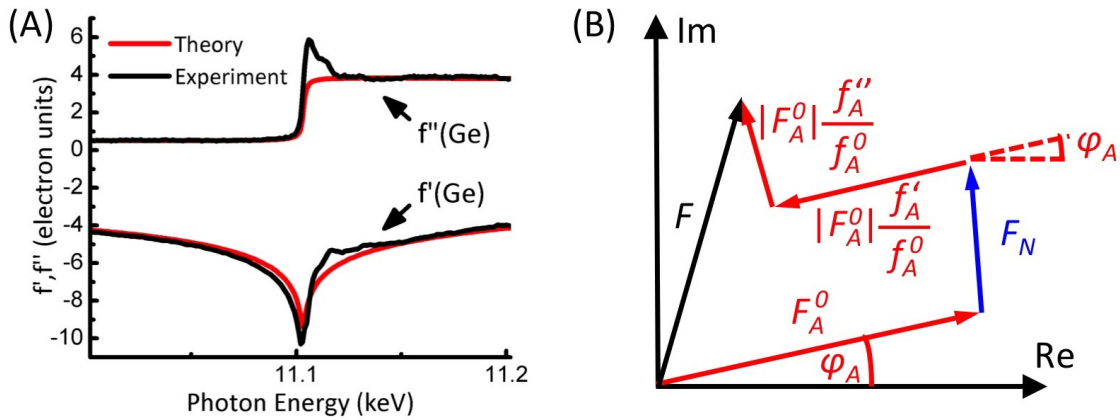

Figure 1-8: (A) The dispersion corrections determined experimentally (black lines) compared to the theoretical values for isolated atoms (red lines) for Ge in the vicinity of its K edge. (B) Schematic representation in the complex plane of the structure factor F, and its relationship with the partial structure factors F_N, F_A^0 and $F_T = F_N + F_A^0$.

In practice, knowing the exact value of μ often proves unnecessary. Instead, one only needs to collect the fluorescence intensity within a few hundred electron volts from the absorption edge, normalize it with the incident intensity I_0, and rescale it to match the theoretical curve at points unaffected by the anomalous behavior. An example of such calibration will be shown in chapter 4.

With the refined f'' at our disposal, the experimental values of f' can now be obtained indirectly, using the Kramers-Kronig relations

$$\begin{aligned} f'(\omega) &= \frac{2}{\pi}\mathcal{P}\int_0^{+\infty} \frac{\omega' f''(\omega)}{(\omega'^2 - \omega^2)}\, d\omega' \\ f''(\omega) &= -\frac{2\omega}{\pi}\mathcal{P}\int_0^{+\infty} \frac{f'(\omega')}{(\omega'^2 - \omega^2)}\, d\omega' \end{aligned} \tag{1-43}$$

$\mathcal{P}$ being the principle value of the integral at the singularity ($\omega' = \omega$). The above equation allows us to calculate, in theory, one of the two dispersion corrections with the knowledge of the other. The major drawback is that it requires integration to be performed from 0 to ∞, which may prove challenging for numerical calculations. Very often the so called difference Kramers-Kronig relations is used instead

$$f'(\omega) = f'_{th}(\omega) + \frac{2}{\pi}\mathcal{P}\int_0^{+\infty} \frac{\omega'|f''(\omega) - f''_{th}(\omega)|}{(\omega'^2 - \omega^2)}\, d\omega' \qquad (1\text{-}44)$$

Here, $f'_{th}(\omega)$ and $f''_{th}(\omega)$ are the theoretical values of the dispersion corrections for isolated atoms. The ingenuity of the idea is that $|f''(\omega) - f''_{th}(\omega)|$ is only non-zero within several hundred electron volts from the absorption edge, which reduces the interval of the integration to a finite energy range.

But MAD does more than just solving the unknown composition in the material compound. Considering the same experiment on a material with only non-anomalous elements, or as we would call it, classic X-ray diffraction. We recall the structure factor of the unit cell to be

$$F(\mathbf{q}) = \sum_{j=1}^{N_c} f_j(q) \exp\left(-B_j\left(\frac{q}{4\pi}\right)^2\right) \exp(i\mathbf{q}\cdot\mathbf{r}_{\mathbf{a,j}}) = |F(\mathbf{q})| \exp(i\varphi) \qquad (1\text{-}45)$$

The intensity that we measure only retains the amplitude $|F(\mathbf{q})|$ of the structure factor, while the phase φ is lost in the process.

$$I(\mathbf{q}) \propto |F(\mathbf{q})|^2 |\exp(i\varphi)|^2 = |F(\mathbf{q})|^2 \qquad (1\text{-}46)$$

φ contains information on the relative positions of the atoms in the unit cell, without which a direct structure resolution from the intensity $I(\mathbf{q})$ is extremely difficult, if not impossible. This is known in crystallography as the phase problem. There exist several other ways to recover the lost phase, for instance by using the Patterson function

or with Coherent Imaging. In the case of MAD, the lost phase is retrieved by first solving the structure of the anomalous element using F_A^0, from which φ_A can be readily deduced. This then allows us to calculate the more complicated phase φ_N with the help of $\varphi_N - \varphi_A$. Note that unlike φ_A, the knowledge of F_N alone may not be sufficient to deduce φ_N, as there may be a huge number of non-anomalous atoms of different elements in the structure (*e.g.* macromolecules).

1.2.5. (GRAZING INCIDENCE) SMALL ANGLE X-RAY SCATTERING

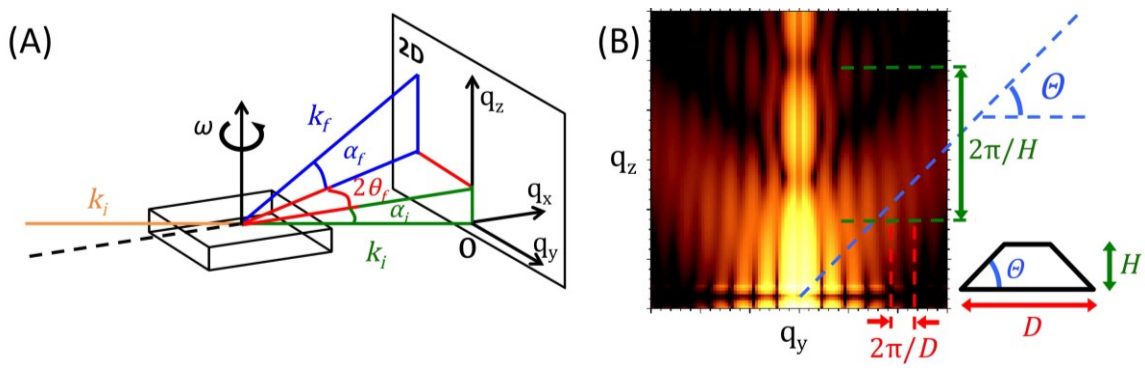

Figure 1-9: (A) Scattering geometry of a GISAXS experiment. (B) GISAXS simulation of a sample with well organized truncated pyramid-shaped nanoparticles at its surface.

Figure 1-9A shows the scattering geometry of a GISAXS experiment. Instead of being mounted on a movable arm, a 2D detector is placed right in the path of the incident beam. Information on a rather small region in the vicinity of the origin of the reciprocal space (**O**) is collected, with

$$\begin{aligned} q_x &= k(\cos\alpha_f \cos 2\theta_f - \cos\alpha_i) \\ q_y &= k(\cos\alpha_f \sin 2\theta_f) \\ q_z &= k(\sin\alpha_f + \sin\alpha_i) \end{aligned} \qquad (1\text{-}47)$$

The sample detector distance is often very large (> 1m). A shorter distance allows a wider q range to be measured while a longer distance offers better resolution per pixel. Figure 1-9B shows what a typical GISXAS image would look like (on simulation) for a

sample surface covered with ordered identical truncated pyramid-shaped nanoparticles. Several morphological parameters such as the slope Θ, the diameter D and the height H can be deduced almost immediately by measuring the angle and the period of the intensity modulation. Although such result remains purely qualitative and can sometimes even be proven misleading, this fast analysis does offer a unique and comprehensive view of the surface morphology which can be particularly helpful during *in situ* experiments.

More accurate and quantitative analysis requires, like we did earlier with GIXD, simulation and fitting of a preconceived model since information on the phase is once again lost during data acquisition. Although seemingly two disparate techniques, *e.g.* one with a fixed camera while the other has a movable detector, one reveals morphological information while the other is intended for structural analysis, GISAXS is in fact merely a special case of GIXD. To illustrate this, let us consider a sample surface covered with dense disordered nanoparticles of identical shape and derive, based on that, the formulae for GISAXS calculation analogous to what we've previously established with GIXD.

(Figure 1-10A) A crystal can be constructed by convoluting its unit cell with a regular array of nodes. The scattered intensity from such crystal $I_{GIXD}(\mathbf{q})$, as was shown in Equation (1-29), is simply the product of the absolute square of the structure factor $|F_{cell}(\mathbf{q})|^2$ and the absolute square of the crystalline interference function $\left|S_{crys}(\mathbf{q})\right|^2$. Similarly, we can reconstruct our sample surface by convoluting one nanoparticle with a set of randomly distributed nodes. The scattered intensity from the ensemble of the disordered nanoparticles $I_{GISAXS}(\mathbf{q})$ should be, by analogy, the absolute square of the structure factor (also known as the form factor) of the nanoparticle $\left|F_{np}(\mathbf{q})\right|^2$ and the absolute square of the amorphous like interference function $|S_{amor}(\mathbf{q})|^2$.

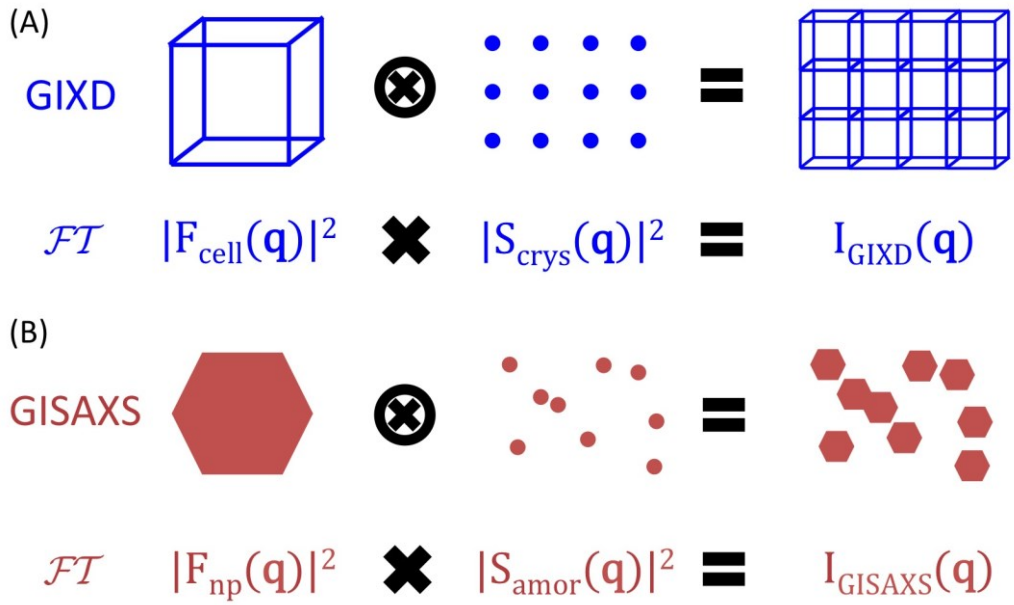

Figure 1-10 : Illustration of the correspondence between real space scenario and their Fourier transform in the case of (A) GIXD and of (B) GISAXS.

Just as the structure factor $F_{cell}(\mathbf{q})$ is the Fourier transform of the electron density of the unit cell, the form factor $F_{np}(\mathbf{q})$ is in fact the Fourier transform of the electron density of the nanoparticle.

$$F_{cell}(\mathbf{q}) = \int^{cell} \rho(\mathbf{r_e}) \exp(i\mathbf{q}\cdot\mathbf{r_e})\, \mathrm{d}\mathbf{r_e} \qquad (1\text{-}48)$$

$$F_{np}(\mathbf{q}) = \int^{particle} \rho(\mathbf{r}'_e) \exp(i\mathbf{q}\cdot\mathbf{r}'_e)\, \mathrm{d}\mathbf{r}'_e \qquad (1\text{-}49)$$

$|\mathbf{r_e}|$ is typically of the order of a fraction of the lattice constant (~ 1Å). $|\boldsymbol{r}'_e|$ however, is often one or two orders of magnitude larger considering the size of the nanoparticles. The direct implication is that the corresponding momentum transfer q is one order of magnitude smaller in GISAXS than in GIXD, which is the reason why GISAXS experiments are performed close to the origin of the reciprocal space ($q \sim 1/|\boldsymbol{r}'_e| \sim 0.01\text{Å}^{-1}$). The fitting of the form factor is one of the main objectives of

GISAXS analysis as it holds the key to unlock all the morphological information (size, shape, etc.) of the surface structure.

Also similar is the amorphous like interference function $S_{amor}(\mathbf{q})$, which has the exact same formulation as Equation (1-27) except that the sum no longer runs over a periodic structure and can thus not be simplified in the same way as $S_{crys}(\mathbf{q})$.

$$S_{amor}(\mathbf{q}) = \sum_{\boldsymbol{n}} \exp(i\mathbf{q} \cdot \mathbf{r_n}) \tag{1-50}$$

$$|S_{amor}(\mathbf{q})|^2 = \sum_{\boldsymbol{m}} \exp(-i\mathbf{q} \cdot \mathbf{r_m}) \sum_{\boldsymbol{n}} \exp(i\mathbf{q} \cdot \mathbf{r_n}) = \sum_{\boldsymbol{n}} \sum_{\boldsymbol{m}} \exp(i\mathbf{q} \cdot (\mathbf{r_n} - \mathbf{r_m})) \tag{1-51}$$

Separate the terms with $n = m$ from those with $n \neq m$, we have

$$|S_{amor}(\mathbf{q})|^2 = N + \sum_{\boldsymbol{n}} \sum_{\boldsymbol{m \neq n}} \exp(i\mathbf{q} \cdot (\mathbf{r_n} - \mathbf{r_m})) \tag{1-52}$$

N is the total number of particles. The intensity contrast of X-ray scattering ultimately arises from deviations in electron density from its average value. If we now introduce the average density of the nanoparticles ρ_a, and $\rho_n(\mathbf{r_m})dV_m$ the number of nanoparticles found in the volume element dV_m centered at $\mathbf{r_m}$, the above equation can be rewritten as

$$|S_{amor}(\mathbf{q})|^2 = N + \sum_{\boldsymbol{n}} \int_{\boldsymbol{V}} (\rho_n(\mathbf{r_m}) - \rho_a) \exp(i\mathbf{q} \cdot (\mathbf{r_n} - \mathbf{r_m})) dV_m \tag{1-53}$$

Equation (1-53) can be further simplified if an average is performed over different choices of origin, in other words, $\rho_n(\mathbf{r_m}) \rightarrow \rho(\mathbf{r})$,

$$\begin{aligned} |S_{amor}(\mathbf{q})|^2 &= N + N \int_{\boldsymbol{V}} (\rho(\mathbf{r}) - \rho_a) \exp(i\mathbf{q} \cdot \mathbf{r}) dV \\ &= N\,(1 + \rho_a \int_{\boldsymbol{V}} (g(\mathbf{r}) - 1) \exp(i\mathbf{q} \cdot \mathbf{r}) dV) \end{aligned} \tag{1-54}$$

Here $\rho(\mathbf{r})$ is the radial density of the nanoparticles and $g(\mathbf{r}) = \rho(\mathbf{r})/\rho_a$ is the reduced radial pair correlation function. In the case of a two-dimensional distribution,

$$\rho(\mathbf{r}) = N(r)/(2\pi r dr) \qquad (1\text{-}55)$$

$N(r)$ is the average number of particles found in an annulus of radius r and thickness dr. For crystalline materials, $g(\mathbf{r})$ exhibits a series of peaks that oscillate towards infinity. For amorphous like materials, such as disordered nanoparticles, $g(\mathbf{r})$ quickly converges to unity as the peaks dampen and broaden out with increasing r. The radial distribution function contains information on the inter-particle distance and can be retrieved through inverse Fourier transform of Equation (1-54) once the interference function $|S_{amor}(\mathbf{q})|^2$ is determined by the fitting of the GISAXS intensity.

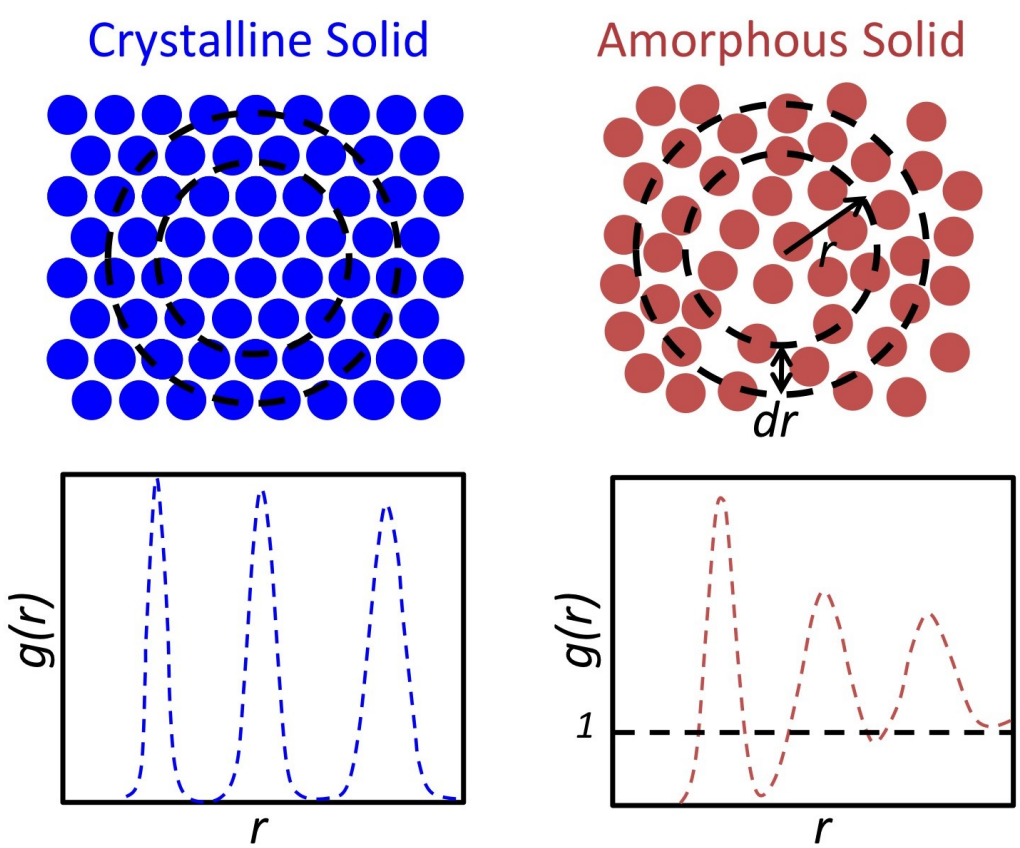

Figure 1-11 : Schematic illustration of the radial distribution function for (left) crystalline and (right) amorphous materials, respectively.

The above consideration is valid for a concentrated system of nanoparticles. In the case of diluted nanoparticles (think of it as a dense system of void), $|S_{amor}(\mathbf{q})|^2 \sim 1$, and the simple form factor described in Equation (1-49) alone is sufficient for the calculation of the GISAXS intensity. But that is not all, multiple scattering event at the surface has to be taken into account as intensity calculation using the kinematic approximation (also known as the first order Born Approximation or BA) deviates significantly from experimental observations, especially for incidence angle close to or below the critical angle. The Distorted Wave Born Approximation (DWBA) is thus introduced, the primary objective of which is to include the contribution of unaccounted for scattering events that arise from the perturbations of the incident and reflected wavefield by surface structures.

The DWBA treatment of multiple scattering events differs for each system. In the case of disordered nanoparticles at the sample surface, the classic form factor is amended to account for three more scenarios in which the incident wave and/or the exit wave is reflected by the sample surface. (Figure 1-12A) The out-of-plane momentum transfer q_z is carefully reevaluated for each scenario and the resulting form factor is further weighted by their corresponding reflectance, which was previously introduced in Equation (1-17).

$$\begin{aligned}\mathcal{F}(\mathbf{q}) &= \mathcal{F}\left(k_{f\parallel} - k_{i\parallel}, \mathrm{q}_z\right) = \mathcal{F}\left(k_{f\parallel} - k_{i\parallel}, k_{fz}, k_{iz}\right) \\ &= F_{np}\left(k_{f\parallel} - k_{i\parallel}, k_{fz} - k_{iz}\right) + R_i F_{np}\left(k_{f\parallel} - k_{i\parallel}, k_{fz} + k_{iz}\right) \\ &+ R_f F_{np}\left(k_{f\parallel} - k_{i\parallel}, -k_{fz} - k_{iz}\right) + R_i R_f F_{np}\left(k_{f\parallel} - k_{i\parallel}, -k_{fz} + k_{iz}\right)\end{aligned} \quad (1\text{-}56)$$

(Figure 1-12B) For a given incidence angle, the 3rd and 4th terms remains significant only for exit angle smaller than the critical angle, beyond that both terms starts to tail off as R_f starts to vanish. Other than that, the amended form factor is primarily dominated by two contributions, the original form factor (BA, 1st term) and the one scattered by a reflected incident wave (2nd term). For subcritical incident angle ($R_i \sim 1$), the only difference between the two contributions is a shift of $2\alpha_i$ on the exit angle.

Alternatively, the result can be perceived as a shifted replica of the entire BA intensity being created by the reflected incident beam. The duplication of the scattered intensity will be further demonstrated in Chapter 3 and 5. (Figure 1-12C) For larger incidence angle, even the 2nd term becomes insignificant as R_i begins to fade. (Figure 1-13B) The DWBA form factor is thus very close to the original BA form factor, except for $\alpha_f \sim \alpha_c$, where an abrupt increase in intensity (the Yoneda wing) can be clearly observed.

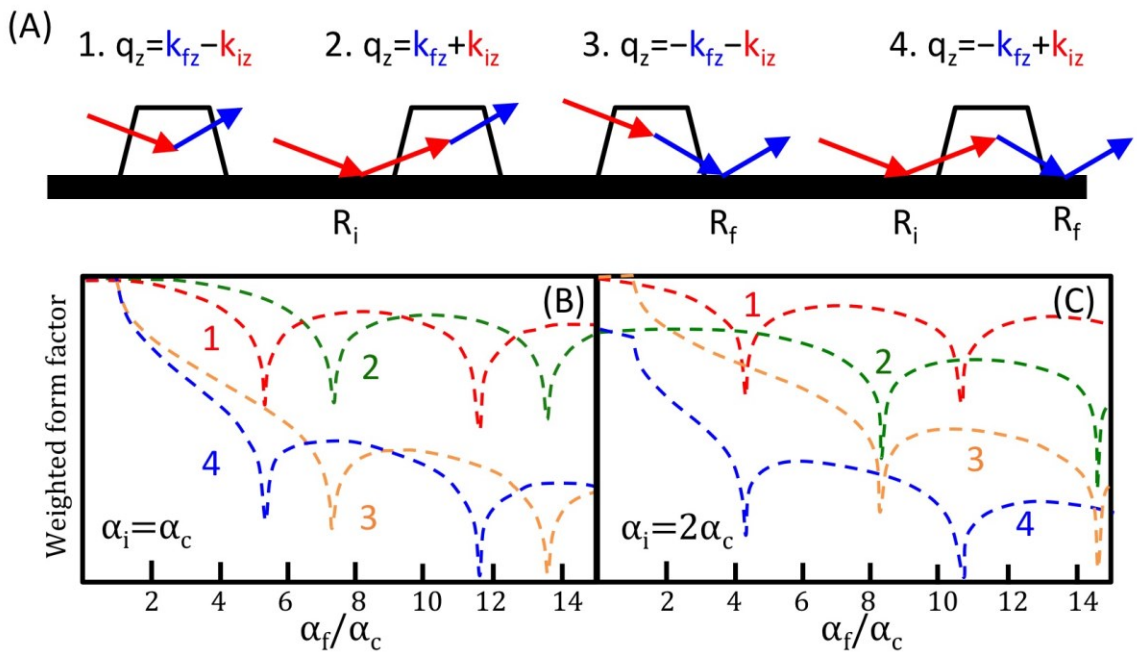

Figure 1-12 : (A) Schematic representation of the four scattering scenarios described in DWBA. The four terms of the new form factor in logarithmic scale, each weighted by their corresponding reflectance, for (B) $\alpha_i=\alpha_c$ and (C) $\alpha_i=2\alpha_c$, respectively. The calculation is based on cylindrical nanoparticles with height equal to 5nm.

With all that in consideration, the complete formula, within the Decoupling Approximation, for GISAXS of a concentrated system of disordered nanoparticles writes

$$I_{GISAXS}(\mathbf{q}) = \left|\overline{\mathcal{F}(\mathbf{q})}\right|^2 \cdot N\left(1+\rho_a \int_V (g(\mathbf{r})-1)\exp(i\mathbf{q}\cdot\mathbf{r})dV\right) + \underbrace{N\left(\overline{|\mathcal{F}(\mathbf{q})|^2} - \left|\overline{\mathcal{F}(\mathbf{q})}\right|^2\right)}_{incoherent\ term} \quad (1\text{-}57)$$

The incoherent term emerges to account for the variation in size, shape and mosaicity of the nanoparticles, therefore vanishes in the ideal case consisting of only identical particles ($\overline{|\mathcal{F}(\mathbf{q})|^2} - \left|\overline{\mathcal{F}(\mathbf{q})}\right|^2 = 0$).

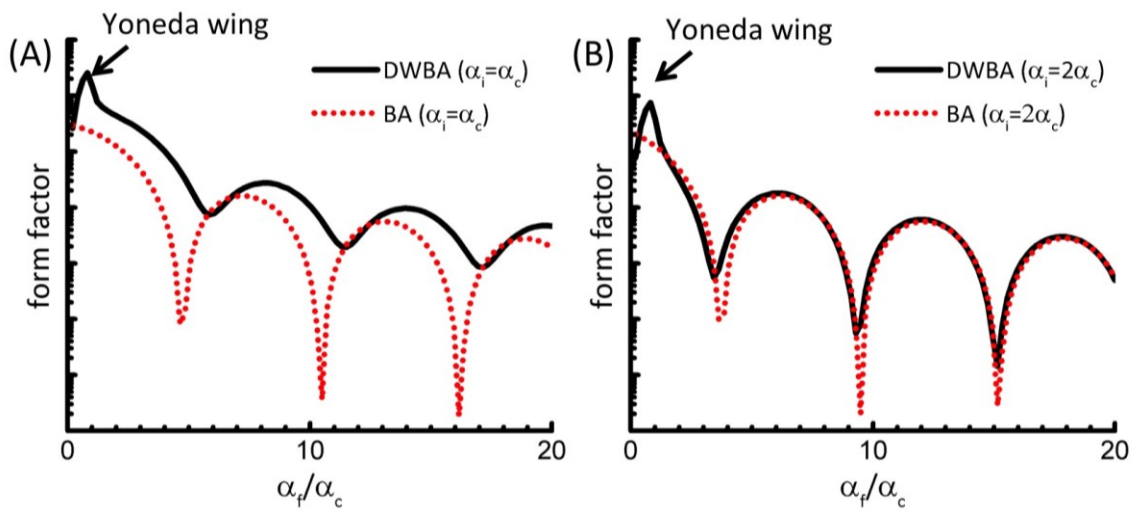

Figure 1-13 : Comparison between the DWBA form factor and the BA form factor for α_i=α_c and α_i=2α_c, respectively.

1.2.6. OTHER TECHNIQUES

Two other techniques were heavily employed over the course of this study, Reflection High Energy Electron Diffraction (RHEED) for qualitative surface characterization under UHV and Scanning Electron Microscopy (SEM) for *ex situ* sample imaging.

RHEED shares many similarities with GIXD, in that both are diffraction based surface sensitive techniques working at very low incidence angles. The electron beam is generated by a cathode ray tube and focused using an electric and a magnetic field. A phosphor screen is placed on the other side of the sample to record constructive interference of the scattered electrons. Typical electron energy ranges from 10-30keV, which corresponds to a wavelength of 0.12-0.07Å. The smaller wavelength (compared to

~1 Å as in GIXD) allows several orders of the Laue Zone to be accessed simultaneously by the detector, making it possible for fast yet comprehensive analysis of the surface structure. RHEED is hence an ideal tool for fast surface quality (surface reconstruction etc.) verification. The major drawback of RHEED is its complexity when it comes to quantitative analysis. Multiple scattering process has to be taken into account due to the much stronger interaction of matter with electrons compared to that with X-ray photons.

SEM, and sometimes its variants, EDS (Energy Dispersive x-ray Spectroscopy), STEM (Scanning Transmission Electron Microscopy) are the only tools employed in this work that grant us access to the microscopic view of the sample surface in real space. SEM scans the sample surface with a focused beam of electrons, the interaction of which produces a wide range of signals (secondary electrons, backscattered electrons, characteristic X-ray, etc.). A detector then collects these signals, most commonly secondary electrons which, when combined with the position of the electron probe, can be used to compute a topographic image of the sample surface. EDS operates in a rather similar fashion except that it works with characteristic X-ray. The characteristic X-ray contains information on the chemical composition of the surface atoms, and can be thus used for elemental mapping of the sample surface. If the sample is thin enough, transmitted electrons can be observed at the back of the sample stage as part of the electron beam manages to break through. STEM detectors collect these electrons and use them for contrast imaging. The sample preparation is much more delicate and more complicated for STEM than for SEM, but the result can sometimes be very rewarding especially when it comes to core-shell heterostructures.

References:

Als-Nielsen, J. & McMorrow, D., 2011. Elements of Modern X-ray Physics, Second Edition. Wiley Online Library. Available at: http://onlinelibrary.wiley.com/book/10.1002/9781119998365.

Warren B.E., X-Ray Diffraction. Dover Publications, Inc., New York (1990).

Guinier, A. X-ray Diffraction in Crystals, Imperfect Crystals, and Amorphous Bodies. Dover Publications, Inc., New York (1994).

Robinson, I. K. & Tweet, D. J. Surface X-ray diffraction. Reports Prog. Phys. 55, 599–651 (1992).

Feidenhans'l, R. Surface structure determination by X-ray diffraction. Surf. Sci. Rep. 10, 105–188 (1989).

Renaud, G., Lazzari, R. & Leroy, F. Probing surface and interface morphology with Grazing Incidence Small Angle X-Ray Scattering. Surf. Sci. Rep. 64, 255–380 (2009).

Vlieg, E. Integrated Intensities Using a Six-Circle Surface X-ray Diffractometer. J. Appl. Crystallogr. 30, 532–543 (1997).

[This Page Intentionally Left Blank]

2. UHV-CVD GROWTH OF SI/GE NWS

This chapter is structured as follows. The first half serves as a general introduction to the VLS growth of Si/Ge NWs. It covers various key aspects ranging from the choice of metal catalysts and growth methods to the size-related behaviors of the NWs. The second half is intended as a literature review on the recent progress in the research community. Instead of citing directly from others' reports, we chose to present each time some *ex situ* SEM images of our own NWs, followed by established explanations in the literature with regard to our observations. The objective, aside from showing the current state of NW growth at our experimental end station, is to provide our understanding regarding some of the subjects still under debate, *e.g.,* the VLS or VSS nature of Ge NW growth, conditions that hinder proper NW growth, etc.

2.1.VLS growth and UHV-CVD

2.1.1. NANOWIRES IN A NUTSHELL

NWs are one dimensional (1D) structures the transverse dimensions of which (diameter, typically 1 to 500nm) are far smaller compared to their axial dimension (length, can be as long as tens of microns). The current research on inorganic NWs can be divided into three categories, metallic NWs (more often called metal whiskers for historical reasons), semiconducting NWs (*e.g.* Si, Ge, ZnO, InAs, etc.) and insulating NWs (or dielectric NWs), due to their distinctive differences in both physical properties and potential applications. Typical synthesis methods for semiconductor NWs consist of two paradigms, namely the top-down and the bottom-up approach. The top-down approach relies on dimensional reductions where the nanostructures are "carved" from a piece of bulk material, primarily via lithography and etching. The bottom-up approach builds the NWs "block by block" with constituent adatoms, usually supplied by Chemical

Vapor Deposition or by Molecular Beam Epitaxy. In short, the bottom-up approach can be used to synthesize NWs with diameter ranging from hundreds of nanometers down to several angstroms but falls short when it comes to position and size control unless aided by patterning techniques (*e.g.* nanoimprint lithography (Costner et al. 2009), nanosphere lithography (Fan et al. 2006), etc.). The top-down approach, on the other hand, has difficulties creating sub-10nm structures, as limited by the Rayleigh criterion (Rai-Choudhury 1997) in the case of optical lithography or by the proximity effect (Alexander Liddle et al. 2011) in the case of Electron Beam Lithography, but is more advantageous in terms of integration, thanks to their compatibility with the standard microelectronics fabrication processes.

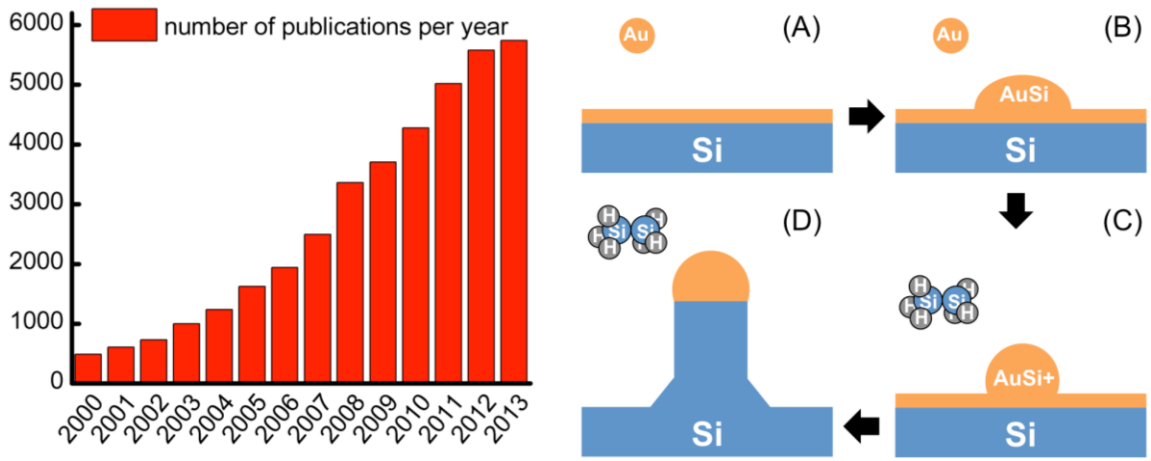

Figure 2-1 : (left) Number of publications on nanowires per year since the beginning of the 21st century, resource from ISI. (right) Schematics of the VLS mechanism with Au as the metal catalyst and Si_2H_6 as the precursor gas, with (A) the formation of the wetting layer (B) the formation of the liquid catalyst alloy (C) supersaturation of the catalyst alloy upon gas injection (D) steady growth of the NWs.

Although research interest can be traced back to the 1960s when R.S. Wagner first detailed his findings on the revolutionary Vapor-Liquid-Solid growth mechanism, or to as far as the 1750s where metal filaments naturally occurred on minerals and slags

were first observed (Henckel 1757), NWs are still receiving steadily growing attention even today (Figure 2-1 left), thanks to their peculiar and fascinating properties superior to their bulk counterparts. Current applications of semiconductor nanowires include electronic (Lieber & Wang 2011), photonic (Hayden et al. 2006), thermoelectric (Snyder & Toberer 2008), spintronic (Awschalom & Flatté 2007), biological (Fischer et al. 2009) and energy (Chan et al. 2008) devices.

2.1.2. VLS AND VSS

Discovered more than half a century ago (Wagner & Ellis 1964), the Vapor-Liquid-Solid mechanism is unarguably the most commonly adopted methods for bottom-up NW synthesis and the driving force behind contemporary NW researches and applications, owing to its sheer simplicity, high productivity (wafer scale growth rate ~ tens of microns per hour), wide applicability (works for almost all kinds of semiconductor NWs and with most metals as catalysts) and low requirement (UHV not necessary, etc.). The name VLS refers to the pathways taken by the building blocks of the NWs (in this case Si). The Si atoms first arrive at the surface in the form of their gas (hence **V**apor) precursors, and then incorporate themselves into the **L**iquid catalyst alloy upon preferential decomposition. The phase diagram of Au-Si at equilibrium dictates that only a limited amount of Si is allowed in the catalyst alloy. The additional Si atoms are being disposed of via precipitation at the liquid/solid interface where they become part of the **S**olid NW body. A simple thermodynamics model suggests that a certain level of supersaturation (higher Si content in the alloy than at equilibrium) is required for the nucleation to occur (Schmidt et al. 2010). The supersaturation ratio during steady growth itself is the subject of various studies and is generally considered to increase with increasing growth rate (Schwarz & Tersoff 2012). In the case of VLS growth using Au as catalyst and Si_2H_6 as precursor gas (Figure 2-1 right), the Si NWs are seeded by the AuSi

liquid alloy droplets. It should be mentioned that the formation of these alloy droplets does not occur immediately after Au deposition. As a matter of fact, the first monolayer (0.8-1 ML or 0.19-0.24 nm) of Au deposited forms a wetting layer at the sample surface, which in the meantime transforms the Si(111)-(7×7) reconstruction to the AuSi-(√3×√3)R30° or the AuSi-(6×6) reconstruction (Lander 1964).

Other mechanisms exist, for example the Vapor-Solid-Solid growth, the most notable case of which being the sub-eutectic Ge NW growth with Au catalysts (Kodambaka et al. 2007). With *in situ* TEM, the researchers were able to observe NW elongation with either a solid or a liquid catalyst. To date, the growth mechanism behind the VSS growth is still not fully understood, but is generally attributed to the formation of silicides (germanides). Indeed, the low Si (Ge) solubility in the silicides (germanides) can somehow explain the slow growth rate during VSS growth as compared to the more conventional VLS growth. It could also explain why no VSS growth has ever been reported in the case of AuSi (as no such silicide exists on the phase diagram, *c.f.* next chapter). More recent findings indicate that the growth proceeds by step flow at the catalyst/nanowire interface (C.-Y. Wen et al. 2010), and that the growth interface is advanced by a complex lateral ledge propagation (Hoffmann et al. 2006) which depends on catalyst orientation and shape (C-Y Wen et al. 2010).

2.1.3. METAL CATALYST

Table 2-1 is an updated version of the summary of the potential metal catalysts for the growth of Si NWs, originally published elsewhere (Schmidt et al. 2010). Successful Si NWs growths have been reported with a variety of metal catalysts other than Au over the years, notably, Al (Wang et al. 2006), Cu (C-Y Wen et al. 2010), Pd (Hofmann et al. 2008) and the list goes on. To understand the role of metal catalysts in the NW growth, we follow the classification given by (Bootsma & Gassen 1971) which divides the metal

catalysts into three main categories, type-i catalysts with a high Si solubility (>10%) at the eutectic point (Figure 2-2 red), type-ii catalysts with a much lower Si solubility (<1%) and without the presence of any metal-silicide phase (Figure 2-2 yellow), and finally type-iii catalysts with one or more metal-silicide phases and a very high eutectic temperature (>800°C) (Figure 2-2 green).

									L+S Al	Si	P
S Ti	V	Cr	S Mn	L+S Fe	Co	L+S Ni	L+S Cu	L Zn	L Ga	Ge	As
Zr	Nb	Mo	Tc	Ru	Rh	L+S Pd	L+S Ag	L Cd	L In	L Sn	Sb
Hf	Ta	W	Re	S Os	Ir	L+S Pt	L Au	Hg	Tl	Pb	Bi

Table 2-1: Periodic table with potential metal catalysts classified according to their phase diagram with Si. The background color red, yellow and green denotes type-i, ii and iii catalysts, respectively. The subscript L, S, L+S denotes if VLS, VSS or both VLS and VSS mechanisms have been reported for the growth of Si NWs catalyzed by the metal.

Alloys formed with type-i catalysts, such as Au and Al, have a high Si content at the eutectic point. This basically implies a more elevated growth rate for the VLS growth compared to, for instance, alloys formed with type-ii catalysts under the same condition. Moreover, some type-i catalysts (Al and Ag) also work with VSS growth, which was explained by the presence of a pocket to the left of the binary phase diagram with low yet non-negligible Si solubility (Wang et al. 2006). Alloys formed with type-ii catalysts can only seed VLS growth, as can be inferred from the results summarized in Table 2-1, due to their simple Au-like phase diagram. Alloys formed with type-iii catalysts, when seeding VSS growth, precipitate Si via silicide particles. This has proven to be problematic for the studies because that more than often several metal-silicide phases coexist at the same time and that the phase of the catalyst may not be the same during and

after growth (Lensch-Falk et al. 2009). Moreover, NWs grown with metal-silicide particles are found to have very poor crystalline qualities (Schmidt et al. 2010). Growing under VLS mode effectively improves the quality of the NWs at the cost of the large thermal budget required by their high eutectic temperatures (*e.g.* ~1330°C for Ti-Si)

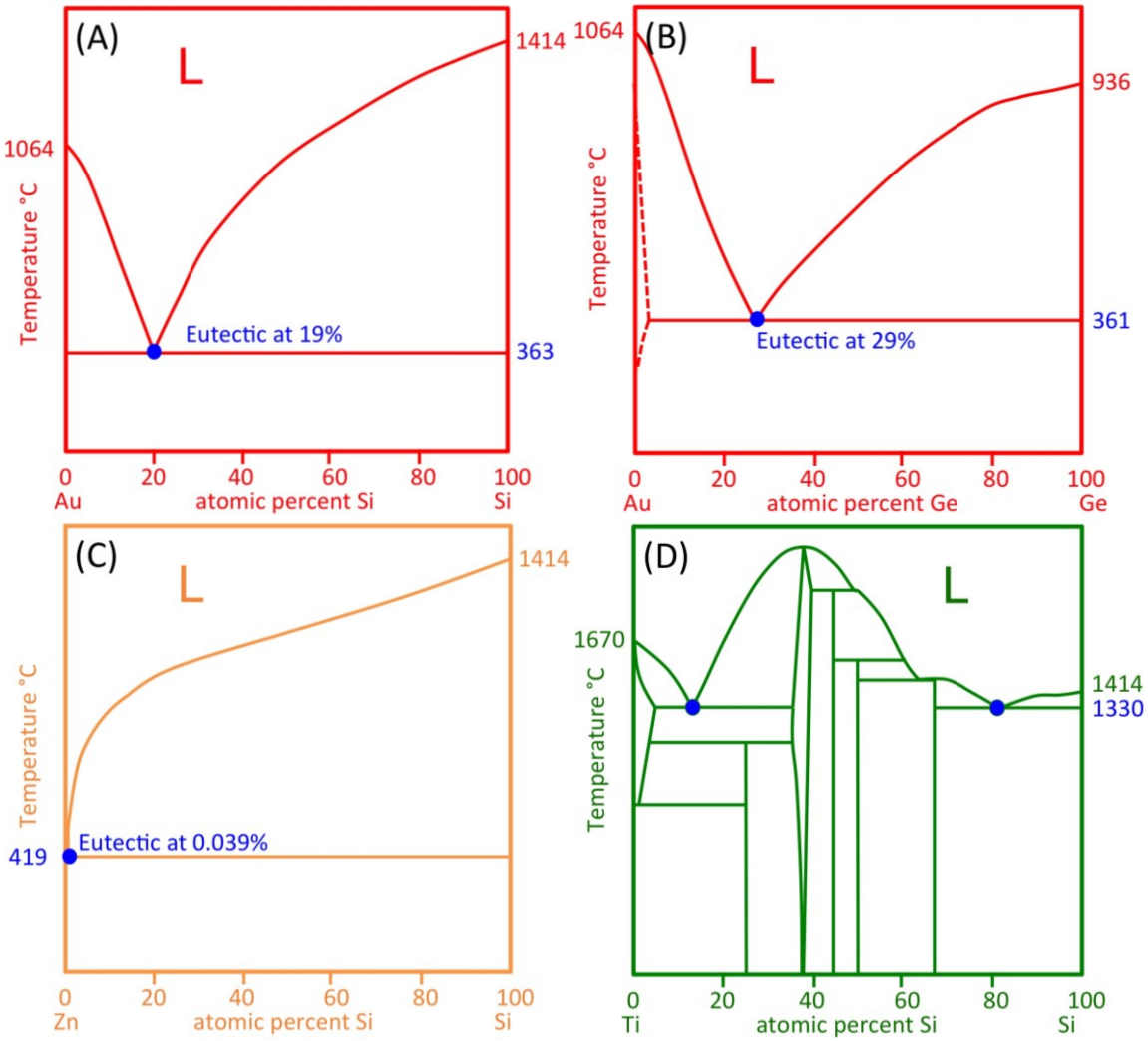

Figure 2-2 : Binary phase diagram of type-i (red) catalysts Au-Si, Au-Ge, type-ii (yellow) catalyst Zn-Si and type-iii (green) catalyst Ti-Si. It should be noted that although Au-Ge is considered as a type-i catalyst here, there exists a tiny pocket (dashed lines) with very low Ge solubility to the left of the diagram, which makes it possible for Ge NWs to be grown via the VSS process.

The growths to be presented later in this chapter were primarily catalyzed by Au, since Au-Si, with a simple binary phase diagram and a low eutectic point, is generally considered as the model system for the study of NW growth. In fact, Au is the most commonly used catalyst for the synthesis of semiconductor NWs, for two reasons. First of all, evaporators equipped with Au or commercially available Au colloids can easily be found in most laboratories. Secondly and most importantly, Au is highly chemically stable and does not oxidize in air. This reduces significantly the technical requirements on pre-growth preparations. However, Au is known to be associated with deep-level defects in Si (Allen et al. 2008), leading to enhanced carrier recombination and consequently shorter carrier lifetime, which hampers its integration with the Si based microelectronics industry. Al (another type-i catalyst), on the other hand, is more microelectronics friendly (essentially a p-type dopant) but is prone to oxidation. Growth seeded with Al has been attempted with our setup, though in the majority of the cases no NW growth was observed at all, most likely due to our low partial gas pressure. As a matter of fact, the maximum gas pressure attainable in our growth chamber (3×10^{-5}mbar) is 4 orders of magnitude lower than those reported in the literature, *e.g.*, 0.25mbar (Wang et al. 2006) and 0.26mbar (Wacaser et al. 2009). A higher partial gas pressure is thought to induce a higher supersaturation level in the liquid alloy (Givargizov 1975), which might in turn reduce the Si nucleation barrier at the catalyst/NW interface.

2.1.4. **CVD, MBE AND UHV-CVD GROWN NWS**

So far, we have presumed that the building blocks of the NWs, synthesized via either the VLS or the VSS process, come only from decomposed Si(Ge) atoms provided by the CVD precursor gases. Alternatively, molecular beam epitaxy (Figure 2-3A) can be used, where the sample is exposed directly to elemental Si(Ge) instead of to a chemical Si(Ge) compound. Several distinctions can be made between the two growth techniques.

First of all, UHV is only optional for CVD growth but is mandatory when depositing with MBE sources. Secondly, since elemental Si(Ge) is readily available, the role of metal catalysts in the case of MBE growth is reduced to merely facilitating Si(Ge) crystallization. In fact, since an equal amount of Si(Ge) atoms is evaporated onto the parts of the surface which are covered by the metal catalysts and the parts which are not, the elongation of the NWs thus relies solely on the diffusion of the adatoms which eventually find their way to the metal catalysts. The direct implication is that there will be a considerable amount of 2D growth (Si film) aside from the growth of the NWs, due to direct crystallization of the adatoms away from the metal catalysts. Also, relatively high growth temperatures (500°C−700°C) are required for the diffusion of the Si(Ge) atoms, which inevitably increases the chance of catalyst agglomeration (formation of larger catalysts and as a result larger NWs) due to Ostwald ripening. Thirdly, the diffusion driven growth process also implies a slower growth rate (1-10nm/min) compared to CVD techniques. Lastly and most importantly, because that the amount of Si(Ge) per unit time reaching the catalyst is proportional to the circumference (~D, D being the diameter) of the nanowire due to uniform deposition onto the sample surface, and that the growth velocity should be inversely proportional to the NW cross-sectional area (~D^{-2}) for a given Si(Ge) supply rate, the overall growth velocity (axial elongation) should be inversely proportional to the diameter (~D^{-1}) of the NWs.

UHV-CVD, sometimes called CBE for Chemical Beam Epitaxy, is similar to conventional CVD except that the base pressure of the growth chamber is maintained below 10^{-9}mbar before growth and that the gas partial pressure usually does not exceed 10^{-4}mbar during growth. Such clean environment presents certain advantages. First of all, annealing under UHV prior to the growth allows preparation of carbide free, oxide free, reconstructed surface with low surface roughness. Secondly, metal catalysts, especially

those susceptible to oxidation (*e.g.* Al), can be deposited *in situ* by MBE sources, without the risk of being oxidized during sample transfer. Moreover, measurements conducted under UHV conditions ensure a certain level of consistency between the data, as opposed to *ex situ* measurements where the NWs might have already been partially oxidized or contaminated due to exposure to air. Last but not least, the ultra clean environment allows relatively low partial gas pressure to be used, which in turn slows down the NW growth rate, making it possible to follow the entire process with *in situ* investigations.

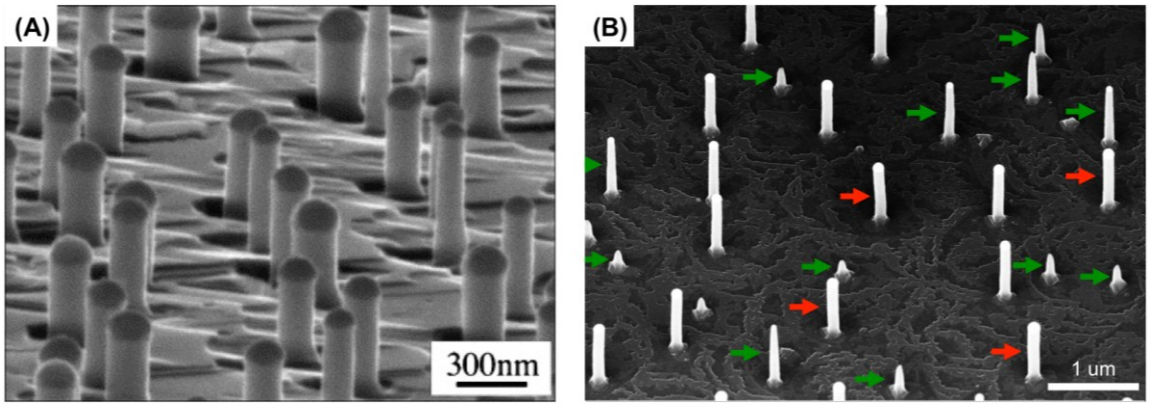

Figure 2-3 : SEM images of Si NWs grown with (A) MBE (Schubert et al. 2004) and (B) UHV-CVD (this work). MBE growth usually resulted in NWs with larger diameters due to catalyst agglomeration at elevated growth temperature prior to Si deposition, and is often accompanied by a considerable amount of 2D (film) growth. The reduced growth rate and clean environment of UHV-CVD allows gold migration to occur during growth. Consequently, (green arrow) some NWs gradually lost their catalyst and eventually ceased to grow while (red arrow) some others gained catalyst progressively, leading to an increase in NW diameter along the axial direction. The observation agrees well with what was reported in the literature (Hannon et al. 2006) under similar growth conditions.

2.1.5. SIZE EFFECT

Size effect is probably one of the most fundamental subjects still under debate regarding the VLS/VSS growth of Si/Ge NWs. The existence or non-existence of a size dependent behavior has puzzled the community for years. In simple words, do NWs with different sizes (diameters) behave differently? While classic thermodynamics analysis

(Givargizov 1975) concluded that larger NWs should grow faster due to Gibbs-Thomson effect, experimental results are widely divided. Some works seem to support such inference (Kikkawa et al. 2005; Dhalluin et al. 2010), some argue the opposite (Schubert et al. 2004), while others show no detectable dependence at all (S. Kodambaka et al. 2006). One possible explanation is that all of the above observations are correct, the discrepancy being simply caused by different growth conditions. The inverse proportionality observed (*i.e.* smaller NWs grow faster) was due to the diffusion driven nature of the MBE grown NWs and was explained in the previous section. To understand the observed direct proportionality (*i.e.* larger NWs grow faster) and size independency (*i.e.* all NWs grow equally fast), let us first consider the question as to what is the rate limiting step during the growth process: the supply (of the Si atoms as they incorporate themselves into the liquid catalyst alloy), the diffusion (of the Si atoms through the liquid) or the nucleation (of the Si atoms at the catalyst/NW interface)? The diffusion step is usually neglected, as diffusion through a microscopic droplet is simply too fast to affect the growth velocity (Givargizov 1987). The steady state growth rate (when the incorporation rate matches the nucleation rate) can be written as

$$v = v_\infty + \frac{\omega\alpha}{\omega - \alpha}\frac{4\Omega\sigma_s}{D} \qquad (2\text{-}1)$$

Where v_∞ is the growth rate in the planar limit (diameter $D \to \infty$), Ω is the volume per atom, σ_s is the surface free energy of Si, α and ω represent the derivative of the incorporation and nucleation rate with respect to the supersaturation $\Delta\mu$. If the Si supply is more than sufficient, as is true in the case of conventional CVD, *e.g.* SiH_4 partial pressure 9.8mbar for (Kikkawa et al. 2005) and 0.13mbar for (Dhalluin et al. 2010), the growth will be limited by the nucleation step (setting α to infinite), hence the direct proportionality. If however, the Si supply is limited, as is possibly true in the case

of UHV-CVD, *e.g.* Si_2H_6 partial pressure 1×10^{-5}mbar (S. Kodambaka et al. 2006), the growth will instead be limited by the incorporation step, which does not depend on the NW diameter (setting α to 0) as the sticking coefficient of the precursor gas molecule is independent of the chemical potential of Si in the liquid alloy. There are other possible interpretations regarding the abovementioned discrepancy, the reader is referred to more comprehensive models by (Schmidt et al. 2007) and by (Lü et al. 2012).

Other size (in)dependent behaviors exist besides the diameter (in)dependent growth rate, such as the diameter dependent composition when synthesizing $Si_{1-x}Ge_x$ NWs (Zhang et al. 2007) and the diameter (in)dependent elastic properties of the Si NWs, the latter will be briefly dealt with in Chapter 5.

2.2.NW Growth at BM32

For details on the preparation procedures for Si and Ge samples, the reader is kindly referred to Appendix III.

2.2.1. **SI NWS**

For the growth of Si NWs, the samples were first brought to the desired growth temperature where subsequent deposition of the Au catalysts took place. Injection of the precursor gases began immediately after the closing of the shutter of the Au source. Compared to the classic way of depositing catalysts at RT followed by annealing, direct catalyst deposition on “hot” substrate can effectively limit Ostwald ripening of the catalysts before growth, resulting in a very narrow distribution of the catalyst (and hence NW) size. Typical amount of Au deposition varies from 3 to 5 ML (0.7-1.2 nm), depending on the average size of the NWs that one intends to achieve (80nm-200nm). The optimal growth temperature range is between 480°C and 560°C, where near 100% yield of straight [111] NWs was observed on the entire sample surface (Figure 2-4AB).

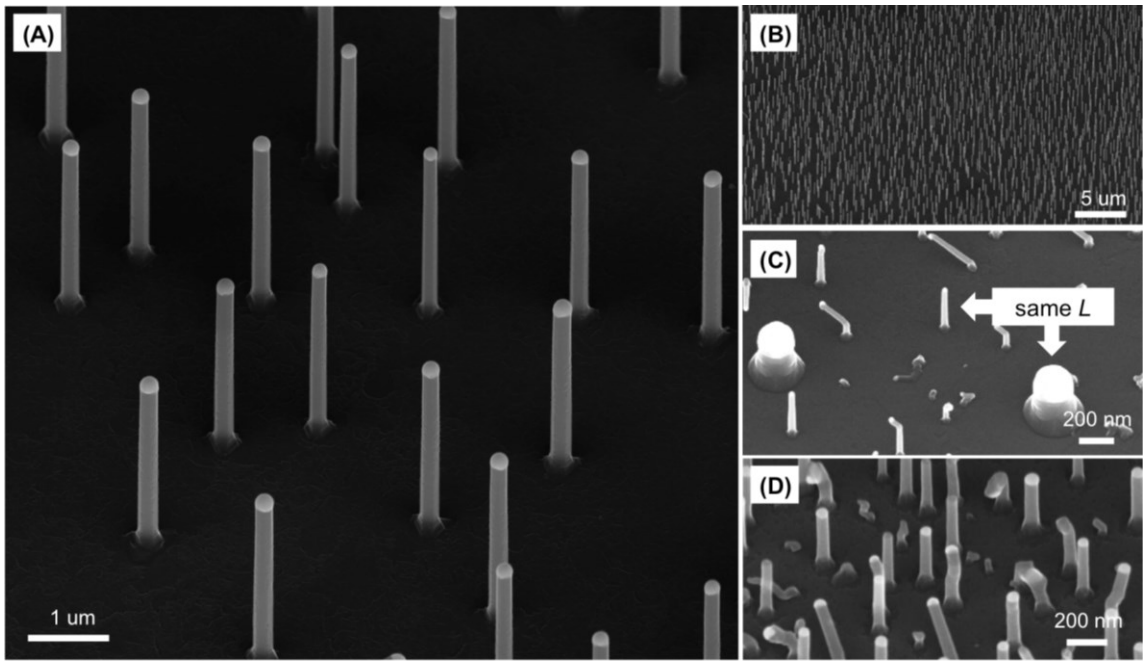

Figure 2-4: (A) 45° perspective view of the Si NWs grown after 2.5 hrs of 3.5×10^{-5}mbar Si_2H_6 injection at 540°C. (B) Zoomed out image of the same sample shows near 100% yield of straight [111] NWs on a larger scale. (C) Bimodal size distribution occurred for growths at higher temperatures or in this case after an overlong annealing (20min at 550°C) of the catalysts before growth. (D) Growth of low quality Si NWs at 440°C.

Growing at higher temperatures (> 600°C) or annealing the catalysts for too long before growth can result in a bimodal size distribution of the NWs due to Ostwald ripening, as is shown in Figure 2-4C. Interestingly, Figure 2-4C also confirms the size independency of the growth rate in our case, which was evoked earlier in Chapter 2.1.5. Growing at lower temperatures (<450°C) significantly reduces the number of straight NWs (Figure 2-4D). As a matter of fact, only curly NWs (*i.e.* yield of straight NWs close to 0%) were observed for the growth of Si NWs at 410°C. The poor NW quality observed for low temperature growth can be understood as the following. First of all, with direct Au deposition on "hot" substrate, lower growth temperature basically implies catalysts (hence NWs) with smaller size and it is a well-known fact that the preferred growth direction of the CVD Si NWs is largely size dependent. While NWs with diameter larger

than 50nm favor the <111> directions, NWs with diameter smaller than 20nm were found to primarily grow along the <110> directions. In between the two limits (20nm and 50nm), <112> NWs can sometimes be found (Wu et al. 2004; Schmidt et al. 2005). With 5ML at 440°C, the average NW size in our case is ~60nm, close to the 50nm-limit for the transition of preferential growth direction. At 410°C, the average NWs size was even smaller, about 40nm. Secondly, a commonly observed phenomenon during NW growth is that some NWs tend to change their direction during growth. The phenomenon is called kinking and has been the subject of various experimental (Shin & Filler 2012) and theoretical (Schwarz & Tersoff 2011) studies. Although its origin still under debate, it has been previously shown (Westwater 1997) that higher partial gas pressure and lower growth temperature tend to increase the chance for kinking to occur. In our case, the increasing amount of kinked NWs observed for the growth at 440°C and the curly NWs observed at 410°C could very well be the result of continuous kinking during growth.

Like most thermally activated processes, the growth rate of Si NWs shows an Arrhenius-type exponential dependence on the growth temperature. As for the pressure dependence, early experiments by (Lew & Redwing 2003) indicate that the growth rate varies almost linearly with the precursor gas partial pressure. These together bring us to the following estimation:

$$v = AP \cdot \exp(\frac{-E_a}{kT}) \qquad (2\text{-}2)$$

where v is the growth rate, A is the pre-exponential factor (in nm•min^{-1}•mbar^{-1}), P is the gas partial pressure, E_a is the activation energy of the process. Although unrelated to our main research focus (no dedicated experiments were conducted), we were still able to deduce the above parameters from the numerous growth experiments over the years. The growth rate (per partial gas pressure) exhibits indeed an Arrhenius behavior (Figure

2-5A), from which we were able to extract an activation energy of 0.33±0.04eV. The value obtained falls in between the values reported by the others, 0.55±0.02eV (S. Kodambaka et al. 2006) and 0.14eV (Boukhicha 2011), under similar conditions. The discrepancy is possibly caused by a variation in temperature readings between different measuring techniques. Nevertheless, the activation energy for VLS Si NW growth with Si_2H_6 is much lower than the values found for the growth with SiH_4, 0.82±0.07eV (Schmid et al. 2008) and 0.95eV (Lew & Redwing 2003), which is essentially the reason why Si_2H_6 is favored by researchers using UHV-CVD. It is worth mentioning that the activation energy for uncatalyzed growth using Si_2H_6 is much higher, ~2eV (Bramblett et al. 1994). This disparity is responsible for the much slower 2D growth than in the case of growing NWs with MBE. Finally, the growth rate at 540±10°C is linearly dependent on the partial gas pressure (black circles, Figure 2-5B). With least squares fitting, we found a pre-exponential factor of A=5.29×10^7, which is in good agreement with the value (1.02×10^8) and uncertainty (~ factor of 2) given by (Schmidt et al. 2010).

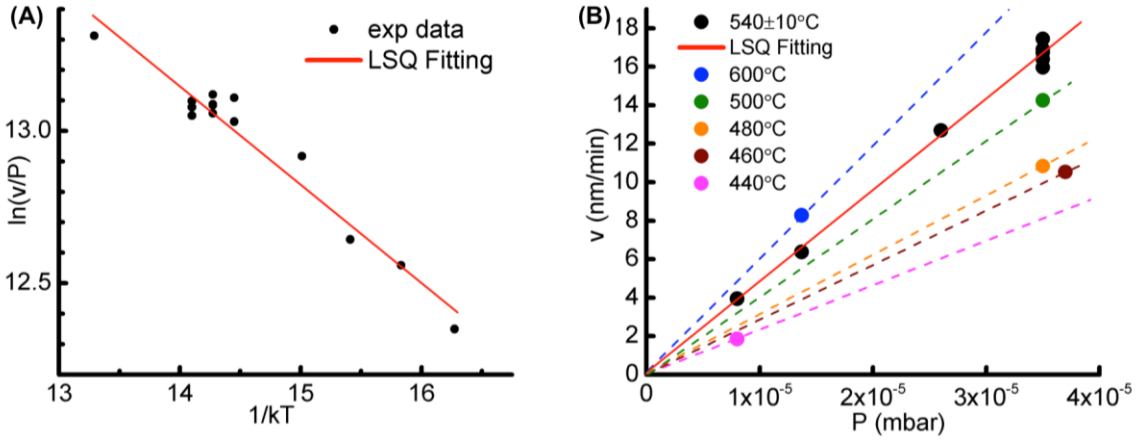

Figure 2-5: (A) Arrhenius plot and least squares fitting of the data extracted from numerous growths at different temperatures. (B) (black circle) Growth rate versus Si_2H_6 partial gas pressure for growths at around 540°C. (red line) Least square fitting of the data. (colored circles) Growth rate measured at other temperatures. (dashed colored lines) estimated growth rate dependence on partial gas pressure for the listed temperatures. The slope increases with the temperature as is evident from the exponent in Equation (2-2).

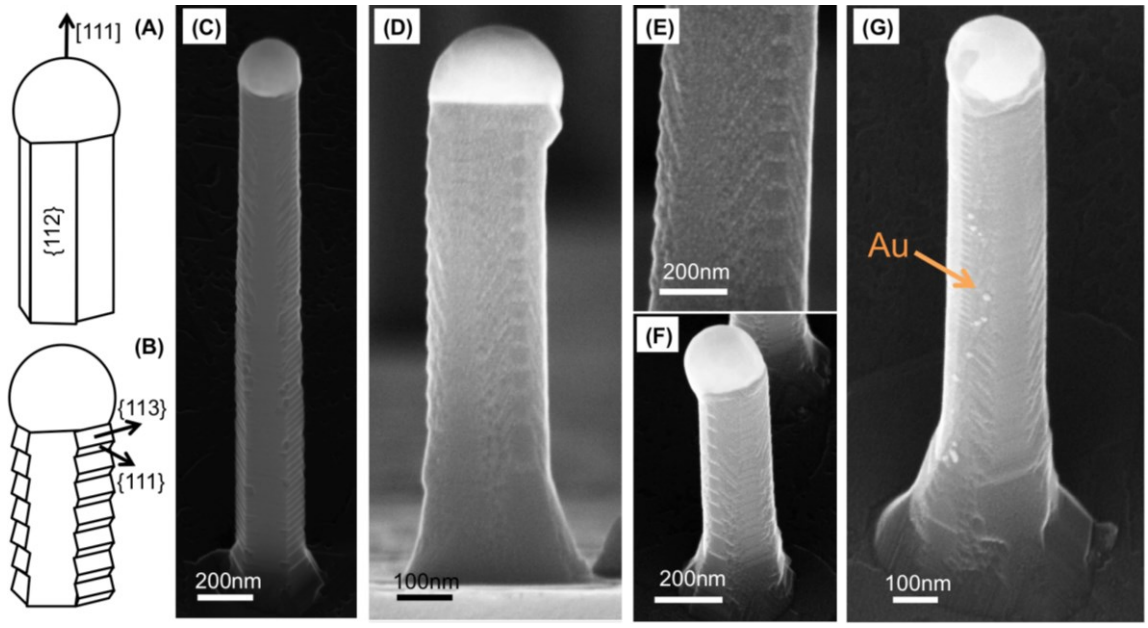

Figure 2-6: Schematics of a NW with sidewalls composed of (A) smooth {112} faces and (B) alternating sawtooth facets. (C) 45° perspective view of a Si NW with sawtooth faceting and a hexagonal cross-section. (D) (E) Side view of a Si NW with a dodecagonal cross-section. (F) 45° Perspective view of a Si NW of which the cross-section evolves gradually from dodecagonal near the base of the NW to hexagonal near the top of the NW. (G) 45° perspective view of a Si NW with Au nanoparticles on its sidewalls.

The fine structure of the Au catalyzed Si NW sidewalls, buried under the conventional understanding of being composed of six smooth {112} faces (Figure 2-6A), was first revealed by (Ross et al. 2005). With the help of *in situ* TEM, they found that three of the {112} faces actually consist of alternating facets of {111} and {113} families while the other three remain featureless, leading to a complex structure which they then called sawtooth faceting (Figure 2-6B). They also noted in their pioneering work that the period of the facets λ depends linearly on the NW diameter D, with $\lambda \sim 0.23D$ ($0.12D$ in our case). It was not until several years later that an even more complex structure was reported. In addition to the hexagonal cross-section formed with the abovementioned facets, a dodecagonal cross-section was occasionally spotted (David et al. 2008). We

have observed both the hexagonal (Figure 2-6C) and dodecagonal facets (Figure 2-6DE), the exact structure of which will be revisited in Chapter 3 with *in situ* X-ray techniques.

The reason behind the formation of the hexagonal sawtooth facets remains debatable. (Ross et al. 2005) speculated it to be related to a size oscillation of the liquid alloy of pure thermodynamics origin. (Wiethoff et al. 2008) however, argued that Au plays a vital role in the facet formation. Their finding, which was based on their observations on the formation of Au-rich {111} and Au-depleted {113} facets on a Si(112) surface for Au coverage of 0.40-0.46ML, was supported by a number of TEM studies. First of all, Au is known to diffuse along the sidewall during NW growth (Hannon et al. 2006), an indirect and a direct evidence are given respectively in Figure 2-3B and in Figure 2-6G for the UHV-CVD growth in our case. The suppression of such diffusion, either by increasing the gas pressure, decreasing the growth temperature (den Hertog et al. 2008), or by introducing gas phase HCl (Oehler et al. 2010) or oxygen (Suneel Kodambaka et al. 2006), have all led to the synthesis of Si NWs with smooth (*i.e.,* without sawtooth facets) sidewalls. Moreover, instead of spreading uniformly along the sidewall, Au NPs were seen anchoring preferably on the {111} facets (Vincent et al. 2011), which further confirms (Wiethoff et al. 2008)'s theory. The formation of the more complex dodecagonal facets is less well understood. A widely accepted model, prompted by the fact that these facets were mostly observed close to the top of the NWs (*i.e.* shorter exposure time to the gases), is that the axial elongation of the NWs initially left behind only the regular dodecagonal (12 fold symmetry) facets, which were then gradually transformed into the irregular hexagonal (3 fold symmetry, sawtooth) facets due to Si overgrowth (radial growth).

2.2.2. GE NWS

The Au catalyzed growth of Ge NWs shows a distinctive difference from that of Si NWs in that successful growths have been reported for temperatures well below the Au-Ge eutectic point. Whether the growth follows a VLS type of process or a VSS one has been at the heart of many studies. Despite experimental evidence that continuous NW growth was observed with both liquid and solid catalysts (Kodambaka et al. 2007), the exact conditions required for the VSS growth to occur remain ambiguous.

Ge NWs were synthesized in our case using Ge_2H_6 as gas precursor. Typical partial gas pressure varies from 4×10^{-5}mbar (normal injection) to 6×10^{-3}mbar (static mode, with reduced turbo pump speed). Au catalysts (5 ML) were deposited at RT and were subsequently annealed at 500°C for 25 min, resulting in an average NW size of 30-60nm. Longer annealing time and/or at higher temperatures lead to a larger size distribution due to enhanced agglomeration between the catalysts whereas shorter annealing time and/or at lower temperatures reduces the number of straight [111] NWs (Figure 2-7C) as their average size approaches the threshold of preferential growth direction transition, ~25 nm after (Sierra-Sastre et al. 2010), from <111> to <110>. The temperature range for which successful growths have been observed (between 280°C and 360°C) agrees fairly well with those found in the literature (Table 2-2). Close to the upper limit (340°C), tapered NWs with a hexagonal cross-section and faceted sidewalls (Figure 2-7A) were observed. The tapering of the NWs was the result of enhanced radial growth, from which we estimate a ratio between the axial and radial growth rate of 26.6±0.6:1 at this temperature. While it is possible that the radial growth was fueled by uncatalyzed decomposition of the precursor gas directly on the NW sidewall or by diffused Ge adatoms originally found at the sample surface, it is more likely to be related to catalyzed decomposition on the Au covered sidewall due to enhanced Au diffusion at

higher temperatures if one also takes into account the formation of the facets, analogous to what we have concluded with Si NWs in the previous section. Without the heavy radial growth, the Ge NWs are characterized by a circular cross-section and smooth sidewalls (Figure 2-7B), as is evident from the growth results close to the lower limit (285°C). Only a small amount of NWs were seen growing at temperatures higher than 360°C. The surface was instead covered by some bizarre 3D structures with no distinguishable trace of the alloy catalysts (Figure 2-7D). The formation of such structures is probably due to the following: At high temperatures, the decomposition of the precursor gas on the catalyst alloy can occur faster than the resulting Ge atoms can be transported to the underlying interface. The excessive Ge atoms continue to accumulate at the surface of the alloy catalysts, passivate (poison) them in the process, eventually leading to the complete burial of the alloy catalysts.

Source	Precursor / Pressure	Temperature	Growth Mode
This work	10^{-5}-10^{-3} mbar Ge_2H_6	280°C - 360°C	VLS
(Boukhicha 2011)	10^{-4}-10^{-2} mbar Ge_2H_6	280°C - 400°C	VLS
(Kodambaka et al. 2007)	10^{-7}-10^{-5} mbar Ge_2H_6	250°C - 400°C	VLS+VSS
(Kamins et al. 2004)	10^{-3} mbar GeH_4	320°C - 360°C	VLS
(Dayeh & Picraux 2010)	0.8 mbar GeH_4	366°C - 440°C	VLS
(Adhikari et al. 2007)	1 mbar GeH_4	300°C - ???°C	VLS
(Wang & Dai 2002)	9 mbar GeH_4	275°C - 600°C	VLS

Table 2-2: Summary of the conditions for successful growth of Ge NWs using a single-step procedure (*i.e.* direct sub-eutectic growth without an initiation step at higher temperatures) in the literature. Those reports that consist of growths only at one specific temperature/pressure were not included in the table.

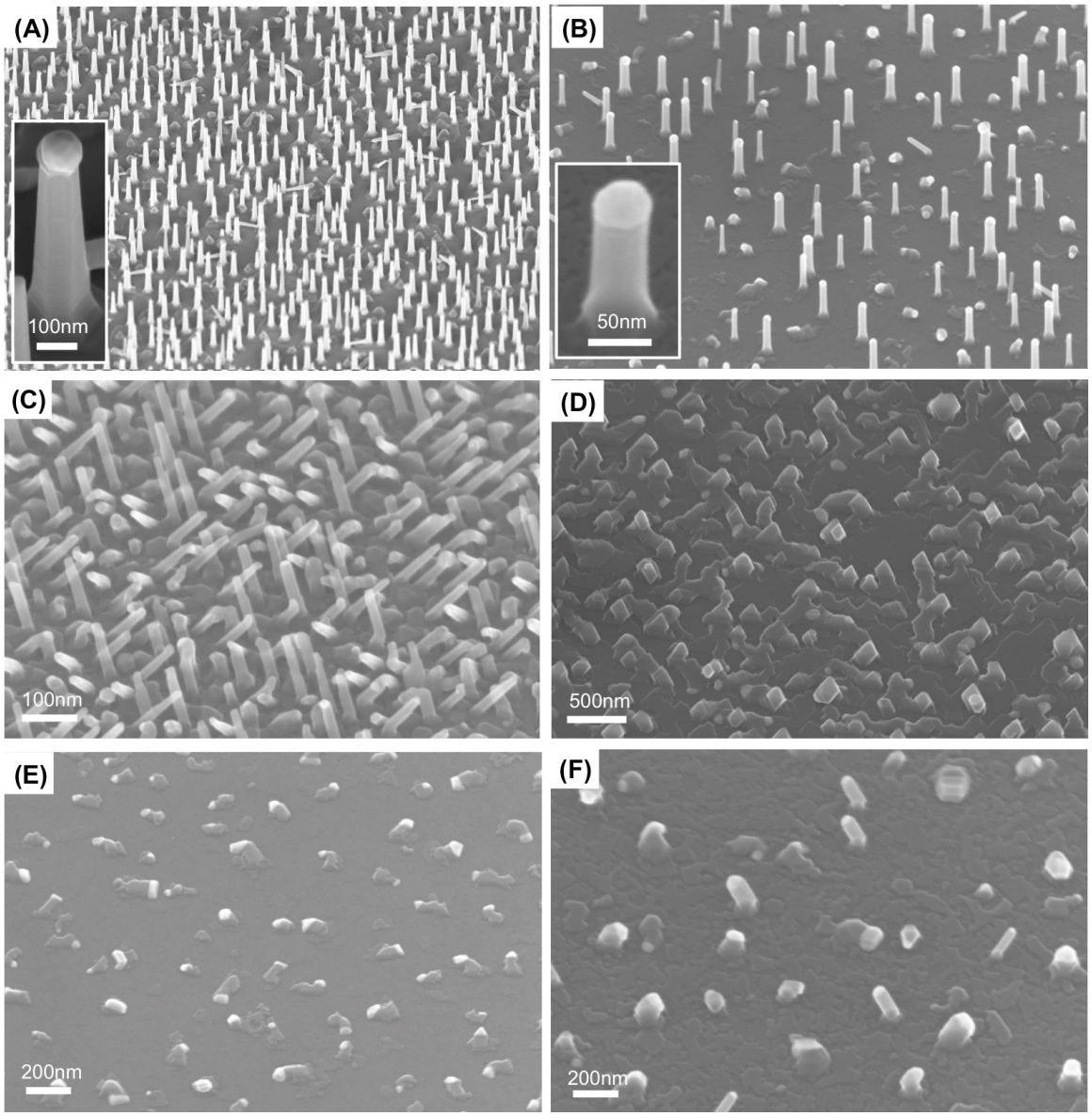

Figure 2-7: 45° perspective view of Ge NWs grown under different conditions. The catalysts were deposited at RT and annealed at 500°C for 25min prior to the Ge_2H_6 injection. (A) 2h of 6×10^{-3}mbar injection at 340°C (B) 40min of 6×10^{-3}mbar injection at 285°C (C) 40min of 6×10^{-3}mbar injection at 285°C, the catalysts were only annealed for 10min at 400°C (D) 40min of 6×10^{-3}mbar injection at 385°C (E) 40min of 6×10^{-3}mbar injection at 285°C with deliberately solidified catalysts (F) 1h30min of 2×10^{-5}mbar injection at 285°C.

Overall, the above observation is consistent with what was reported by (Kamins et al. 2004). One should be particularly careful, however, when comparing the results of Ge NW growth in the literature, as in most cases the NWs were grown using a two-step method (Adhikari et al. 2006). The two-step growth, where part of the NWs were initially grown at ~400°C before lowering the growth temperature to below eutectic, is known to have lower pressure and temperature requirements than the single-step growth (Adhikari et al. 2007). During our experiments we opted not to use the two-step growth method due to its complex growth mechanism and the difficulty to carry out *in situ* experiments.

No vertical [111] NWs was found at the sample surface (Figure 2-7E) after repeating the optimal growth condition on deliberately solidified catalysts (the solidification was ensured by cooling the catalysts down to <200°C after annealing), which inevitably brings us to the question as to whether (and how) Ge NW growth can proceed with a solid catalyst. Despite the possible variations between the temperature readings by different methods (authors), and the fact that there is no means to measure the exact temperature at the tip of the NWs, Ge NWs can indeed be synthesized at temperatures below the eutectic one. Most authors (Table 2-2) claimed, regardless of what is expected from the AuGe phase diagram (Figure 2-2B), that their NWs were grown via the VLS mode, in other words, their catalysts stayed liquid during growth. It is true that the phase diagram can only account for the in-equilibrium state and composition of the catalyst alloy for bulk materials and needs be revised (Sutter & Sutter 2008) when it comes to nano-objects. For example, AuSi nanoparticles were reported to remain liquid (called supercooled or undercooled) at as low as 120°C below their equilibrium eutectic point when cooling down after annealing (Schülli et al. 2010). In the case of AuGe, there are in general two factors that could possibly contribute to the lowering of the melting point, namely, the capillary effect and Ge supersaturation. The capillary effect reduces

the melting temperature by increasing the free energy of single-component nanoparticles relative to their bulk values. Moreover, both theoretical and experimental results (Sutter & Sutter 2010) indicate that the smaller is the diameter of the NWs, the more significant is the effect of capillarity, and hence a even lower melting point. Although some (Schwalbach & Voorhees 2008) argued differently, it is sometimes suggested that the capillary effect alone cannot be responsible for the observed huge depression of the eutectic temperature. Instead, the authors (Adhikari et al. 2007) theorized that an increase in the Ge chemical potential in the gas phase (higher gas pressure) should lead to an increase in the Ge chemical potential in the liquid phase (catalyst), which could in turn stabilize the liquid alloy at temperatures far below the equilibrium eutectic point. The stabilizing effect of the precursor gas has been confirmed by other groups. A nice demonstration was given by (Gamalski et al. 2010) where they showed the melting of a solid Au nanoparticle under 1.4×10^{-3} mbar of Ge_2H_6 at 240°C. We have also studied the state of Au during Ge NW growth with *in situ* X-ray scattering techniques. The result revealed the presence of metastable β-AuGe and γ-AuGe phase catalysts (Gamalski et al. 2012) and will be presented in Chapter 3.

So far we have discussed the VLS pathway of Ge NW growth at sub-eutectic temperatures. Regarding the possible VSS pathway, continuous elongation of Ge NWs with a solid catalyst has been observed with *in situ* TEM (Kodambaka et al. 2007), together with a 1-2 order of magnitude of difference between the growth rate of NWs grown via VLS and via VSS. However, their result only showed Ge precipitation from pre-grown NWs. It is possible that to initiate the VSS growth one has to either start with catalysts atop a NW (different environment compared to pre-growth catalysts attached to the substrate) or apply more elevated gas pressure (higher Ge chemical potential). The

above speculation is so far our only conceivable explanation as to why no NW growth was observed in our case with solid catalysts under similar growth conditions.

There also exists a minimum pressure required for the sub-eutectic growth of high quality Ge NWs. For the growth around 300°C, this (partial) pressure, below which the number of straight [111] NWs is significantly reduced (Figure 2-7F), was found to be around 1×10^{-4} mbar (285°C). This value is consistent with that (~3×10^{-4}mbar, 320°C) reported by (Boukhicha 2011) for Ge_2H_6 and is much lower compared to the value (~0.3mbar, 280°C) reported by (Adhikari et al. 2007) for GeH_4. (Adhikari et al. 2007) also suggests that such value corresponds to the minimum precursor gas pressure necessary to melt a solid Au core or to maintain a liquid Au core when cooling down from above T_e, which is mandatory for the VLS growth to proceed. However, their interpretation does not apply in our case as it fails to explain as to why NW growth can be achieved with undercooled catalysts and not with deliberately solidified catalysts under otherwise the same growth condition. We think that our minimum pressure is below the value required for melting solid Au at the given temperature, but is just about sufficient to increase the supersaturation in the liquid alloy catalyst, presumably to a state that facilitates Ge nucleation at the liquid/solid interface.

Finally, size effects on the growth rate have been reported for the sub-eutectic growth of Ge NWs by various authors. As discussed previously in Chapter 2.1.5, the growth rate can be dependent on the diameter of the NWs if limited by the nucleation step, which is possibly true under the circumstance of low temperature growth. Multiple theories have been proposed, including the empirical quadratic dependence proposed by (Givargiz.EI & Chernov 1973) and further demonstrated by (Dayeh & Picraux 2010), and the linear dependence which is the direct result of Equation (2-1) and was demonstrated by (Renard et al. 2012).

$$v = C \cdot (1 - \frac{D_c}{D})^n \qquad (2\text{-}3)$$

Where D_c is the critical (cutoff) diameter below which no growth occurs (v=0), C is the prefactor which takes into account the supersaturation at the planar limit, the coefficient for kinetic crystallization and the coefficient for effective adsorption. n equals to 1 for the linear dependency and 2 for the quadratic dependency. For the growth of Ge NWs at 285°C under 6×10^{-3}mbar of Ge_2H_6, we have indeed observed a size dependent growth rate, *i.e.* larger NWs grow faster (Figure 2-8A). However, our limited data range (diameter between 20 and 60 nm) does not allow us to confirm which of the above two theories is correct (Figure 2-8BC). As a matter of fact, both dependencies fit quite well with our data, from which we derive a cutoff diameter of 2.96 nm for the quadratic rule and 8.63 nm for the linear rule.

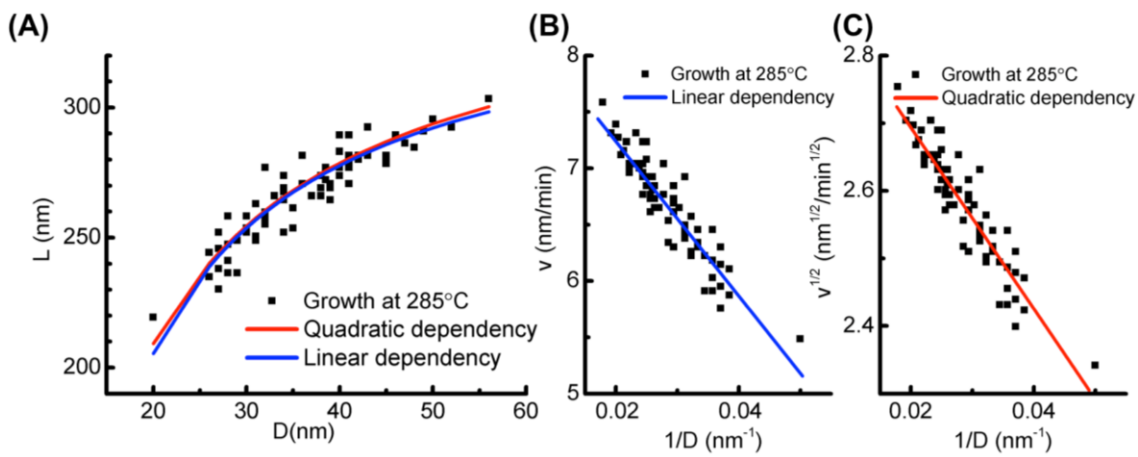

Figure 2-8: (A) Measured length of the NWs as a function of their diameters, after 40min of 6×10^{-3}mbar Ge_2H_6 injection at 285°C. (B) Growth rate as a function of inverse NW diameter, for the fitting of linear rule. (C) Square root of the growth rate as a function of inverse NW diameter, for the fitting of the quadratic rule.

2.2.3. Ge/Si Radial NW Heterostructures

For the growth of Ge/Si radial NW heterostructures (also known as Si-Ge core-shell NWs), we began by growing the Si part following the same procedures described in section 2.2.1. After that, the samples were cooled down to below 200°C to ensure the solidification of the Au catalysts. This effectively eliminated the possibility of any axial elongation of the NWs during subsequent Ge_2H_6 injection. Typical growth temperature for the Ge shell varies from 220°C to 300°C.

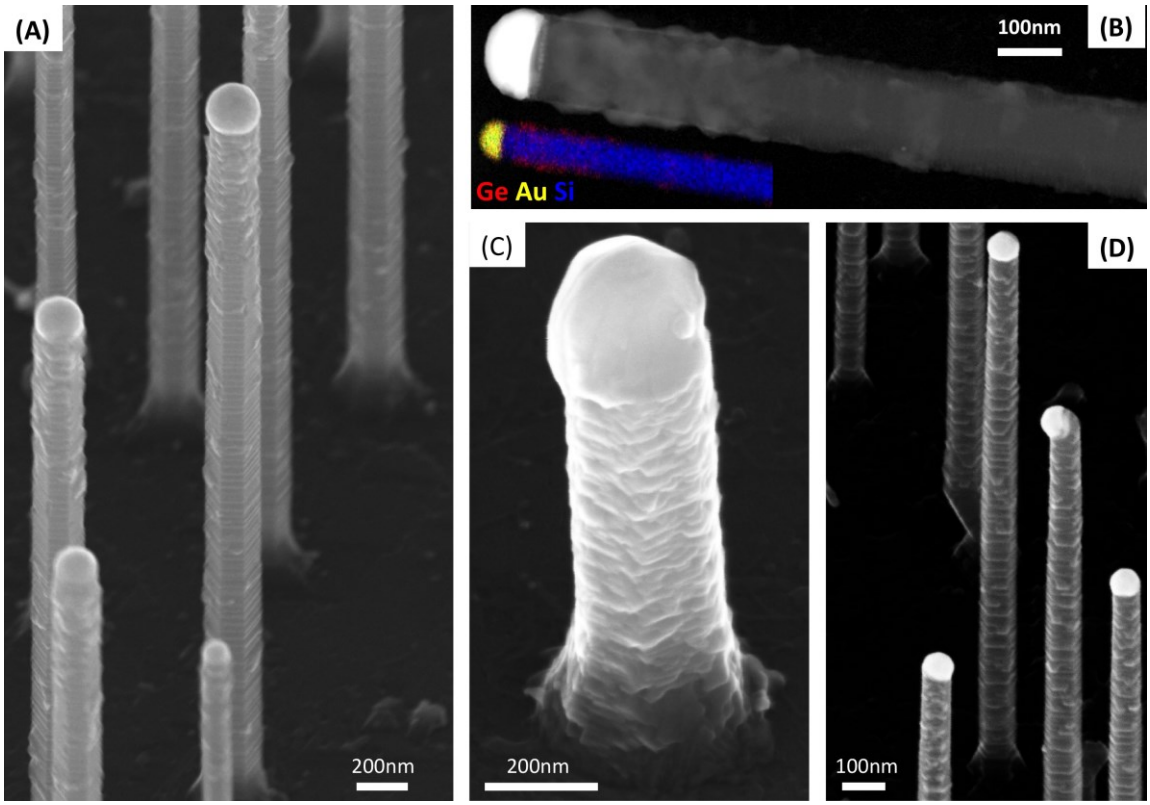

Figure 2-9 : (A) 40° perspective view of the SiGe coreshell NWs. The Ge shell was grown by injecting 40min of 6×10^{-3} mbar (partial pressure) Ge_2H_6 at 300°C. (B) STEM image and (inset) EDS analysis showing that the shell is composed of 3D Ge islands rather than of a smooth 2D wetting layer. The measurements were performed by Laetitia Vincent and Gilles Patriarche. (C) 40° perspective close-up view of a SiGe coreshell NW. The Ge shell was grown by injecting 60min of 6×10^{-3} mbar (partial pressure) Ge_2H_6 at 290°C. (D) 40° perspective view of the SiGe coreshell NWs with a MBE Ge shell grown at 220°C. The shell thickness is estimated to be around 12.5nm.

(Figure 2-9A) For very long NWs, heavy Ge overgrowth was only observed on the upper part of the NWs. (Figure 2-9B) STEM and EDS analysis indicate that the rough Ge shell is composed of 3D islands rather than of a smooth 2D wetting layer (Lauhon et al. 2002), indicating a Stranski-Krastanov mode of growth as predicted for NWs with large diameters (Li & Yang 2014). The morphology of the lower part of the NWs was also modified. The alternating smooth and sawtooth faceted sidewalls (Figure 2-6C) were replaced by six faceted sidewalls of equal periodicity, similar to what was observed for Ge NWs grown at higher temperatures (Figure 2-7A). The thicker Ge shell on the upper part of the NWs can be understood as follows. First, even when solidified, the Au catalysts still serve as the primary source for Ge_2H_6 decomposition, thus providing more Ge to the region close to the tip than to the rest of the NWs. Secondly, it is possible that the Ge growth rate is faster for regions with a dodecagonal cross-section (found on the upper part of the NWs) than for regions with a hexagonal cross-section (found on the lower part of the NWs). Nevertheless, a homogeneous shell along the axial direction can be achieved by growing with shorter Si NWs (Figure 2-9C) or with longer Ge_2H_6 exposure. The overall morphology of the CVD Ge shell is very similar to that grown with MBE (Figure 2-9D). A detailed analysis on the strain evolution during shell growth and during subsequent annealing will be presented chapter 4.

2.2.4. GE/SI AXIAL NW HETEROSTRUCTURES

Despite our numerous attempts, direct growth of Ge NWs on Si substrates has turned out to be fruitless. “Crawling” NWs (Figure 2-10A) were observed even when the same growth condition that gave rise to nice Ge NWs on Ge(111) substrates was applied. The presence of crawling NWs has already been explained in the literature. In the early stages of growth, the droplet sits on a tapering pedestal, which must introduce new facets to evolve into steady-state nanowire growth. If the introduction of new facets is impeded,

the initial base continues to taper until the catalyst droplet rolls off. The catalyst then crawls along the surface, growing into a lateral wire (Schwarz & Tersoff 2011).

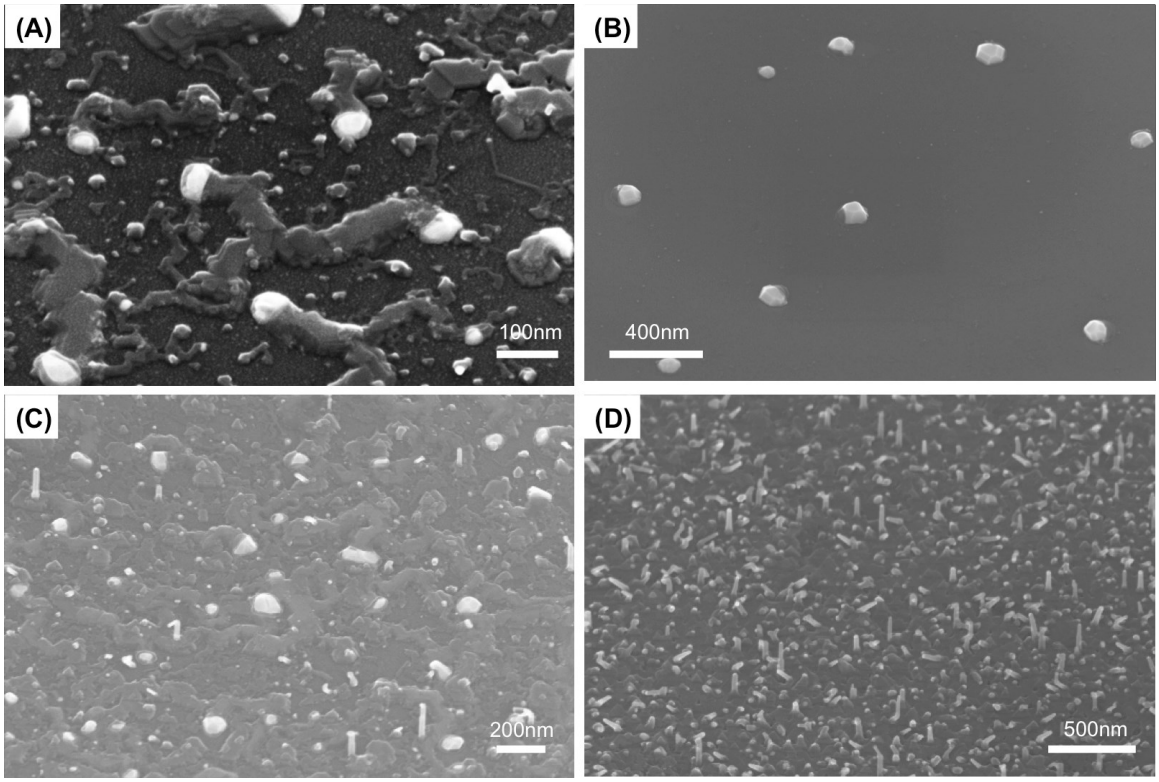

Figure 2-10: 40° perspective view of attempts of growing Ge NWs directly on Si(111) substrates with 6×10^{-3} mbar (partial pressure) of Ge_2H_6 at 280°C (A) The same condition that gives rise to nice Ge NWs on Ge substrates: with 5ML of Au catalysts deposited at 300°C and annealed at 500°C for 25min. (B) with 5ML of deliberately solidified Au catalysts after annealing. (C) with 5ML of Au catalysts annealed at 450°C for 50min. (D) with 5ML of Au catalysts annealed at 450°C for 15min.

Various growth conditions have been tested for growth temperature between 270°C and 360°C with liquid or deliberately solidified Au catalysts, but still no NWs growth was observed (Figure 2-10B). Successful growth has been reported elsewhere (Kodambaka et al. 2007; Jagannathan et al. 2006; Woodruff et al. 2007), although it seems that only catalysts (and hence NWs) with very small diameter (typically 10-40nm) were used in those cases. The assumption of having a size limit below and only below

which successful growth can take place agrees well with our observations (Figure 2-10C), where vertically aligned Ge NWs with small diameters were seen growing among crawling NWs with considerably larger diameters. To our knowledge, no upper (size) limit was ever reported for the VLS process. Instead, thermodynamic calculation (Tan et al. 2003) seems to predict the existence of a lower limit at which point the growth rate is reduced to zero, as can be inferred from Equation (2-3). Finally, even with rather small catalysts, the yield (Figure 2-10D) in our case was still less than satisfactory.

A simple solution to the problem is to grow the Ge NWs on the existing Si NWs instead, the result of which is known as the Ge/Si NW axial heterostructure. Although the size limit for successful growth still exists, as is evident from Figure 2-11A, the barrier is significantly lowered. As a matter of fact, Ge NW parts were seen growing on top of Si NWs with diameter as large as 80-100nm. By intentionally bombarding the reconstructed surface with Ar^+ and by lowering the temperature at which Au nucleation occurred, we were able to synthesize Ge/Si NW heterostructures with an acceptable yield. Figure 2-11B shows a zoom-in SEM image of such structures. The Ge part (upper half) resembles that of a Ge NW grown on Ge substrates. The tapered shape is due to Ge overgrowth on the NW sidewalls under our relatively high partial gas pressure. The Si part (lower half) is featured with large and irregular facets, which is also caused by the Ge overgrowth during the process. The optimal growth temperature for the Ge part is found to be the same as that for growing Ge NWs on Ge substrates. Growing with a solid catalyst resulted in no axial elongation (c.f. Chapter 2.2.3) while growing at higher temperatures (400°C-500°C) resulted in a distorted structure on top of the Si NWs. A non-negligible amount of kinking was observed (Figure 2-11CD). As a matter of fact, the large amount of kinking is expected due to disparate growth temperatures and chemical potential-induced instabilities (Dick et al. 2007) in the liquid growth seed upon switching

between Si and Ge (Dayeh et al. 2011). The majority of the kinking in our case was found along the equivalent <111> directions, although <112> kinking was also observed. Finally, it is worth mentioning that, despite the absence of any chemical analysis, we expect the Si/Ge transition at the heterojunction to be rather gentle. More compositionally abrupt Si/Ge interface can be achieved, by lowering the solubility of the semiconductors in the alloy catalyst with either Al (Wen et al. 2009) or Ga (Perea et al. 2011).

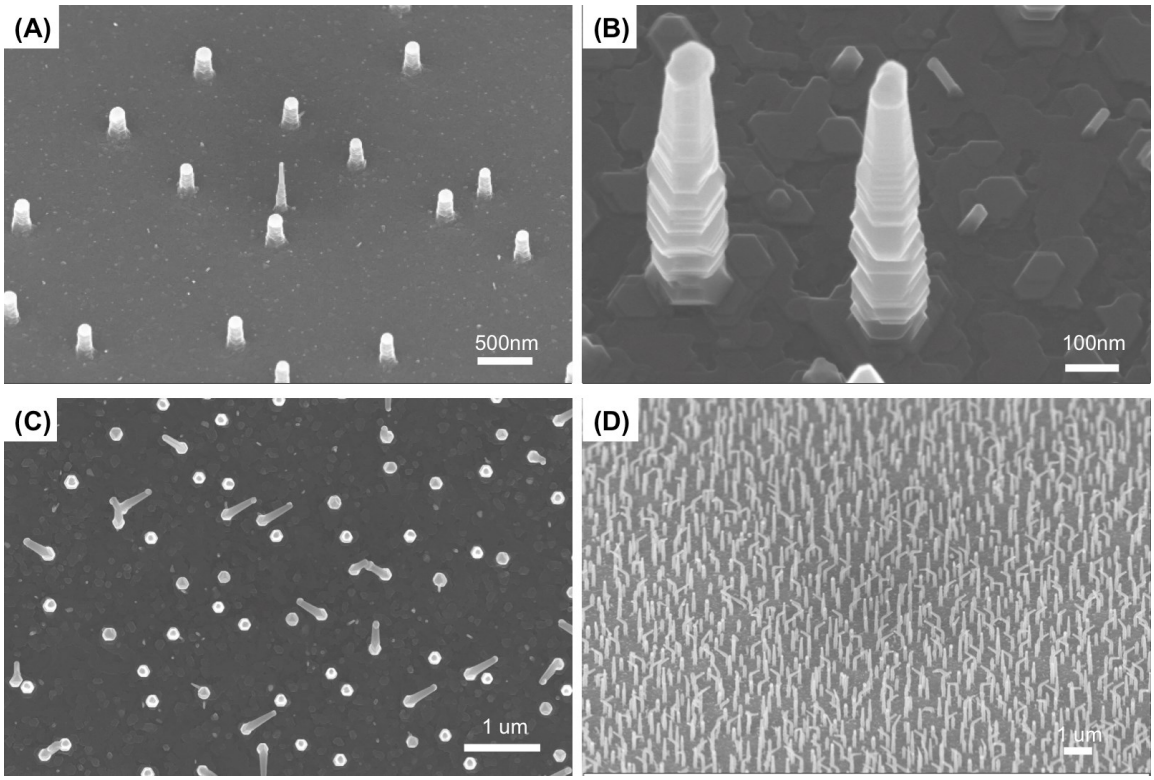

Figure 2-11: (A) 40° perspective view of the Ge/Si axial NW heterostructures. The Si NW parts were grown with 20min of 3×10^{-5}mbar Si_2H_6 injection at 500°C right after the deposition of 3ML Au. The sample was then cooled down to 285°C for the growth of Ge NW parts with 40min of 6×10^{-3}mbar of Ge_2H_6 injection. It appeared that subsequent Ge growth occurred only for NWs with smaller size. (C) Top view and (B)(D) 40° perspective view of the Ge/Si axial NW heterostructures with a better yield. Prior to the deposition of the metal catalysts, the (7×7) reconstructed surface was bombarded with 0.8mA of Ar^+ at RT to limit Au diffusion. The temperature for the growth of the Si NW parts (and for Au deposition) was also lowered to 450°C in order to synthesize NWs with smaller diameters. The rest of the growth conditions were kept the same.

2.2.5. Si/Ge Axial NW Heterostructures

Growing Si directly on Ge(111) substrates turned out to be just as difficult. The surface was predominately occupied by crawling NWs (Figure 2-12A) even after injections of Si_2H_6 at relatively high partial gas pressure (2×10^{-2}mbar as opposed to 3×10^{-5}mbar that we used for standard Si NWs growth). Si/Ge axial NW heterostructures can be synthesized by growing the Si parts on top of the Ge NWs. The major challenge arises from the large temperature gap between the two stages of growth, *i.e.*, that of the lower part (Ge NWs at ~280°C) and that of the upper part (Si NWs at ~550°C). As a matter of fact, the high mobility of the alloy catalyst at elevated temperatures required for the 2nd stage of growth and its chemical instability upon switching between the precursor gases make it more favorable for the catalysts to diffuse away rather than staying still at the top of the NWs. The result is some random Si growth over the existing Ge NWs, often with no distinct trace of the hemisphere-shaped catalysts (Figure 2-12B). By lowering the temperature of the 2nd stage of growth to around 400°C, the catalyst diffusion can be effectively limited. Half-grown structures (those with only the Ge part as their catalysts have diffused away before the growth of the Si part) can still be spotted occasionally but the yield is, in general, acceptable (Figure 2-12C). It also seemed that for some samples, the upper (Si) part of the heterostructure resembled that of an individual Si NW with sidewalls covered by alternating facets (Figure 2-12C), while for others smooth (featureless) sidewalls were observed (Figure 2-12D). Although we were not able to draw a definite conclusion even after a dozen of test experiments, a plausible explanation is that below a certain temperature (~360°C-380°C), Au diffusion along the NW sidewall becomes negligible. The presence of diffused Au on the sidewall is known to be responsible for the formation of the sawtooth facets (Oehler et al. 2010), and the absence of which would lead to the growth of NWs with smooth sidewalls. In either case,

the faceting of the lower (Ge) part is always well preserved thanks to the low uncatalyzed decomposition rate of Si_2H_6 (*i.e.,* low radial Si growth rate) under the given conditions.

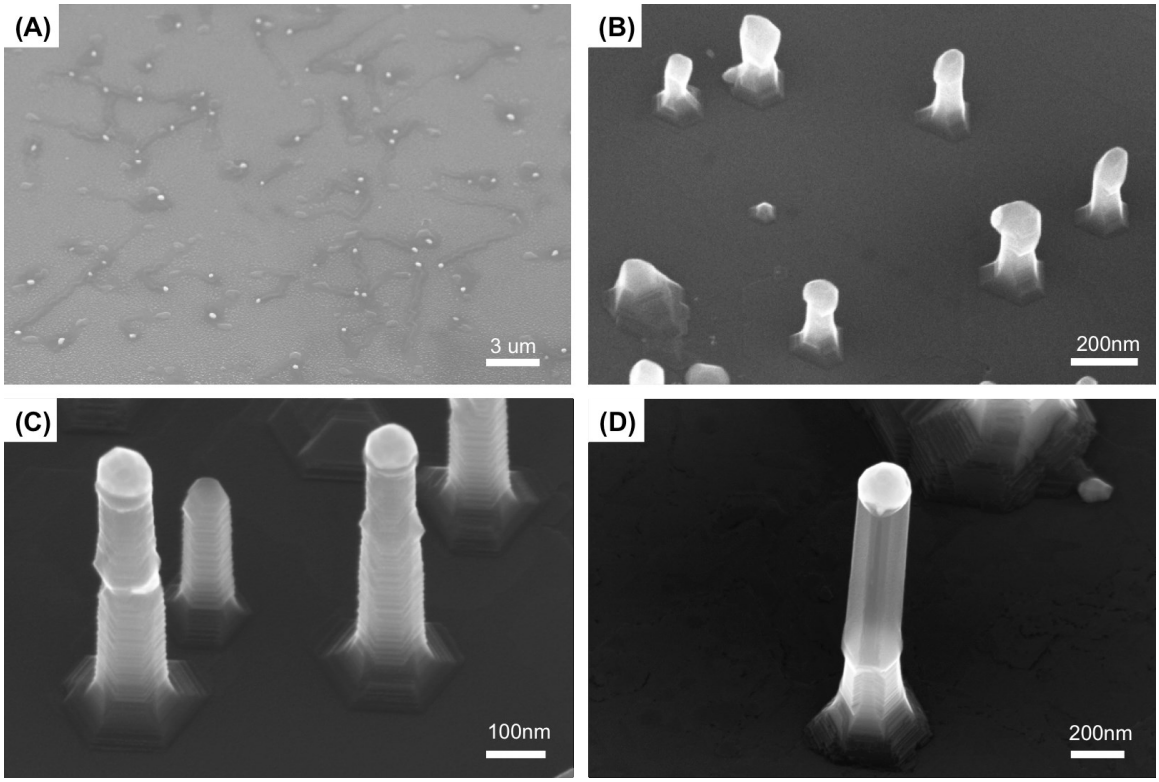

Figure 2-12: 40° perspective view of the result after (A) 20min of 2×10^{-2} mbar Si_2H_6 injection at 550°C directly on Ge(111) substrates (B) 40min of 2×10^{-5} mbar Si_2H_6 injection at 500°C on Ge NWs (C) 60min of 3×10^{-5} mbar Si_2H_6 injection at 400°C on Ge NWs. (D) 110min of 3×10^{-5} mbar Si_2H_6 injection at 380°C on Ge NWs.

2.2.6. GROWTH WITH COLLOIDAL GOLD

A quasi-monodisperse distribution of the NW diameter is ideal for studying systematically the size effects on various aspects of growth (kinetics, stress relaxation, etc.). Thanks to the simple nature of the VLS (VSS) growth, control of the size of the NWs can be achieved by controlling the size of the metal catalysts. Despite that a rather narrow size distribution was already achieved in our case by limiting the diffusion length (relatively low growth temperatures) and diffusion time (deposition on “hot” substrates)

of the Au catalysts, more precise control is possible if the NWs were seeded with commercially available colloidal gold.

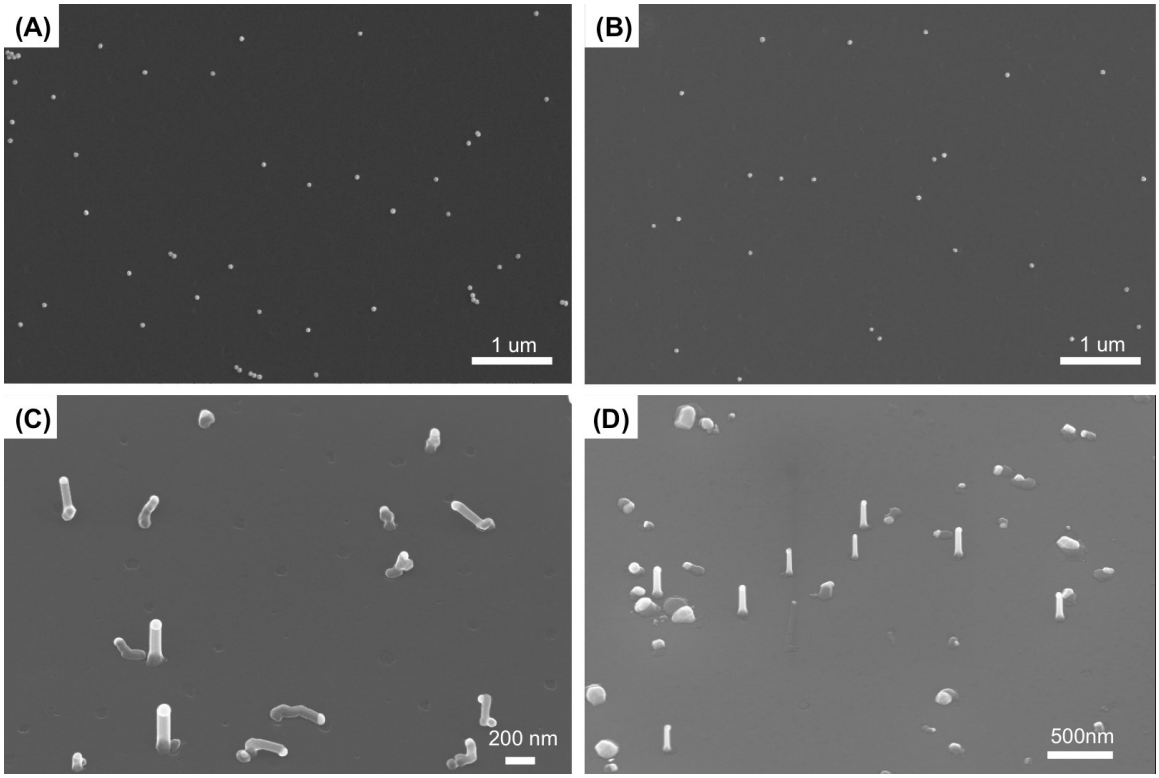

Figure 2-13: Top view of the sample surface after 2 cycles of 30-sec exposure to (A) 10% HF + colloid solution and (B) colloid solution (BBI solutions©, 50nm OD1). (C) 40° perspective view of Si NWs growth with colloidal Au. The Au nanoparticles were annealed during 25min under 9×10^{-3}mbar of Ar at 475°C prior to Si_2H_6 injection. (D) 40° perspective view of Ge NWs growth with colloidal Au. The Au nanoparticles were annealed during 10min at 400°C prior to 40min of 3×10^{-3}mbar Ge_2H_6 injection at 285°C.

The deposition of the nanoparticles was achieved by exposing the sample surface (Si or Ge, cleaned with the procedures described in Appendix III) to a mixture of one drop (~0.05mL) of 10% HF and two drops of colloid solution for 30 sec, a recipe recommended by D. Buttard at the CEA and by others (Woodruff et al. 2007). The resulted density is ~0.5 particles/μm^2 and can be further increased to 2-4 times the initial value by simply repeating the deposition step. SEM observations (Figure 2-13AB)

confirmed that adding HF acid to the solution significantly enhances the adsorption of the nanoparticles to the surface (and hence the density, by a factor of 2-5) while ensuring in the mean time a clean epitaxial contact between Au and the deoxidized sample surface, though at the cost of an increase in the agglomeration between neighboring particles. After the deposition, the samples were mounted with the Indium glue technique (Appendix III), during which a thermal oxide was inevitably formed at the surface. As will be shown later, this oxide layer plays a vital role in the subsequent growth process.

In the case of Si NWs (Figure 2-13C), the result of the growth was underwhelmed by the low yield of vertical orientated NWs. In fact, very few NWs exhibit continuous elongation along the [111] direction, others were either kinked or "crawling" at the surface. The Au nanoparticles were annealed under 10^{-2}-10^{-4} mbar of Ar gas prior to Si_2H_6 injection. We found that while longer annealing time slightly improves the yield, overlong annealing and/or under ultra high vacuum (*i.e.* without the presence of inert gas) could eventually lead to the agglomeration of the nanoparticles, thus destroying the monodispersity of the system. Moreover, the thermal oxide formed during the mounting procedure is considered as a contamination to the clean sample surface, and should be, in general, avoided. However, without the thermal oxide (*e.g.* by depositing colloidal Au only after the mounting procedure), there is no means of preventing the Au NPs from dissolving and wetting the surface layer once the eutectic temperature is reached, in which case, no NWs growth was observed at all due to the disappearance of the catalytic NPs.

The low yield of vertically oriented NWs seeded by colloidal Au has also been observed by our colleagues at the CEA (Gentile et al. 2008) and at Orsay. In their growth experiment using the same colloidal solution, they reported a progressive improvement of the yield by decreasing the growth temperature (from 600°C to 450°C) and by increasing

the SiH_4 flux (up to 200 sccm). While the result of their growth with 50nm colloids at 550°C resembles ours at the same temperature, the yield of their optimal growth condition (450°C, 20 sccm SiH_4) is significantly better. This is probably due to the much higher flux (and hence partial gas pressure) used in their experiment as compared to the maximum flux (1 sccm) that can be attained in our case. It is worth mentioning that the yield can be further increased by adding a moderate amount of HCl to the gas precursor (Potié et al. 2011), although such gas is not available in our growth chamber.

The growth of Ge NWs is more promising. The Ge NWs, if not crawling at the surface, grew predominately along the [111] direction. The result (Figure 2-13D) was similar to what was reported in the literature (Woodruff et al. 2007), the lower yield in our case is probably again caused by the difference in partial gas pressure. Au NPs were annealed at 400°C for 10min prior to Ge_2H_6 injection. Interestingly, we found, based on reproducible results from various experiments, that an intermediate annealing time (10min at 400°C) exists for the optimal growth condition. As a matter of fact, both shorter (3min) and longer (25min-50min) annealing time seemed to reduce significantly the yield of [111] NWs.

2.2.7. GROWTH WITH PATTERNED SUBSTRATES

Another way to achieve a monodisperse size distribution of the metal catalysts (and hence the NWs) is via patterning techniques. In this way, not only their size but also their position and arrangement can be perfectly controlled, which is of great interest for industrial applications. Typical patterning techniques include photolithography (Greyson et al. 2004), e-beam lithography (Mårtensson et al. 2003), nanoimprint lithography (Mårtensson et al. 2004), nanosphere lithography (Fuhrmann et al. 2005), etc. Thanks to the collaboration with L. Vila at the CEA, we were able to produce arrays of ordered Au nanopad of various sizes (30-200nm) on an area of 5mm×5mm (Figure 2-14A).

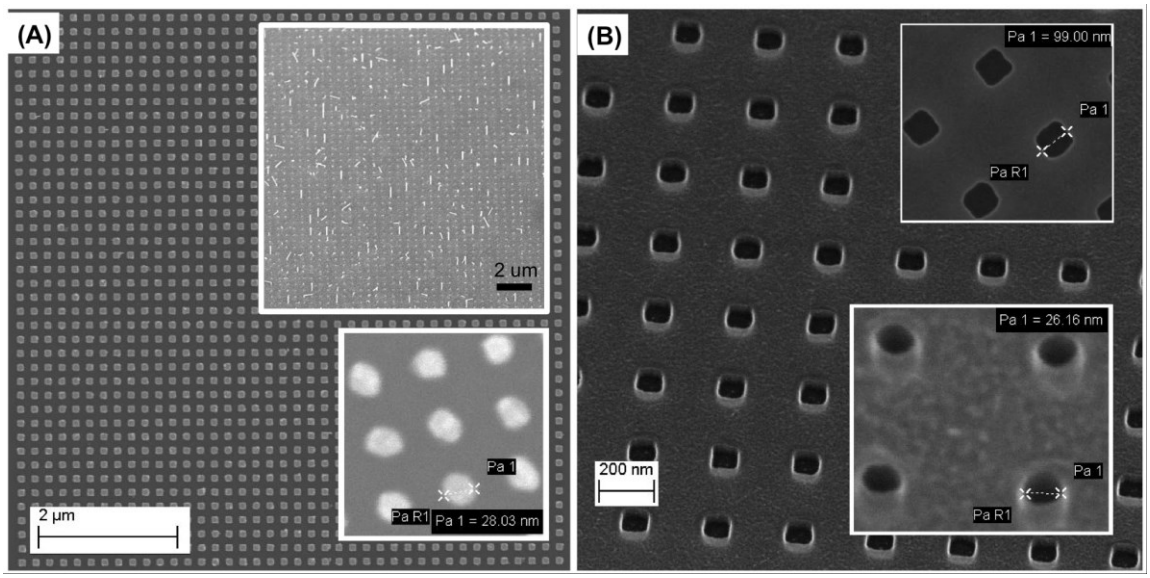

Figure 2-14: (A) Si(111) substrate with arrays of metal catalysts (side length 100nm spacing 100nm) patterned with e-beam lithography + lift-off. (top inset) 45° perspective view of the sample after Si NW growth. (bottom inset) Pattern with the minimum achievable feature size (side length 30nm, spacing 30nm). (B) 45° perspective view of a Si(111) substrate patterned with pits (side length 100nm, spacing 200nm, depth 50nm) by e-beam lithography + reactive ion etching. (top inset) Top down view of the same pattern. (bottom inset) Pattern with the minimum achievable feature size (side length 30nm, spacing 100nm, depth 50nm).

Subsequent NWs growth suffered the same poor yield as with colloidal Au, *i.e.,* straight NWs were seen growing from only a small proportion (~5%) of the patterned catalysts (top inset Figure 2-14A), compared to the close-to-100% ratio reported in the literature (Schmid et al. 2008). The low yield observed in our case is possibly again related to our growth condition. Most of the Au catalysts, instead of remaining in their patterned location, would have either diffused away or dissolved into a localized wetting layer by the time the sample was heated to the growth temperature, which is not unexpected under the clean UHV environment. Some improvements have been made, such as trapping the catalysts in preformed pits (Figure 2-14B), intentionally oxidizing the sample prior to the growth, etc.. The yield was eventually increased to ~30%, but the

presence of some curly NWs amongst the straight ones makes it difficult for even qualitative X-ray studies as a result of our relatively large beam size.

2.3.Conclusion

In this chapter, we have demonstrated the VLS growth of high quality Si, Ge NWs as well as SiGe radial and axial NW heterostructures (Figure 2-15) using our UHV-CVD equipment attached to the BM32 beamline at the ESRF.

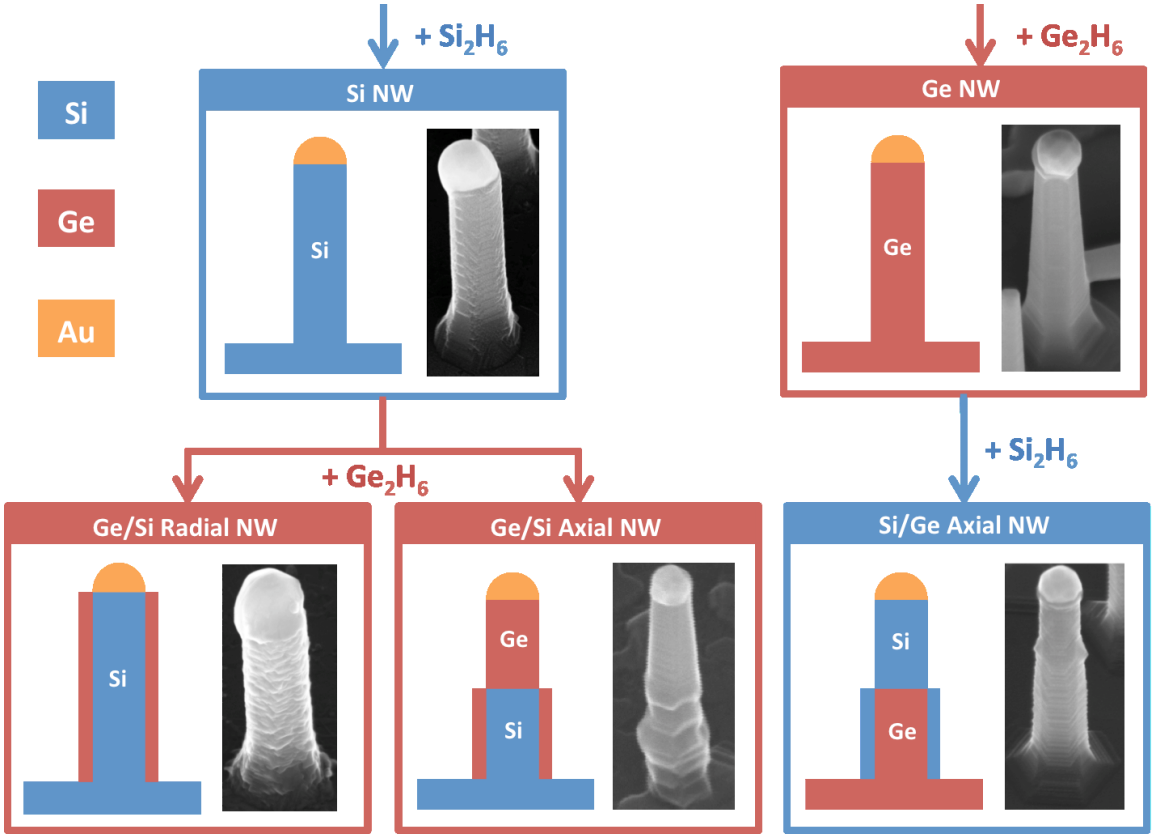

Figure 2-15: Schematics and SEM images of the NW structures grown over the course of this work.

The Si NWs were synthesized using ~1×10^{-5}mbar Si_2H_6 at ~500°C. The growth rate of the Si NWs shows an Arrhenius-type exponential dependence on the growth temperature and a linear dependence on the precursor gas partial pressure. There is no detectable difference between the growth rate of the NWs with larger and smaller diameters, which is expected for low pressure growths due to the limited Si supply. The Si NWs have either a hexagonal or a dodecagonal cross-section, depending on the extent of the overgrowth on the sidewall. Out-diffused Au nanoparticles were found anchoring the sidewall. They were thought to be responsible for the formation of the alternating facets of {111} and {113} family observed in the case of hexagonal sawtooth faceting.

The Ge NWs were synthesized using ~1×10^{-4}mbar Ge_2H_6 at temperatures below the eutectic point. Ge NWs grown at lower temperatures are intrinsically characterized by a circular cross-section and smooth sidewalls whereas those grown at higher temperatures have faceted sidewalls with a hexagonal cross-section, as a result of Ge overgrowth. Only VLS growth was observed in our case. The liquid AuGe alloy was stabilized at sub-eutectic temperature by capillary effects and by Ge supersaturation. Larger Ge NWs were found to grow faster, unlike what was observed in the case of Si NWs growth, possibly due to reduced Ge nucleation rate at lower temperatures.

NW heterostructures can be synthesized by injecting sequentially the two precursor gases.

A thicker Ge shell was observed on the upper part of the Ge/Si radial heterostructure NWs, probably due to the preferential decomposition of the precursor gas on the solid Au catalysts or due to a higher Ge growth rate on the dodecagonal sub-facets. The shell layer is composed of 3D Ge islands as a result of Stranski-Krastanov growth on NWs with a larger diameter, as opposed to the 2D wetting layer (Frank-van der Merwe

growth) observed on NWs with a smaller diameter. The morphology of the Ge shell is otherwise similar to that grown with MBE at the same temperature.

A size limit was observed when synthesizing Ge/Si axial heterostructures, much to our surprise. It seemed that subsequent Ge growth could only occur, on Si NWs or directly on Si substrates, for catalysts with a limited diameter. The observed upper limit is at odds with classic thermodynamic understandings where a lower limit should be expected instead. Both the Si and the Ge parts were covered with a thick Ge shell due to the elevated decomposition rate of the precursor gas and the high mobility of the Ge adatoms during the 2nd stage of growth.

The main challenge for synthesizing Si/Ge axial heterostructures is the large temperature gap between the two stages of growth. Higher yield can be achieved by lowering the growth temperature of the Si part to below 400°C. Contrary to what was observed for the synthesis of Ge/Si axial heterostructures, shell growth in this case is rather limited thanks to the low spontaneous decomposition rate of Si_2H_6 at 400°C.

Lastly, growths with colloidal gold and with patterned substrates have been attempted. The idea was to achieve a monodisperse distribution of the NW diameter to study systematically the size effects on various aspects of growth. However, practical applications of these samples for X-ray experiments were hindered by the low yield of vertically oriented NWs, partially due to our limited precursor gas pressure and the clean UHV environment.

References:

Adhikari, H. et al., 2007. Conditions for subeutectic growth of Ge nanowires by the vapor-liquid-solid mechanism. Journal of Applied Physics, 102(9), p.094311.

Adhikari, H. et al., 2006. Germanium nanowire epitaxy: shape and orientation control. Nano letters, 6(2), pp.318–23.

Alexander Liddle, J., Gallatin, G.M. & Ocola, L.E., 2011. Resist Requirements and Limitations for Nanoscale Electron-Beam Patterning. MRS Proceedings, 739, p.H1.5.

Allen, J.E. et al., 2008. High-resolution detection of Au catalyst atoms in Si nanowires. Nature nanotechnology, 3(3), pp.168–73.

Awschalom, D.D. & Flatté, M.E., 2007. Challenges for semiconductor spintronics. Nature Physics, 3(3), pp.153–159.

Bootsma, G.A.A. & Gassen, H.J.J., 1971. A quantitative study on the growth of silicon whiskers from silane and germanium whiskers from germane. Journal of Crystal Growth, 10(3), pp.223–234.

Boukhicha, R., 2011. Croissance et caractérisation de nanofils de silicium et de germanium obtenus par dépôt chimique en phase vapeur sous ultravide. Thesis, Université Paris Sud.

Bramblett, T.R. et al., 1994. Si(001)2×1 gas-source molecular-beam epitaxy from Si2H6: Growth kinetics and boron doping. Journal of Applied Physics, 76(3), p.1884.

Chan, C.K. et al., 2008. High-performance lithium battery anodes using silicon nanowires. Nature nanotechnology, 3(1), pp.31–5.

Costner, E.A. et al., 2009. Nanoimprint Lithography Materials Development for Semiconductor Device Fabrication. Annual Review of Materials Research, 39, pp.155–180.

David, T. et al., 2008. Structural investigation of silicon nanowires using {GIXD} and GISAXS: Evidence of complex saw-tooth faceting. Surface Science, 602(15), pp.2675–2680.

Dayeh, S.A. et al., 2011. Growth, defect formation, and morphology control of germanium-silicon semiconductor nanowire heterostructures. Nano letters, 11(10), pp.4200–6.

Dayeh, S.A. & Picraux, S.T., 2010. Direct observation of nanoscale size effects in Ge semiconductor nanowire growth. Nano letters, 10(10), pp.4032–9.

Dhalluin, F. et al., 2010. Silicon nanowires: Diameter dependence of growth rate and delay in growth. Applied Physics Letters, 96(13), p.133109.

Dick, K.A. et al., 2007. The morphology of axial and branched nanowire heterostructures. Nano letters, 7(6), pp.1817–22.

Fan, H.J., Werner, P. & Zacharias, M., 2006. Semiconductor nanowires: from self-organization to patterned growth. Small (Weinheim an der Bergstrasse, Germany), 2(6), pp.700–17.

Fischer, K.E. et al., 2009. Biomimetic nanowire coatings for next generation adhesive drug delivery systems. Nano letters, 9(2), pp.716–20.

Fuhrmann, B. et al., 2005. Ordered Arrays of Silicon Nanowires Produced by Nanosphere Lithography and Molecular Beam Epitaxy. Nano Letters, 5(12), pp.2524–2527.

Gamalski, A.D. et al., 2010. Formation of metastable liquid catalyst during subeutectic growth of germanium nanowires. Nano letters, 10(8), pp.2972–6.

Gamalski, A.D. et al., 2012. Metastable Crystalline AuGe Catalysts Formed During Isothermal Germanium Nanowire Growth. Physical Review Letters, 108(25), p.255702.

Gentile, P. et al., 2008. The growth of small diameter silicon nanowires to nanotrees. Nanotechnology, 19(12), p.125608.

Givargiz.EI & Chernov, A.A., 1973. Growth-Rate Of Whiskers Grown By Vapor-Liquid-Solid Mechanism, And Role Of Surface-Energy. Kristallografiya, 18(1), pp.147–153.

Givargizov, E.I., 1975. Fundamental aspects of VLS growth. Journal of Crystal Growth, 31(null), pp.20–30.

Givargizov, E.I., 1987. Highly anisotropic crystals, D. Reidel Publishing Company.

Greyson, E.C., Babayan, Y. & Odom, T.W., 2004. Directed Growth of Ordered Arrays of Small-Diameter ZnO Nanowires. Advanced Materials, 16(15), pp.1348–1352.

Hannon, J.B. et al., 2006. The influence of the surface migration of gold on the growth of silicon nanowires. Nature, 440(7080), pp.69–71.

Hayden, O., Agarwal, R. & Lieber, C.M., 2006. Nanoscale avalanche photodiodes for highly sensitive and spatially resolved photon detection. Nature materials, 5(5), pp.352–6.

Henckel, J., 1757. Pyritologia or, a history of the pyrites, the principal body in the mineral kingdom. ... Translated from the German of J.F. Henckel ..., London ;And A. Linde: Printed for A. Millar ;

Den Hertog, M.I. et al., 2008. Control of gold surface diffusion on si nanowires. Nano letters, 8(5), pp.1544–50.

Hoffmann, S. et al., 2006. Measurement of the bending strength of vapor-liquid-solid grown silicon nanowires. Nano letters, 6(4), pp.622–5.

Hofmann, S. et al., 2008. Ledge-flow-controlled catalyst interface dynamics during Si nanowire growth. Nature materials, 7(5), pp.372–5.

Jagannathan, H. et al., 2006. Nature of germanium nanowire heteroepitaxy on silicon substrates. Journal of Applied Physics, 100(2), p.024318.

Kamins, T.I. et al., 2004. Growth and Structure of Chemically Vapor Deposited Ge Nanowires on Si Substrates. Nano Letters, 4(3), pp.503–506.

Kikkawa, J., Ohno, Y. & Takeda, S., 2005. Growth rate of silicon nanowires. Applied Physics Letters, 86(12), p.-.

Kodambaka, S. et al., 2006. Control of Si nanowire growth by oxygen. Nano letters, 6(6), pp.1292–6.

Kodambaka, S. et al., 2006. Diameter-Independent Kinetics in the Vapor-Liquid-Solid Growth of Si Nanowires. Physical Review Letters, 96(9), p.096105.

Kodambaka, S. et al., 2007. Germanium nanowire growth below the eutectic temperature. Science (New York, N.Y.), 316(5825), pp.729–32.

Lander, J.J., 1964. Chemisorption and ordered surface structures. Surface Science, 1(2), pp.125–164.

Lauhon, L.J. et al., 2002. Epitaxial core-shell and core-multishell nanowire heterostructures. Nature, 420(6911), pp.57–61.

Lensch-Falk, J.L. et al., 2009. Alternative catalysts for VSS growth of silicon and germanium nanowires. Journal of Materials Chemistry, 19(7), p.849.

Lew, K.-K. & Redwing, J.M., 2003. Growth characteristics of silicon nanowires synthesized by vapor–liquid–solid growth in nanoporous alumina templates. Journal of Crystal Growth, 254(1–2), pp.14–22.

Li, X. & Yang, G., 2014. Modification of Stranski-Krastanov growth on the surface of nanowires. Nanotechnology, 25(43), p.435605.

Lieber, C.M. & Wang, Z.L., 2011. Functional Nanowires. MRS Bulletin, 32(02), pp.99–108.

Lü, Y.Y. et al., 2012. Diameter-dependent or independent: toward a mechanistic understanding of the vapor-liquid-solid Si nanowire growth rate. Nano letters, 12(8), pp.4032–6.

Mårtensson, T. et al., 2003. Fabrication of individually seeded nanowire arrays by vapour–liquid–solid growth. Nanotechnology, 14(12), pp.1255–1258.

Mårtensson, T. et al., 2004. Nanowire Arrays Defined by Nanoimprint Lithography. Nano Letters, 4(4), pp.699–702.

Oehler, F. et al., 2010. The Importance of the Radial Growth in the Faceting of Silicon Nanowires. NANO LETTERS, 10(7), pp.2335–2341.

Perea, D.E. et al., 2011. Controlling heterojunction abruptness in VLS-grown semiconductor nanowires via in situ catalyst alloying. Nano letters, 11(8), pp.3117–22.

Potié, A. et al., 2011. Controlled growth of SiGe nanowires by addition of HCl in the gas phase. Journal of Applied Physics, 110(2), p.024311.

Rai-Choudhury, P., 1997. Handbook of Microlithography, Micromachining, and Microfabrication: Microlithography,

Renard, C. et al., 2012. Size effect on Ge nanowires growth kinetics by the vapor–liquid–solid mechanism. Thin Solid Films, 520(8), pp.3314–3318.

Ross, F.M., Tersoff, J. & Reuter, M.C., 2005. Sawtooth Faceting in Silicon Nanowires. Physical Review Letters, 95(14), p.146104.

Schmid, H. et al., 2008. Patterned epitaxial vapor-liquid-solid growth of silicon nanowires on Si(111) using silane. Journal of Applied Physics, 103(2), p.-.

Schmidt, V., Senz, S. & Gösele, U., 2007. Diameter dependence of the growth velocity of silicon nanowires synthesized via the vapor-liquid-solid mechanism. Physical Review B, 75(4), p.045335.

Schmidt, V., Senz, S. & Gösele, U., 2005. Diameter-dependent growth direction of epitaxial silicon nanowires. Nano letters, 5(5), pp.931–5.

Schmidt, V., Wittemann, J. V & Gösele, U., 2010. Growth, thermodynamics, and electrical properties of silicon nanowires. Chemical reviews, 110(1), pp.361–88.

Schubert, L. et al., 2004. Silicon nanowhiskers grown on ⟨111⟩Si substrates by molecular-beam epitaxy. Applied Physics Letters, 84(24), p.4968.

Schülli, T.U. et al., 2010. Substrate-enhanced supercooling in AuSi eutectic droplets. Nature, 464(7292), pp.1174–7.

Schwalbach, E.J. & Voorhees, P.W., 2008. Phase equilibrium and nucleation in VLS-grown nanowires. Nano letters, 8(11), pp.3739–45.

Schwarz, K.W. & Tersoff, J., 2011. Elementary processes in nanowire growth. Nano letters, 11(2), pp.316–20.

Schwarz, K.W. & Tersoff, J., 2012. Multiplicity of steady modes of nanowire growth. Nano letters, 12(3), pp.1329–32.

Shin, N. & Filler, M.A., 2012. Controlling silicon nanowire growth direction via surface chemistry. Nano letters, 12(6), pp.2865–70.

Sierra-Sastre, Y. et al., 2010. Epitaxy of Ge Nanowires Grown from Biotemplated Au Nanoparticle Catalysts.

Snyder, G.J. & Toberer, E.S., 2008. Complex thermoelectric materials. Nature materials, 7(2), pp.105–14.

Sutter, E. & Sutter, P., 2008. Phase diagram of nanoscale alloy particles used for vapor-liquid-solid growth of semiconductor nanowires. Nano letters, 8(2), pp.411–4.

Sutter, E.A. & Sutter, P.W., 2010. Size-dependent phase diagram of nanoscale alloy drops used in vapor--liquid--solid growth of semiconductor nanowires. ACS nano, 4(8), pp.4943–7.

Tan, T.Y., Li, N. & Gösele, U., 2003. Is there a thermodynamic size limit of nanowires grown by the vapor-liquid-solid process? Applied Physics Letters, 83(6), p.1199.

Vincent, L. et al., 2011. Faceting mechanisms of Si nanowires and gold spreading. Journal of Materials Science, 47(4), pp.1609–1613.

Wacaser, B.A. et al., 2009. Growth system, structure, and doping of aluminum-seeded epitaxial silicon nanowires. Nano letters, 9(9), pp.3296–301.

Wagner, R.S. & Ellis, W.C., 1964. Vapor-Liquid-Solid Mechanism Of Single Crystal Growth. Applied Physics Letters, 4(5), p.89.

Wang, D. & Dai, H., 2002. Low-temperature synthesis of single-crystal germanium nanowires by chemical vapor deposition. Angewandte Chemie (International ed. in English), 41(24), pp.4783–6.

Wang, Y. et al., 2006. Epitaxial growth of silicon nanowires using an aluminium catalyst. Nature nanotechnology, 1(3), pp.186–9.

Wen, C.-Y. et al., 2009. Formation of compositionally abrupt axial heterojunctions in silicon-germanium nanowires. Science (New York, N.Y.), 326(5957), pp.1247–50.

Wen, C.-Y. et al., 2010. Step-Flow Kinetics in Nanowire Growth. Physical Review Letters, 105(19), p.195502.

Wen, C.-Y. et al., 2010. Structure, growth kinetics, and ledge flow during vapor-solid-solid growth of copper-catalyzed silicon nanowires. Nano letters, 10(2), pp.514–9.

Westwater, J., 1997. Growth of silicon nanowires via gold/silane vapor–liquid–solid reaction. Journal of Vacuum Science & Technology B: Microelectronics and Nanometer Structures, 15(3), p.554.

Wiethoff, C. et al., 2008. Au stabilization and coverage of sawtooth facets on Si nanowires grown by vapor-liquid-solid epitaxy. NANO LETTERS, 8(9), pp.3065–3068.

Woodruff, J.H. et al., 2007. Vertically oriented germanium nanowires grown from gold colloids on silicon substrates and subsequent gold removal. Nano letters, 7(6), pp.1637–42.

Wu, Y. et al., 2004. Controlled Growth and Structures of Molecular-Scale Silicon Nanowires. Nano Letters, 4(3), pp.433–436.

Zhang, X. et al., 2007. Diameter-dependent composition of vapor-liquid-solid grown Si(1-x)Ge(x) nanowires. Nano letters, 7(10), pp.3241–5.

3. IN SITU GROWTH STUDY OF SI/GE NWS

This chapter centers on our preliminary efforts to understand the growth of Si and Ge NWs with *in situ* synchrotron X-ray techniques. The objective is to demonstrate the possibility of using X-ray scattering as a viable tool for the study of growth kinetics, morphological change and strain evolution during NW growth. Compared to Electron Microscopy studies (*c.f.* Chapter 2) which is, to date, the dominating technique for NW characterization, X-ray gathers statistically averaged information on the entire illuminated area thus providing us with a more comprehensive view on the subject.

The rest of the chapter is structured as follows. Chapter 3.1 describes the instrument parameters related to the experiments. Chapter 3.2 and 3.3 are devoted to the *in situ* X-ray study of Si and Ge NWs, respectively. At the end of each chapter, a discussion is held which summarizes some of the observations that are yet to be completely understood. General aspects on the growth and morphology of SiGe coreshell NWs will be presented in the next chapter (Chapter 4).

3.1.Experimental Setup

The general growth conditions for Si and Ge NWs in our case have been described in Chapter 2. For GIXD experiments, the vertical slit before the detector is closed to less than 1mm in order to achieve a better in plane resolution while the horizontal slit is left wide open to fully exploit the large out-of-plane acceptance of the 2D detector. The sample-slit distance varies from 190mm to 270mm and the sample-detector distance varies from 640mm to 720mm, depending on the out-of-plane scattering angle. The CCD camera used for the GISAXS experiments has a total of 1528×1528 pixels after binning, and a typical sample-detector distance of 1.5 meters. In Table 3-1 is

listed a set of parameters detailing the resolution of the experiments in the reciprocal space, considering an ideal monochromatic beam.

At 11keV	GIXD in plane resolution (V-slit)	GIXD pixel resolution at 640mm	GISAXS pixel resolution at 1.5m
Physical size	0.6 mm	55µm	43.965 µm
Reciprocal space	0.0052 $Å^{-1}$	0.00048 $Å^{-1}$	0.00016 $Å^{-1}$

Table 3-1 :List of parameters on the resolution of the experiments in the reciprocal space.

The majority of the results in this work use surface indices (subscript s) as their notation system, the corresponding bulk Miller indices (subscript b) can be calculated via

$$\begin{pmatrix} h_b \\ k_b \\ l_b \end{pmatrix} = \frac{1}{3}\begin{pmatrix} 2 & \bar{2} & 1 \\ 2 & 4 & 1 \\ \bar{4} & \bar{2} & 1 \end{pmatrix}\begin{pmatrix} h_s \\ k_s \\ l_s \end{pmatrix} \qquad (3\text{-}1)$$

3.2. Si NWs

3.2.1. Si NWs as seen by GIXD

For the *in situ* study of Si NW growth with GIXD, we shall start by presenting the intensity evolution of sample #021211 around the Si $(110)_s$ and $(300)_s$ peak, respectively. The alloy catalysts were formed by depositing 5ML of Au directly on a "hot" substrate (T_{sub} = 525°C). Once the injection started, the narrow bulk Si Bragg peak (Figure 3-1, reference black curves) quickly submerged itself under the broader Si NW peak. Several notable observations can be made.

(Figure 3-1AB) In the case of rocking scans, a periodic undulation can be seen modulating the intensity profile. This modulation is indicative of a narrow size distribution along the direction of the scans, and can be traced directly back to the form factor of the nano-objects. Moreover, the modulation period (Figure 3-2A) is slightly larger around $(300)_s$ than around $(110)_s$, which is expected if one takes into account the asymmetry due to the hexagonal cross-section of the NWs (Figure 3-2B). The real

situation is often more complicated. The six-fold symmetry of the regular hexagon is reduced to a three-fold one if one of the consecutive sides is longer than the other (Figure 3-2C). The form factor of such trigonal hexagon can be calculated as

$$F(\mathbf{q}, R_a, R_b) = \frac{6}{3q_y^2 - q_x^2}[\exp(-iq_y(\frac{\sqrt{3}}{6}R_a - \frac{\sqrt{3}}{6}R_b)) \quad (2\mathcal{M}(R_a + R_b)) - \exp(-iq_y(-\frac{\sqrt{3}}{3}R_a - \frac{\sqrt{3}}{6}R_b))(\mathcal{M}(R_b) + \mathcal{N}(R_b)) + \exp(-iq_y(\frac{\sqrt{3}}{6}R_a + \frac{\sqrt{3}}{3}R_b)) \quad (-\mathcal{M}(R_a) + \mathcal{N}(R_a))] \tag{3-2}$$

$$\mathcal{M}(R) = \sqrt{3}/3 \cdot \cos(-q_x R/2) \qquad \mathcal{N}(R) = i\, q_y R/2 \cdot \mathrm{sinc}(-q_x R/2)$$

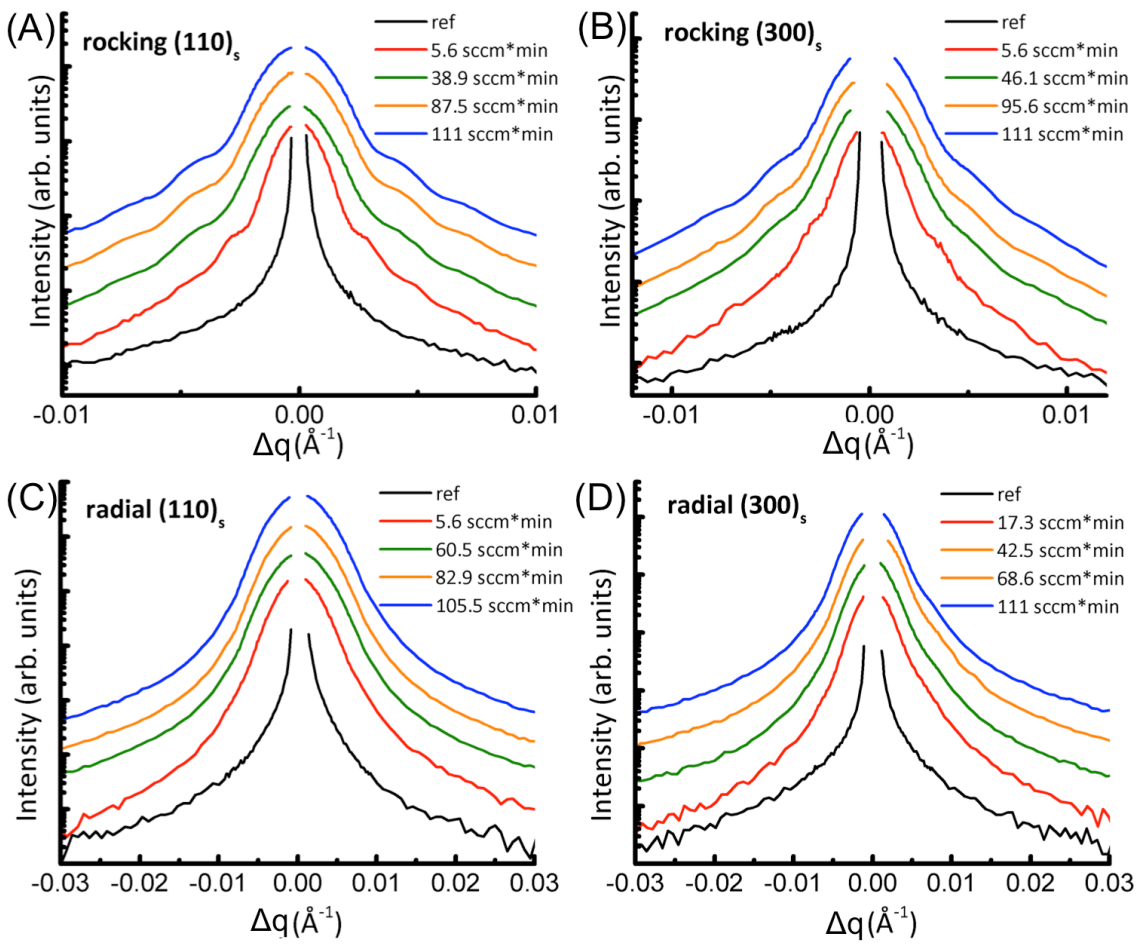

Figure 3-1 : Intensity evolution of sample #021211 during NW growth around the Si (A and C) $(100)_s$ and around the Si (B and D) $(300)_s$ peak, respectively. The vertical scale has been readjusted to aid the eye.

$\mathbf{q_x}$ and $\mathbf{q_y}$ are at right angles to each other with $\mathbf{q_y}$ along one of the apothems. $q_x = 0$ for rocking scans around $(110)_s$. $q_y = 0$ for rocking scans around $(300)_s$. The cardinal sine function is defined as $\mathrm{sinc}(x) = \sin(x)/x$. For NWs with a regular hexagonal cross-section $R = R_a = R_b$, Eq. (3-2) can be reduced to

$$F(\mathbf{q}, R) = \frac{4\sqrt{3}}{3q_y^2 - q_x^2}\left[\frac{3}{4}q_y^2 R^2 \,\mathrm{sinc}\left(q_x \frac{R}{2}\right)\mathrm{sinc}\left(q_y \frac{\sqrt{3}R}{2}\right) + \cos(q_x R) - \cos\left(q_y \frac{\sqrt{3}R}{2}\right)\cos\left(q_x \frac{R}{2}\right)\right] \quad (3\text{-}3)$$

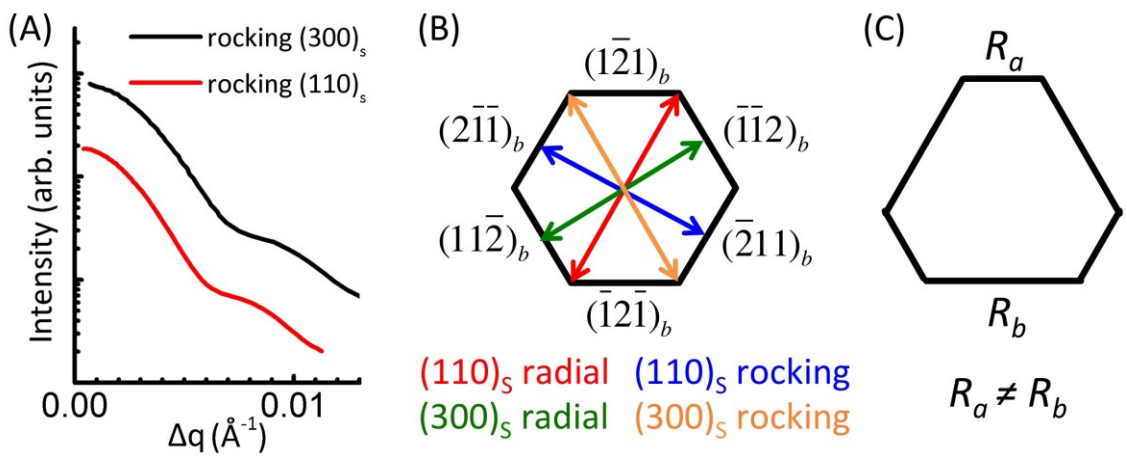

Figure 3-2: (A) Comparison between the modulation period around $(110)_s$ and around $(300)_s$ for rocking scans on sample #041211. (B) Schematic representation detailing the scanning direction of each specific type of scan for a NW with a regular hexagonal cross-section. (C) Schematics of the trigonal hexagon with a three-fold symmetry.

For future reference, we shall define D the diameter of a NW as the distance between two opposing faces.

$$D = \sqrt{3}R = \frac{\sqrt{3}}{2}(R_a + R_b) \quad (3\text{-}4)$$

(Figure 3-3 blue curves) For NWs with a regular hexagonal cross-section, the form factor along $\mathbf{q_x}$ has all its minima located exactly at $4n\pi/3R$ or $4\sqrt{3}n\pi/3D$ with n being a positive integer. Along the $\mathbf{q_y}$ direction, the minima are found at

$2nm\pi/\sqrt{3}R$ or $2nm\pi/D$, for even n, the variable m = 1, for odd n, $m \epsilon \{1.169, 1.022, 1.008, 1.004 \ldots\}$ and tends to 1 at larger q values. *Ex situ* SEM reveals a typical ratio of $1.1 < R_b/R_a < 1.5$ for the NWs synthesized with our growth conditions. For the sake of discussion, we shall consider a trigonal hexagon with $R_b/R_a = 2$ (Figure 3-3 red curve) and demonstrate that even in the exaggerated scenario a regular hexagon can be used as a good approximation to the real life situation for quantitative analysis.

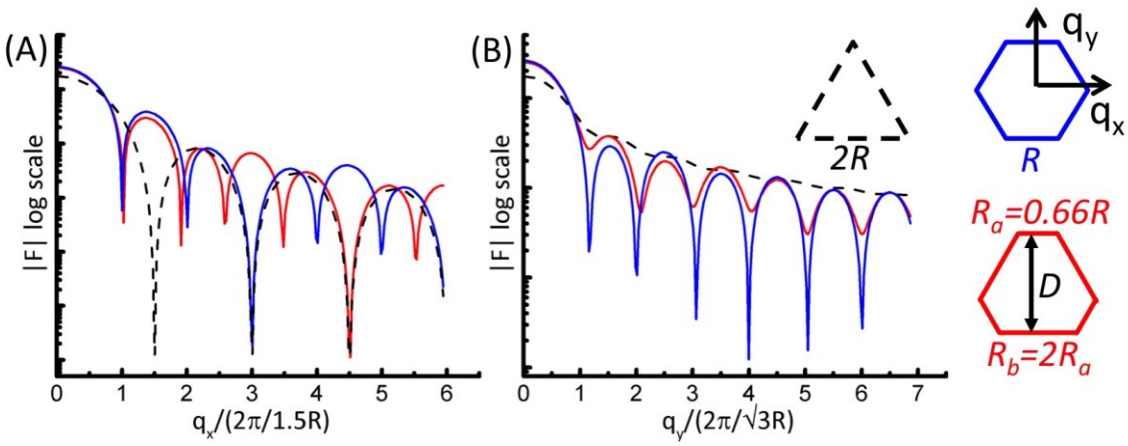

Figure 3-3 : Comparison between the form factors of a NW with a regular hexagonal cross-section ($R_b/R_a = 1$, blue curve) and that with a trigonal hexagonal cross-section ($R_b/R_a = 2$, red curve). The form factor of the extreme case of a trigonal hexagon, a triangle ($R_b/R_a = \infty$, black dashed curve) is also plotted.

The result is listed in Table 3-2. For rocking scans around $(300)_s$, the two form factors only become dissimilar after the 2nd local minima. The positions of the first two local minima can thus be used to estimate the diameter of the NWs, with which we obtain D equals to 217±13 and 223±13, respectively. The estimation is consistent with *ex situ* SEM observations which reveal an average diameter of ~230nm for this sample. In the case of rocking scans around $(110)_s$, the magnitude of the undulation is less significant for the trigonal hexagon than for the regular one but the positions of their local minima

are less than 3% different. This again allows us to estimate the diameter of the NWs (D = 239±16 and D = 225±9 respectively with the first two minima) regardless of the exact ratio between R_b and R_a.

Positions of local minima		1st	2nd	3rd	4th	5th	6th
along $\mathbf{q_x}$ $q_y = 0$ rocking $(300)_s$ radial $(110)_s$	regular hexagon with side length R unity = $4\sqrt{3}\pi/3D$	1	2	3	4	5	6
	trigonal hexagon with $R_b/R_a = 2$ unity = $4\sqrt{3}\pi/3D$	1.026	1.910	2.578	3.485	4.512	5.539
along $\mathbf{q_y}$ $q_x = 0$ rocking $(110)_s$ radial $(300)_s$	regular hexagon with side length R unity = $2\pi/D$	1.169	2	3.066	4	5.040	6
	trigonal hexagon with $R_b/R_a = 2$ unity = $2\pi/D$	1.158	2.067	3.005	4.052	5.045	6.010

Table 3-2 : Comparison between the positions of the local minima of the form factors for a NW with a regular hexagonal cross-section and that with a trigonal one.

Moreover, it can be noted, from Figure 3-1A, that the period of the size modulation increases as the NWs grow. This seems to indicate that the diameter of the NWs shrank from 334±20nm (red curve, 5.6 sccm*min of injection) to 234±9nm (green curve, 38.9 sccm*min) before stabilized at 225±9nm (orange and blue curve, >87.5 sccm*min). The decrease of the measured value is understood as follows. With X-ray we measure the average diameter of the NWs. (Figure 3-4A) At the very early stage of growth, the measured value was dominated by the base of the NWs which is much larger in size compared to the body of the NWs. As the NWs grew longer, the contribution from the base became less significant, the measured value then quickly converged towards that of the NW body. Finally, it is also possible to deduce D using the FWHM of the NW Bragg peaks. The resulted values, 234±1nm for rocking scans around $(110)_s$ and

221±1nm for rocking scans around $(300)_s$, agree well with our previous estimations. It is worth mentioning that the good agreement also implies a very low level of mosaicity (less than 0.010) among the synthesized NWs.

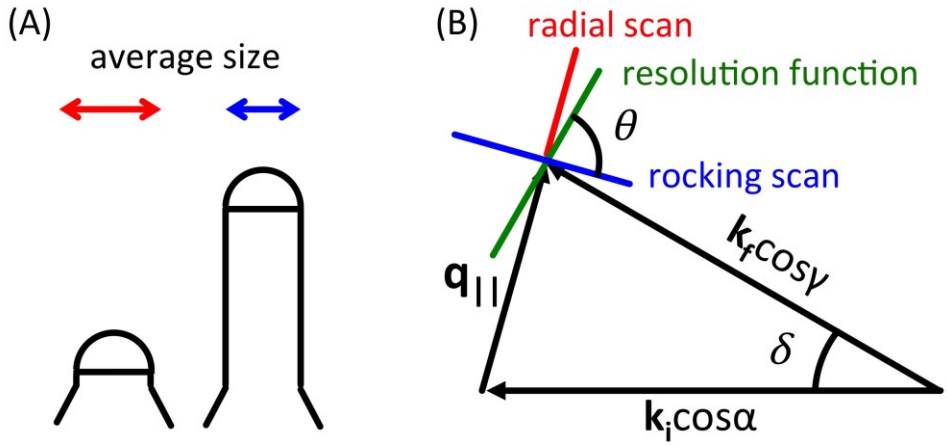

Figure 3-4: (A) Schematic representation showing how the average size measured decreases as the NW grows. (B) Schematics for calculating the in plane resolution function for a radial scan and for a rocking scan. $\mathbf{q}_{||}$ is the in plane projection of the momentum transfer. δ is the in plane detector angle.

From Figure 3-2B it can be inferred that with radial scans around $(110)_s$ the dimension of the NW we measure is the same as with rocking scans around $(300)_s$. However, the FWHM (0.00638 $Å^{-1}$ as opposed to 0.00329 $Å^{-1}$) is considerably larger (Figure 3-1CD). Multiple sources can contribute to the broadening of the peak, internal stress, bended NWs, dislocations, stacking faults, etc., all of which would result in peak asymmetry and/or peak shift (Singh 2005), which was not observed here. The peak broadening in our case can be simply attributed to the resolution function of the detector slits. (Figure 3-4B) Take $(110)_s$ peak as an example, the resolution function for a radial scan is the projection along the scanning direction ($\sin\theta, \theta = 75°$) of the size of the detector slits in the reciprocal space (0.0052 $Å^{-1}$, Table 3-1). The resulted value (0.0050$Å^{-1}$) fits well with what we expect from the broadening of a Gaussian shape peak

($\sqrt{0.00638^2 - 0.00329^2} = 0.0055$Å^{-1}). The resolution function for a rocking scan on the same peak is much smaller thanks to the large angle ($\cos\theta, \theta = 75°$) between the detector slits and the scanning direction. The same calculation can be done for the $(300)_s$ peak. The resolution function is also responsible for the absence of size modulated intensities in the radial scans. As a matter of fact, although convolution with the resolution function does not affect the period of the modulation (which makes the use of size modulation a more reliable source for diameter estimation than FWHM), it could effectively smoothen the already weak undulation, smearing it out in the process. Compared to rocking scans, radials scans are not without their benefits. The centers of the NW peaks are found to be located exactly on bulk Si positions for radial scans around both $(110)_s$ and $(300)_s$, which indicates the absence of internal stress inside the Si NWs.

Method	Reciprocal space (Å^{-1})	Real space (nm)	Comment (considering a regular hexagon)
ex situ SEM		~ 230	$D = \sqrt{3}R = \sqrt{3}/2\ (R_a + R_b)$=230
radial $(110)_s$ FWHM	0.00638	99(1)	significantly broadened by the resolution function
rocking $(110)_s$ FWHM	0.00268	234(1)	$D = 234$
rocking $(110)_s$ 1st min.	0.00307	205(14)	the 1st zero corresponds to $D/1.169$ hence $D = 239$
rocking $(110)_s$ 2nd min.	0.00558	113(5)	the 2nd zero corresponds to $D/2$ hence $D = 225$
radial $(300)_s$ FWHM	0.00505	124(1)	significantly broadened by the resolution function
rocking $(300)_s$ FWHM	0.00329	191(1)	this corresponds to $D/\sqrt{3} * 1.5$ hence D = 221
rocking $(300)_s$ 1st min.	0.00335	188(11)	this corresponds to $D/\sqrt{3} * 1.5$ hence D = 217
rocking $(300)_s$ 2nd min.	0.00651	97(6)	this is $D/\sqrt{3} * 1.5/2$ hence D = 223

Table 3-3 : Comparison between the NW diameters estimated by various methods. The numbers in the brackets are the corresponding uncertainties.

So far we have only considered the use of diffraction methods for the determination of the diameter of the NWs. The result is summarized in Table 3-3 which also details how the same result was derived from seemingly different values measured in the reciprocal space.

This thesis work also has the privilege to witness the popularization of the 2D detectors amongst synchrotron beamlines, below is one of the few examples intended to demonstrate how the 2D detectors can help us better perceive the changes in the reciprocal space (in Chapter 5 there is an experiment that solely relies on the use of 2D detectors for continuous observation!).

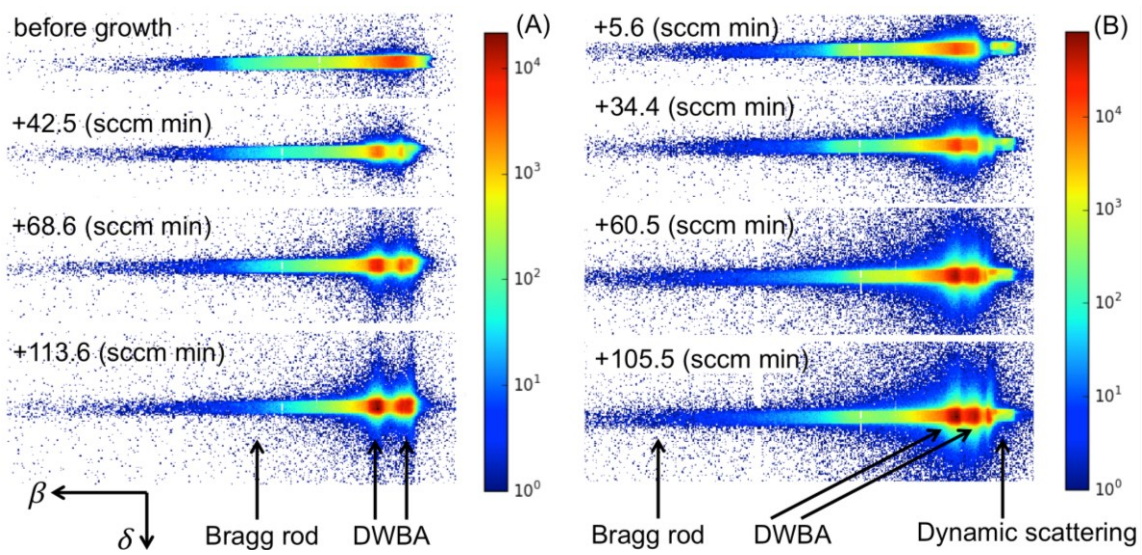

Figure 3-5: Raw images from the 2D detector during NW growth at (A) $Si(300)_s$ Bragg position and (B) $Si(110)_s$ Bragg position. δ and β are respectively the in plane and out-of-plane detector angle as was described in Figure 1-6.

(Figure 3-5A) The 2D image of a bare Si substrate is a narrow streak that extends in the β direction as the $(300)_s$ Bragg rod intersects the lower part of the Ewald's sphere. The intensity in the δ direction is cut off by the small opening of the detector slits. As the growth progresses, a duplicate of the original peak, as predicted by the DWBA theory,

can be clearly observed and is further enhanced by the Yoneda wing. (Figure 3-5B) Around the $(110)_s$ peak, the situation is similar except for the emergence of other dynamic effects due to the larger scattering factors at smaller momentum transfers.

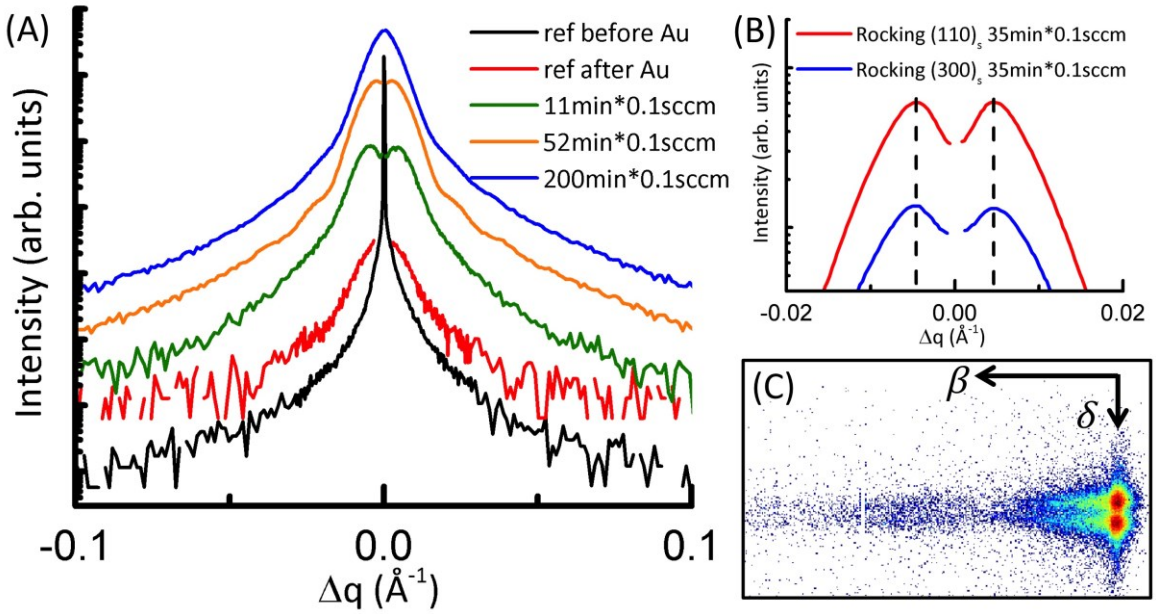

Figure 3-6: Sample #280612 (A) rocking scans in the vicinity of the $(110)_s$ reflection at different stages of growth. The vertical scale was readjusted to aid the eye. (B) Close-up look of the twin peaks after 35min of 0.1sccm disilane injection for rocking scans near $(110)_s$ and $(300)_s$, respectively. (C) The twin peaks as seen by the 2D detector at position close to the Bragg reflection, after 35min*0.1sccm of disilane injection at 530°C.

For a highly concentrated system (*i.e.* the average spacing between the NWs $\bar{d}$ is of the same order of magnitude as the average diameter of the NWs $\bar{D}$), contribution from the interference function $|S_q|^2$ can be sometimes observed at low Δq values. This is illustrated in Figure 3-6 for sample #280612. The high NW density (short Au diffusion length) is the result of annealing (4ML, 50min at 530°C) gold catalysts under high pressure of inert gas (P_{Ar} ~10^{-4}mbar compared to base pressure P_b~10^{-10}mbar) after their deposition at room temperature. The same can be achieved by direct Au deposition and subsequent NW growth at relatively low temperatures (*e.g.* 460°C, sample #041112C).

The FWHM (0.01426±0.00010Å^{-1}) of the reference scan (red curve) before the gas injection corresponds to the size ($\bar{D}$=44±1nm) of the pit as Au etches its way into the Si surface upon melting. No significant change was observed after 5min of injection of low flux disilane (0.1 sccm). After 11min of injection (green curve), a pair of twin peaks appears in the vicinity of the $(110)_s$ Bragg peak. The position of the twin peaks (±0.0046Å^{-1}) is indicative of the mean distance $\bar{d}$ between the NWs (137nm), although the real distance might be slightly smaller as the peak centers may be shifted by the form factor. After 52min of injection (orange curve), the size modulation was once again observed. As demonstrated in previous discussions, we shall use the second minimum for more reliable NW size estimation, which reveals an average size of $\bar{D}$=39±4nm at this stage of growth. As the injection proceed further, the twin peaks grew closer together (orange curve) until they disappeared completely at the center of the Bragg reflection (blue curve). The final intensity profile is again dominated by the form factor, the FWHM of which (0.01003±0.00005Å^{-1}) is a slight exaggeration (63±1nm) of the real NW size as can be foreseen from our previous analysis. The disappearance of the twin peaks is the combined result of deteriorating NW quality due to prolonged gas exposure (some NWs ceased to grow as they ran out of catalyst) and multiple growth interruptions for the sake of more accurate scans (which is unique to this specific sample). The mean distance (~135nm) and average size (~40nm) is consistent with *ex situ* SEM observations. The pair of twin peaks was also observed in radial scans and in the vicinity of the $(300)_s$ peak. In the case of rocking scans, while the size modulation near the $(300)_s$ peak shows a slightly larger period than that observed near the $(110)_s$ peak, as is expected for NWs with a hexagonal cross section, the position of the twin peaks stays exactly the same (Figure 3-6B). This is also expected since the growth was seeded by a dewetted Au film, and should hence have no preferential orientation in the spatial distribution (same $\bar{d}$ in

every direction) of the NWs. (Figure 3-6C) Finally, with the 2D detectors it is possible to directly observe the twin peaks by measuring at off-Bragg positions.

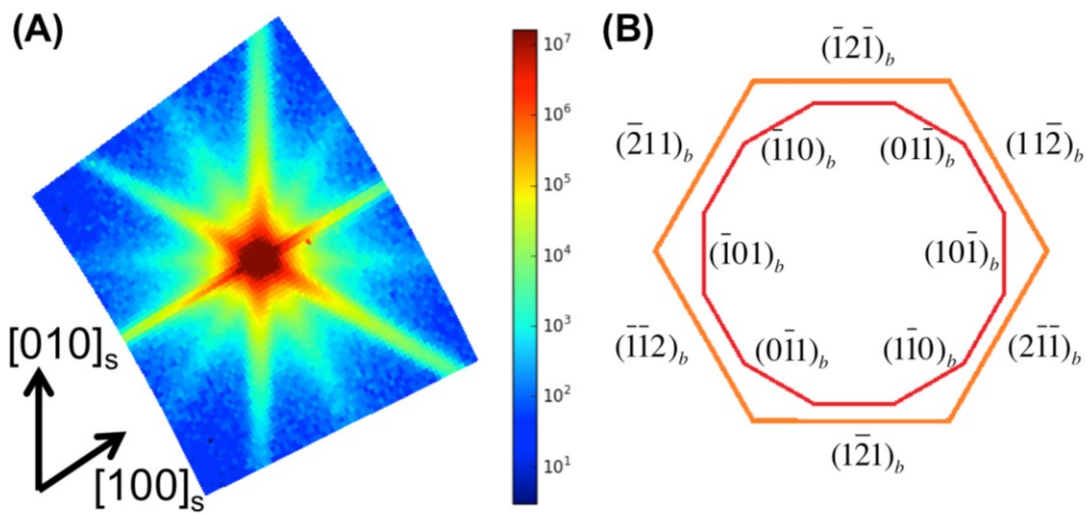

Figure 3-7 : (A) RSM around the Si $(101)_s$ peak for sample #051211. The RSM covers a 10° sector in the reciprocal space and a $q_{||}$ range of 1.75-2.02 $Å^{-1}$ (B) Schematics of the hexagonal and the dodecagonal cross-section of the Si NWs deduced from the RSM.

We have shown earlier in Chapter 2, with the help of *ex situ* SEM observations, that Si NWs with a hexagonal cross-section have three of their sidewalls decorated with sawtooth facets while the other three remain smooth and featureless. Occasionally a dodecagonal cross-section can be observed near the tip of the NWs, most likely due to limited disilane exposure after formation. The orientation of the hexagonal and the dodecagonal cross-section can be studied by performing a Reciprocal Space Mapping (RSM) around one of the Si Bragg peak. (Figure 3-7) The result reveals that NWs with a hexagonal cross-section have six sidewalls belonging to the $\{11\bar{2}\}$ family while NWs with a dodecagonal cross-section has six additional sidewalls from the $\{01\bar{1}\}$ family. The broader scattering streaks from the dodecagonal sidewalls compared to those from

the hexagonal ones are explained by their relative size in the real space. It is worth clarifying that the in plane mapping only picks up scattering streaks parallel to the sample surface, and thus does not distinguish between signals from the smooth sidewalls and those from the sawtooth faceted sidewalls.

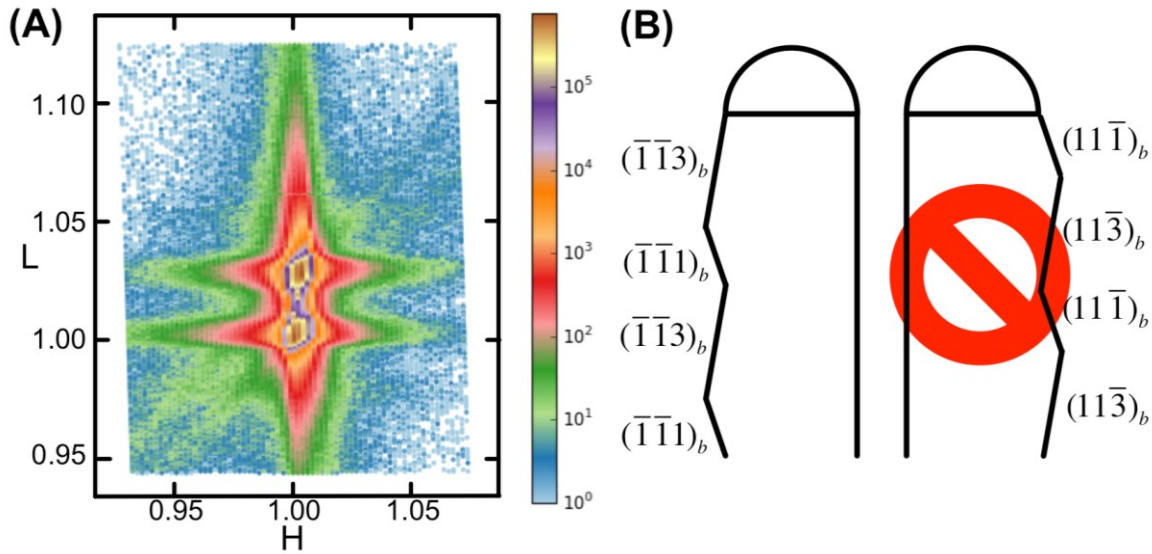

Figure 3-8 : (A) Intensity map in the HL plane around the $(101)_s$ peak. (B) Schematics of the two possible configurations of the sawtooth facets.

The understanding in the literature regarding the configuration of the sawtooth facets has been divergent. Some (Ross et al. 2005) reported seeing downward {111} facets and upward {113} facets while some (Vincent et al. 2011) argue that the formation of upward {111} facets are energetically more favorable. To resolve this, it is possible to reconstruct an out-of-plane intensity map using our previous data, thanks to the large out-of-plane acceptance of the 2D detector. Our findings (Figure 3-8A) seem to support the former theory as more intense scattering streaks from the {111} family were found pointing downwards. However, the above statement should be treated with skepticism and caution. The intensity contrast from X-ray scattering ultimately boils down to the

variation in electron density. A downward {111} facet should, in theory, produce two scattering streaks of equal intensity pointing in opposite directions. Absorption (by the NW body) alone cannot be responsible for the intensity contrast observed between the downward scattering streak and the upward one. As a matter of fact, the intensity attenuation by passing through one Si NW ($\bar{D} = 250nm$) is less than 1% (176.792µm, absorption depth at 11keV).

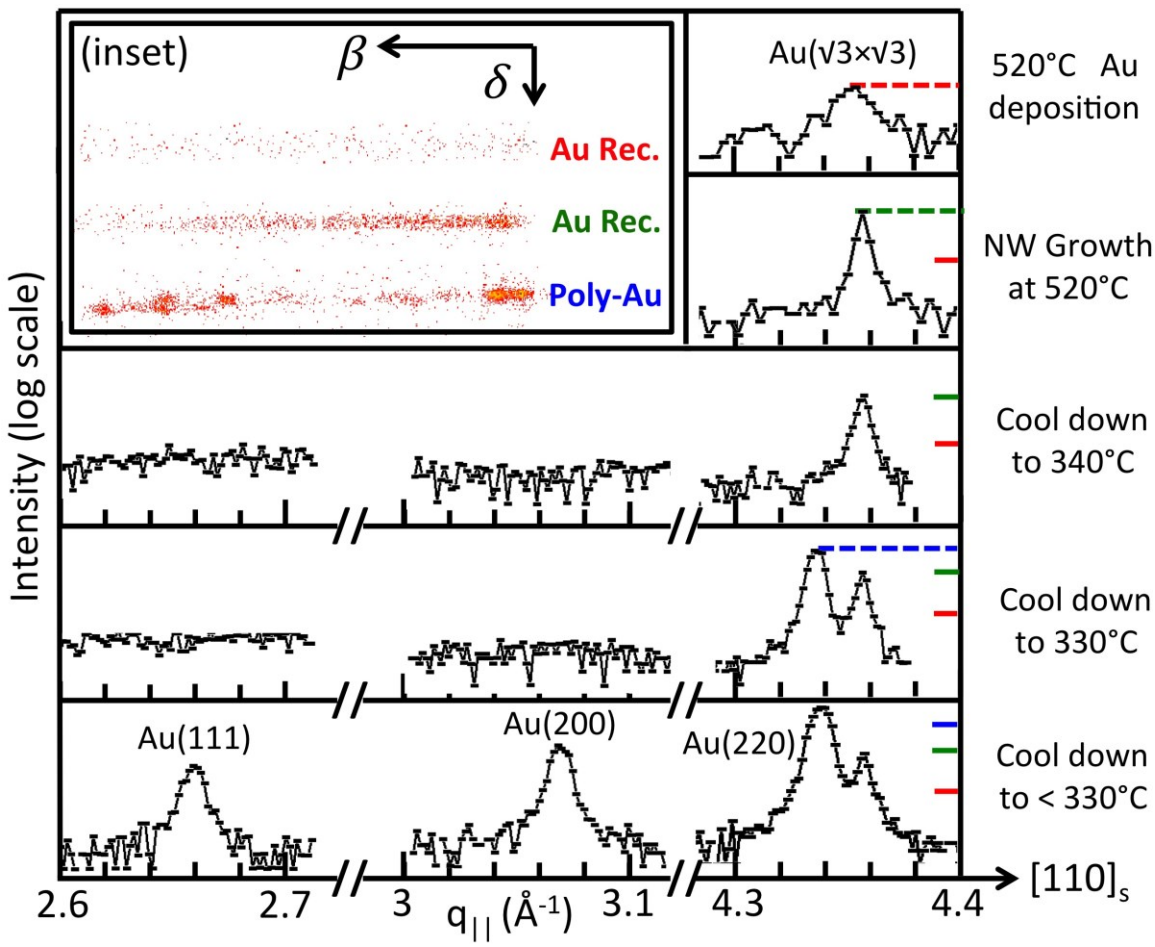

Figure 3-9: The state of Au before, during and after NW growth in the case of sample #021211 as revealed by radial scans along the $[110]_s$ direction. (inset) Raw images from the 2D detector on various Au signals. The peak at $q_{||}$ = 4.36Å^{-1} corresponds to the AuSi(√3×√3)R30° reconstruction signal while the peaks at $q_{||}$ = 2.66, 3.07, 4.34Å^{-1} are the solid Au peaks for the $(111)_b$, $(200)_b$ and $(220)_b$ reflections, respectively.

Before moving on to the GISAXS observations, we shall take a final peek at the state of Au during the entire growth process. (Figure 3-9) When deposited directly on a "hot" substrate, the first ML of Au forms a wetting layer. The remaining Au dewet the surface as they form larger and larger liquid alloy droplet with Si from the substrate, which will then catalyze the NW growth. For a clean surface and at sufficiently high temperature, the Au in the wetting layer further rearrange themselves to lower the surface energy. The resulted $(\sqrt{3} \times \sqrt{3})\ R30°$ reconstruction can be characterized by a line scan along the $[110]_s$ direction. The initial quality of the reconstruction was rather poor as evidenced by the broad peak width and low intensity. The main reason behind this is the low temperature and the short interval (annealing time) between Au deposition and the NWs growth in order to avoid the formation of oversized catalysts due to Ostwald ripening. As soon as disilane was introduced into the growth chamber, the reconstruction peak quickly became narrower and more intense, much to our surprise. A possible explanation is that the surface was originally covered by Si (7×7) reconstruction which was only partially destroyed upon Au deposition. The decomposition of disilane further broke the underlying Si reconstruction and left the surface with unreconstructed Si (1×1) atoms which in turn facilitated the transition to Au reconstruction. The enhanced reconstruction signal then stayed unchanged for the remainder of the growth process. The constant presence of the reconstruction peak during growth indicates that the Au wetting layer acts as a surfactant for the decomposition of disilane by always remaining on top of the newly grown 2D Si layer. Upon cooling down, Au does not solidify until below 330°C at which point the $Au(220)_b$ was the first to precipitate, followed by $Au(111)_b$ and $Au(200)_b$. The supercooling level found in this case (33°C) is lower than that found for a less disturbed system (Schülli et al. 2010), which is not unexpected. (Figure 3-9 inset) Last but not least, it is possible to distinguish the various Au peaks by looking at the 2D

images. The reconstruction signal is characterized by a straight scattering rod with close-to-homogeneous intensity. The solid Au signal, on the other hand, is composed of a series of dots lying on a curved trajectory which outlines the Bragg conditions on the Ewald's sphere for polycrystalline Au of different orientations.

3.2.2. Si NWs as seen by GISAXS

For the *in situ* study of Si NW growth with GISAXS, let us begin with the intensity evolution in the early stage of growth recorded with sample #280912B. Unless otherwise specified, the GISAXS images to be presented were taken at an incident angle of $\alpha_i = 0.10°$ (below the critical angle $\alpha_c = 0.16°$) and cover a q range of approximately -2.3Å^{-1}< q_y < 2.3Å^{-1}, 0Å^{-1} < q_z< 4.6Å^{-1}.

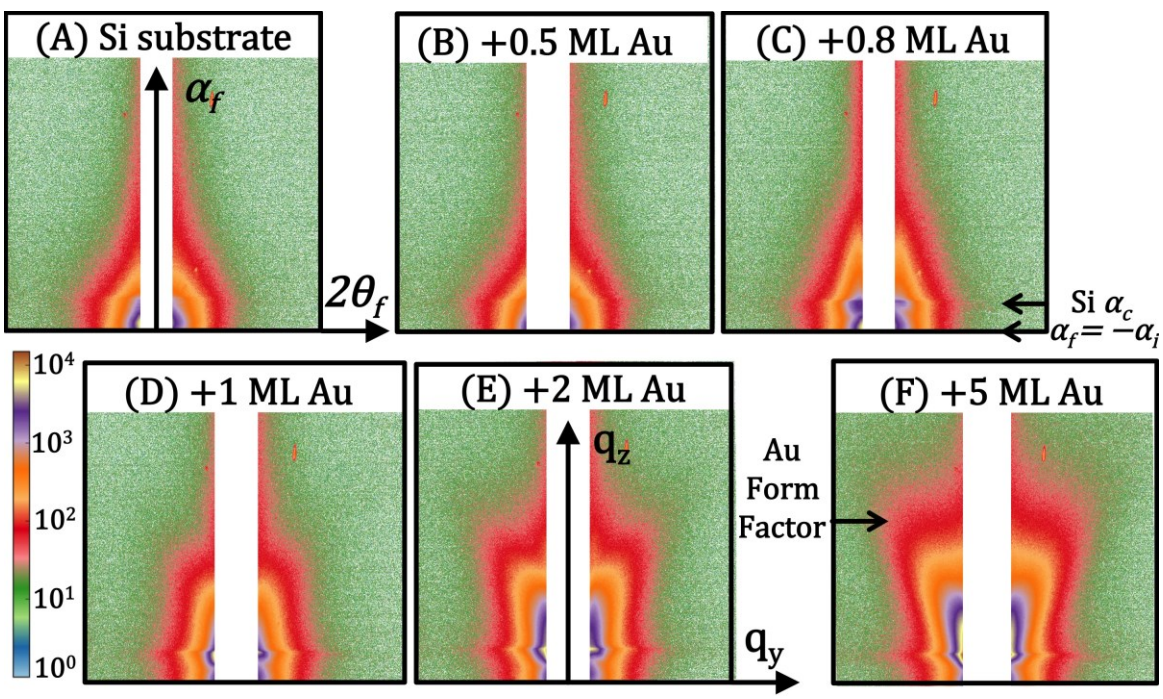

Figure 3-10: GISAXS images during 5ML of gold deposition (sample #280912B). The direct and reflected beams were blocked by a beamstop during the experiment. The choice of $\mathbf{q_y}$ was arbitrary and was not aligned with any specific crystallographic direction. α_f and θ_f are the scattering angles described in Figure 1-9.

(Figure 3-10) The first ~0.8ML (0.19nm) of Au forms a wetting layer on the clean Si(111) surface. No visible change was observed on the GISAXS image except for a hint of a slight increase in intensity at $\alpha_f = 0.16°$. This corresponds to the critical angle of Si at 11keV and is related to the reflectance of the Si substrate. Starting at 0.8ML of deposition, we started to observe intensities scattered by the AuSi alloy catalyst, the shape of which is mainly dominated by the form factor of the liquid droplet. In our case, the interference function ($\bar{d} > 1\mu$m, disordered system) has its first maximum located extremely close to the origin of the reciprocal space ($2\theta_f = 0$) and quickly tends to one for larger $2\theta_f$ values. With further Au deposition, the signal simply got stronger and stronger as more matter was contributing to the scattering.

In order to limit Ostwald Ripening between the liquid droplets and to maintain a narrow size distribution, NW growth was initiated immediately after the deposition of 5ML Au (1.18nm). (Figure 3-11) As soon as the disilane gas was introduced into the chamber, the Au signal retracted (along the $\mathbf{q_z}$ direction), indicating a sudden increase in the average height of the liquid droplets. Moreover, a streak emerged from the initial signal, the average direction of which (indicated by the black arrow) then decreased gradually until after 8min of injection where it became steady for a brief period of time. This observed evolution is reflective of the change in the shape of the liquid alloy under the presence of disilane. Indeed, *ex situ* SEM studies (Schmid et al. 2008) have revealed different contact angles for the AuSi catalyst at different stages of growth, which is explained by changes in surface tension (Schmidt et al. 2009) or by Si supersaturation. The gradual increase in the contact angle inevitably causes a reduction in the diameter of the droplet, which is in turn responsible for the formation of the larger base of the NWs.

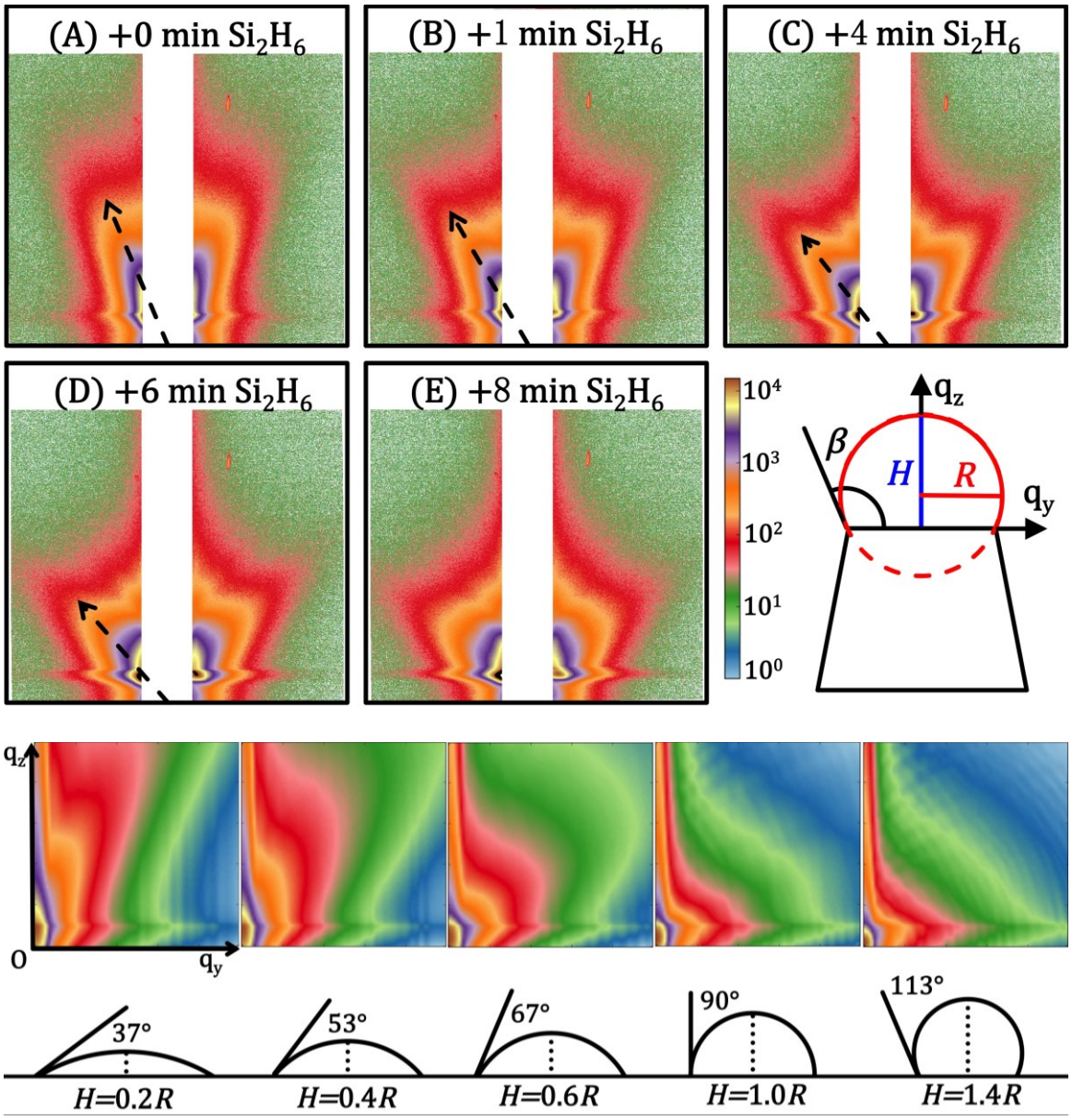

Figure 3-11: GISAXS images during the first 8min of 0.1sccm disilane injection (sample #280912B) compared to the form factor calculated for various cases of truncated sphere. The choice of $\mathbf{q_y}$ was arbitrary and was not aligned with any specific crystallographic direction. The first image (A) is the same as the last image (F) in Figure 3-10.

To qualitatively investigate the evolution of the liquid droplet in the early stage of growth, we shall employ a simple model using truncated spheres. Depending on the different *H/R* ratio (*i.e.*, the level of submergence of the sphere into the supporting

material, being it the Si substrate or part of the Si NW), which is limited to 0-2, the entire range of contact angle (0-180°) can be achieved. A first Gaussian distribution was applied on both *H* and *R* to take into account the size variation while a second one with a smaller standard deviation was used uniquely on *H* to take into account the contact angle spread (supersaturation ratio) expected for liquid droplets of different size. The DWBA form factor of a selected group of cases is shown in Figure 3-11. The first image (Figure 3-11A) right before the injection has most of its intensities contracted near the center of signal, and resembles very much the 1st case with H/R = 0.2 and a contact angle of 37°. This is confirmed by early SEM studies (Ressel et al. 2003) which reported a similar angle (43°) for dewetted AuSi alloy droplets. Immediately after disilane exposure, a streak was seen separated from the center with an average angle of close to 60° (Figure 3-11B). This matches the 2nd case with a contact angle of 53°. Note that the retracted front (along the $\mathbf{q_z}$ direction) of the scattered intensity was also reproduced by the simulation. With further injection, the average angle of the streak slowly moved to 45° where it became steady for a brief period of time. The contact angle at this stage of growth is likely to be around 67° due to the similarities between the experimental data (Figure 3-11D) and the simulation result of the 3rd case (H/R = 0.6). The observed time frame (~8min) was not to be confused with the so-called incubation time. The latter is the time needed for the droplet to reach supersaturation and is measured as the characteristic delay prior to which no growth occurs. It is true that changes in the contact angle should be expected during the incubation time as it involves an increase in the Si content in the alloy droplet, but the duration should be much shorter, typically less than 200 seconds.

(Figure 3-12) With even longer injection, we started to observe a modulation in the intensity along the $\mathbf{q_z}$ direction, the period of which is indicative of the length of the NWs. Notice that the modulations were only visible because they were enhanced by the

Yoneda wing spread between the critical angle of Si (0.16°) and the sample horizon (0°). The NWs length (Figure 3-12E) calculated from the data shows a clear linear dependence on the injection time, although for longer NWs length the estimation may become less reliable (larger error bar) due to the extremely short period of modulation (~20 pixels).

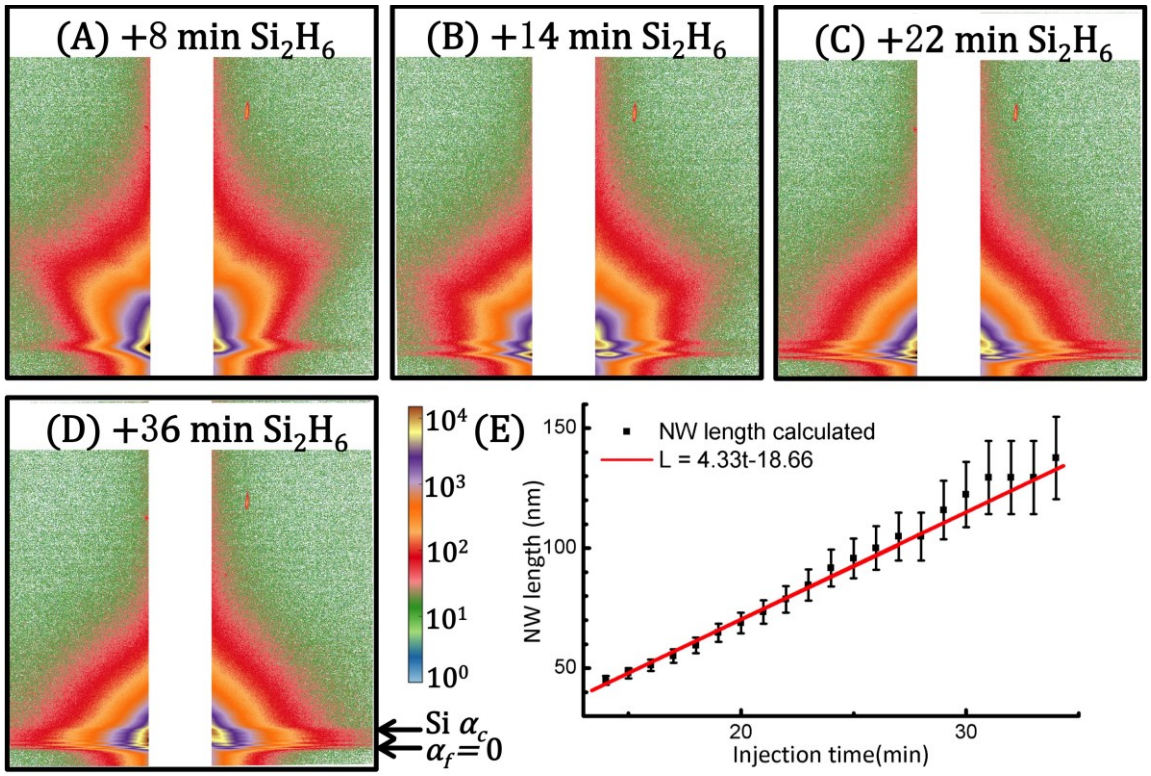

Figure 3-12: GISAXS images from 8 to 36min of 0.1sccm disilane injection (sample #280912B). The first image (A) is the same as the last image (E) in Figure 3-11. Also shown is the calculated NW length from the modulation period versus the injection time.

Two conclusions can be drawn by the LSQ fitting of the data. First, the slope indicates that the growth rate for 0.1sccm disilane at 530°C is about 4.33nm/min. Second, the non-zero intercept on the abscissa confirms the existence of the incubation time, though its value (4.30min) might not be as accurate as those measured by more direct methods. Finally, we would like to point out that the scattered intensity eventually evolved into the bell-like shape as shown after 22min of injection (Figure 3-12C), at

which point it stayed unchanged for the remainder of the experiment. We believe that the conclusion of the shape evolution marks the end of the growth of the NW base and the beginning of the steady growth regime for the NW body. The final shape of the intensity resembles that of the 4th or 5th case calculated previously for truncated spheres with a contact angle equals to 90 and 113° respectively. These values (between 90-120°) are consistent with results from *in situ* TEM measurements (Kodambaka et al. 2006).

So far, we have only considered the scattered intensity from the catalyst alloy, with the sample aligned along an arbitrary direction. The same evolution however can be observed for all azimuth angles due to the circular symmetry of the liquid droplet. It is now time to skip to the end of the NWs growth and have a look at what was happening elsewhere in the reciprocal space. For pure demonstration purpose, we shall pick a sample with a considerate amount of kinking to illustrate the different kinds of signals that should be expected from these experiments. The kinking in this case (sample #290912B) was induced by depositing a few layers of MBE Ge in the middle of an ongoing growth process. Almost all Si NWs were kinked and only kinked at the position where the Ge was inserted.

There are in total five different groups of scattering streaks that might appear on the GISAXS images of Si NWs. The first one is the famous sawtooth faceting signals which can only be observed when the detector plane is perpendicular to one of the six hexagonal facets (Figure 3-13A). The included angle of φ_A = 19.5° and 170° matches the scattering from the $(11\bar{1})_b$ and $(\bar{1}\bar{1}3)_b$ plane, respectively. The apparent intensity contrast between the two streaks is explained by the presence of Au on the $(11\bar{1})_b$ facets. The second group consists of some more intense streaks found at $\varphi_A = \varphi_B$ = 0°/180° as they were enhanced by the Yoneda wing. The pair of streaks in the first image comes from the scattering by the $(11\bar{2})_b$ and $(\bar{1}\bar{1}2)_b$ sidewalls of NW segments with a

hexagonal cross-section, while that in the second image comes from the scattering by the $(01\bar{1})_b$ and $(0\bar{1}1)_b$ sidewalls of NW segments with a dodecagonal cross-section. The third group is composed of uniquely the sharp streak at φ_A = 119.5°, the narrow FWHM of which indicates that it must come from something extremely large in the real space. Indeed, the direction of the streak corresponds to the scattering by the $(112)_b$ sidewall, which is the equivalent of the $(\bar{1}\bar{1}2)_b$ sidewall for NWs kinked to the $[11\bar{1}]_b$ direction. Signals originally found in other azimuths may also be captured if they are simply broad enough. This constitutes the fourth group of signal which includes the sharp streak labeled $(\bar{1}\bar{1}0)_b$ (φ_A = 54.7°) found in the first image and those labeled $(231)_b$, $(213)_b$ (φ_B = 67.8° and 112.2°, respectively) found in the second image. The original included angle φ and observed included angle φ' are related by the following formula

$$\tan\varphi\cos\theta = \tan\varphi' \qquad (3\text{-}5)$$

θ being the angle between the original azimuth and the observer azimuth. With the help of Equation (3-5), it becomes evident that all of the three streaks were originated from the $(112)_b$ streak of kinked NWs (group III), with θ equals to 60, 30 and 150°, respectively. This is further confirmed by their characteristic narrow FWHM just like the original one. The above analysis leaves us with only three more streaks to identify, namely the one labeled $(113)_b$ (φ_A = 119.5°) in the first image and the pair labeled $(1\bar{1}3)_b$ and $(13\bar{1})_b$ (φ_B = 31.5° and 148.5°, respectively) in the second image. We believe that all three were part of the {113} facets involved in the formation of the dodecagonal cross-section (group V). To our knowledge, not much effort was made on the identifications of these facets, primarily due to their complex composition, small physical size and rare occurrences. X-ray offers a fast and straightforward way for resolving the complete structure of the dodecagonal cross-section, although better

statistics may be required by either increasing the NW density or by measuring on an undulator beamline. Additionally, there is a hint of a signal assigned to the scattering by the $(001)_b$ plane (φ_A = 144.7°), whether it is an artifact or a real faceting streak remains unclear due to its weak scattered intensity. $\{001\}_b$ facets have previously been observed by TEM measurements on the dodecagonal part of the NWs (Boukhicha et al. 2011). First principle studies (Lu et al. 2005) have also reported high stability of the these facets at high temperatures once reconstructed.

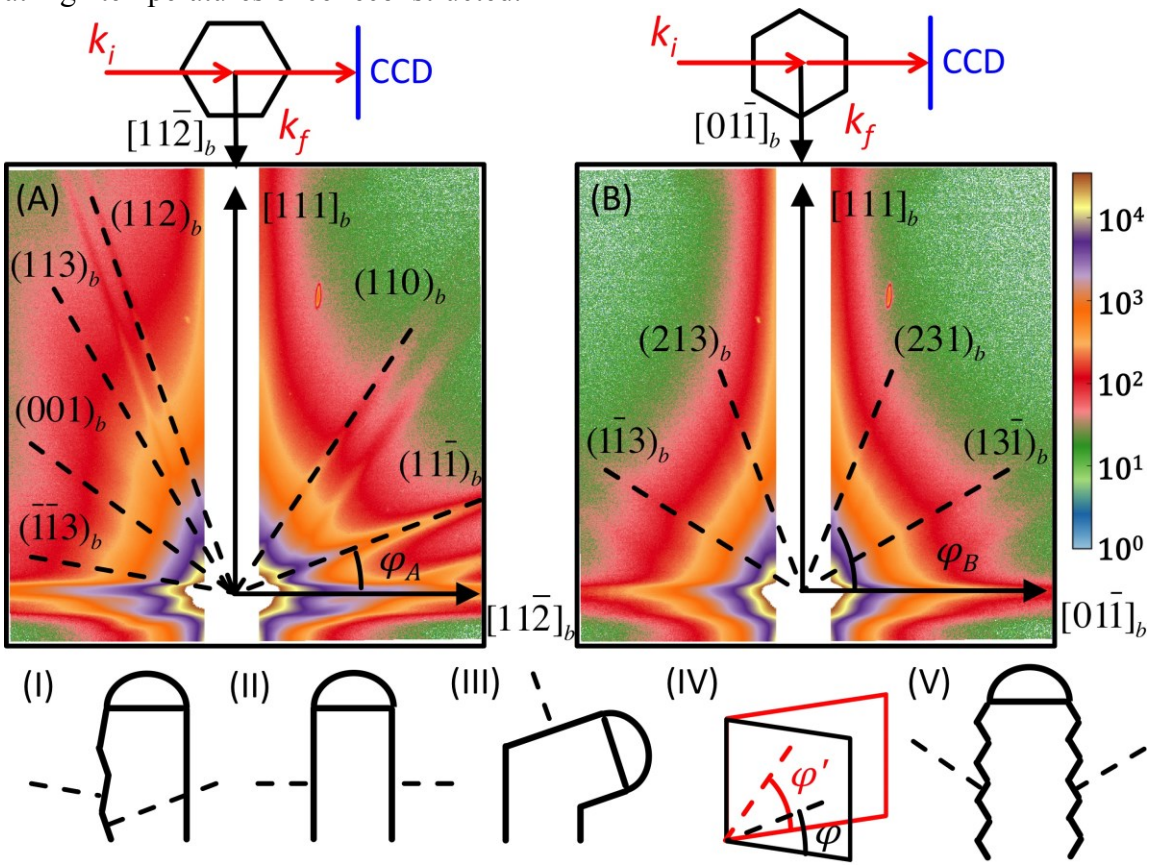

Figure 3-13: GISAXS images taken with $\mathbf{q_y}$ aligned along the (A) $[11\bar{2}]_b$ and the (B) $[01\bar{1}]_b$ direction after 1h of 0.9sccm disilane injection at 540°C (sample #290912B). Also shown is the top view of the scattering geometry for both images and schematics of the five groups of facets that contribute to the scattering. Note that the streaks identified in (A) and (B) were results of multiple scattering events at grazing incidence as predicted by the second term of the DWBA. There is a duplicate of every streak located slightly below the identified ones which traces back to the real origin of the reciprocal space.

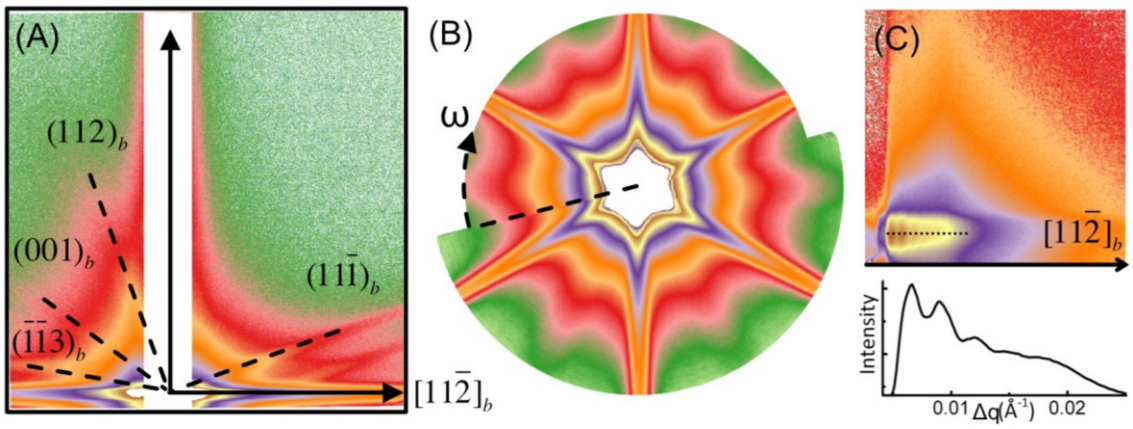

Figure 3-14: (A) GISAXS image taken with $\mathbf{q_y}$ aligned along the $[11\bar{2}]_b$ for a more ordinary sample (#051211). The q range covered in this case is -1.0Å^{-1} < q_y < 1.5Å^{-1} and 0Å^{-1} < q_z < 2.5Å^{-1} (B) Result of GISAXS mapping on a different sample (#241112). (C) The modulation period along the $\mathbf{q_y}$ direction observed on sample #011211. The dotted line indicates the direction of the line cut.

(Figure 3-14A) For a more ordinary sample (#051211), we can barely observe the $(112)_b$ streak from the kinked NWs besides the usual signals from the sawtooth facets. The $(001)_b$ streak was still present, and was yet too weak to be property identified. Most of the time during growth, the dodecagonal facets $(1\bar{1}3)_b$ and $(13\bar{1})_b$ showed up prior to the appearance of the sawtooth facets $(11\bar{1})_b$ and $(\bar{1}\bar{1}3)_b$. This seems to support the common belief that the hexagonal cross-section was the result of Si overgrowth on the preformed dodecagonal cross-section. We can also perform a GISAXS mapping by measuring while continuously rotating the sample. The result (Figure 3-14B) is similar to GIXD RSM (Figure 3-7A), which revealed a 6-fold symmetry formed by intense and narrow streaks overlaid on a 12-fold symmetry composed of weaker and broader signals. Last but not least, it is also possible to calculate the lateral size of the NWs on GISAXS images, although this would require us to measure the modulation period observed along the $\mathbf{q_y}$ direction close to the incident beam which was previously blocked (saturated) in the other images. For instance (Figure 3-14C), the period

(0.0030±0.0002Å) measured on sample #011211 indicates an average size of 209±13 nm. The result agrees well with those calculated from GIXD line scans and by *ex situ* SEM measurements.

3.2.3. DISCUSSION

The objective of the previous sections is three-fold. First, we would like to establish *in situ* X-ray scattering (GIXD and GISAXS) as a viable tool for acquiring statistically averaged information on the morphology (size, spacing, length, growth rate, orientation) of the NWs during growth on a large area of the sample surface. This could become potentially interesting when it is the overall property of the sample that needs to be assessed and not just that of one or two single NWs. Secondly, we would like to address the possibilities of using X-ray scattering to provide not just structural analysis (*e.g.* internal strain) but also insights on the morphological information of the NWs. This is perhaps better illustrated by our attempt to solve the ongoing debate regarding the configuration of the sawtooth facets. Our data seems to support the formation of downward $\{111\}_b$ facets rather than the upward ones, although a more plausible explanation might be required to account for the observed intensity contrast. Meanwhile with GISAXS measurements we managed to determine some of the facets constituting the dodecagonal cross-section of the NWs, the identification of these facets was proven difficult for Electron Microscopy studies due to their small physical size. Finally, we would like to demonstrate the capability of *in situ* X-ray scattering to follow closely the evolutions happening in the frame of a few seconds. A good example is the study of the changes in the shape of the liquid droplet under the presence of disilane. Although the result remains purely qualitative, it does shed light on the possible contact angles during each stage of growth and paves way for follow-up thermodynamic studies on the relation between surface tension and droplet supersaturation in nanoscale systems.

3.3.Ge NWs

3.3.1. GE NWS AS SEEN BY GIXD

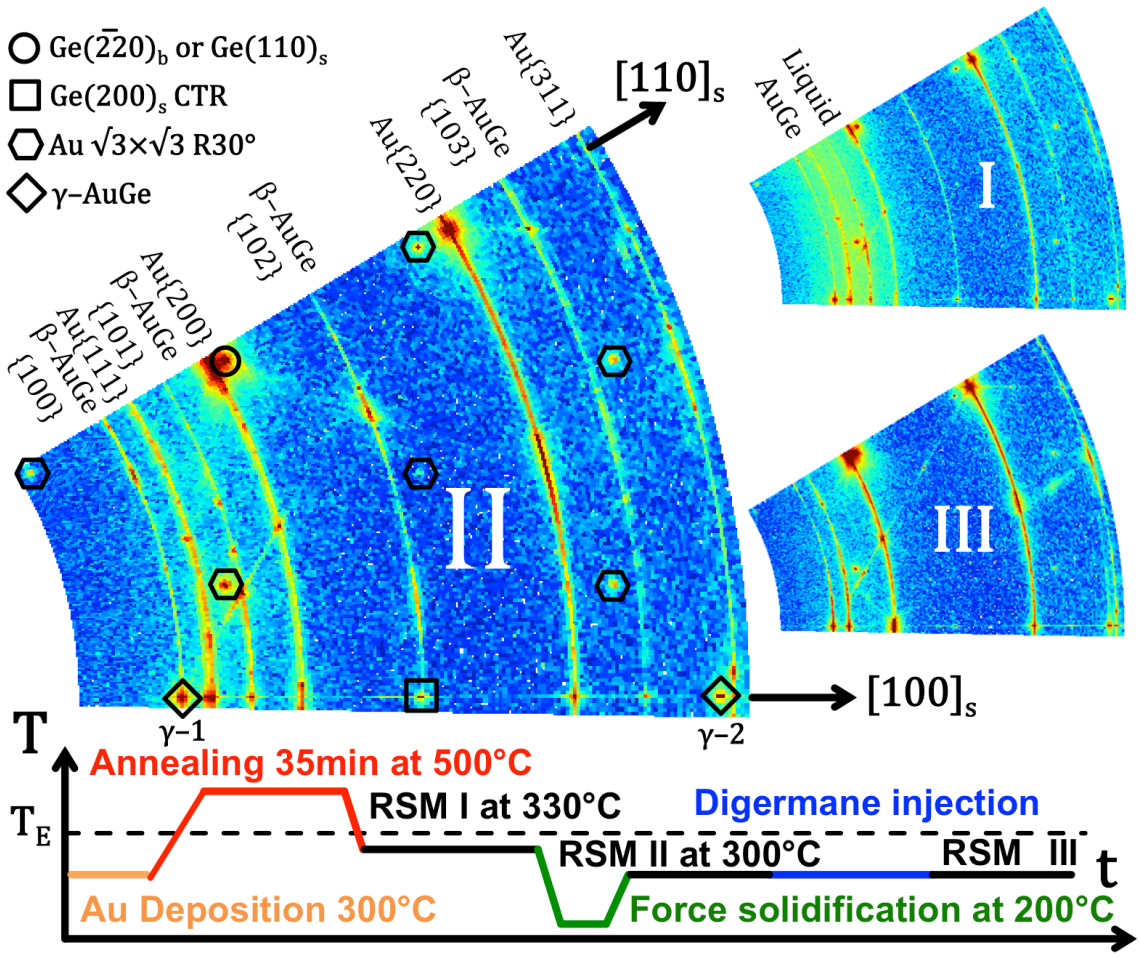

Figure 3-15 : (upper part) Results of RSM following the experimental procedures (lower part) described for sample #040313. The mappings cover a 30° sector in the reciprocal space between the $[100]_s$ and the $[110]_s$ direction, and a q range of 2.05-5.16 $Å^{-1}$.

One big mystery that has stumped researchers for years is the true nature of the sub-eutectic Ge NW growth, whether it follows a VLS or a VSS type of process. It would seem that the possible growth mode depends largely on the environmental parameters as the conditions for growing straight Ge NWs vary significantly in the literature (*c.f.* Chapter 2). Multiple attempts have been carried out in the scope of this work with the aim of complementing the existing findings with X-ray scattering techniques. One

example is sample #030413 where we sabotaged the growth of nice straight Ge NWs by deliberately solidifying the Au catalysts. (Figure 3-15) The sample, with 5ML of Au deposited at 300°C, was annealed at 500°C for 35min before being brought down to 330°C (30°C below T_E). A first RSM (I) was performed at this stage which reveals the state of Au that can catalyze the growth of high quality Ge NWs should we choose to proceed immediately with digermane injection. We then intentionally solidified the supercooled Au catalysts by bringing the sample further down to 200°C. The sample was subsequently reheated to 300°C where a second RSM (II) was performed. This RSM corresponds to the state of Au that only enables the growth of crawling Ge NWs, as confirmed later by *ex situ* SEM observations. It can be concluded that despite some slight adjustment in the intensity level, all the solid Au signals that appeared in the first map were present on the second one, with the only exception of the liquid AuGe peak. This strongly suggests that supercooled Au plays a vital role in the growth of straight Ge NWs under our growth condition, and that the growth process is mostly probably VLS. We now take a closer look at the Au signals, which were primarily presented in the form of Debye-Scherrer rings. The most intense peaks are from fcc Au. The preferential orientation of the Au {200} and {220} peak along the Ge$[110]_s$ direction indicates that they were more likely to be found at the catalyst-substrate interface. Several metastable phases (Anantharaman et al. 1966) have also been identified. The rings at q equals to 2.517, 2.838, 3.643 and 4.677Å^{-1} belong to β-AuGe (hexagonal close-packed, a=2.89, c=4.75) which has their theoretical positions at 2.512, 2.838, 3.647 and 4.695Å^{-1}, respectively. This is the Ge depleted metastable phase which contains only 10-30 at.% of Ge. For the reference, the Ge composition in the eutectic alloy is 28 at.%. Hcp AuGe has previously been reported by (Marshall et al. 2010). The author suggested that the formation of hcp AuGe is likely to be associated with Ge supersaturation since they have

only been observed during the cool-down procedure after NWs growth and not during subsequent re-melting and re-solidification. Our results contradict theirs in that our hcp AuGe was formed by simple annealing. The discrepancy might be due to oxidation and contamination of the alloy catalysts during *ex situ* experiments. The intense peak (diamond symbol) at q = 2.522Å^{-1} along the $[100]_s$ axis belongs to γ-AuGe (tetragonal, a=11.63, c=22.49) with a rich(er) Ge concentration of 25-65 at.%. The same signal was observed by (Sutter & Sutter 2011) in their *in situ* heating experiment of as-grown NWs. They attributed the peak to the (044) lattice planes (q = 2.433Å^{-1}) while in our case the interplanar distance is found to be slightly smaller, closer to the value for the (144), (208) or (242) reflections. There is yet another signal from γ-AuGe positioned at twice the momentum transfer of the first peak (q = 5.036Å^{-1}). The presence of an individual peak (rather than a ring) indicates that the γ phase alloy is single crystal, and is in direct epitaxial contact with the Ge substrate. We attribute the formation of both metastable alloys to the stabilization of off-equilibrium Ge content by slow (near equilibrium) cooling down from high temperature and by nanoscale size effects. Such formation would otherwise require more extreme methods such as quenching (Scott 1975) to achieve under normal circumstances. Finally, the $\sqrt{3} \times \sqrt{3}\, R30°$ reconstruction can be observed on both maps which is unsurprising under our experimental procedures.

To complete the study, a third RSM (III) was performed after 40min of 0.8sccm digermane injection at 300°C. While the injection only resulted in the growth of crawling NWs, as can be anticipated by our previous test experiments, the data is almost identical to what we have obtained for straight Ge NWs growth (*e.g.* sample #010413, not shown here). The close resemblance of Au state between both cases is not unexpected, as it is believed that (Schwarz & Tersoff 2011) the formation of crawling NWs is simply a case went awry in the beginning of an ordinary growth process. The final state of Au after

growth is characterized by the disappearance of all signals associated with β-AuGe. There are two possible explanations as to why only the γ phase metastable alloy survived the digermane injection. First of all, being it VLS or VSS, straight NWs or crawling ones, the need for precipitation would naturally favor the Ge rich(er) phase which in this case is the γ phase. Secondly, the observed preferential orientation along the $[100]_s$ direction indicates that the γ-AuGe alloy might be further stabilized by the epitaxial bonding with substrate Ge.

	γ-1	fcc{111}	β{101}	fcc{200}	β{102}	fcc{220}	β{103}	γ-2	fcc{311}
q	2.522	2.667	2.838	3.080	3.643	4.356	4.677	5.036	5.108
-I	↑↑	↑	↑	↑	↑	↑↑↑	↑	↑	↑
I-II	↑	↑	→	↑	↑	↑	→	↑	↑
II-III	↓	↑	↓↓↓	↑↑	↓↓↓	↑	↓↓	↓	↑↑

Table 3-4 : Indicators of the changes in integrated intensities between RSMs based on rocking scans covering 30° of the reciprocal space. The arrows signify the relative changes with regard to their previous intensity level. ↑↑ indicates a larger increase than ↑ while → indicates no visible changes. Note that the measurement on the γ-1 peak at $q = 2.522 Å^{-1}$ also includes the intensity from the β{100} peaks.

In Table 3-4 is listed the changes in the level of integrated peak intensities between consecutive RSMs for the Au signals concerned in this study, calculated from large rocking scans that cover 1/12 of the reciprocal space. It should be noted that the information provided in the table could only be regarded as a qualitative indicator of the relative changes in peak intensities. The real integrated intensity is considerably underestimated due to the small in-plane (~$0.0045 Å^{-1}$ compared to the peak FWHM which is often more than twice as large) and out-of-plane (unable to measure peaks with large q_z values) detector acceptance. Nevertheless, the data shows a clear preference for the crystallization of γ-AuGe than of β-AuGe during both cool-down procedures (I and II). Moreover, it would seem that part of the γ phase alloy also vanished under the presence of digermane (III). The decrease in the integrated intensity of γ-AuGe peak is

better understood by looking at the raw detector images. (Figure 3-16) While both the fcc-Au and the β-AuGe exhibit typical polycrystalline signatures on the 2D detector before (I) and after (II) the solidification at 200°C, the situation involving the γ-AuGe peak appeared to be much more complex. The first part of the signal follows a curved trajectory like others, consisting of Bragg diffractions from small crystals of random orientations. This is in fact the collective scattered intensity from the β-AuGe-{100} peaks which is indistinguishable at $\beta = 0$ on the stationary image from the γ-AuGe peak. The second part is a straight scattering rod which can only come from structures with a flat surface. Taking further into account the observed preferential orientation, we can speculate that the γ-AuGe nanostructures were single crystal, and formed a sharp interface with the substrate Ge. We can also estimate the thickness of these nanostructures by measuring the out-of-plane FWHM of the straight scattering rod, from which we obtained a vertical size comparable to the lateral size (74.0±1.6nm) that we calculated with the in plane FWHM. This indicates that instead of having a thin layer of epitaxial γ-AuGe at their interface, some of the catalytic nanoparticles are composed of an entire block of single crystal γ-AuGe. The curved rod of both the β{100} and the β{101} reflections vanished after the digermane injection (III), leaving behind only signals from the epitaxial γ-AuGe. The discovery of epitaxial single crystal γ-AuGe at the catalyst-substrate joint, should it be confirmed, is of great significance to the understanding of the VSS growth of Ge NWs. Hypothetically, it is possible that it is only through those Ge-rich crystals that the newly arrived atoms are able to reach and precipitate at the interface. On the other hand, it is equally probable that the removal of these crystals is the key to avoid growing crawling NWs as they prefer precipitation of Ge in the lateral direction. To prove either of the above assumptions would require more profound theoretical consideration and is beyond the scope of this work.

(Figure 3-17) To summarize, our study seems to indicate the presence of nanoparticles composed entirely of single crystal epitaxial γ-AuGe alongside those containing polycrystal fcc-Au and/or polycrystal β-AuGe, after the annealing at 500°C. The polycrystal β -AuGe was then transformed into fcc-Au upon digermane injection.

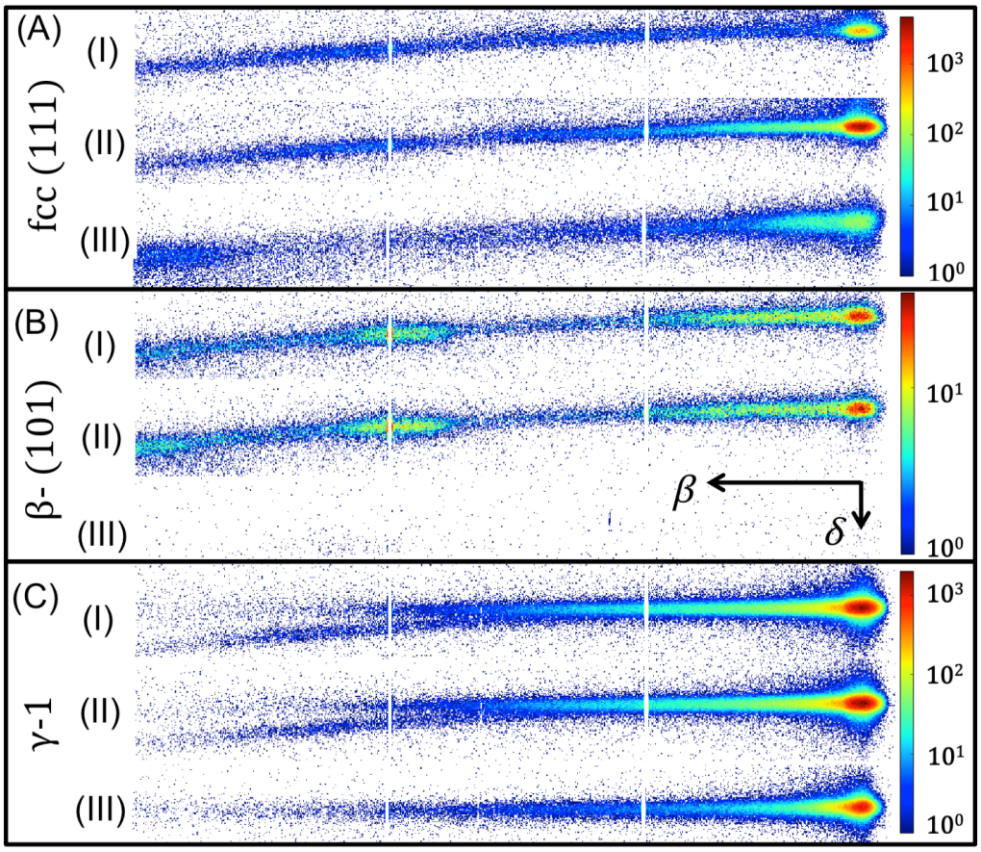

Figure 3-16 : Raw 2D images of the (A) fcc (111) peak, (B) the β-(101) peak and (C) the γ-1 peak on the Ge $[100]_s$ axis during RSM I, II, and III respectively.

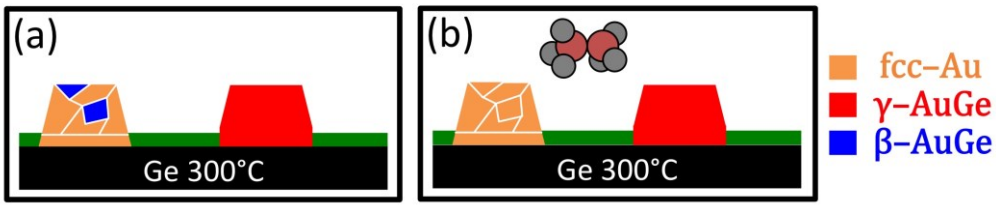

Figure 3-17 : Schematic representation of the solid AuGe catalyst alloys before (a) and after (b) digermane injection.

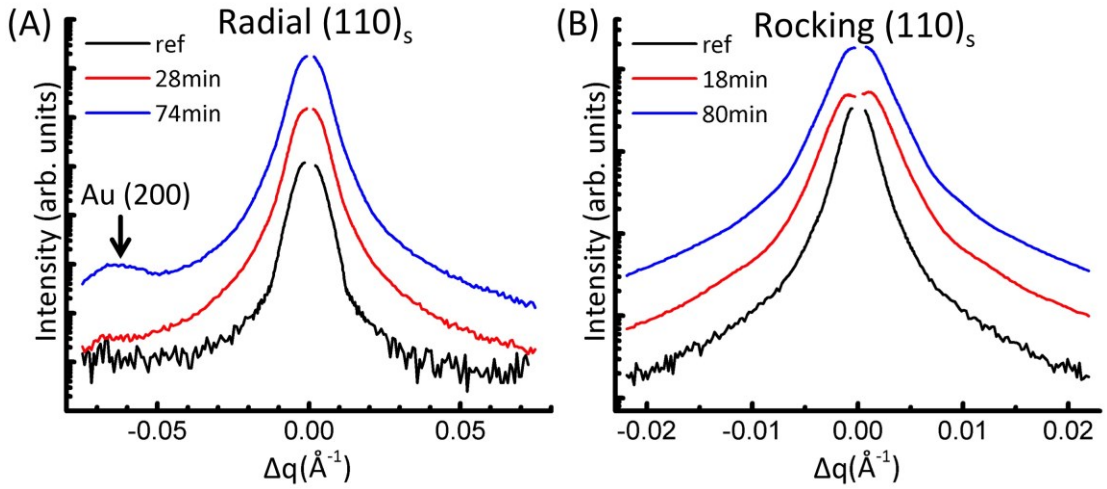

Figure 3-18: Sample #251112. Results from (A) radial and (B) rocking scans around the $Ge(110)_s$ peak during 6×10^{-3} mbar of Ge_2H_6 injection at 330°C. The vertical scale was readjusted to aid the eye.

The line scan analysis on Ge NWs is similar to what was previously shown for Si NWs, as shall be demonstrated with sample #251112. The NWs, grown after 2h of 6×10^{-3} mbar digermane injection at 330°C, are featured with a hexagonal cross-section and a diminishing diameter along the axial direction. Both the tapering and the hexagonal facets are known to be the result of Ge overgrowth on preformed segments of the NWs. At lower growth temperature (*e.g.* 280°C) the overgrowth is significantly suppressed, leaving the NWs with a circular cross-section and uniform diameter. (Figure 3-18B) The twin peaks from the interference function was briefly observed (red curve) with the rocking scans, indicating a good spatial correlation between the NWs. No size modulation was observed, which is expected considering that the NWs were tapered. The diameter was thus estimated using the FWHM of the final peak (blue curve). The average spacing ($\bar{d} = 546 \pm 29$nm) and size ($\bar{d} = 140 \pm 1$nm) calculated from these data are in good agreement with *ex situ* SEM measurements. (Figure 3-18A) Along the radial direction, the peak FWHM was again broadened by the resolution function. To the left of

the Ge Bragg peak we found a weak signal belonging to the (200) reflection of fcc Au. The intensity of the Au peak then gradually increased throughout the whole injection.

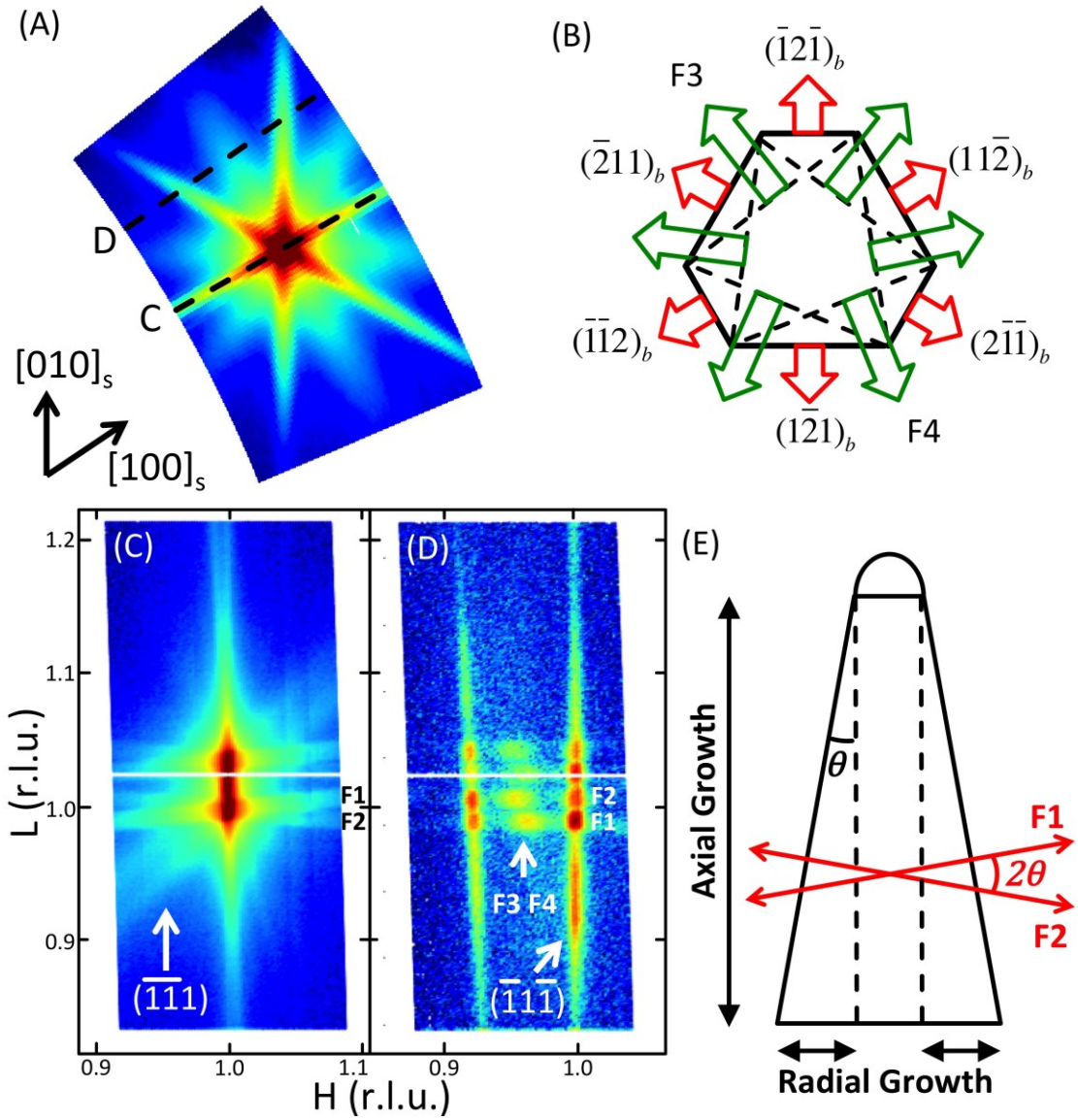

Figure 3-19 : (A) Result of the in plane RSM around the Ge(101)$_s$ peak. The mapping covers a 16° sector in the reciprocal space and a $q_{||}$ range of 1.66-1.97 Å^{-1} (B) Schematics of the hexagonal cross-section of the Ge NWs. (C) and (D) Out-of-plane intensity map reconstructed from the RSM data. (E) Schematics of the tapered Ge NWs.

The RSM result of the same sample (#251112) is perhaps more intriguing, but also more confusing in the meantime. (Figure 3-19A) The in plane mapping around the

$(101)_s$ Ge peak revealed an astonishing twelve-fold symmetry, in addition to the six-fold one expected for NWs with a hexagonal cross-section. We believe that the six weaker streaks (hereinafter referred to as W-streaks) are simply artifacts arising from the scattering by the average of two adjacent sidewalls (Figure 3-19B). To confirm this, we again resort to out-of-plane intensity maps with reconstructed images, the in plane component of which is given by the dashed lines. (Figure 3-19C) Like in the case of Si NWs, the only facet that can produce a signal strong enough to be resolved by GIXD is the downward $\{\bar{1}\bar{1}1\}$. Apart from that, one can also make out two scattering streaks (denoted F1, F2) almost parallel to the surface. Those streaks (hereinafter referred to as S-streaks) are in fact surface rods of the six tapered sidewalls (Figure 3-19E). We can measure the angular difference between the S-streaks, from which the tapering angle (±2.20±0.12°) can be deduced. The tapering angle can then be used to calculate the ratio between the catalyzed axial growth and the uncatalyzed radial (over)growth. The result (26.08±1.44) is consistent with the value deduced previously with *ex situ* SEM observations (26.6±0.6). Finally, we shall take a look at the out-of-plane intensity map (Figure 3-19D) reconstructed slightly away from the Ge Bragg reflection. The observed peaks can be understood as the result of outward-pointing scattering streaks intersecting the canvas (detector). Two important observations can be made. First, the W-streak peaks (denoted F3 and F4) are positioned almost at the same L (q_z) value as the S-streak peaks (F1 and F2). This confirms that the W-streaks came indeed from the scattering by the tapered NWs and not by any other structures (crawling NWs, 2D Ge layer, etc.) found at the sample surface. Secondly, the two W-streak peaks were not centered at the same H value. This rules out the possibility of them being originated from actual crystallographic planes. In fact, the in plane angular difference between the two peaks is expected if one takes into account the trigonal hexagonal cross-section of the NWs. The observed angular

difference is actually the angle between two opposing green arrows, as depicted in Figure 3-19B. Its value (6.49+0.21°) can be used to retrieve the asymmetry ratio of the trigonal hexagon R_b/R_a. The result (1.218±0.008) agrees well with *ex situ* SEM measurements, from 1.5±0.1 for the newly grown NWs (near the Au tip) to ~1.0±0.1 near the bottom.

3.3.2. GE NWS AS SEEN BY GISAXS

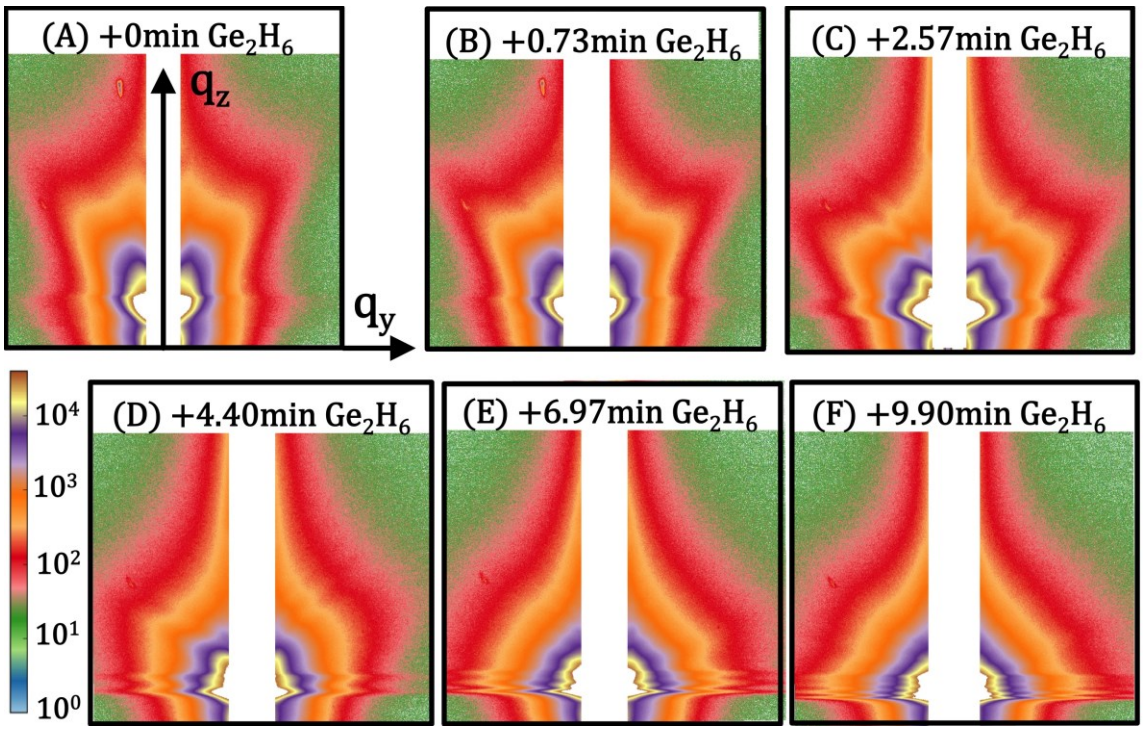

Figure 3-20: GISAXS images during digermane injection (sample #251112). The direct and reflected beams were blocked by a beamstop during the experiment. The choice of $\mathbf{q_y}$ was arbitrary and was not aligned with any specific crystallographic direction.

The GISAXS evolution for the growth of Ge NWs follows the exact same route as previously seen for the growth of Si NWs, which is expected considering that both (in our case) can be described by the VLS process. (Figure 3-20) Upon digermane injection, the liquid AuGe droplet grew immediately taller as is evident from the decrease in intensity along the $\mathbf{q_z}$ direction. The scattered intensity then continued to evolve until it reached the bell-like shape after about 7min of injection, at which point it remained unchanged

for the rest of the experiment. The contact angle of the liquid droplet as well as the instant length (growth rate) of the Ge NWs can be calculated via the methods demonstrated in the previous sections. The faster evolution (compared to Si NWs #280912B) is explained by the much higher gas partial pressure (~60 times) used in the growth.

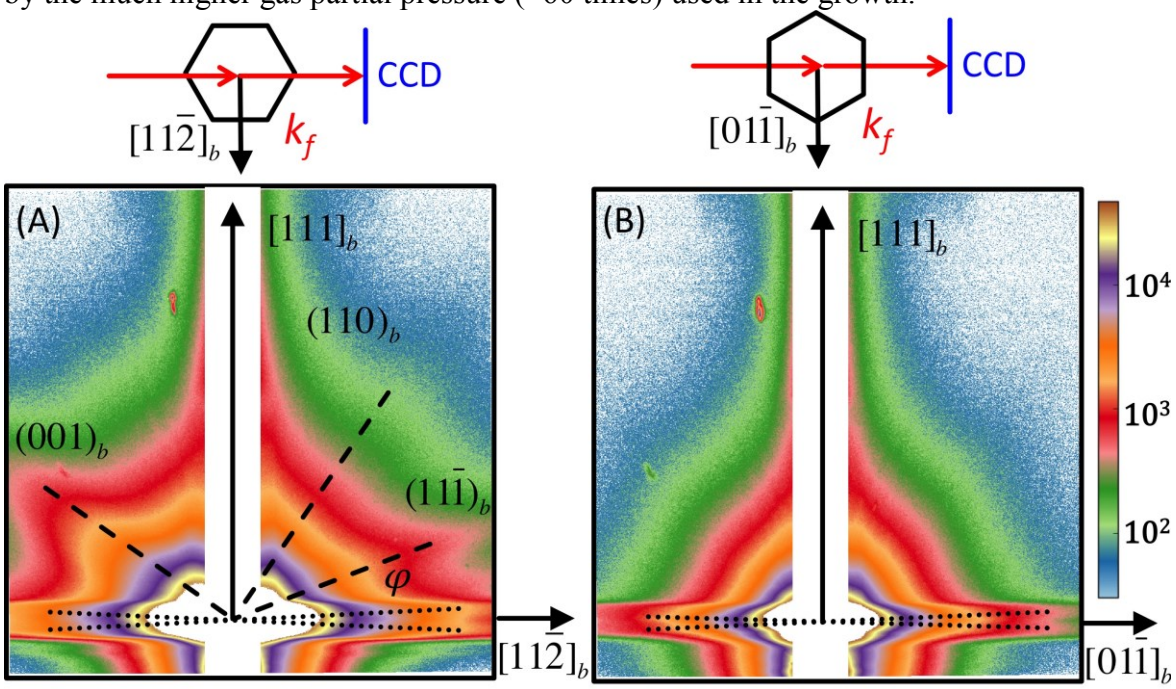

Figure 3-21: GISAXS image taken with $\mathbf{q_y}$ aligned along the (A) $[11\bar{2}]_b$ and the (B) $[01\bar{1}]_b$ direction after 2h of 6×10^{-3} mbar digermane injection at 330°C (sample #251112). Also shown is the top view of the scattering geometry for both images.

As stated earlier, Ge NWs grown at this temperature (330°C) are faceted with a hexagonal cross-section. These facets can be studied by aligning $\mathbf{q_y}$ with the $[11\bar{2}]_b$ direction. Before the measurement, the sample was heated to 400°C to avoid interference from the faceted solid Au. (Figure 3-21A) We immediately recognized the $(11\bar{1})_b$ streak found at $\varphi = 19.5°$. The strongest streak however turned out to be the one labeled $(001)_b$ (φ = 144.7°). We think that those are the two families that constitute the faceted $\{112\}_b$ sidewalls. Indeed, $(117)_b$ and $(7\ 7\ 13)_b$ surfaces were found on well annealed

$(115)_b$ and $(112)_b$ Ge substrates, where were in turn composed of stable nanoscale facets of $\{111\}_b$ and $\{001\}_b$ (Gai et al. 1998). Also observed is the weak signal perpendicular to the $(001)_b$ streak, which might come from the scattering by the $(110)_b$ facets (φ = 54.7°). Near the Yoneda wing, the scattered intensity by the opposite sidewalls is split into two tilted streaks (dotted lines) due to the strong tapering of the NWs, similar effects have already been analyzed with GIXD out-of-plane mapping. Along the other direction ($\mathbf{q_y}$ parallel to $[01\bar{1}]_b$), no extra streaks were observed, indicating that the cross-section of the NWs is indeed a hexagon.

3.3.3. DISCUSSION

We started off this section by showing an intriguing case on the evolution of Au state before and after Ge_2H_6 injection. After the solidification at 200°C, we have observed the existence of both the metastable β- and γ- phase AuGe, in additional to the more commonly occurring fcc Au. The β phase eventually disappeared under the presence of digermane, together with part of the γ- phase AuGe that were not epitaxially connected to the substrate. Our data strongly suggests that the remaining γ- phase AuGe resides at the interface between the catalyst and the Ge substrate and could be responsible for the different outcome of the VSS growth (straight NWs, crawling NWs). We then demonstrated that, with some geometric considerations, the bizarre streaks observed in the out-of-plane mapping could be used to calculate the tapering angle and the asymmetry ratio of the hexagonal cross-section. Last but not least, our GISAXS images indicated that the faceted $\{112\}_b$ sidewalls, found for Ge NW growths at higher temperatures, are composed of nanoscale facets of the $\{111\}_b$ and $\{001\}_b$ families. The result, however, needs to be further verified by more direct methods such as Electron Microscopy studies.

References:

Anantharaman, T.R., Luo, H.L. & Element, W., 1966. Formation of New Intermetallic Phases in Binary Eutectic Systems by Drastic Undercooling of the Melt. Nature, 210(5040), pp.1040–1041.

Boukhicha, R. et al., 2011. Gold anchoring on Si sawtooth faceted nanowires. EPL (Europhysics Letters), 95(1), p.18004.

Gai, Z. et al., 1998. Faceting and nanoscale faceting of Ge (hhl) surfaces around (113). Physical Review B, 58(8), pp.4572–4578.

Kodambaka, S. et al., 2006. Diameter-Independent Kinetics in the Vapor-Liquid-Solid Growth of Si Nanowires. Physical Review Letters, 96(9), p.096105.

Lu, G.-H. et al., 2005. Relative stability of Si surfaces: A first-principles study. Surface Science, 588(1-3), pp.61–70.

Marshall, A.F. et al., 2010. Hexagonal close-packed structure of au nanocatalysts solidified after ge nanowire vapor-liquid-solid growth. Nano letters, 10(9), pp.3302–6.

Ressel, B. et al., 2003. Wetting of Si surfaces by Au–Si liquid alloys. Journal of Applied Physics, 93(7), p.3886.

Ross, F.M., Tersoff, J. & Reuter, M.C., 2005. Sawtooth Faceting in Silicon Nanowires. Physical Review Letters, 95(14), p.146104.

Schmid, H. et al., 2008. Patterned epitaxial vapor-liquid-solid growth of silicon nanowires on Si(111) using silane. Journal of Applied Physics, 103(2), p.024304.

Schmidt, V. et al., 2009. Silicon Nanowires: A Review on Aspects of their Growth and their Electrical Properties. Advanced Materials, 21(25-26), pp.2681–2702.

Schülli, T.U. et al., 2010. Substrate-enhanced supercooling in AuSi eutectic droplets. Nature, 464(7292), pp.1174–7.

Schwarz, K.W. & Tersoff, J., 2011. Elementary processes in nanowire growth. Nano letters, 11(2), pp.316–20.

Scott, M.G., 1975. X-ray diffraction and differential thermal analysis of splat-quenched gold-germanium alloy. Materials Science and Engineering, 18(2), pp.279–284.

Singh, A.K., 2005. Advanced X-ray Techniques in Research and Industry (Stand Alone): A.K. Singh: 9781586035372: Amazon.com: Books,

Sutter, E. & Sutter, P., 2011. Formation and stabilization of single-crystalline metastable AuGe phases in Ge nanowires. Nanotechnology, 22(29), p.295605.

Vincent, L. et al., 2011. Faceting mechanisms of Si nanowires and gold spreading. Journal of Materials Science, 47(4), pp.1609–1613.

4. STRAIN IN CORE-SHELL NWS

After the successful growth of Si and Ge NWs, the next logical step would be to combine the two processes together. Injecting both precursor gases simultaneously would result in the growth of $Si_{1-x}Ge_x$ alloy NWs with tunable lattice parameters while injecting them sequentially would form the so-called NW heterostructures. The Si-core/Ge-shell NW is probably one of the most well known among all the SiGe NW heterostructures, first popularized by (Lauhon et al. 2002). Indeed, both theoretical calculations and experimental results show promising application potentials in the field of electronics (Musin & Wang 2005), optoelectronics (Migas & Borisenko 2007) and thermoelectricity (Hu et al. 2011), mostly through bandgap manipulation by quantum size effect (Musin & Wang 2006) or more importantly, by strain engineering (Huang & Yang 2011). Contrary to common belief, we found no apparent strain in the CVD grown Ge shell in our case, even when growing at a temperature as low as 220°C. Moreover, it would seem that at 220°C the shell is formed solely by a homogeneous compound with a uniform composition of $Si_{0.25}Ge_{0.75}$. Other composition only emerges as a result of intermixing either by annealing or by directly growing the sample at higher temperatures (300°C), the Ge shell meanwhile remains fully relaxed.

The rest of the chapter is structured as follows. Results of general *in situ* measurements during the Ge shell growth will first be presented, to be complemented by strain analysis using anomalous scattering techniques. We then proceed to study the influence of post-growth annealing, NW size and Ge growth temperature on the strain/composition of the Ge shell. We will also spend a few words on our failed attempt to extend our research to MBE grown Ge shells, which incidentally led to the experiment that would later become the subject of the entire Chapter 5. Finally, a brief discussion can

be found at the end of this chapter which summarizes all our results as well as comparing them to the existing literature.

4.1.CVD Ge on Si NWs

4.1.1. General in situ measurements

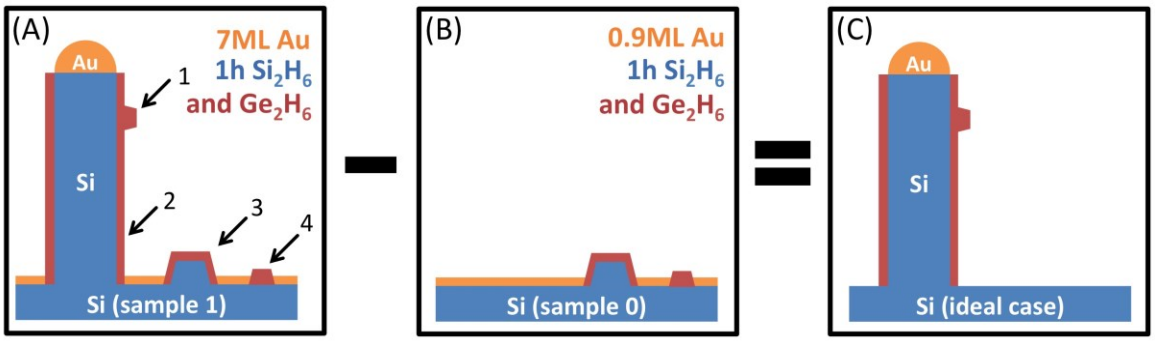

Figure 4-1: Schematic representations of the surface structures found on the subject sample (sample 1, A) as well as on the reference sample (sample 0, B), and how the difference of the two would yield the ideal result (C).

For the study of strain evolution in SiGe coreshell NWs with a CVD grown Ge shell, we shall present the results on sample #260713 (hereinafter referred to as sample 1). The Si NWs were grown with 1h of 0.9sccm Si_2H_6 injection at 570°C right after the deposition of 7ML (1.65nm) of Au. *Ex situ* SEM observations revealed that the NWs were about 2.6µm long with an average diameter of 300nm. After the NW growth, the sample was cooled down to 220°C where subsequent deposition of the Ge shell layer took place. For the purpose of *in situ* study, the Ge_2H_6 (0.8sccm) injection was carried out in multiple steps with an initial duration of 5min, each additional injection then doubled the current amount of deposition (except for the last one). (Figure 4-1A) The aim of this study was to investigate the strain in the Ge islands (1) and in the possible Ge wetting layer (2) surrounding the Si NWs. Unfortunately, we would also be expecting unwanted signals scattered by the Ge shell enclosing the existing Si islands (3) and by the Ge

islands formed directly at the surface (4). To discriminate between the two contributions, a reference sample #310713 was grown (hereinafter referred to as sample 0). (Figure 4-1B) The reference sample underwent the exact growth procedure as sample 1 except for the amount of Au deposited. From previous chapters, we already know that the Au wetting layer serves as a catalyst for the decomposition of the precursor gases and probably even as a surfactant for the 2D growth. The 0.9 ML of Au on sample 0 is hence pivotal to reproducing the exact same surface conditions as found on sample 1.

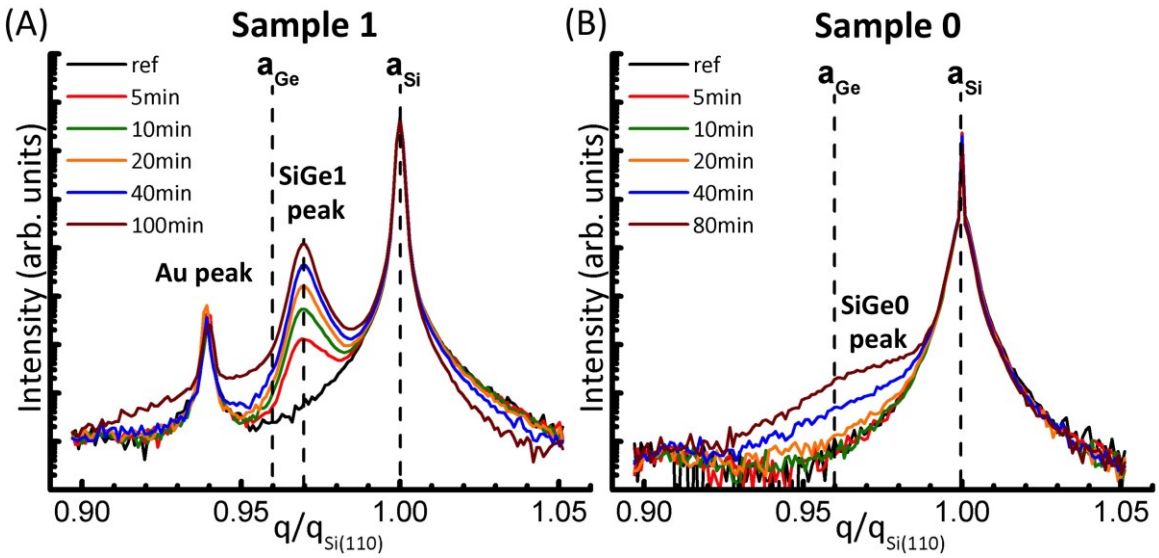

Figure 4-2: Results of radial scans around $Si(110)_s$ peak on both samples. The same vertical scale was used on both images so that the intensity level is directly comparable.

(Figure 4-2 black curve) The most noticeable difference between the two samples prior to the Ge growth is the presence (absence) of the solid Au (200) peak on the radial scans around $Si(110)_s$. This confirms that Au only existed as the wetting layer on the reference sample, and as a result could not have catalyzed the growth of any Si NWs. (red curve) Immediately after the first Ge_2H_6 injection, a peak was seen emerging from position (q/q_{Si} = 0.9696±0.0005) in between that of bulk Si and that of bulk Ge.

Meanwhile on the reference sample, nothing was yet to be observed, indicating that the SiGe1 peak observed on sample 1 came indeed from the Ge deposition on Si NWs. It was not until after 40min of Ge_2H_6 injection (blue curve) that a much broader peak appeared on the reference sample. This peak, hereinafter referred to as SiGe0, can only be the result of the scattering by the Ge structures residing at the sample surface. Notice that the SiGe0 peak was at the same time also observed on sample 1 (which became obvious after 100min of injection, brown curve).

A different strain relaxation mechanism might settle in should the size of the Ge islands approaches the diameter of the Si NWs (*i.e.* the NW sidewall can no longer be considered as an infinitely large surface), it is hence important to have quasi-monodisperse NWs for a controlled study. (Figure 4-3A) A narrow size distribution was achieved on sample 1 as is evidenced by the modulation observed on the rocking scans around the Si Bragg peak, the period of which is indicative of the average size of the NWs ($\bar{D} = 289.5 \pm 7.2nm$). This is further confirmed by the FWHM of the peak and by *ex situ* SEM observations. It would seem that the FWHM (so did the modulation period though the measurement was less precise) gradually decreased for increasing amount of Ge deposition, which was translated into a steady increase in the calculated size of the NWs (Figure 4-3B). To explain this, we need to first clarify that the dimension measured here corresponds to the size of the objects along the direction of the rocking scan, having the same lattice parameter as bulk Si along the direction of the radial scan. With that in mind, it would seem that the observed size increase can be understood as the presence of a pseudomorphic Ge wetting layer on the NW sidewall. As illustrated in Figure 4-3C, the lattice parameter of the pseudomorphic Ge along the radial scan direction is confined to that of the Si underneath whereas its lattice parameter along the rocking scan direction

expands in response to the transverse compression. For cubic materials the ratio of the expansion can be calculated with the following formula

$$\frac{a_j}{a} - 1 = (\frac{a_i}{a} - 1)\frac{1 + \nu_{i,j}}{1 - \nu_{i,j}} \qquad (4\text{-}1)$$

The initial compression reduces (stretching increases) the lattice parameter from a to a_i, the crystal then reacts by expanding (contracting) the lattice parameter in the perpendicular direction to a_j. In our case $a_i = a_{Si} = 0.9598a_{Ge}$, the Poisson's ratio $\nu_{[01\bar{1}],[\bar{2}11]} = 0.2487$ we have $a_j = 1.0696a_{Ge}$.

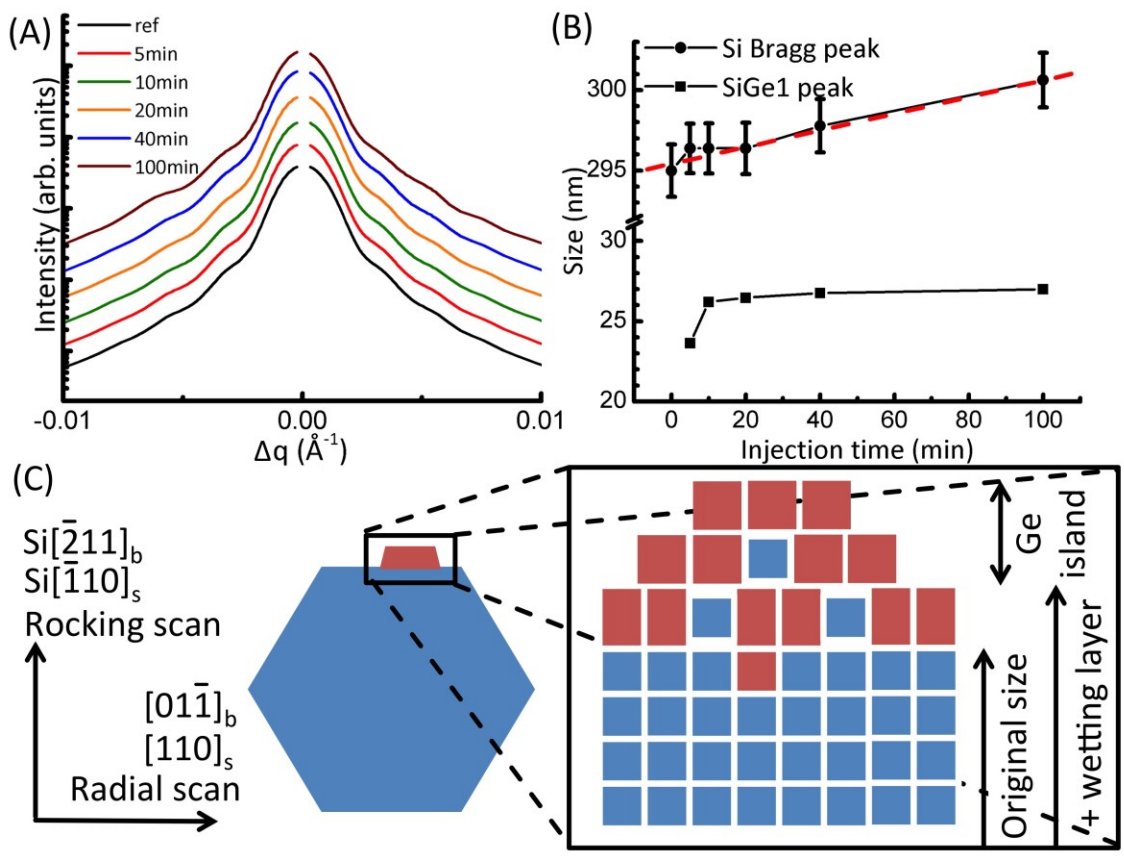

Figure 4-3: (A) Results of rocking scans around $Si(110)_s$ peak on sample 1. The vertical scale has been readjusted to aid the eye. (B) Calculated size from the FWHM of the rocking scans on the Si Bragg peak and on the SiGe1 peak as a function of Ge_2H_6 injection. (C) Schematic representation showing how the Ge wetting layer can contribute to the size of the Si NWs measured by the rocking scans.

There are however two additional questions that need to be answered. Why did the calculated size continue to increase even after 100min of injection and is it really possible to have a Ge wetting layer of 2.8nm thick (half of the overall increase value)? The first question can be answered by taking into account the extremely slow uncatalyzed decomposition at this temperature (220°C). From our previous experience with Ge NWs growth, we know that the Ge overgrowth (on Ge NWs) is almost completely suppressed by simply reducing the growth temperature to 280°C. The sticking coefficient of Ge_2H_6 on Si at 220°C should be even lower. Moreover, *ex situ* SEM observations on sample 1 revealed that heavy growth of the rough Ge shell layer mostly occurred near the top of the NWs, while the rest of the NWs remained faceted with no apparent roughness. It is thus possible that even with 100min of injection the critical thickness was still not reached on the lower part of the NWs due to the delayed growth. With regard to the second question, 2.8nm does seem unrealistic even with the 6.96% expansion from the Poisson effect. MBE Ge on Si(111) substrates at 400°C is reported to have a critical thickness of about 0.69nm (Voigtländer 2001). CVD grown Ge typically has a larger critical thickness (2 times larger), and is attributed to hydrogen acting as a surfactant during growth. Although there is no direct evidence in the literature, we could imagine the critical thickness to be even larger with Au as a surfactant. Furthermore, thicker critical layer on NW sidewalls than on planar substrates has previously been reported for the growth of InAs shell on GaAs NWs (Yan et al. 2011), which the author attributed to the strain relief by the nanosize curved surface of the cylindrical NWs. Although our Si NWs do not possess a circular cross-section, one could nevertheless expect effective strain relaxation at the joints between the {111} and {113} sawtooth facets and between adjacent hexagonal sidewalls. Still, the thickness we estimated falls largely below the

measured value. As a result, we do not rule out the possibility of some other mechanisms being partially or even solely responsible for the observed decrease in FWHM.

We now turn our focus to the Ge islands on the NW sidewalls. Their average height (Figure 4-3B), as calculated from the FWHM of the SiGe1 peak, increased rapidly from 0 to 26.2nm within the first 10min and then remained relatively steady for the rest of the injection. This seems to imply a self-limiting growth mechanism for such islands. It is worth mentioning that while the "magic" size (~26nm) can be simply characteristic of the Au-catalyzed CVD growth at 220°C, it may also be the result of as being limited by the finite size of the NW structures (sawtooth facets period ~ 35nm, etc.).

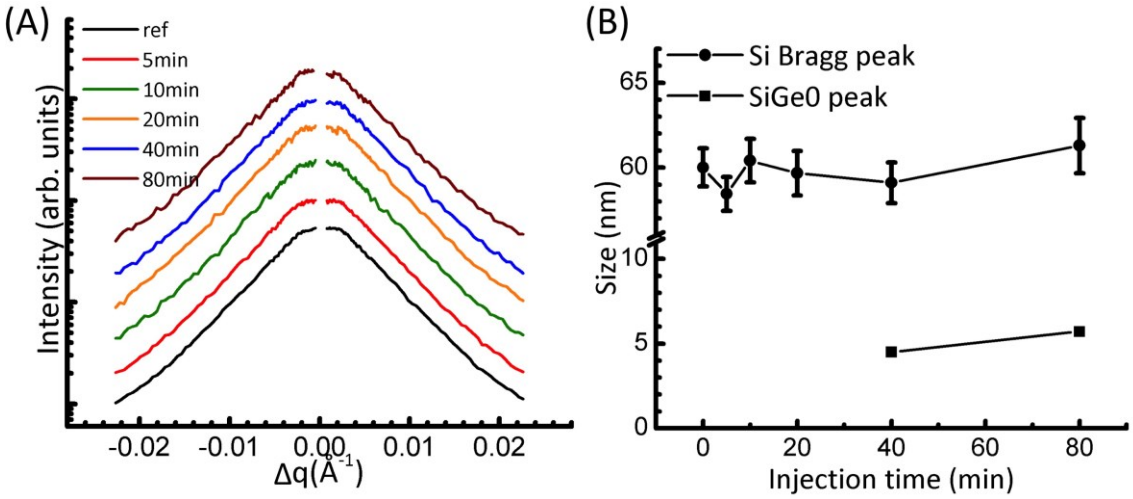

Figure 4-4: (A) Results of rocking scans around $Si(110)_s$ peak on sample 0. The vertical scale has been readjusted to aid the eye. (B) Calculated size from the FWHM of the rocking scans on the Si Bragg peak and on the SiGe0 peak as a function of Ge_2H_6 injection.

For comparison, the result of rocking scans on the reference sample is also shown (Figure 4-4). The ~60nm as deduced from the FWHM of the Si Bragg peak corresponds to the size of the Si islands formed at the sample surface during the initial Si_2H_6 injection. The ~5nm as calculated from the FWHM of the SiGe0 peak is indicative of the average

width of the Ge shell enclosing the Si islands and that of the Ge islands formed directly at the surface. Note that no size increase (due to the presence of pseudomorphic Ge layer or other unexplained reasons) was observed on the reference sample, instead, the FWHM of the Si Bragg peak remained (relatively) constant during the entire Ge_2H_6 injection.

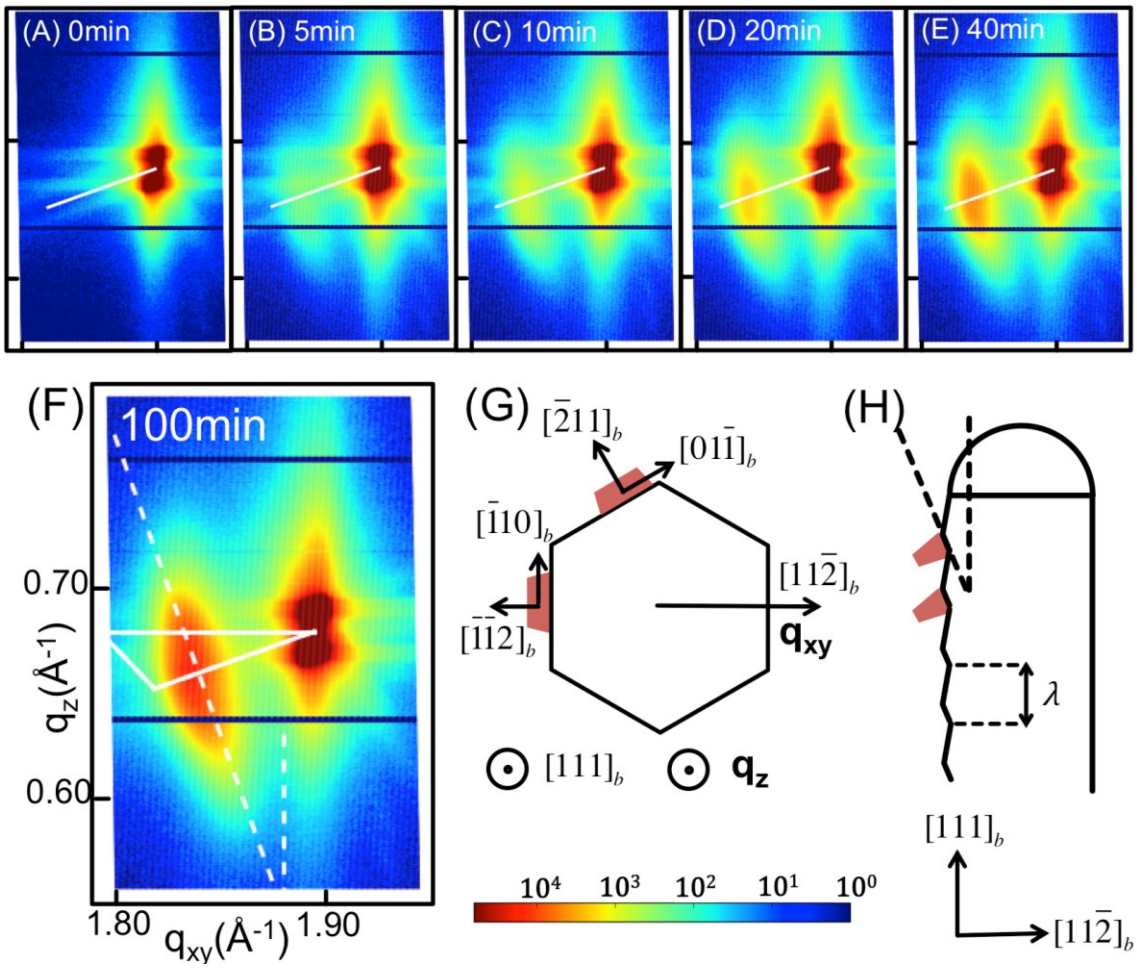

Figure 4-5: Sample 1 (A-F) Out-of-plane mapping around the $(101)_s$ Si Bragg peak during digermane injection with $\mathbf{q_{xy}}$ along the in plane radial direction. The white line in each subplot graph denotes the relaxation line. The white triangle in (F) is the relaxation triangle assuming that the Ge islands were strained along the $\{110\}_b$ direction. (G) Cross-sectional view and (H) side view of the NW schematics. The dashed lines in both (F) and (H) correspond to the inclination of the Au anchored $(\bar{1}\bar{1}1)_b$ sawtooth facets. The Ge deposition between the islands and on the opposite sidewall are hidden in (H) for the sake of simplicity.

Although we have yet to determine the composition of (and as a result, strain in) the Ge islands residing on the Si NW sidewalls, we do have confirmation, from previous radial scans, that they are dominated by a SiGe alloy with an average in-plane lattice parameter which is 3.14% larger than that of bulk Si (q_{SiGe}/q_{Si} = 0.9696). If the Ge islands are indeed strained by the Si NWs, the lattice will compensate by expanding in the other directions (Poisson effect), resulting in an anisotropic distribution of the lattice parameters. To study this, we have performed a series of out-of-plane mapping around the $(101)_s$ Si Bragg peak. The result is shown in Figure 4-5. The relaxation line (which connects the bulk Si Bragg and bulk Ge Bragg peak) is added to each of the subplot graphs. It is obvious that while the intensity of the out-of-plane SiGe peak got stronger and stronger with increasing amount of Ge_2H_6 injection, its peak center was always found at the same position on the relaxation line. Further analysis indicates that this position corresponds to an isotropic lattice parameter that is ~3% larger than that of bulk Si, both in plane (along $\mathbf{q_{xy}}$) and out of plane (along $\mathbf{q_z}$). The above finding agrees well with our previous in plane analysis (3.14%) and is our first clue towards the fact that the Ge islands on the NW sidewalls may be fully relaxed.

Relaxation triangle analysis (such as the one drawn in Figure 4-5F) is not really helpful in this case as we do not know along which directions are the Ge islands actually strained, that is, if they are strained at all. However, it does help us realize one important thing. Since no strained signal should be found outside the relaxation triangle, the oval-shape intensity that we observed for the SiGe peak is likely to be reflective of its form factor rather than of actual variations in the lattice parameters. This prompts the question as to why the (oval-shape) form factor is tilted counterclockwise? To answer this we shall first recall our *ex situ* SEM observations which indicate heavier growth to occur mostly near the top of the NWs. While it is possible that the Au tip acted as the major source of

atomic Ge, let us not forget the Au nanoparticles anchoring the $\{111\}_b$ sawtooth facets. Indeed, those nanoparticles can serve not only as the catalyst for Ge_2H_6 decomposition, but also as a surfactant for subsequent growth, making the Au rich $\{111\}_b$ facets the major growth front for Ge islands. This is further supported by the inclination angle of the form factor which matches that of the $(\overline{1}\overline{1}1)_b$ plane (white dashed line). However, the current explanation raises yet another question, as the observed aspect ratio of the form factor would suggest the height of the Ge islands to be three times as large as their width. This seems to contradict the common image of the flat islands frequently observed in Ge/Si heteroepitaxy, *e.g.* height/width ~ 7/80 for MBE grown Ge islands on Si(111) surface at 350°C (Voigtländer 2001). To explain the discrepancy, let us first calculate the size of the sawtooth facets using the empirical formula given in Chapter 2.

$$\lambda \sim 0.12D \qquad (4\text{-}2)$$

where λ is the period of the sawtooth facets. For D = 290nm, this yields a period of 35nm. The $\{111\}$ facets is almost half as long as the $\{113\}$ ones. Taking further into account the inclination angle, we obtain the length of the Au anchored $(\overline{1}\overline{1}1)_b$ facet (and hence the width of the Ge islands) to be 12.3nm, which is less than half the value (26.2nm) of the height calculated previously with the rocking scans. While this simple demonstration does not account for the factor of 3 estimated using out-of-plane peak FWHMs, it does answer the question as to how the height of the Ge islands in our case can largely exceed their width. It also proves that the growth of 3D Ge islands on Si NWs can be distinctly different from that on bare Si substrates due to the small size of the sidewall fine structures. Finally, it is worth mentioning that the formation of twin boundaries and stacking faults cannot be used to explain the observed aspect ratio. As a

matter of fact, those defects, commonly found in the {111} planes (Dayeh et al. 2013), will only result in the apparent interpretation of even "taller" Ge islands.

We have also performed a similar out-of-plane mapping on the reference sample. The result (Figure 4-6) shows continuous intensity that spreads along the relaxation line with no distinct peak feature. The observed intensity is likely to be indicative of a variation in the lattice parameters rather than of the form factor as the latter would usually result in a more symmetrical distribution of the intensity (such as the one described above).

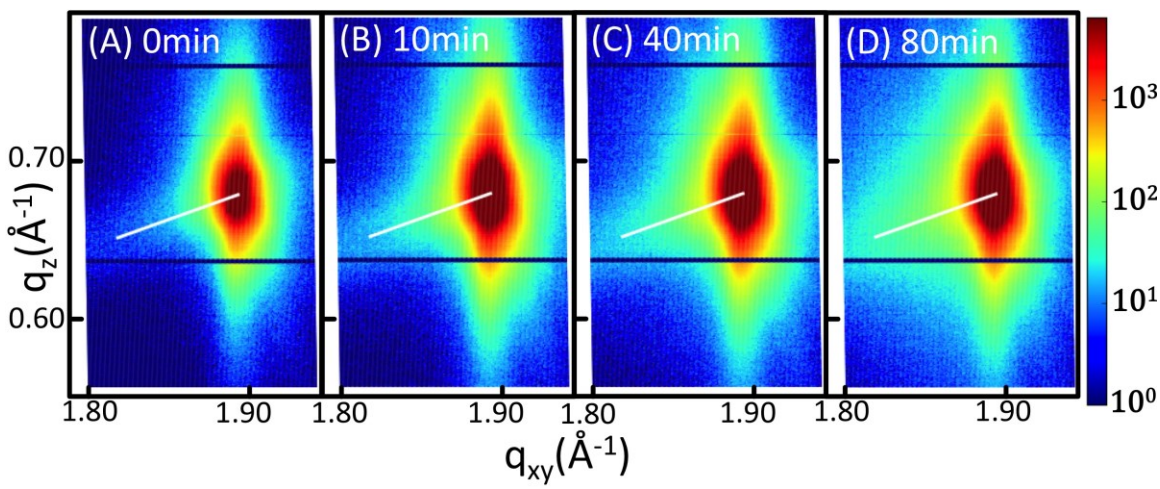

Figure 4-6: Sample 0 (A-D) Out-of-plane mapping around the $(101)_s$ Si Bragg peak during digermane injection. $\mathbf{q_{xy}}$ is along the in plane radial direction.

4.1.2. STRAIN ANALYSIS BY ANOMALOUS SCATTERING

The next step is to calculate the actual Ge content in the Ge islands (SiGe1 peak). Anomalous scattering technique is best suited for the task thanks to its high chemical sensitivity when operating near the absorption edges. However, being highly sensitive also calls for careful calibration of the dispersion corrections $f'(\hbar\omega), f''(\hbar\omega)$. This is usually achieved by simply measuring the fluorescence emission of the anomalous element (Ge in our case). The result (Figure 4-7A black curve) is rescaled to match the

tabulated pre-edge and post-edge values (red curve) of $f'(\hbar\omega)$. The curve may also be shifted along the x-axis if the experimental absorption edge differs from the theoretical one but the wiggling features (related to the chemical environment of the atoms) are perfectly preserved. Once calibrated, the $f'(\hbar\omega)$ values are used to compute the $f''(\hbar\omega)$ ones (inset, black curve) using (difference) Kramer-Kronig relations. MAD experiments require measurements at at least three different energies. In practice, often more than 10 measurements are carried out to increase the accuracy (reliability) of the method. Additionally, it is advised to perform a "double verification" by comparing the fluorescence intensity from each individual MAD measurement to the calibrated $f'(\hbar\omega)$ curve (Figure 4-7 blue circles). This is particularly helpful to measurements near the absorption edge, as a misalignment of even 1eV can cause significant errors in both terms of the dispersion corrections.

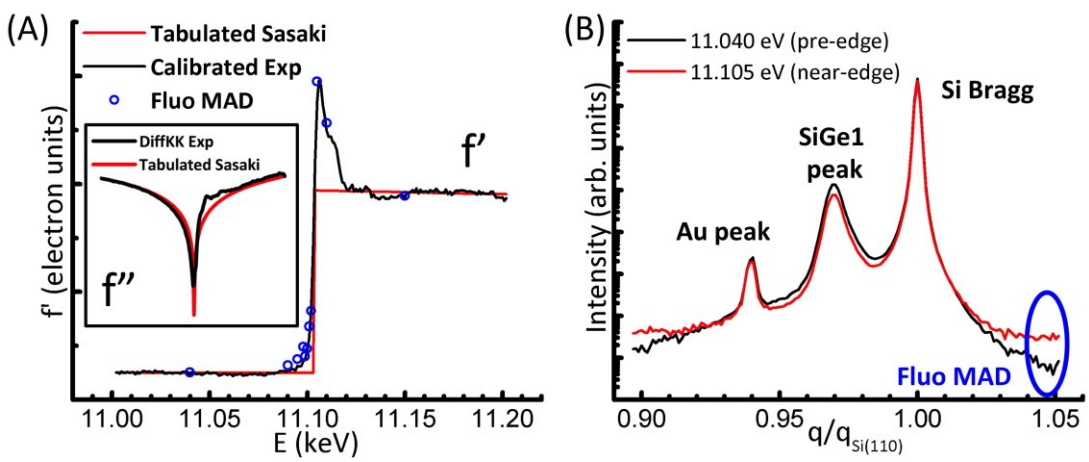

Figure 4-7: (A) Calibrated dispersion corrections of Ge near its K edge (black curves) against tabulated theoretical values (red curves). (B) Results of MAD around the $Si(110)_s$ peak. For simplicity only two measurements, pre-edge and near-edge, are shown here. The fluorescence intensity far away from the Bragg peaks (blue circles) is used to verify the X-ray energy of each scan.

We use the NanoMAD toolkit (developed by Vincent Favre Nicolin) for the data analysis. The output of NanoMAD consists of the amplitude of the partial structure factors F_T, F_N, F_A, as well as the phase difference between each of them (for the definition of each term please refer to the diagram in Figure 1-8). The Ge content is then

$$x_{Ge} = 1/(1 + \frac{F_N f_A^0}{F_A f_N}) \qquad (4\text{-}3)$$

Figure 4-8A shows the calculated Ge content after 100min of digermane injection. Outside the SiGe1 peak, the result fluctuates (dashed red lines) as there is almost zero anomalous effect in those regions. As soon as we approach the SiGe1 peak, the Ge content quickly rises from 0 to ~75%. The sharp increase and the almost constant value of the Ge content inside the SiGe1 peak is not surprising as we have already suspected the peak to be reflective of the form factor of the Ge islands rather than of actual variations in the lattice parameter. Moreover, the close to 75% Ge content indicates that the Ge islands are strain-free since $a_{SiGe1} = 1.031 a_{Si}$ ($q_{SiGe1}/q_{Si} = 0.9699$) is exactly the lattice parameter one should expect for a fully relaxed $Si_{0.25}Ge_{0.75}$ alloy.

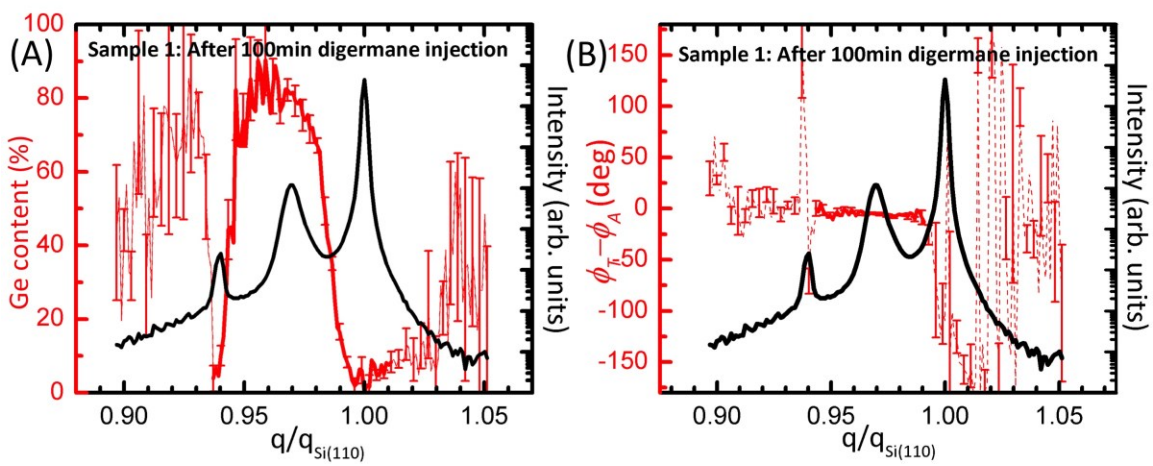

Figure 4-8: (A) The calculated Ge content and (B) phase difference between F_T and F_A after 100min of digermane injection on sample 1 using MAD data collected at 11 different energies. Only one in two error bars is shown for demonstration.

One major drawback of the MAD method is the long duration it takes to repeat the same measurement at multiple energies. As a result, it was only performed at the end of the Ge_2H_6 injection. To fill in the gaps between each increment of Ge deposition, a simple two-wavelength measurement (one pre-edge and one near-edge) is carried out instead. Unlike MAD, the two-wavelength measurement works under the assumption that the phase is a known quantity and is thus applicable only to a selection of cases (disordered material for instance). Fortunately for us, (Figure 4-8B) the previous MAD experiment reveals that there is almost no phase difference between F_T and F_A (again the fluctuation outside the SiGe1 peak is due to the absence of the anomalous effect). The Ge content is hence calculated by fixing $\phi_T - \phi_A = 0$. The result shows a sharp transition of the Ge content from 0 to ~75% at the tail of the SiGe1 peak consistent with what we have observed with MAD data, except for maybe the one after 5min of injection (Figure 4-9A) where a more gentle slope was observed instead. Combining this with the results from Figure 4-3B, we speculate that part of the signal we observed after 5min of injection comes from the newly formed (and smaller) Ge islands that were slightly strained. With longer digermane exposure, more and more Ge islands reached the "magic" size, the signal thus became dominated by the full grown Ge islands that were completely relaxed.

4.1.3. EFFECT OF POST-GROWTH ANNEALING

We then proceed to study the effect of post-growth annealing on the Ge islands. (Figure 4-10A) Annealing sample 1 at 300°C saw a decrease in peak intensity of the SiGe1 peak and the emergence of a new peak (referred to as the SiGe2 peak) with a smaller lattice parameter (larger q). The peak center of the SiGe1 peak was also slightly shifted to the right. This could indicate one of the two things, either the fully relaxed Ge islands became strained after the annealing (which is less likely to happen) or simply that more Si were intermixed into the relaxed islands (more likely). For longer annealing

time, the new SiGe2 peak continued to grow with its peak center moving closer and closer to that of bulk Si. The SiGe1 peak almost completely disappeared after the final annealing (8min) at 400°C, its whole intensity being absorbed into the now enormous SiGe2 peak which was centered at $q/q_{Si} = 0.9860$.

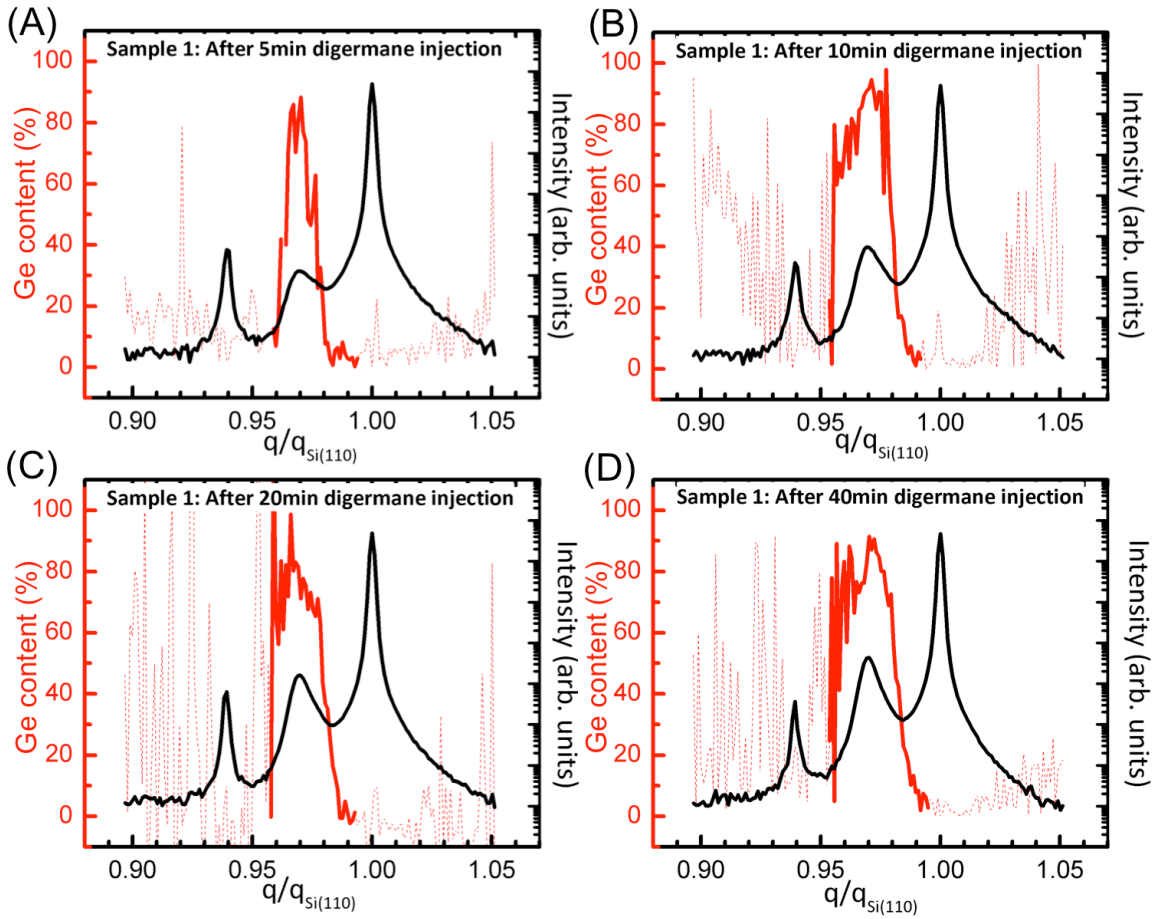

Figure 4-9: Ge content calculated from two-wavelength anomalous measurements after (A) 5min (B) 10min (C) 20min (D) 40min of Ge_2H_6 injection on sample 1.

For the strain-stress analysis, we again resorted to MAD measurements. The result (Figure 4-10B) shows a Ge content that moderately increases from 0% at bulk Si position ($q/q_{Si} = 1$) to ~ 60% at $q/q_{Si} \sim 0.975$, the Ge content then remained relatively constant before starting to wear off as we approaches the Au peak ($q/q_{Si} \sim 0.95$). As

stated earlier, a gentle slope of the Ge content usually implies an actual variation in the lattice parameters. As a result, we can no longer consider the strain level at the peak center to be representative of that of the entire peak (which we did earlier when the peak intensity was dominated by its form factor).

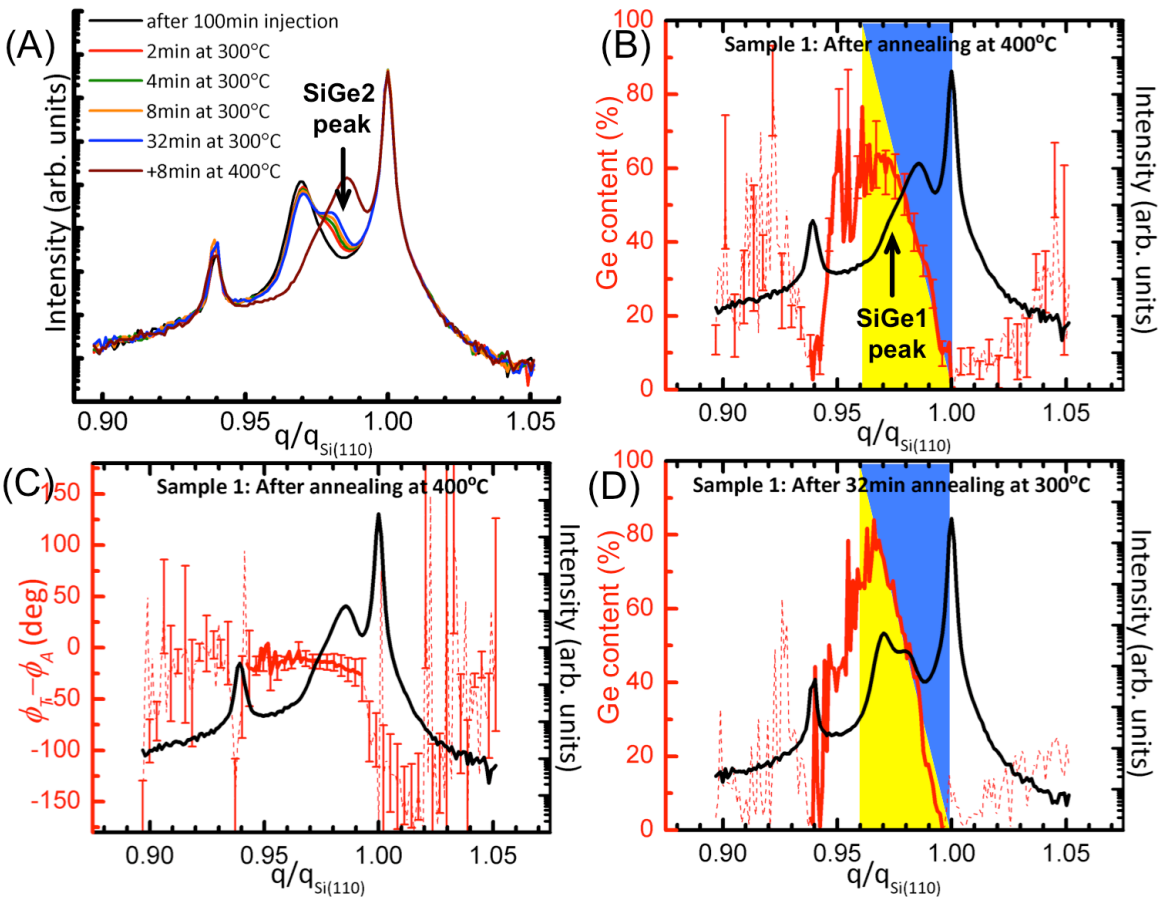

Figure 4-10: (A) Results of radial scans on sample 1 after each annealing step. (B) The calculated Ge content and (C) phase difference between F_T and F_A after the final annealing at 400°C using MAD data collected at 11 different energies. Only one in two error bars is shown for demonstration. (D) Ge content calculated from two-wavelength anomalous measurements after annealing 32min sample 1 at 300°C.

In order to analyze the strain level independently for each segment, we shall introduce the relaxation line which connects the bulk Ge point (Ge% = 100%, q/q_{Si} =

0.9599) and the bulk Si point (Ge% = 0%, q/q_{Si} = 1). If the actual Ge content is found below the relaxation line (yellow triangle), then the SiGe alloy is under tensile strain. If the actual Ge content is found above the relaxation line (blue triangle), then the SiGe alloy is under compressive strain. In our case, the Ge content lies exactly on the relaxation line, indicating that despite a different Ge content, the Ge islands after annealing are still fully relaxed. It should be noted that the plateau at Ge% ~ 60% to the left of the slope is once again caused by the form factor (and hence not by tensile strain), since it is otherwise impossible to have a non-zero Ge% beyond the bulk Ge point ($q < q_{Ge}$). This part of the intensity belongs to the remnant of the old SiGe1 peak. As a matter of fact, its submerged peak center can be vaguely identified at one end of the plateau.

MAD measurements were only conducted after the final annealing at 400°C, for the initial multi-step annealing at 300°C, two-wavelength measurements were used instead. As usual, the calculation of the Ge content is guided by the phase difference recovered with MAD data (Figure 4-10C). The results are pretty similar to one another due to the slow intermixing rate at low temperatures, therefore only result of the last annealing step (32min) is shown in Figure 4-10D. Although the scattered intensity was still, at the time, dominated by the SiGe1 peak, we can already observe the onset of the intermixing from the gradual variation of the Ge content. The Ge islands remained otherwise fully relaxed as the calculated Ge content falls right on the relaxation line.

With all that, we can now piece together the hidden scenario behind the annealing process (Figure 4-11). The Ge islands before the annealing forms a chemically sharp interface with the Si NWs, and were composed of fully relaxed SiGe alloy with an equilibrium Ge content of 75%. At 300°C, the intermixing is slow and is spread over only a small region close to the island-NW interface. The Ge content is the lowest (0%) at the bottom and gradually increases with increasing distance from the interface. Even after

32min of annealing, the majority of the Ge islands remained relatively unaffected by the intermixing despite a slight drop in the equilibrium Ge content (to ~72%). At 400°C the intermixing process is drastically accelerated. The initial SiGe alloy was almost completely taken over after merely 8min of annealing. The new alloy has a varying Ge content that increases slowly from 0% at the bottom of the islands to ~60% at the top. The dominating composition after the final annealing is $Si_{0.7}Ge_{0.3}$, as deduced by the position of the SiGe2 peak center. Despite the dramatic changes, the Ge islands remained fully relaxed the whole time.

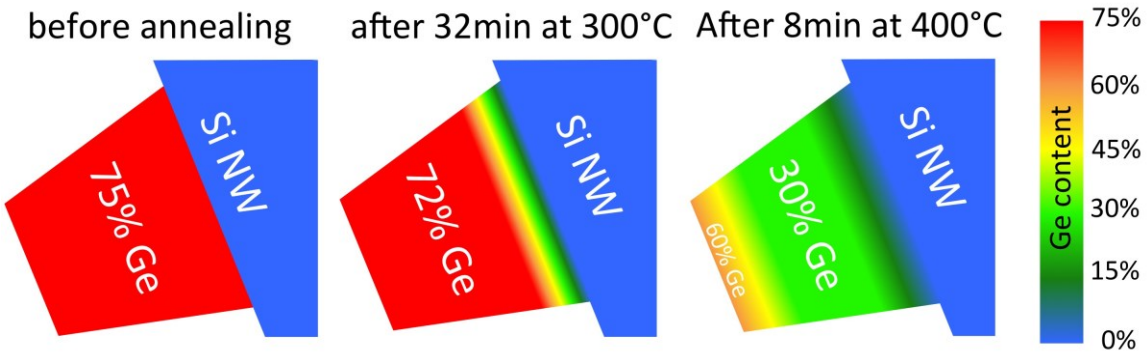

Figure 4-11: Schematic representation of the degree of intermixing during the annealing process. The Ge island was pictured on a {111} sawtooth facet.

4.1.4. Effect of NW size

One important conclusion that can be drawn from the previous experiments involving sample 1 is that the equilibrium Ge content doesn't seem to be affected by the duration of the growth. The calculated Ge content started off at ~75% and remained unchanged even after 100min of Ge_2H_6 injection, which bears the question, what is the decisive factor for the equilibrium concentration? Is it the (magic) size of the Ge islands, the growth temperature, or both? Moreover, is it possible to grow strained Ge islands by tweaking the growth conditions?

Let us first consider the size factor. Indeed, because of the self-limiting growth process of the Ge islands, prolonged injection would only result in the formation of more and more magic-size islands rather than agglomerating them into bigger ones. If we could somehow reduce/increase the diameter of the Si NWs (sidewall side length, width of sawtooth facets), we might be able to change the average size of the Ge islands. This was achieved by growing a sample (#290713, hereinafter referred to as sample 2) at a lower temperature (455°C) and with a smaller amount of catalyst (3ML Au). Rocking scans on the Si Bragg peak (not shown here) reveals that the Si NWs have an average diameter of ~70nm (65.7±2.6 according to the first minimum, 70.0±0.4 according to the FWHM) and a very narrow size distribution (size modulation observed). Subsequent growth of the Ge islands followed the same procedure as before (220°C, 0.8sccm).

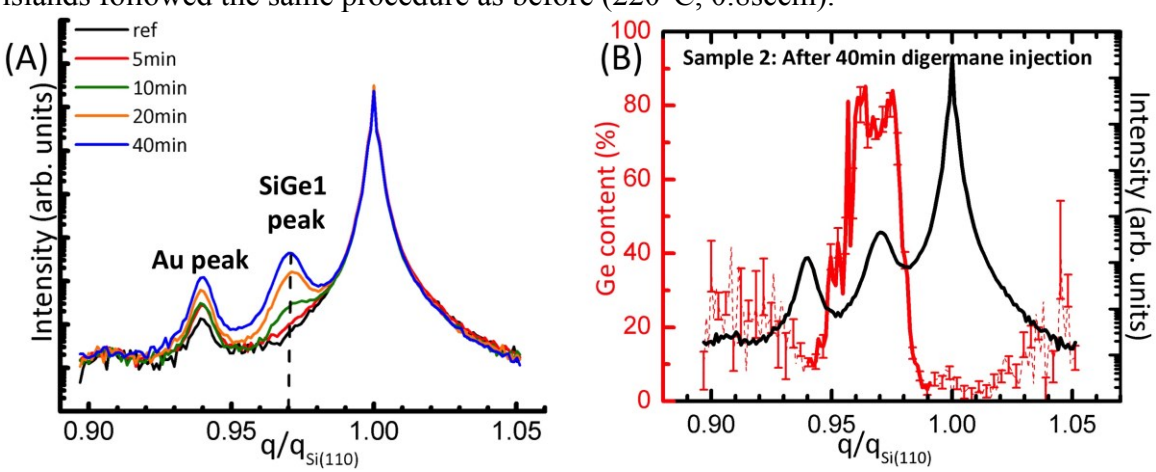

Figure 4-12: (A) Results of radial scans around $Si(110)_s$ peak on sample 2. The changes in the Au peak are due to a similar effect as what was described in Chapter 3.3. (B) The calculated Ge content after 40min of digermane injection on sample 2 using MAD data collected at 11 different energies. Only one in two error bars is shown.

It would seem from the radial scans (Figure 4-12A) and MAD measurements (Figure 4-12B) that the Ge islands have the same lattice parameter (q_{SiGe}/q_{Si} = 0.9707±0.0005) and composition (~75% Ge) as in the previous case (sample 1), while

rocking scans on the SiGe1 peak (not shown here) indicate that the Ge islands were indeed much (~30%) smaller with an average height of 20.9±0.5nm. It is worth mentioning that although we have not observed changes in the equilibrium Ge content for smaller island size, our finding does not rule out the existence of a possible size effect. In fact, 70nm is still considered relatively large. It is entirely possible that by reducing the diameter of the NWs further into the 10nm range one could change completely the growth mechanism of the attached Ge islands.

4.1.5. EFFECT OF GE GROWTH TEMPERATURE

A new sample (#100513, hereinafter referred to as sample 3) was selected for the study of the temperature factor. The Si NWs were grown with the same procedure as for sample 1 (540°C, 7ML Au) whereas the Ge island growth took place at a much higher temperature (290°C). Radial scans (Figure 4-13A) reveal that the majority of the SiGe alloy in the Ge islands has a slightly smaller lattice parameter (q/q_{Si} = 0.9760±0.0005) than what was found in the previous cases (q/q_{Si} = 0.9696). Moreover, a second peak was seen rising from position (q/q_{Si} = 0.9630±0.0005) close to that of bulk Ge (q_{Ge}/q_{Si} = 0.9699). This second peak belongs to the Ge structures at the sample surface as was confirmed by measurements (Figure 4-13A inset) on the corresponding reference sample (0.9ML Au, no Si NWs, 290°C for Ge growth). Its much stronger intensity is explained by the fact that more Ge were deposited on the sample surface due to the elevated rate of uncatalyzed Ge_2H_6 decomposition at higher temperatures.

Results from two-wavelength measurements (Figure 4-13BCD) indicate that the Ge islands on the NW sidewalls were fully relaxed. However, it does seem odd at first glance that the calculated Ge content does not show any sign of a form factor (steep slope, constant value), at variance with our previous observations on Ge growth at 220°C (Figure 4-8 and Figure 4-9). Instead, the calculated Ge content looks a lot more like what

was found on sample 1 after 32min of annealing at 300°C (Figure 4-10D). This can be understood as due to the enhanced intermixing at 290°C. Indeed, growing directly at 290°C can be equivalent to annealing the Ge islands at the same temperature, resulting in a gradual variation in the lattice parameters. The enhanced intermixing at 290°C can also explain the smaller lattice parameter found with the radial scans since more Si was incorporated into the islands. Note that the dominating compound in this case was $Si_{0.40}Ge_{0.60}$ (deduced by the position of the peak center).

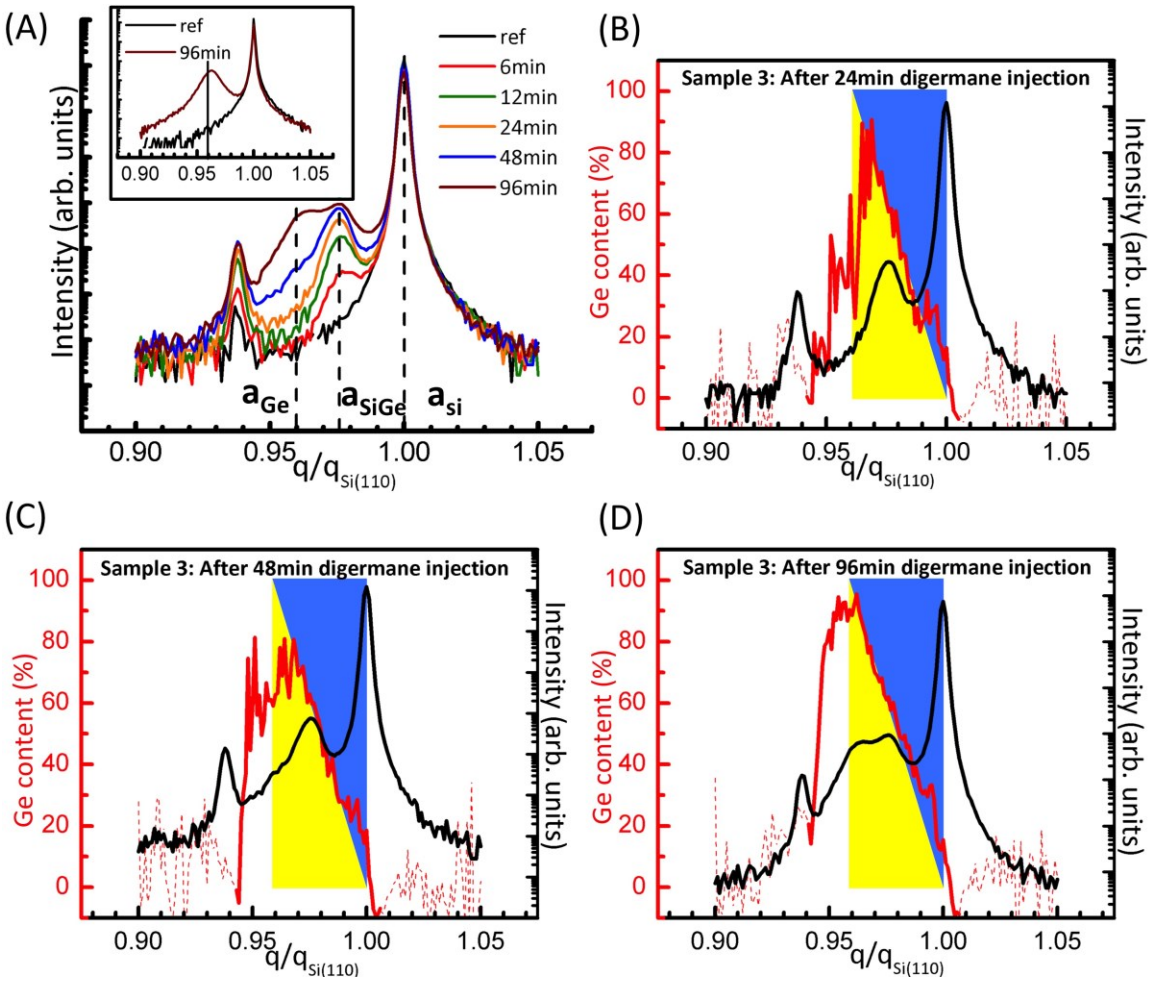

Figure 4-13: (A) Results of radial scans around $Si(110)_s$ peak on sample 3. (inset) Result of radial scans on the corresponding reference sample with no NWs. (B-D) Calculated Ge content on sample 3 using two-wavelength measurements.

4.2.MBE Ge on Si NWs

One of the original objectives of this study was to compare the composition and strain between the Ge shell grown by CVD and that grown by MBE. Unfortunately, this has proven difficult due to the huge interference coming from the Ge structures formed at the sample surface. In fact, less Ge was deposited on the NW sidewall than directly on the sample surface due to the small angle η (21.43°) between the Ge source and the sample normal. The ratio is further reduced by the fact that the sample has to be constantly rotated (ω) in order to maintain a homogeneous deposition on all sides.

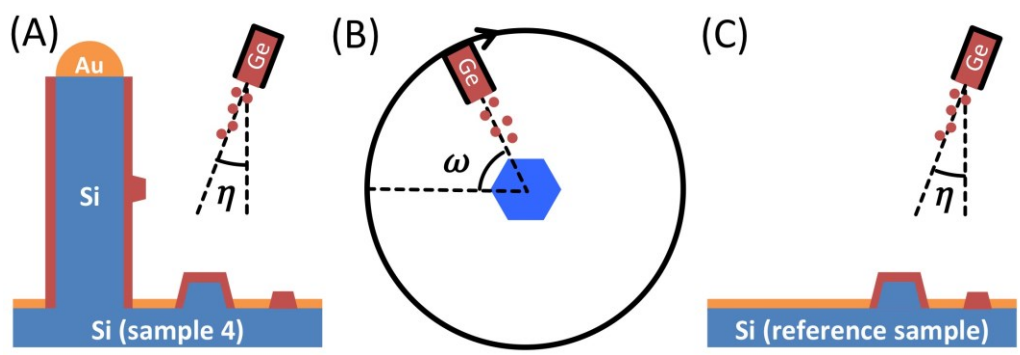

Figure 4-14: Side view schematics of the MBE Ge growth involved in (A) sample 4 and in (C) the corresponding reference sample. (B) Top view schematics of the same experiment. The sample was constantly rotated during the Ge deposition.

$$\frac{h_{NW}}{h_{nominal}} = \frac{\tan\eta \int_0^{\pi} \sin\omega \, d\omega}{2\pi} = 0.125 \qquad (4\text{-}4)$$

The above equation shows that for every BL of Ge deposited on the NW sidewall, 8BL were deposited on the sample surface. The ratio between the actual amounts of Ge deposited was even lower due to the low density of the NWs.

$$\frac{n_{Ge,NW}}{n_{Ge,surface}} = \frac{h_{NW}}{h_{nominal}} \frac{\pi D L}{\pi d^2} \ll 0.125 \qquad (4\text{-}5)$$

where D and L are the diameter and length of the Si NWs, d is the average distance between adjacent NWs. In order the make the result comparable with our previous data, the Si NWs (sample #031013C, hereinafter referred to as sample 4) were synthesized under the same growth conditions (550°C, 7ML Au). MBE Ge was deposited using a Knudsen effusion cell while maintaining a surface temperature of 220°C. Additionally a reference sample (#071013A) was grown which underwent the exact same procedures except for the amount of catalyst (0.9ML Au).

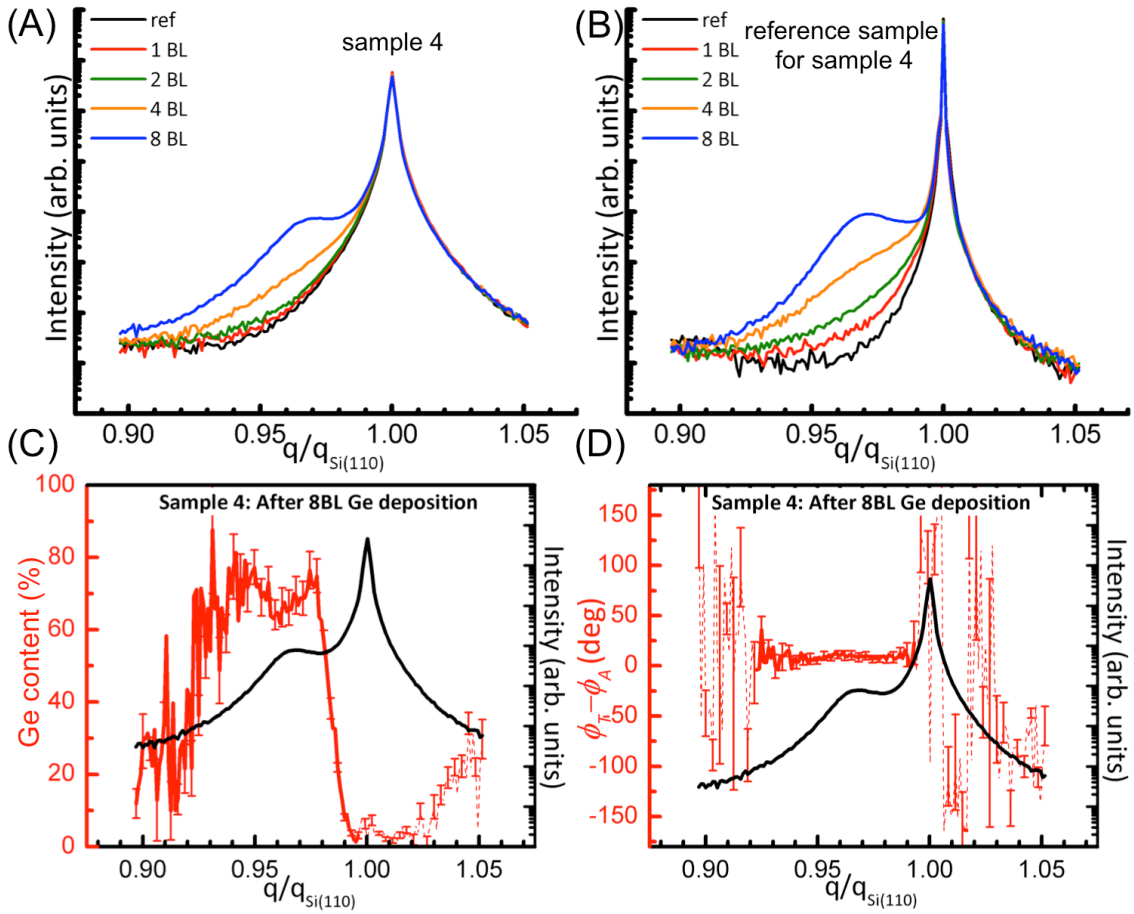

Figure 4-15: Results of radial scans around the $Si(110)_s$ peak on (A) sample 4 and (B) on its corresponding reference sample. (C) The calculated Ge content and phase difference between F_T and F_A after 8BL of Ge deposition on sample 4 using MAD data collected at 13 different energies. Only one in two error bars is shown for demonstration. Note that the amount of Ge deposition displayed is the nominal value.

Radial scans (Figure 4-15AB) show one single peak emerging from q/q_{Si} = 0.9714±0.0005 on both samples. The fact that intensity evolution was observed during the first 2BL of Ge deposition on the reference sample (red, green curves) and not on sample 4 can be simply understood as due to the large form factor of the Si NWs. The two graphs were otherwise similar to one another, which confirmed our early suspicion that the scattered intensity would be dominated by the surface Ge structures (rather than those on the NW sidewalls).

We have nevertheless performed MAD measurements on both samples. The calculated Ge content for sample 4 is shown in Figure 4-15C. The dominating compound in this case is $Si_{0.20}Ge_{0.80}$. Note that the result only applies to the MBE Ge islands formed at the sample surface.

4.3.Discussion

The most important conclusion from our study on the strain in Si-core/Ge-shell NWs is perhaps the fact that our Ge shell is not strained at all. This seems to be at variance with, for instance, the pioneering work of (Lauhon et al. 2002) in which they reported coherent strain along the axial direction and full relaxation in the radial direction. The disagreement can be understood by taking into account the difference in morphology between the two samples. The Ge shell in their case is a smooth 2D layer surrounding the core NW surface whereas the Ge shell in our case is rough and mainly composed of 3D islands. Indeed, theoretical calculation (Li & Yang 2014) indicates Frank-van der Merwe (FM) mode for shell growth on thinner NWs with diameter less than 50 nm (10-15nm in their case) and Stranski-Krastanov (SK) mode for the growth on thicker NWs with diameter larger than 100nm (~280nm in our case). The axial strain they

observed is essentially the misfit strain of the 2D wetting layer (Liang et al. 2005) while in our case this strain is effectively released by the formation of 3D islands (with defects).

To our knowledge, little is known regarding the SK growth on NW sidewalls, neither theoretically nor experimentally. Naively, one would expect to have a thicker wetting layer (consistent with our speculations) since part of the misfit strain can be readily released at the joints of the sawtooth facets and at the joints of adjacent sidewalls. Moreover, the critical size of the islands should be limited by various geometrical factors such as the side length of the NW cross-section and the width of the sub-facets (also in agreement with our analysis). Ge islands growth (GeH_4, 500°C) on Si NWs (D=100nm) has previously been studied by (Pan et al. 2005). While the authors were unable to measure the strain in their Ge shell, they did report Ge islands to grow preferably on the {111} facets, which further supports our interpretation of the tilted form factor observed in out-of-plane mappings. However, the 85% Ge content they deduced from their EDS analysis is significantly higher than our findings, which brings us to the second important conclusion of this study. At 220°C it seems that the shell forms a chemically sharp interface with the NWs and is composed solely of a homogeneous compound $Si_{0.25}Ge_{0.75}$. Other compositions only emerge as a result of intermixing either by annealing or by directly growing the sample at higher temperatures (290°C), the Ge shell meanwhile remains fully relaxed. This is particularly interesting since the above conclusion seems to apply exclusively to the Ge islands on the NW sidewalls. The SiGe alloys on the substrate are strained (not shown here) and possess in general a much larger lattice parameter (Figure 4-13A). As a matter of fact, similar results have previously been reported for the MBE growth of ~7ML of Ge at ~650°C on Si(001) substrates. By the use of two-wavelength (Schülli et al. 2003) and MAD (Katcho et al. 2011) measurements, both authors have concluded a Ge content of ~80% in their islands which also form a

chemically sharp interface with the underlying substrate. The major difference is that our Ge islands are fully relaxed while those in their case were found to be under compressive strain. We think that a great amount of strain was released in our case by the formation of defects. Indeed, growth at lower temperatures is known to produce Ge islands with poor crystalline quality and high defect density. Furthermore, by carefully comparing the FWHM of the rocking scans performed at different locations along the SiGe peak, (Schülli et al. 2003) found out that the measured "size" of the islands increased for increasing q values, leading to the conclusion that the peak shape is reflective of different lattice parameters found in different regions of their islands. We have also performed similar measurements on sample 1. The measured FWHM is the largest at the center of the SiGe1 peak and only slightly increases as we move further away. This again strengthened our belief that the peaks shape observed in Figure 4-2A is due to the form factor of the Ge islands and not actual variations in the lattice parameters. The only remaining question is, what mechanism was responsible for transporting the 25% Si up to the top of the Ge islands when surface diffusion was greatly limited by the low sample temperature?

Finally, our attempt to extend the current study to the MBE grown Ge shells was hindered by the huge interference from the surface Ge structures. As a matter of fact, the sample has to be constantly rotated in order to maintain a homogeneous shell layer, which significantly reduces the amount of Ge deposited on each sidewall. This got us thinking, what will happen if we simply don't rotate the sample? The answer will be revealed in the next chapter.

References:

Dayeh, S.A. et al., 2013. Direct Measurement of Coherency Limits for Strain Relaxation in Heteroepitaxial Core/Shell Nanowires. Nano letters, 13(5), pp.1869–1876.

Hu, M. et al., 2011. Significant reduction of thermal conductivity in Si/Ge core-shell nanowires. Nano letters, 11(2), pp.618–23.

Huang, S. & Yang, L., 2011. Strain engineering of band offsets in Si/Ge core-shell nanowires. Applied Physics Letters, 98(9), p.093114.

Katcho, N.A. et al., 2011. Composition and strain of Ge domes on Si(001) close to the dome/susbtrate interface. EPL (Europhysics Letters), 93(6), p.66004.

Lauhon, L.J. et al., 2002. Epitaxial core-shell and core-multishell nanowire heterostructures. Nature, 420(6911), pp.57–61.

Li, X. & Yang, G., 2014. Modification of Stranski-Krastanov growth on the surface of nanowires. Nanotechnology, 25(43), p.435605.

Liang, Y. et al., 2005. Critical thickness enhancement of epitaxial SiGe films grown on small structures. Journal of Applied Physics, 97(4), p.043519.

Migas, D.B. & Borisenko, V.E., 2007. Structural, electronic, and optical properties of ⟨001⟩-oriented SiGe nanowires. Physical Review B, 76(3), p.035440.

Musin, R.N. & Wang, X.-Q., 2006. Quantum size effect in core-shell structured silicon-germanium nanowires. Physical Review B, 74(16), p.165308.

Musin, R.N. & Wang, X.-Q., 2005. Structural and electronic properties of epitaxial core-shell nanowire heterostructures. Physical Review B, 71(15), p.155318.

Pan, L. et al., 2005. Stranski-Krastanow growth of germanium on silicon nanowires. Nano letters, 5(6), pp.1081–5.

Schülli, T.U. et al., 2003. Direct Determination of Strain and Composition Profiles in SiGe Islands by Anomalous X-Ray Diffraction at High Momentum Transfer. Physical Review Letters, 90(6), p.066105.

Voigtländer, B., 2001. Fundamental processes in Si/Si and Ge/Si epitaxy studied by scanning tunneling microscopy during growth. Surface Science Reports, 43(5–8), pp.127–254.

Yan, X. et al., 2011. Growth of InAs quantum dots on GaAs nanowires by metal organic chemical vapor deposition. Nano letters, 11(9), pp.3941–5.

[This Page Intentionally Left Blank]

5. IN SITU NANOWIRE BENDING

Despite the tremendous progress made over the past decade in nanoscience and in nanotechnology, characterization of the mechanical properties of NWs remains a challenge. Difficulties in manipulating such extremely small objects prohibit the application of most established test methods. For example, optical methods, commonly used for the curvature measurement of wafer/micro-cantilevers, are not readily applicable as the size of the nano-objects is often less than a visible wavelength. In most cases, mechanical properties such as Young's modulus E are determined using resonance analysis. With electron microscopy techniques such as TEM, direct and quantitative determination of the mechanical resonance is possible by applying an actuating signal between the nanostructure and the counter-electrode. Elastic beam theory is then employed to deduce E from the observed frequency (Nam et al. 2006). Alternatively, if the elastic properties are presumed known, mechanical response to a given stimulation can be studied. Such stimulations are induced, in most cases, by nano-manipulators, ranging from a simple AFM tip (Wu et al. 2005) to specially engineered devices (Agrawal et al. 2008). Again, classic elastic beam theory is employed to relate the magnitude of the deflection, measured predominantly by direct observations using electronic microscopies (Wang 2000), to the strain/stress applied on the NWs.

In this chapter, we present a new approach for the *in situ* study of strain/stress evolution during NW bending using solely X-ray diffraction techniques. The bending was induced by depositing a second material (Ge or Au) on one side of the (Si) NWs. For the strain/stress analysis, (Figure 5-1A) surface diffraction measurements were carried out for the as-grown NWs and after each step of Ge (Au) deposition. (Figure 5-1B) The strain, along the longitudinal and the transverse direction of the NWs, was obtained by analyzing the position shift of the displaced Bragg peaks whereas (Figure 5-1C) the total

stress applied on the NWs was deduced by fitting the NW curvature, retrieved from the integrated intensities of the displaced Bragg peaks, with a formula based on Euler-Bernoulli beam theory.

This chapter is organized as follows. Chapter 5.1 describes the procedures for sample preparation and the deposition geometry. Chapter 5.2 demonstrates in details the above mentioned analysis routine (dubbed the Displaced Bragg Method) with our experiment of Ge deposition on Si NW sidewalls at 220°C. Chapter 5.3 shows that a completely different scenario can be created by depositing Ge at RT. It will also introduce the so-called Stationary Method which allows us to follow in real time, though qualitatively, the entire bending process. Chapter 5.4 deals with the results of depositing Au on Si NW sidewalls at RT. Chapter 5.5 is reserved for discussions.

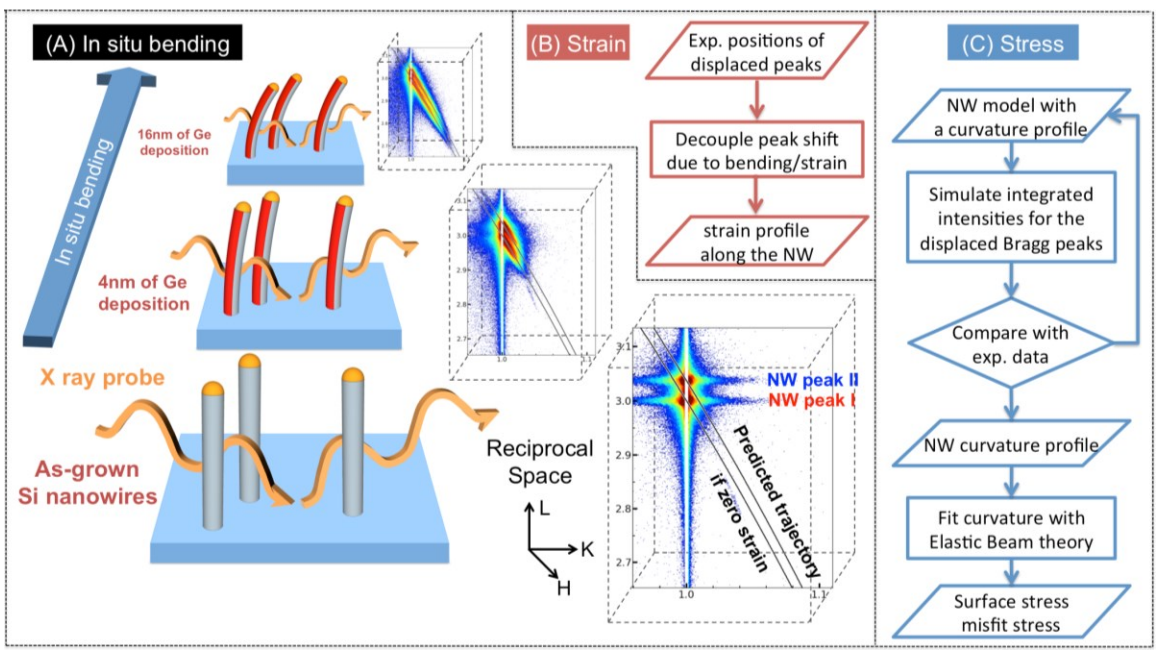

Figure 5-1: (A) Schematics of the bending experiment and process flow chart of the analysis routine used for retrieving (B) strain and (C) stress information from the diffraction data.

5.1. Experimental Setup

Si NW growth and subsequent bending experiments were carried out in the UHV chamber (base pressure, 2×10^{-11} mbar) attached to a Z-axis goniometer on the BM32 beamline at the European Synchrotron Radiation Facility. The size of the illuminated area was ~ 0.3mm×1mm. Subcritical incident angle was used to enhance the surface sensitivity. To facilitate surface diffraction experiments, Si(111) substrates with very low miscut angle were used. The miscut angle was determined experimentally with X-ray diffraction to be ~0.072°±0.003° along the $[10\bar{1}]_b$ direction. A modified Shiraki etch (Ishizaka 1986) was applied before transferring the samples into the UHV chamber, leaving a thin chemical oxide at the surface. The protective oxide layer was subsequently desorbed by a 5min flash at 830°C. Reflection High Energy Electron Diffraction (RHEED) measurements showed no trace of SiC and a nice (7×7) reconstructed surface.

The deposition of the metal catalyst (5ML or 1.18nm Au) was carried out on a "hot" substrate (T = 480°C > T_E), followed immediately by the injection of the precursor gas (0.9sccm Si_2H_6, 3.5×10^{-5} mbar). This effectively limited Ostwald ripening of the Au catalysts, allowing a very narrow size distribution to be achieved. The result was an array of 1700nm long, 70nm wide Si NWs with regular sawtooth faceting on the sidewall. For more details on the quality of the Si NWs grown with our setup, the reader is kindly referred to Chapter 2.

For the bending experiment, the samples were first brought to the desired temperature (220°C or RT). Stress was applied by depositing either Ge or Au on the NW sidewalls. Both the Ge and the Au source form an angle of η=21.43° with regard to the sample normal, resulting in a factor of 0.392 between the actual amount deposited on the sidewall of a straight $[111]_b$ NW and the nominal deposition value on the $(111)_b$ sample surface. Unless otherwise specified, the deposition amount mentioned in this work is the

nominal value, calibrated with a quartz crystal microbalance. During the deposition, the samples were oriented in a way that the in plane component of molecular beam is along the $[\bar{1}2\bar{1}]_b$ or $[010]_s$ direction (the subscript "s" denotes the coordinate system for surface diffraction), perpendicular to one of the hexagonal facets (Figure 5-2A).

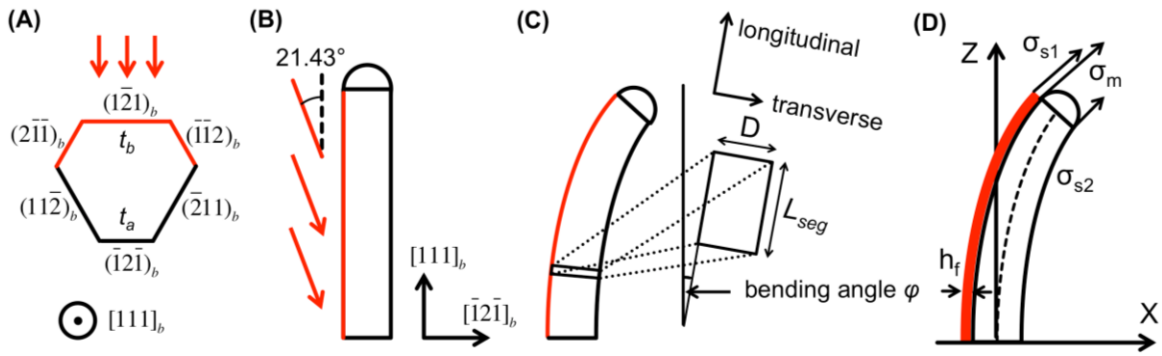

Figure 5-2 (A) Top view and (B) side view schematics of the bending experiment. Red arrows indicate the direction of the Ge (Au) deposition. Red facets are those exposed to the deposition. The longer side length of the trigonal hexagon is denoted t_b, the shorter one is denoted t_a with $t_a + t_b \sim 80nm$. The diameter D of the NW is defined as the distance between two opposing sidewalls with $D = \sqrt{3}/2 \times (t_a + t_b) \sim 70nm$. (C) The NW is modeled as a number of segments of length (longitudinal direction) L_{seg} and width (transverse direction) $D \sim 70nm$ with a regular hexagonal cross-section. Each segment is characterized by its bending angle φ which is the angle between the average crystallographic orientation of the segment and that of the Si substrate. (D) For a film of thickness h_f deposited on the sidewall, the NW is submitted to a combined force consisting of the surface stress on the Ge exposed sidewalls σ_{s1} and that on the non-exposed sidewalls σ_{s2}, as well as the misfit (interface) stress σ_m. The dashed line denotes the hypothesized location of the neutral surface.

5.2.Ge on Si NWs at 220°C

5.2.1. Strain: Peak Shift

A reciprocal space mapping (RSM) was performed in the vicinity of the Si $(13\bar{1})_b$ peak, for the as-grown NWs ("reference") and after each step of Ge deposition (total amount = 2nm, 4nm, 8nm, 16nm and 32nm respectively). The majority of the result presented below is extracted from these data. Additionally, line scans were performed on

the Si $(33\bar{3})_b$, $(\bar{3}33)_b$, $(3\bar{3}3)_b$, $(\bar{1}\bar{1}5)_b$, $(\bar{1}5\bar{1})_b$, $(5\bar{1}\bar{1})_b$ peaks. Like RSM, the line scans also measure the three-dimensional intensity distribution in the reciprocal space, thanks to the large acceptance of the 2D detector. These supplementary data were used to verify that our observations were consistent for different values of moment transfer, to estimate the mosaicity of the NWs, and to correct the intrinsic miscut of our sample. The sample temperature was maintained at 220°C during the entire process.

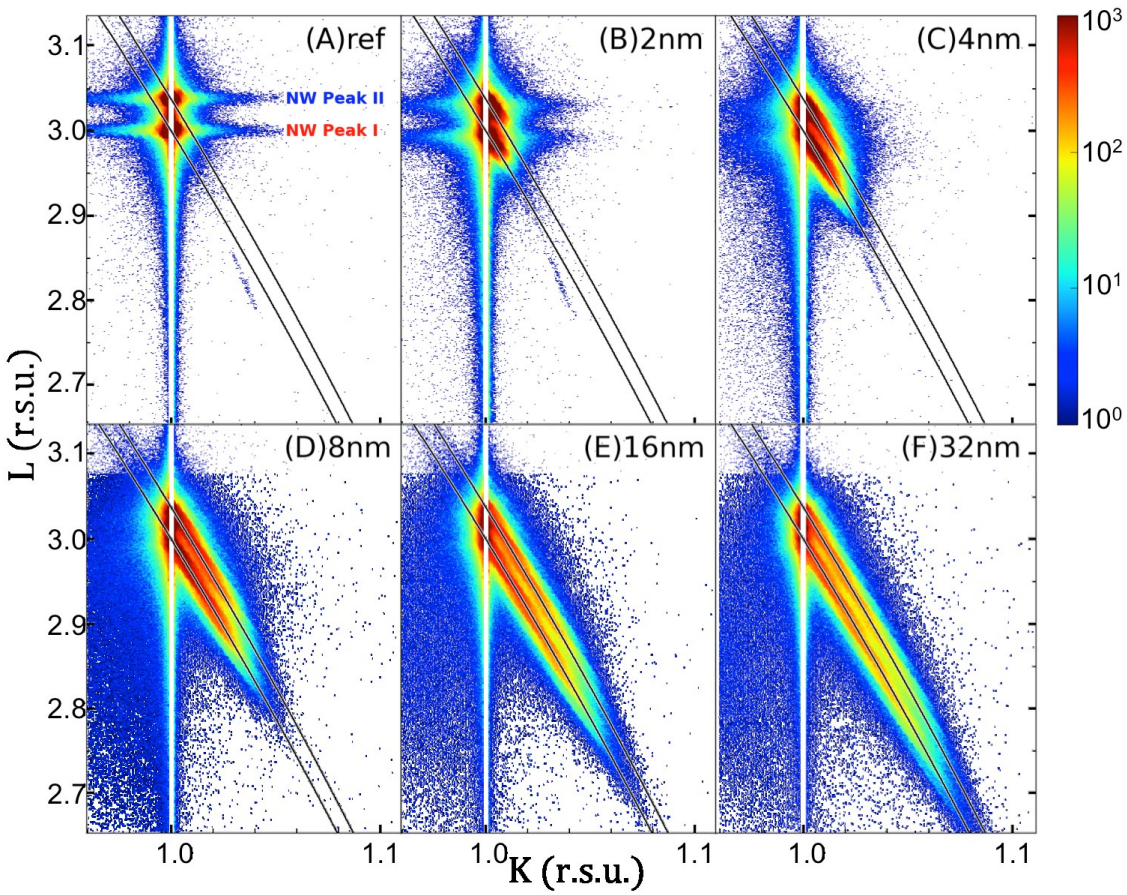

Figure 5-3: KL plane intensity distribution in the vicinity of the $(13\bar{1})_b$ or $(113)_s$ Si peak for as-grown NWs and for NWs with 2, 4, 8, 16, 32nm of Ge deposition at 220°C, respectively. The black lines illustrate the estimated positions of displaced Bragg peaks expected for NW segments with zero total strain.

(Figure 5-3A) For the as-grown Si NWs, the intensity distribution near the $(13\bar{1})_b$ or $(113)_s$ peak is characterized by a double NW peak originated from the DWBA effect (Vineyard 1982; Rauscher et al. 1995), one (hereinafter called NW peak I) centered at L=3 and the other (hereinafter called NW peak II) centered at L=3.0365 for incident angle = 0.125° ($\alpha_c = 0.162°$, $E = 11043\ eV$). The two peaks were identical, both with scattering streaks from the NW sidewalls, having an in plane FWHM of $\Delta Q_{ip} = 0.064 \pm 0.001\ nm^{-1}$, with the exception that the intensity of peak II was attenuated by a factor of ~1.25 due to surface roughness. The $(113)_s$ Bragg peak of the substrate was also shifted to L=3.0181 due to refraction at grazing incidence (Feidenhans'l 1989).

To study the strain distribution in the NWs bent by Ge deposition, we now consider the NWs to be composed of a number of segments, each with a reasonable length L_{seg} and a bending angle φ (Figure 5-2C). If the total amount of strain is found to be zero for a given segment, then the situation can be assimilated to that of a fully relaxed Si nanocrystal. Of course the peak will be stretched due to variations in the lattice constant within the segment (nanocrystal), but the position of its peak center can be very well predicted. A fully relaxed nanocrystal rotated by φ will have its Bragg peak displaced in the plane of rotation (also called the principal plane of bending) spanned by the surface normal $[001]_s$ and the bending direction. Naturally we would expect the latter to be along the $[\bar{1}2\bar{1}]_b$ or $[010]_s$ direction given that this is where the in plane component of the combined force lies (Figure 5-2D). We shall defer the verification of the bending direction until later in this chapter and proceed to showing the evolution of the diffracted intensities in the presumed principal plane of bending (*i.e.*, the KL plane).

Figure 5-3 shows the KL plane intensity distribution in the vicinity of the $(13\bar{1})_b$ or $(113)_s$ Si peak before and after Ge depositions. In general, the further away a peak is from its original Bragg position, the larger the bending angle is of the corresponding

segments. Figure 5-3 hence depicts a scenario where the NWs became more and more "bent" with increasing amount of Ge deposition on their sidewalls. It also appears that the trace of the displaced NW peaks (I and II) lies exactly on the calculated trajectory (black curves) for segments with zero total strain. If however a segment is submitted to tensile (compressive) strain, in the longitudinal direction and/or in the transverse direction, the center of the displaced peak shall be found to the left (right) of the zero-strain curve.

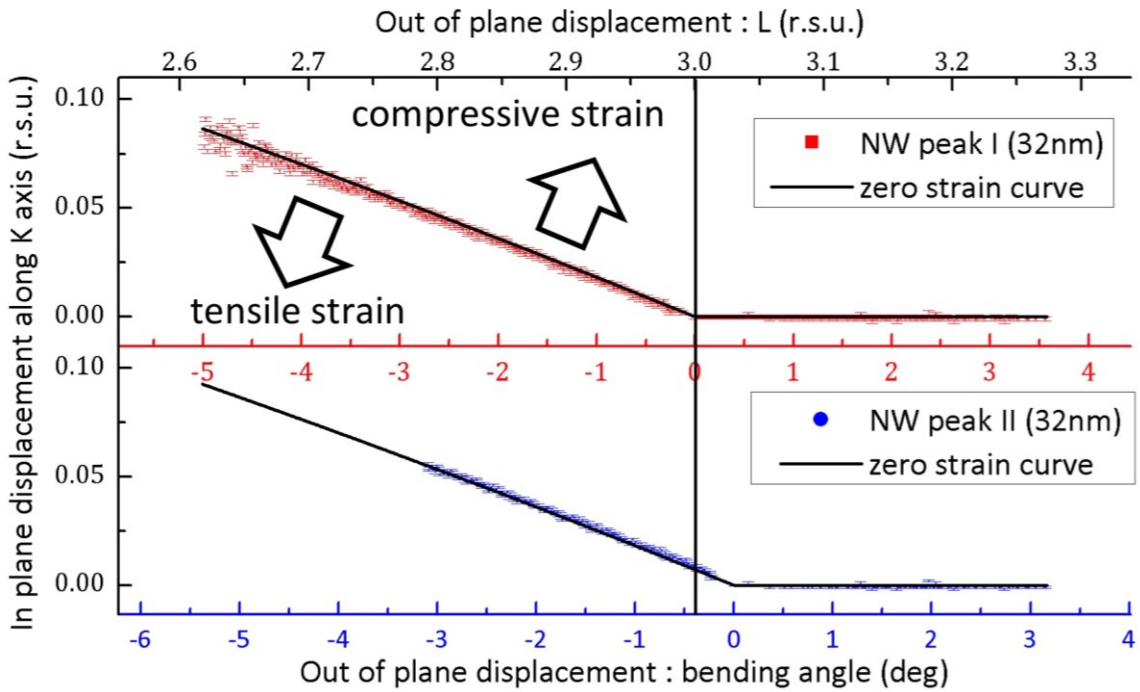

Figure 5-4: Relative displacement in K-coordinates, of the displaced NW peaks I (red square) and II (blue circle), as a function of the bending angle or of the L-coordinates, after 32nm of Ge deposition at 220°C. The error bar here is ± 0.001 in reciprocal space units, given by the size of a detector pixel in the reciprocal space. Also shown are the estimated displacements for rotated fully relaxed nanocrystals (black line).

More precise evaluation of the strain profile requires tracking the positions (K-coordinates) of the displaced peaks at different L values. The result is shown in Figure 5-4 for NWs with 32nm of Ge deposition. The displacements of these peaks lie exactly

on those predicted for rotated fully relaxed nanocrystals (black lines), indicating a zero total strain inside the bent NWs. For 32nm of deposition, we found the presence of segments with a bending angle of as large as −5.00° by tracking the position of the displaced NW peaks I. In theory the same can be achieved by tracking the position of the displaced NW peaks II although in reality the peaks beyond φ=−3.09° were simply too weak for their centers to be correctly located. Finally, it is worth pointing out that a displaced NW peak I does not contain the same information as a displaced NW peak II found at the same L value. For instance, the displaced NW peak I found at L=3.0 corresponds to a rotated fully relaxed nanocrystal with φ=0.000° whereas the displaced NW peak II found at the same L value corresponds to a rotated fully relaxed nanocrystal with φ=−0.393° (vertical line, Figure 5-4).

We shall now repeat the same procedure for data with 2nm, 4nm, 8nm and 16nm of Ge deposition, respectively. (Figure 5-5) In general, the largest bending angle found with the position tracking process (black arrow) increases with increasing amount of Ge deposition but the total strain inside the NWs remained zero during the entire bending process. The direct implication of the result is that the neutral surface is located in the middle of a NW (*i.e.* with equal distance to the concave and convex surface) and that the tensile strain near the convex side of the bent NW counteracts the compressive strain near the concave side.

We have thus found ourselves in a unique situation where the total strain is always zero inside the NWs. It is worth mentioning that the described method is equally capable of determining the values of non-zero strain should that be the case. If the trace of the displaced peaks is found above (below) that predicted for rotated fully relaxed nanocrystals, then the corresponding NW segments are under compressive (tensile)

strain. To further determine whether the strain is along the longitudinal direction or along the transverse one, it suffices to perform measurements at two or more moment transfers.

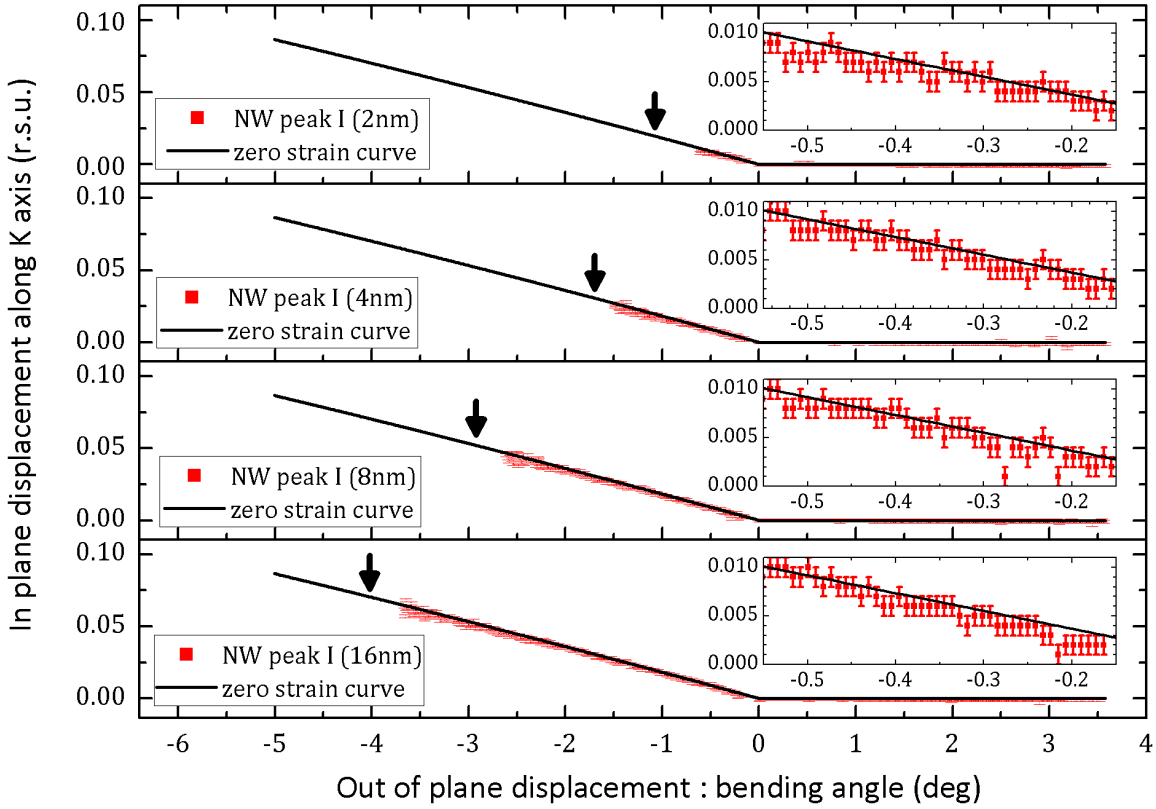

Figure 5-5: Relative displacement in K-coordinates of the displaced NW peaks I (red square) as a function of the bending angle, for NWs with 2nm, 4nm, 8nm and 16nm of Ge deposition at 220°C, respectively. The error bar here is ± 0.001 in reciprocal space units, given by the size of a detector pixel in the reciprocal space. Also shown are the estimated displacements for rotated fully relaxed nanocrystals (black line). The black arrows indicate the positions of the displaced peaks with the largest bending angle that we could detect in each case, despite their peak centers being too weak to be precisely located. Insets: zoom in areas of the results between φ=−0.15° and φ=−0.55°.

So far we have presumed the bending direction to be along the $[\bar{1}2\bar{1}]_b$ or $[010]_s$ direction. This can be confirmed by looking at the intensity distribution in the HK plane at different L values. With 32nm of Ge deposition and at L=3, (Figure 5-6A) the non-displaced NW peak I (φ=0°) of the $(113)_s$ reflection overlaps the substrate Bragg rod at H=1 K=1. The non-displaced NW peak II (φ=0°) is centered at L=3.0365 as mentioned

earlier, and thus would not show up in the figure. The peak centered at H=1 K=1.00915 is in fact a displaced NW peak II corresponding to segments with a bending angle of φ=−0.393°. At lower L values (L=2.9, Figure 5-6B), we would also expect to find a displaced NW peak I away from its non-displaced position (H=1 K=1). The observed displaced NW peak I (H=1 K=1.02414) is the result of scattering by segments with φ=−1.338° whereas the observed displaced NW peak II (H=1 K=1.03285) is the result of scattering by segments with φ=−1.725°. Both peaks were shifted purely along the K axis with no additional displacement along the H axis, hence confirming that the NWs were indeed bent towards the $[010]_s$ or $[\bar{1}2\bar{1}]_b$ direction. The asymmetry of the NW peaks is due to increased mosaic spread of the NWs (and hence not to an actual variation in the lattice parameter), as was confirmed by measurements at different moment transfers. The mosaicity was not observed until after a large amount of Ge was deposited and was found to be 0.10±0.02° (0.05±0.01°) for 32nm (16nm) of Ge deposition, respectively.

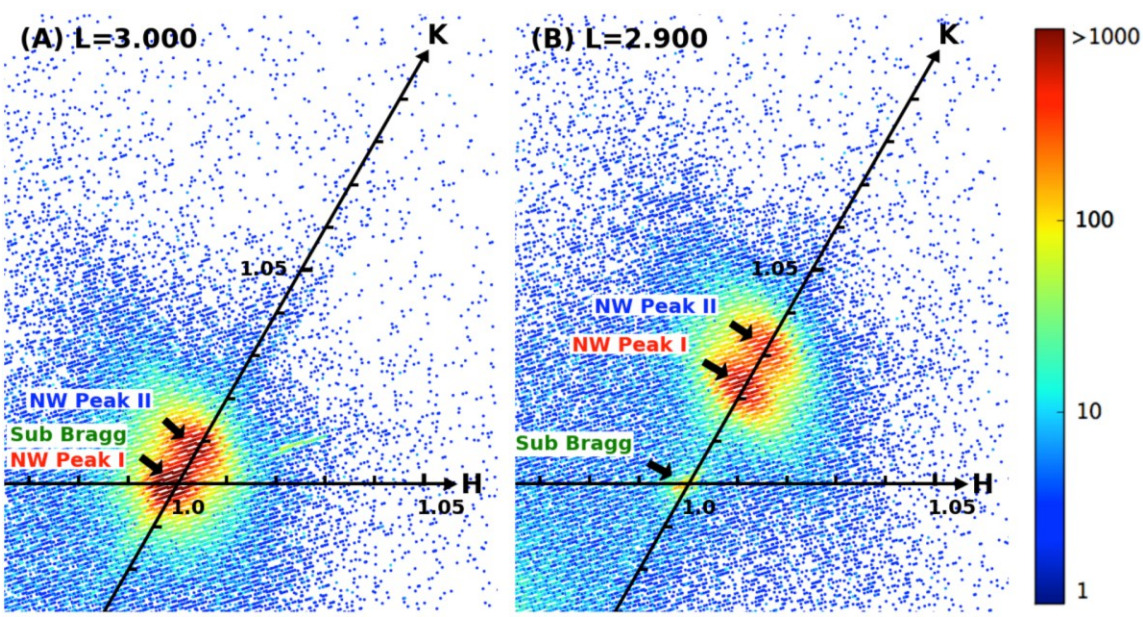

Figure 5-6: HK plane intensity distribution near the $(13\bar{1})_b$ or $(113)_s$ Si Bragg peak at L = 3.0 (A) and at L = 2.9 (B) after 32nm of Ge deposition at 220°C.

5.2.2. CURVATURE: INTEGRATED INTENSITIES

The peak position tracking only provides information on the strain and the maximum bending angle of the NWs. To reconstruct their exact shape, we first recall our early model, which reduces the calculation of the diffracted intensity of a bent NW to that of a number of rotated segments. The segment length L_{seg}, chosen to be 0.9395nm, is equal to the height of a Si unit cell at 220°C along the surface normal. The NW is thus divided into 1809 segments, with its first segment (n=1) located at the sample surface (Z=0). A bending angle was then assigned to each individual segment. A monotonic function of the angle distribution was presumed, $|\varphi_m| \leq |\varphi_n|$ for $m < n$. The diffracted intensities from different segments are added coherently if the distance between the two segments along the longitudinal direction is smaller than the coherence length L_c and incoherently if otherwise.

$$\sum_{m=1}^{N_c}\sum_{n=1}^{N_c}|F_n\overline{F_m}|\cdot\frac{\sqrt{4\ln(2)}}{N_c\sqrt{\pi}}\exp\left(\frac{-4\ln(2)\cdot(m-n)^2}{N_c^2}\right) \qquad (5\text{-}1)$$

where N_c is the number of segments found within a coherence length with $N_c = 1700nm\ /\ L_c$, $1700nm$ being the length of the NWs. The shape of the interference function (Gaussian) as well as the value of L_c (85.95 nm) were deduced by fitting the NW peaks I and II of as-grown NWs (*i.e.* with no Ge deposition). The latter is close to the transverse coherence length of the incident beam (1mrad) in the measuring direction, indicating that the coherence length is dominated by beamline characteristics (insusceptible to sample conditions) rather than by NW domain size (might change with Ge deposition). Equation (5-1) is thus applicable to all cases concerned in this chapter. F_n is the form factor of the nth segment projected onto the principal plane of bending, bar denotes complex conjugate, with

$$F_n(q_z) = L_{seg}\cdot\mathrm{sinc}\left(\frac{q_z - q_{z_0}\cos\varphi}{2\pi\cos\varphi}\cdot L_{seg}\right)\cdot\exp\left(jZ_n\frac{q_z - q_{z_0}\cos\varphi}{\cos\varphi}\right) \qquad (5\text{-}2)$$

Z_n is the coordinate of the nth segment along the Z-axis (Figure 5-2D), q_{z_0} is the out of plane moment transfer of the non-displaced peak. A Monte Carlo approach was applied next to simulate a certain level of inhomogeneity amongst the NWs. Each segment of a given NW was allowed to have a limited degree of freedom ($\varphi_n' \in [\varphi_n - 0.027°, \varphi_n + 0.027°]$), and the intensities from different NWs were added incoherently. The result was compared to the integrated intensities obtained from the experimental data, based on which an adjustment was then made to the NW shape. The above procedures were repeated till a good agreement was reached, the quality of which is shown in Figure 5-7. In Figure 5-8A, we present the deflection of the neutral surface (where there is no extension or compression, Figure 5-2D) in the principal plane of bending calculated with our best-fit results. The shape of the NW after 32nm of Ge deposition agrees well with what was observed with *ex situ* SEM (Figure 5-8C).

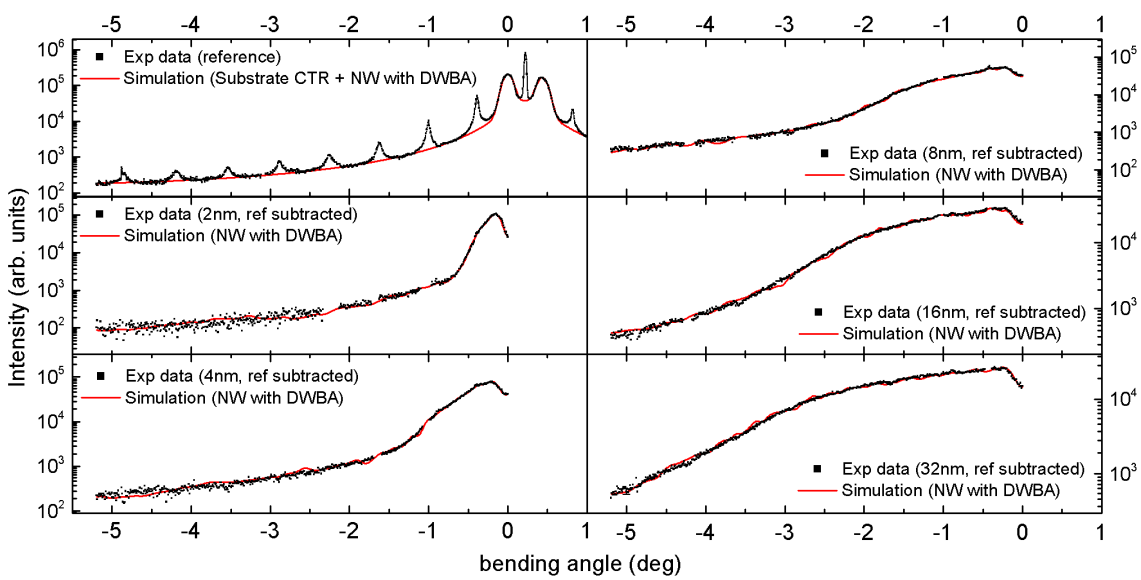

Figure 5-7: Comparison between the experimental integrated intensities (black squares) of the displaced Bragg peaks and the simulated integrated intensities (red lines) of our best-fit results for the bending of Si NWs by Ge deposition at 220°C. The periodic peaks that appeared in the reference figure are artifacts due to repeated interceptions of some pixels with the substrate Bragg rod, and were removed during reference subtraction. Only data of interest ($\varphi \leq 0$) is presented here for clarity.

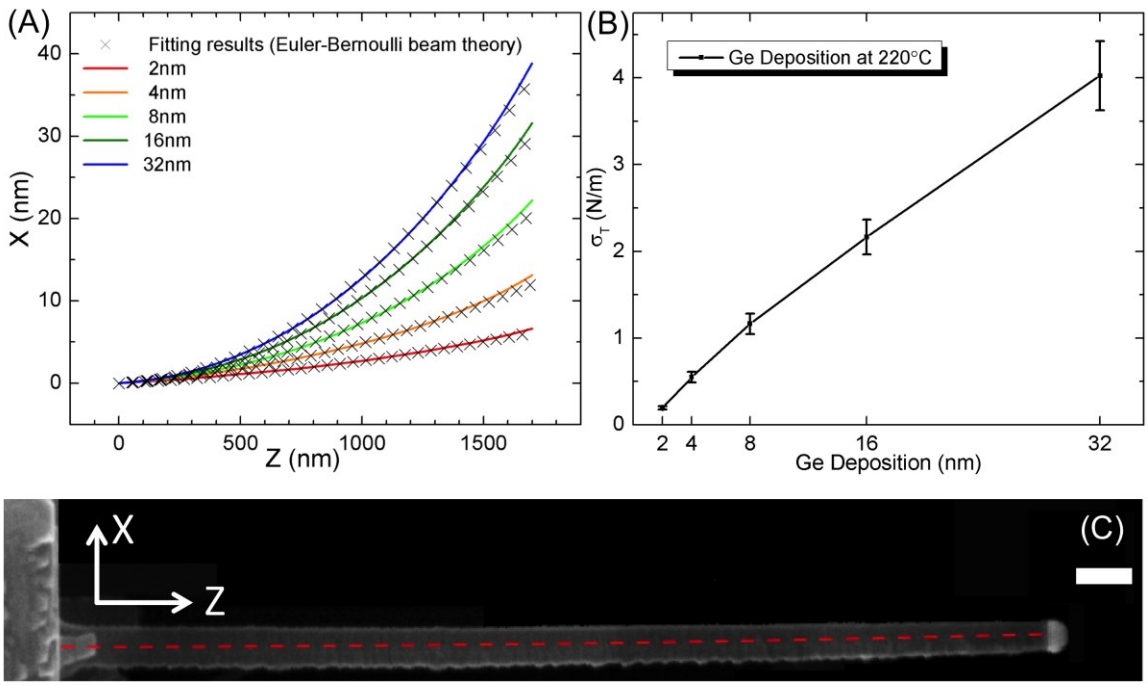

Figure 5-8: (A) Reconstructed NW shape based on integrated intensities of the displaced Bragg peaks. In the figure is shown the deflection of the neutral surface X as a function of Z in the principle plane of bending for Si NWs with 2, 4, 8, 16, 32nm of Ge deposition respectively. The black crosses are best-fit results using Euler-Bernoulli beam theory for a tapered NW. (B) The extracted total stress as a function of Ge deposition at 220°C. (C) Side view of a tapered Si NW after 32nm of Ge deposition at 220°C. Scale bar: 100nm. The viewing direction is perpendicular to the principal plane of bending. The red dashed line denotes the deflection of the neutral surface calculated with our best-fit results.

5.2.3. STRESS: CURVATURE

To go one step further, we proceed to fit our result with a theoretical model based on Euler-Bernoulli beam theory (Landau & Lifshitz 1986). The NW is modeled as a rod with one free end (Z=L) and one fixed end (Z=0) attached to the substrate. For a Ge film with thickness h_f deposited on the $(1\bar{2}1)_b$ sidewall, the NW is submitted to a combination of forces consisting of the surface stress applied on the Ge exposed sidewalls σ_{s1} (in N/m) and that applied on the non-exposed sidewalls σ_{s2} (in N/m), as well as the misfit (interface) stress σ_m (in N/m^2). If we take into account the hexagonal cross-section of the NW, the total stress σ_T (in N/m) can be written as

$$-\sigma_T = \sigma_s + \frac{3}{4} h_f \sigma_m \qquad (5\text{-}3)$$

where $\sigma_s = \sigma_{s1} - \sigma_{s2}$ is the effective surface stress. The factor 3/4 is to account for the larger film thickness on the $(1\bar{2}1)_b$ sidewall than on the $(2\bar{1}\bar{1})_b$ and $(\bar{1}\bar{1}2)_b$ sidewalls (Figure 5-2A). The negative sign before σ_T stems from the fact that the total stress is applied on one side of the NW whereas σ_{s1} and σ_m are intrinsic stress in the film. From *ex situ* SEM observations we know that the equation of equilibrium in small deflection regime (*i.e.* the deflection $\Delta X \ll L$ for $Z=L$) holds true even for 32nm of deposition, hence

$$-EIX'' = M = \sqrt{3} t^2 \sigma_T \qquad (5\text{-}4)$$

where $t = (t_a + t_b)/2$ is the side length of an equivalent regular hexagon. E and I are Young's modulus and area moment of inertia of the NW. Here we consider the case of a regular hexagon instead of a trigonal one for simplicity, as it can be easily demonstrated (*c.f.* Appendix II) that the area moment of inertia of a trigonal hexagon is close to (~0.25% difference) that of a regular one even for $t_b = 2t_a$. Finally, the increase in stiffness due to Ge deposition should be taken into account.

$$EI = E_{Si}(1 - \upsilon_{Si}^2) I_{Si} + E_{Ge}(1 - \upsilon_{Ge}^2) I_{Ge} \qquad (5\text{-}5)$$

E_{Si} = 187.5 GPa, ν_{Si} = 0.18125, E_{Ge} = 155.1 GPa, ν_{Ge} = 0.15564 are values for a $[111]_b$ orientated NW computed using the parameters found in the literature (Wortman & Evans 1965; Brantley 1973). Detailed calculation of the area moment of inertia for NWs with Ge deposition can be found in Appendix II.

Solving Equation (5-5) would result in something similar to Stoney's formula (Stoney 1909; Berry 1988) which assumes a constant curvature κ for the entire NW.

However, the experimental integrated intensity as a function of the bending angle (Figure 5-7) strongly suggests that κ increases monotonically from the fixed end (Z=0) to the free end (Z=L). This can be explained by taking into account the slight tapering of the NWs, which is caused by radial growth (Oehler et al. 2010) on the NW sidewalls due to catalyst diffusion (Hannon et al. 2006; den Hertog et al. 2008). In short, segments near the bottom of the NWs were submitted to longer disilane exposure (larger diameter due to heavier radial growth) as compared to the newly formed segments near the top of the NWs. It is thus reasonable to assume that the side length varies linearly as a function of Z.

$$t(Z) = t_0 - \frac{Z}{L}(t_0 - t_L) \qquad (5\text{-}6)$$

t_0 = 40nm is the side length at the fixed end. t_L = 32nm is the side length at the free end. Both values were extracted from *ex situ* SEM observations (Figure 5-8C) by averaging over 50 NWs. With the side length t now dependent on Z, analytical solution of Equation (5-4) becomes cumbersome. In Appendix II we listed a number of analytical solutions that can be used when the required conditions are met. Fitting the solutions with the reconstructed NW shape allowed us to determinate the total stress σ_T (Figure 5-8B). The best-fit results are shown in Figure 5-8A (black crosses) for comparison. σ_T in this case is found to vary almost linearly with h_f, which indicates the bending by Ge deposition at 220°C to be mainly driven by the misfit stress. The slight deviation from a perfect linear relationship is due to changes in both the surface stress and the interface stress with increasing Ge film thickness. While it is impossible to isolate the relatively small (negligible for large h_f) surface stress, we were able to estimate the value of the dominating misfit stress to be −0.46±0.03 GPa (the negative sign denotes compression in the film), which in turn corresponds to an average misfit value of −0.25±0.016%.

Even by taking into account the tapering of the NWs, we still under-estimate the curvature close to the tip of the NW, probably due to the limitations of our linear elastic model. It is worth mentioning that fitting the reconstructed NW tip deflection directly with Stoney's formula (*i.e.* considering t to be independent of Z) would cause an over-estimation of σ_T of 25%~30% in this case.

5.3. Ge on Si NWs at RT

5.3.1. The Stationary Method

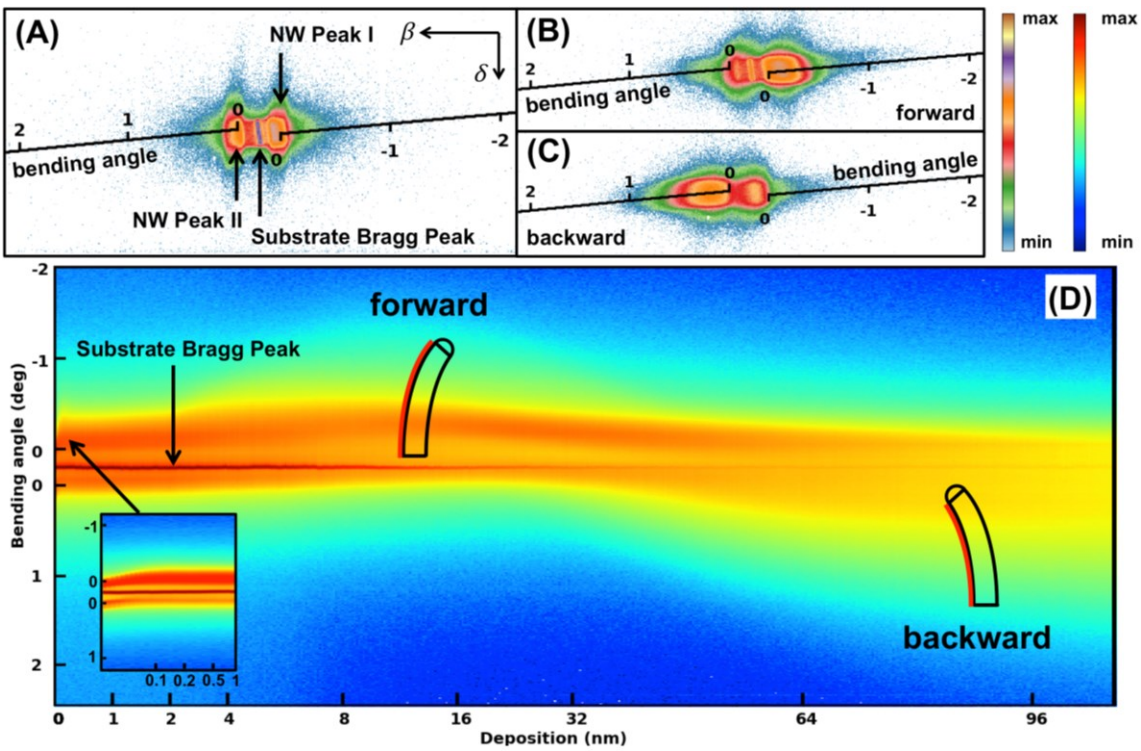

Figure 5-9: Stationary images taken with the 2D detector centered at the $(22\bar{4})_b$ substrate Bragg peak, for (A) the as-grown NWs, for (B) forward bent NWs with 8nm of Ge deposition at RT and for (C) backward bent NWs with 96nm of Ge deposition at RT, respectively. (D) Data assembled from stationary images taken during the entire deposition process showing that the NWs were bent forth and back with increasing amount of Ge deposition. (inset) Zoomed-in view of the swift bending of the NWs with less than 0.1 nm of Ge deposition. The irregular intervals on the abscissa is due to changes in the deposition amount per image acquisition (to 2×, 4×, 8× of the initial value) occurred at 2, 8, 16nm of deposition, respectively.

The Displaced Bragg Method (peak position tracking and intensity simulation) is ideal for the precise determination of the strain and stress in the NWs. However, the duration of the measurements required for such method (RSM or multiple line scans) makes it too time consuming to be applied regularly during the bending process. To follow in real time the bending of the NWs, we employ the so called Stationary Method which consists of continuously taking images at a fixed position in the vicinity of a Bragg peak with the 2D detector during Ge deposition (or any other means that would bend the NWs). Some peaks are better suited for the measurement, allowing for detection of segments with larger bending angle, some are not, but the principle is the same. At a fixed detector position, only few (very often only one) peak center(s) of the displaced NW peaks can intersect the Ewald's sphere at the same time. However, intensity spread of the displaced peaks may still be detected by the 2D detector thanks to their large peak breadth broadened by their large form factor (small objects). This is illustrated in Figure 5-9 for the RT deposition of Ge on one side of the Si NWs. The deposition geometry was the same as in the previous case. For the as-grown NWs, (Figure 5-9A) the detector was centered at the substrate $(22\bar{4})_b$ Bragg position, but was also able to measure the intensity spread of both NW peaks I and II. Again the pixel positions at which the displaced Bragg peaks intersect the detector (black line, Figure 5-9A) can be calculated for rotated fully relaxed nanocrystals with a bending angle φ. (Figure 5-9BC) Increasing level of intensities would be detected at lower (higher) β values if the NWs were bent forward towards the $[\bar{1}2\bar{1}]_b$ direction (backward towards the $[1\bar{2}1]_b$ direction). Images taken during the deposition were then assembled together by adding up the intensities of the pixels corresponding to the same bending angle. The result is shown in Figure 5-9D. For Ge deposition at RT, the Si NWs were quickly bent forward for ~ 0.12nm of deposition. The curvature of the NWs then gradually increased until it reached its maximum at

~9.68nm of deposition. For Ge deposition beyond this value, the NWs started to be bent backward. A summary of the different bending scenarios can be found in Table 5-2.

5.3.2. Strain and Stress

The stationary method only provides qualitative information on the evolution of the bending process, as with a fixed detector we are able to measure neither the peak intensity nor the integrated intensity of the displaced Bragg peaks. However, the result can serve as a general guideline for determining when and whether to pause the deposition and to launch the lengthy measurements required for quantitative analysis using the Displaced Bragg Method.

Peak position tracking and intensity simulation (Figure 5-10) were carried out for Si NWs with 1, 2, 4, 8, 16, 32 and 64nm of Ge deposition at RT. The trace of the displaced Bragg peaks lies exactly on the predicted positions for segments with zero total strain, as in the previous case. However, (Figure 5-11A) the deflection in this case was found to be much smaller (tip deflection $\Delta X \sim 3.54$nm at RT compared to $\Delta X \sim 22.18$ nm at 220°C for 8nm of Ge deposition). The fitted value of σ_T was small as a result and even changed sign in the later stage of the deposition. This implies that the bending by Ge deposition at RT is mainly driven by the surface stress. The initial compressive stress in the film is probably due to the atomic size effect (R. D. Meade & Vanderbilt 1989) or due to changes in surface reconstruction, as a result of some surface Si atoms (or H atoms) being replaced by the larger Ge atoms. The later change of sign in the effective surface stress (from compressive to tensile) can be understood as due to the 3D growth of Ge islands at larger film thickness. Indeed, the coalescence between adjacent Ge islands to form grain boundaries with lower surface free energy (Hoffman 1976) should induce a compressive stress on the Ge exposed sidewalls (tensile stress in the film), making them the concave side of the bent NWs.

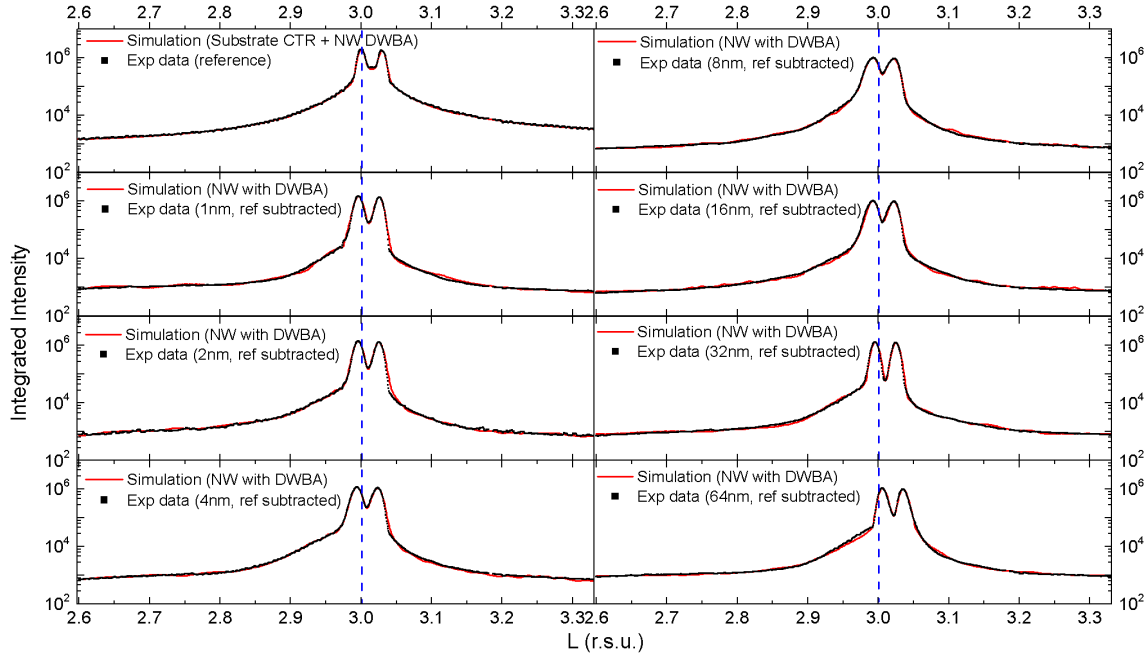

Figure 5-10: Comparison between the experimental integrated intensities (black squares) of the displaced Bragg peaks and the simulated integrated intensities (red lines) of our best-fit results for the bending of Si NWs by Ge deposition at RT. A blue dashed line is added at L=3.0 to aid the eye. Note that the simulation reproduced the integrated intensities of both the displaced NW peaks I and II.

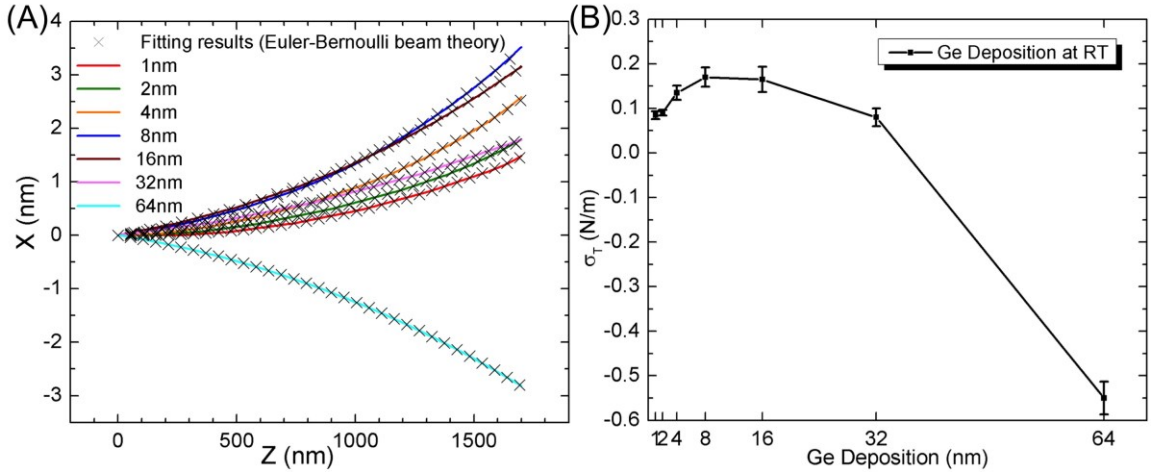

Figure 5-11: (A) Reconstructed NW shape based on the integrated intensities of the displaced Bragg peaks. In the figure is shown the deflection of the neutral surface *X* as a function of *Z* in the principle plane of bending for Si NWs with 1, 2, 4, 8, 16, 32 and 64nm of Ge deposition respectively. The black crosses are best-fit results using Euler-Bernoulli beam theory for a tapered NW. (B) The extracted total stress as a function of Ge deposition at RT.

5.4. Au on Si NWs at RT

Au was used as a replacement for Ge to bend the NWs as it was readily available in our growth chamber. Epitaxial growth of Au on Si is radically different from what was described in the previous cases, as the large bulk lattice mismatch, *e.g.* 33% for Au(111) on Si(111), should place the metal film growth in Volmer-Weber growth regime, possibly accompanied by a regular network of edge dislocations with an interface registry of 3 Si atoms to 4 Au atoms. Bending experiments with Au were carried out at RT to limit gold diffusion and to avoid the formation of AuSi liquid alloy above the eutectic point.

5.4.1. Au on Si NWs at RT

For the bending experiment with Au deposition on Si NW sidewalls at RT, we have kept the same growth condition and the same bending geometry as in the previous cases. The Si NWs were 1700nm long, 70nm wide with regular sawtooth faceting. The in plane component of the molecular beam was along the $[\bar{1}2\bar{1}]_b$ or $[010]_s$ direction.

(Figure 5-12) Data assembled from stationary measurements indicates, to our surprise, that the total stress changed its sign not once but twice (*i.e.* from tensile to compressive then back to tensile) during the entire bending process. Quantitative measurements were carried out at different stages of Au deposition (specified by the arrows on top of Figure 5-12) to allow for peak position tracking and intensity simulation. The NWs were initially bent forward and started to be bent backward after only ~0.10nm of Au deposition (nominal value). This value is about ~100 times smaller than that found in the case of Ge deposition at RT (~9.68nm). The huge difference can be explained by the earlier formation of 3D islands in the case of Au growth (Volmer-Weber) than that of Ge growth (Stranski-Krastanov). The compressive stress that caused the NWs to be bent backward (tensile stress in the film) was induced by the coalescence between adjacent islands, as in the previous case. The NWs were later bent forward again

for Au deposition >2.74nm. The much slower bending process (Au deposition 2.74-18.053nm) compared to the previous one (Au deposition 0.10-2.74nm) is attributed to the increasing stiffness of the NWs with thicker Au deposition. This final change of sign in the surface stress (from tensile back to compressive) was explained by (Spaepen 2000) as due to the incorporation of extra atoms between adjacent ledges and was commonly observed for thin film depositions of high-mobility materials (Cu, Ag, etc.) at RT.

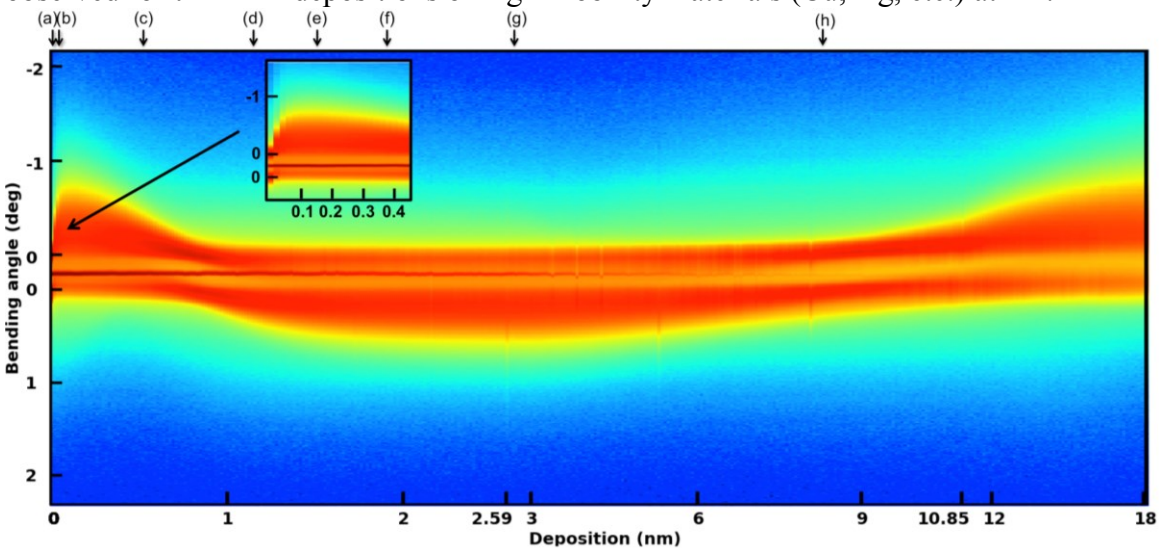

Figure 5-12: Data assembled from stationary images taken during the entire deposition process showing that the NWs were bent forth and back and then forth again with increasing amount of Au deposition at RT. (inset) Zoomed-in view of the initial forward bending of the NWs for less than 0.1 nm of Au deposition. The irregular intervals on the abscissa is due to changes in the deposition amount per acquisition (3×, 6× of the initial value) occurred at 2.59, 10.85 of deposition, respectively. Au deposition was paused to perform quantitative measurements at points indicated by the arrows on top of the figure.

Once again, zero total strain was found for the entire NWs as the trace of the displaced Bragg peaks lies exactly on the predicted positions for rotated fully relaxed nanocrystals. The reconstructed NW shape at different stages of Au deposition is shown in Figure 5-13A. The fitted value of total stress (Figure 5-13B) is of the same order of magnitude as what was found for Ge on Si NWs at RT, which confirms that the bending

process of Au on Si NW at RT is mainly driven by the surface stress. Figure 5-14 shows *ex situ* SEM images of this sample after 50nm of deposition.

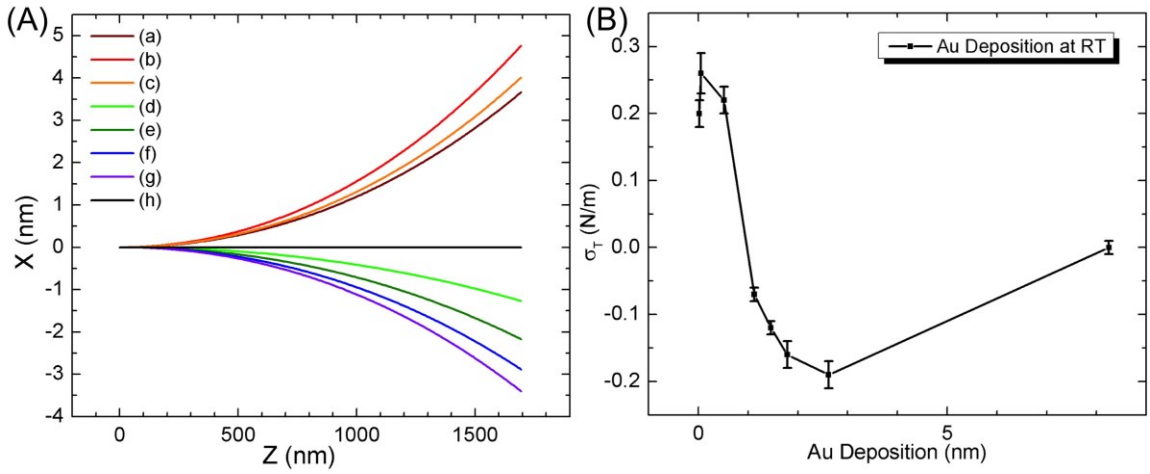

Figure 5-13: (A) Reconstructed NW shape based on integrated intensities of the displaced Bragg peaks. In the figure is shown the deflection of the neutral surface *X* as a function of *Z* in the principle plane of bending, for Si NWs with Au deposition amount indicated in Figure 5-12. (B) The extracted total stress as a function of Au deposition at RT.

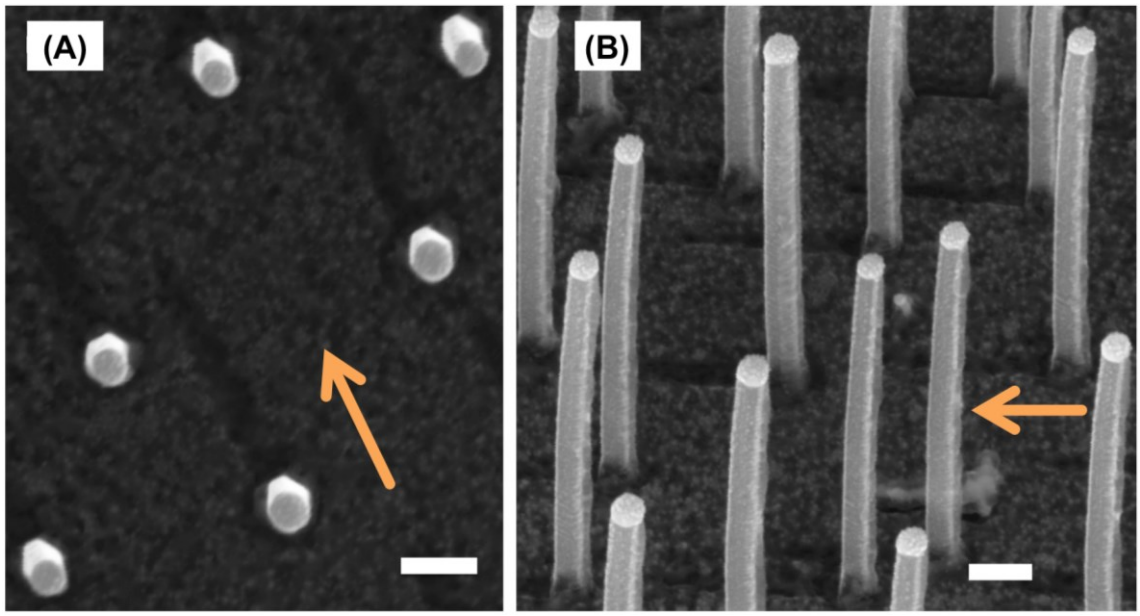

Figure 5-14: (A) Top view and (B) 40° perspective view of the Si NWs after 50nm of Au deposition at RT. The Au film on the NW sidewalls as well as the shaded areas on the sample surface can be clearly observed. The scale bar is 200nm. The orange arrow denotes the in plane component of the Au deposition.

5.4.2. SIDEWALL CONFIGURATION

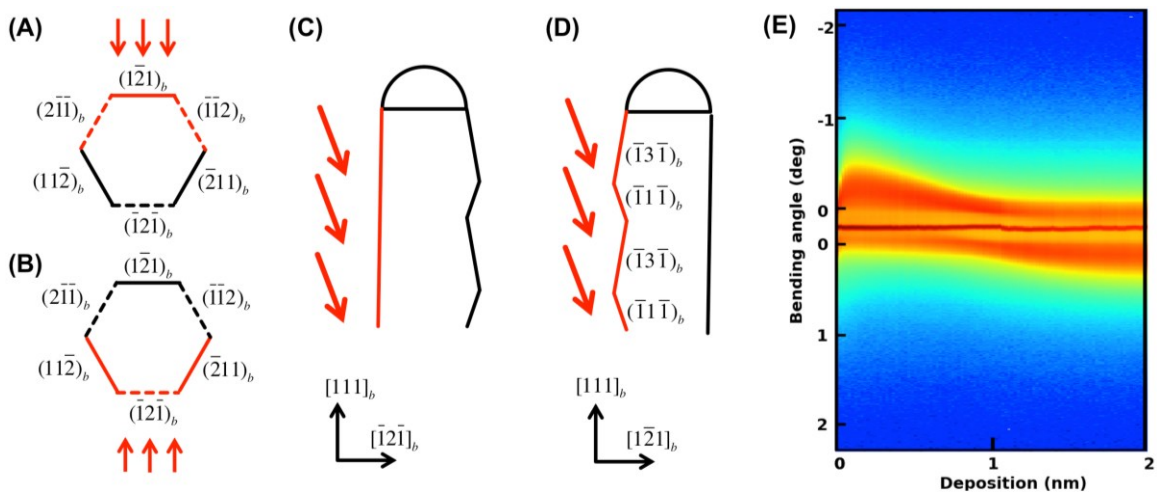

Figure 5-15: (A) Cross-sectional view of the deposition geometry, three of the {112} sidewalls (dashed lines) actually consist of alternating facets of the {111} and {113} families while the other three (solid lines) remain smooth. (B) Side view of the deposition geometry, the in plane component of the molecular beam is along the $[\bar{1}2\bar{1}]_b$ direction. This is the scenario for most of the cases presented in this chapter. (C) Side view of the other possible deposition geometry. The in plane component of the molecular beam is along the $[1\bar{2}1]_b$ direction. The data assembled from stationary measurements in this specific case is shown in (D).

Our simplistic model considers the NWs to be comprised of six smooth sidewalls of the $\{112\}_b$ family. (Figure 5-15A) When the in plane component of the molecular beam is aligned with the $[\bar{1}2\bar{1}]_b$ direction, the $(1\bar{2}1)_b$ sidewall (referred to as the primary sidewall) receives the full amount of the Ge (Au) deposition (0.392 times the nominal value) whereas the two adjacent sidewalls $(\bar{1}\bar{1}2)_b, (2\bar{1}\bar{1})_b$ (referred to as the secondary sidewalls) each receives only half of the calculated amount (0.196 times the nominal value). In the cases where the total stress is dominated by the misfit stress, the resulted inhomogeneous deposition has already been taken into account by the pre-factor 3/4 applied to σ_m in Equation (5-3). In the cases where the total stress is dominated by the surface stress however, Equation (5-3) has to be rewritten as

$$-\sigma_T = \frac{1}{2}\sigma_{s1}(h_f) + \frac{1}{2}\sigma_{s1}\left(\frac{h_f}{2}\right) - \sigma_{s2} \qquad (5\text{-}7)$$

Here, $\sigma_{s1}(h_f)$ is the surface stress on the primary sidewall and $\sigma_{s1}\left(\frac{h_f}{2}\right)$ is the total surface stress on the two secondary sidewalls. The real situation is even more complicated. Rather than remaining smooth, the two secondary sidewalls actually consist of alternating sawtooth facets of the {111} and {113} families. In Table 5-1 is listed the calculated film thickness on a smooth sidewall and on a sawtooth faceted sidewall for 1nm (nominal value) of Ge (Au) deposition. The result seems to indicate the existence of a discontinuous film on the sawtooth faceted sidewall, as the value found for an upward {113} facet is more than 15 times larger than that found for a downward {111} facet.

nominal value	film thickness					
	on primary sidewall			on secondary sidewalls		
	smooth {121}	upward {131}	downward {111}	smooth {121}	upward {131}	downward {111}
1 nm	0.392 nm	0.561nm	0.037nm	0.196nm	0.281nm	0.019nm

Table 5-1: Comparison between the nominal value of deposition and the calculated film thickness on smooth and sawtooth faceted sidewalls.

Ex situ SEM observations, meanwhile, found no presence of such discontinuous film. In fact, it would seem that there is no visible difference between the morphology of the Ge (Au) film deposited on a smooth sidewall and that on a sawtooth faceted sidewall at all. To prove this, we have performed another bending experiment (Figure 5-15D) by aligning this time the in plane component of the molecular beam with the $[1\bar{2}1]_b$ direction. The three $\{112\}_b$ faces exposed to the Au deposition are now composed of one sawtooth faceted primary sidewall plus two smooth secondary sidewalls (Figure 5-15B). The result from stationary measurements is shown in Figure 5-15E. The transition values (Table 5-2 IV) for forward bending and backward bending are close to those found in the previous case (section 5.4.1, Table 5-2 III). With Equation (5-7) this basically implies

$$\sigma_{s1,\text{smooth}}(h_f) + \sigma_{s1,\text{faceted}}\left(\frac{h_f}{2}\right) \cong \sigma_{s1,\text{faceted}}(h_f) + \sigma_{s1,\text{smooth}}\left(\frac{h_f}{2}\right) \qquad (5\text{-}8)$$

In other words, $\sigma_{s1,\text{smooth}} \cong \sigma_{s1,\text{faceted}}$. The above conclusion is particularly important as it allows us to overlook the complex structure of the sawtooth faceted sidewall in our simple model based on classic beam theory.

5.4.3. SIZE EFFECT

Whether there is a size dependent effect on the elastic constants when it comes to nanoscale objects such as the NWs has been long under debate. Experimentally, Young's modulus of Ag and Pb NWs (Cuenot et al. 2004) were found to increase dramatically with decreasing diameters whereas those of Au NWs (Wu et al. 2005) and of GaAs NWs (Paulitschke et al. 2013) were reported to be size independent. Most size dependent elastic properties observed can be explained by the so-called "surface effects" (He & Lilley 2008) as due to the presence of either an oxide layer or a modified surface layer (Chen et al. 2006) which bears a different elastic modulus as the bulk material.

Size effect has also been studied in our case by repeating the same experimental procedures (section 5.4.1) on NWs with a larger diameter (120nm instead of 70nm). Stationary measurements (Figure 5-16) revealed a similar behavior as what was observed previously with smaller NWs, *i.e.,* the total stress changed its sign twice during the experiment, although larger transition values were found (Table 5-2 V) for switching between forward bending and backward bending. Quantitative analysis using the Displaced Bragg Method (Figure 5-17B) showed σ_T values close to those found for smaller NWs under the same bending conditions (Figure 5-13B), indicating that a size dependent effect, should it exist, is negligible. The (~2.5 times) smaller tip deflection found in Figure 5-17A than those in Figure 5-13A is simply due to the (~3.0 times) bigger area moment of inertia for NWs with larger diameters.

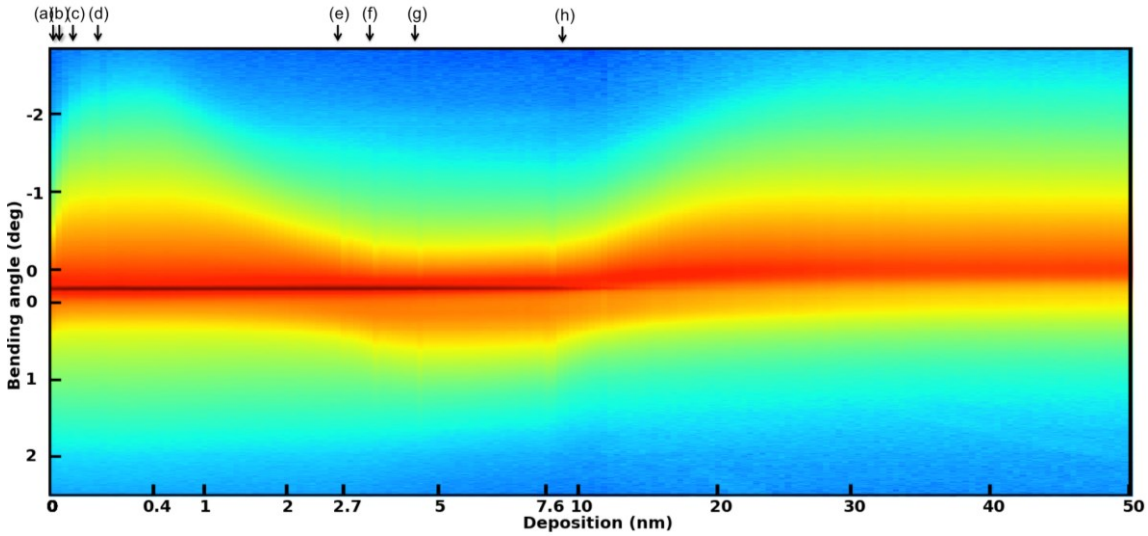

Figure 5-16: Assembled data from stationary images taken during the entire deposition process showing that the larger NWs (*D*=120nm) were bent forth and back and then forth again with increasing amount of Au deposition at RT, similar to what we have previously observed with smaller NWs (*D*=70nm). The irregular intervals on the abscissa is due to changes of deposition amount per acquisition (3×, 6×, 18× of the initial value) occurred at 0.4, 2.7, 7.6nm of deposition, respectively. Au deposition was paused to perform quantitative measurements at points indicated by the arrows on top of the figure.

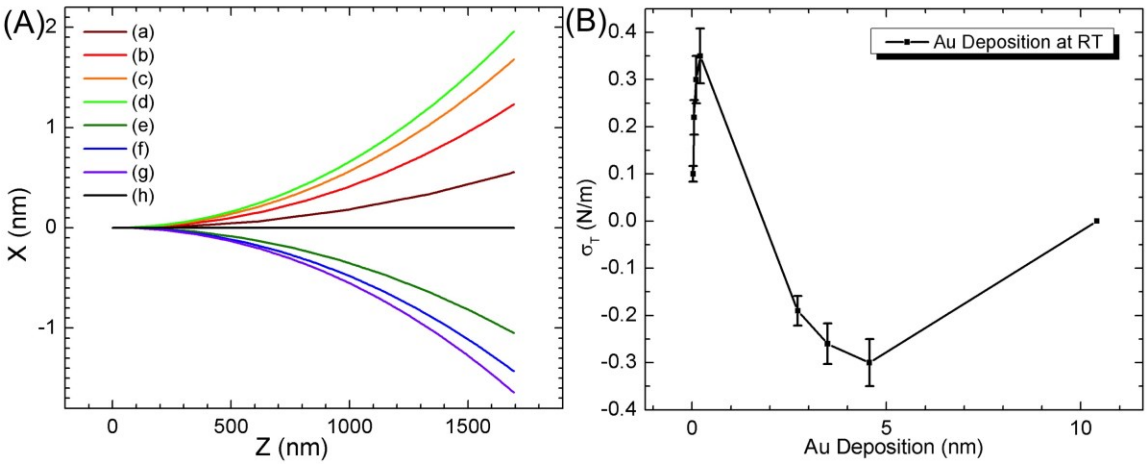

Figure 5-17: (A) Reconstructed NW shape based on the integrated intensities of the displaced Bragg peaks. The average size of the NWs is 120nm. In the figure is shown the deflection of the neutral surface *X* as a function of *Z* in the principle plane of bending for Si NW with Au deposition amount indicated in Figure 5-16. (B) The extracted total stress as a function of Au deposition at RT.

5.5.Discussion

	I: Ge at 220°C along $[\bar{1}2\bar{1}]_b$ L = 1700nm D = 70 nm	II: Ge at RT along $[\bar{1}2\bar{1}]_b$ L = 1700nm D = 70 nm	III: Au at RT along $[\bar{1}2\bar{1}]_b$ L = 1700nm D = 70 nm	IV: Au at RT along $[1\bar{2}1]_b$ L = 1700nm D = 70 nm	V: Au at RT along $[\bar{1}2\bar{1}]_b$ L = 1700nm D = 120 nm
	0 - >21.474	0 - 3.795±0.392	0 - 0.041±0.007	0 - 0.047±0.007	0 - 0.070±0.010
		3.795±0.392 - 19.806±0.660	0.041±0.007 - 0.324±0.014	0.047±0.007 - 0.392±0.016	0.070±0.010 - 0.884±0.060
		19.806±0.660 - >45.885	0.324±0.014 - 1.074±0.101	0.392±0.016 - >0.784	0.884±0.060 - 2.030±0.120
		film thickness too large $h_f > t/2$	1.074±0.101 - 3.062±0.061	not enough Au deposited	2.030±0.120 - 4.805±0.362
			3.062±0.061 - >7.077	not enough Au deposited	4.805±0.362 - >19.821

Table 5-2: Summary of all the bending experiments presented in this chapter which details in particular the transition values (in nm) for switching between forward (tensile total stress) and backward bending (compressive total stress). The values in this table correspond to the actual amount calculated for depositions on a smooth $(1\bar{2}1)_b$ sidewall.

5.5.1. THE DISPLACED BRAGG METHOD

We present the Displaced Bragg Method for the *in situ* investigation of strain/stress evolution during NW bending using grazing incidence X-ray diffraction. The strain, along the longitudinal and the transverse direction of the NWs, was obtained by analyzing the position shift of the displaced Bragg peaks whereas the total stress applied on the NWs was deduced by fitting the NW curvature, retrieved from the integrated intensities of the displaced Bragg peaks, with a model based on classic beam theory. The above-mentioned method possesses certain advantages compared to existing techniques.

First, although similar methods have already been applied to the study of adsorption induced surface stress on micro-cantilevers (Ibach 1997), in those cases, X-ray was only employed for strain determination, while optical methods (laser deflection) were used for the curvature measurement. This latter is not applicable when it comes to nanoscale objects. Moreover, simultaneous measurement of the strain and stress can be achieved with our method as both are obtained using the same technique.

Secondly, compared to electron microscopy techniques (Zhu et al. 2009) which allow for direct measurements of the NW curvature (and hence the stress), very often only the average axial strain can be deduced by measuring the overall elongation of the NWs, whereas with our method, local strain, along both the transverse and the longitudinal direction, can be determined independently for any given segment along the NW, not to mention the other advantages such as the non-destructive nature of X-ray scattering, its larger field of view and its low requirement on sample preparations.

Last but not least, the stress in our case was deduced by fitting the theory with the complete reconstructed shape of the NWs rather than with just their tip deflection (Hoffmann et al. 2006). This allows us to verify the validity of our simple linear elastic model which might not be applicable to NWs with large deflections.

5.5.2. Ge/Si NWs at 220°C

The bending induced by Ge deposition on Si NW sidewalls at 220°C is mainly driven by the misfit stress, which is evident from the linear dependence of the total stress σ_T on the film thickness h_f. While theoretical estimation of the surface stress is a complex problem as it depends on a variety of factors (Sander 2003), *e.g.* surface reconstruction, shape transitions in nano-particles, surface alloying, epitaxial growth, etc., most calculations suggest an order of magnitude of ~1 N/m, for instance, 2.08 N/m for a 7×7 reconstructed and −0.68 N/m for a 1×1 Si(111) facet (R. Meade & Vanderbilt 1989). The

differential surface stress between the convex and concave side of the bent NWs should be even smaller, of the order of ~0.1 N/m. Consequently, it is not surprising that the total stress σ_T in this case is dominated by the misfit stress σ_m, as the latter can easily surpass −2 N/m even for a moderate film thickness (h_f = 5nm) and a very small misfit (−0.25%).

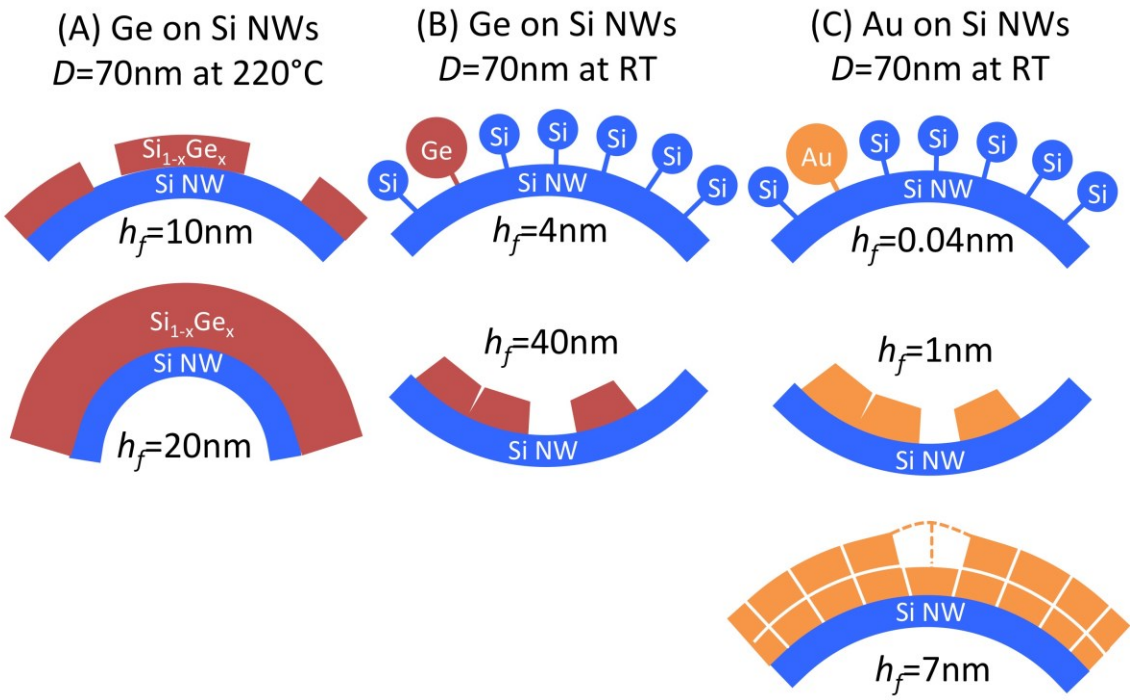

Figure 5-18 : Schematic representation of the different bending scenarios encountered in this work, with Ge deposition on one side of the Si NWs (A) at 220°C, (B) at RT and with (C) Au deposition at RT, respectively. The film thickness h_f is the actual amount calculated for depositions on a smooth $(1\bar{2}1)_b$ sidewall. Both the film thickness and the NW curvature are greatly exaggerated in the illustration.

It would seem that no pseudomorphic Ge wetting layer was formed in the initial stage of growth, as otherwise extrapolating the total stress listed in Figure 5-8B will result in a positive value of σ_T at 0nm of deposition instead of a negative one. Moreover, even 1BL (0.33nm) of pseudomorphic Ge would induce a misfit stress of as large as −2.26 N/m, which greatly exceeds the total stress value (0.19 N/m) found for 2nm of Ge

deposition. The absence of the pseudomorphic wetting layer and the low misfit value (−0.25%) found between the Ge film and the Si NWs can be understood as due to the poor crystalline quality and large defect density of the Ge grown at lower temperatures. Indeed, our growth temperature (220°C) is close to the transition temperature (225°C) reported (Sorianello et al. 2011) between growing single crystal and growing amorphous Ge on Si(001). The linearity of the total stress (*i.e.,* constant misfit value) indicates that the Ge content x_{Ge} (Figure 5-18A) in the MBE Ge film is fixed and is independent of the film thickness h_f, This agrees well with our previous findings of a uniform and invariant composition ($Si_{0.25}Ge_{0.75}$) in the CVD Ge shell grown at the same temperature (*c.f.* Chapter 4). It is worth mentioning that the determination of the crystalline quality (single crystal, amorphous), the lattice constant (strained, relaxed) and the compound composition (x_{Ge}) of the MBE Ge shell in this case is extremely difficult, if not impossible, as for signals coming from every 1nm of Ge deposited on the NW sidewalls we receive interference originating from 2.55nm (nominal value) of Ge deposited directly on the sample surface.

Finally, like all the other studies presented in this chapter, the sample was kept under UHV during the entire experiment to avoid post-growth modifications (oxidation, particle contamination, etc.). Sub-critical incident angle is chosen here not only because it offers an enhanced surface sensitivity but also because it helps separate the NW Bragg peaks from the substrate Bragg peak of the same material (thanks to refraction at grazing incidence). The latter is particularly important if one intends to perform position tracking and intensity integration of the displaced NW peaks corresponding to segments with small bending angles (*i.e.* close to the position of the substrate Bragg peak).

5.5.3. GE/SI NWS AT RT

The bending induced by Ge deposition on Si NW sidewalls at RT is mainly driven by the surface stress, as can be inferred from the non-linearity of the total stress σ_T and from its much smaller values compared to those found in the previous case. The NWs were initially bent forward (tensile stress on the Ge exposed sidewalls, compressive stress in the film) due to the atomic size effect (R. D. Meade & Vanderbilt 1989) and/or due to changes in surface reconstruction, as a result of some surface Si atoms (or H atoms) being replaced by the larger Ge atoms (Figure 5-18B). For a thicker Ge deposition (h_f > 3.80nm), the NWs started to be bent backward. The tensile surface stress (compressive stress on the Ge exposed sidewalls) in this case was attributed to the coalescence between adjacent Ge islands to form grain boundaries with lower surface free energies (Hoffman 1976; Nix & Clemens 1999).

5.5.4. AU/SI NWS AT RT

The bending induced by Au deposition on Si NW sidewalls at RT is also driven by the surface stress. However, in this case a larger tip deflection (ΔX = 4.7nm) was observed for a much smaller film thickness (h_f = 0.02nm) as compared to the bending induced by Ge deposition at the same temperature (ΔX = 3.5nm for h_f = 3.14nm). The dramatic increase in the tensile surface stress, apart from being caused by the apparently larger atomic size effect, is explained by charge redistributions (Ibach 1997) as some of the surface Si atoms were replaced by Au atoms which possess a distinctly different electronic structure. Moreover, the film thickness at which point the NWs started to be bent backwards is also found to be significantly smaller (h_f = 0.04nm for Au versus h_f = 3.80nm for Ge). This can be understood as due to the earlier onset of island formation in the case of Volmer-Weber growth (Au) compared to that of Stranski-Krastanov growth (Ge). The compressive stress that caused the backward bending of the NWs (tensile stress

in the film) was induced by otherwise the same mechanism as was described in the previous case (coalescence between adjacent islands). The NWs were later bent forward again for h_f >3.06nm. (Figure 5-18C) This last change of sign in the surface stress (from tensile back to compressive) is likely to be caused by the incorporation of extra atoms between adjacent ledges of coalesced islands (Spaepen 2000). Finally, the comparison between the transition values in Table 5-2 and the total stress found in Figure 5-13 and Figure 5-17 indicate that both the sawtooth faceting and the NW diameter have little effect on the bending of Si NWs by low temperature depositions. As a matter of fact, no size effect is expected in our case as we have eliminated all the possible "surface effects" (Sohn et al. 2009) by keeping the NWs under UHV during the entire experiment.

References:

Agrawal, R. et al., 2008. Elasticity Size Effects in ZnO Nanowires-A Combined Experimental-Computational Approach. Nano letters, 8(11), pp.3668–3674.

Berry, B.S., 1988. Anelastic Relaxation and Diffusion in Thin-Layer Materials. In D. Gupta & P. S. Ho, eds. Diffusion Phenomena in Thin Films and Microelectronic Materials. Park Ridge, New Jersey: Noyes Publications, pp. 73–145.

Brantley, W.A., 1973. Calculated elastic constants for stress problems associated with semiconductor devices. Journal of Applied Physics, 44(1), p.534.

Chen, C. et al., 2006. Size Dependence of Young's Modulus in ZnO Nanowires. Physical Review Letters, 96(7), p.075505.

Cuenot, S. et al., 2004. Surface tension effect on the mechanical properties of nanomaterials measured by atomic force microscopy. Physical Review B, 69(16), p.165410.

Feidenhans'l, R., 1989. Surface structure determination by X-ray diffraction. Surface Science Reports, 10(3), pp.105–188.

Hannon, J.B. et al., 2006. The influence of the surface migration of gold on the growth of silicon nanowires. Nature, 440(7080), pp.69–71.

He, J. & Lilley, C.M., 2008. Surface effect on the elastic behavior of static bending nanowires. Nano letters, 8(7), pp.1798–802.

Den Hertog, M.I. et al., 2008. Control of gold surface diffusion on si nanowires. Nano letters, 8(5), pp.1544–50.

Hoffman, R.W., 1976. Stresses in thin films: The relevance of grain boundaries and impurities. Thin Solid Films, 34(2), pp.185–190.

Hoffmann, S. et al., 2006. Measurement of the bending strength of vapor-liquid-solid grown silicon nanowires. Nano letters, 6(4), pp.622–5.

Ibach, H., 1997. The role of surface stress in reconstruction, epitaxial growth and stabilization of mesoscopic structures. Surface Science Reports, 29(5–6), pp.195–263.

Ishizaka, A., 1986. Low Temperature Surface Cleaning of Silicon and Its Application to Silicon MBE. Journal of The Electrochemical Society, 133(4), p.666.

Landau, L.D. & Lifshitz, E.M., 1986. Theory of Elasticity,

Meade, R. & Vanderbilt, D., 1989. Adatoms on Si(111) and Ge(111) surfaces. Physical Review B, 40(6), pp.3905–3913.

Meade, R.D. & Vanderbilt, D., 1989. Origins of stress on elemental and chemisorbed semiconductor surfaces. Physical Review Letters, 63(13), pp.1404–1407.

Nam, C.-Y. et al., 2006. Diameter-dependent electromechanical properties of GaN nanowires. Nano letters, 6(2), pp.153–8.

Nix, W.D. & Clemens, B.M., 1999. Crystallite coalescence: A mechanism for intrinsic tensile stresses in thin films. Journal of Materials Research, 14(08), pp.3467–3473.

Oehler, F. et al., 2010. The Importance of the Radial Growth in the Faceting of Silicon Nanowires. Nano letters, 10(7), pp.2335–2341.

Paulitschke, P. et al., 2013. Size-independent Young's modulus of inverted conical GaAs nanowire resonators. Applied Physics Letters, 103(26), p.261901.

Rauscher, M., Salditt, T. & Spohn, H., 1995. Small-angle x-ray scattering under grazing incidence: The cross section in the distorted-wave Born approximation. Physical Review B, 52(23), pp.16855–16863.

Sander, D., 2003. Surface stress: implications and measurements. Current Opinion In Solid State & Materials Science, 7(1), pp.51–57.

Sohn, Y.-S. et al., 2009. Mechanical Properties of Silicon Nanowires. Nanoscale research letters, 5(1), pp.211–216.

Sorianello, V. et al., 2011. Low-temperature germanium thin films on silicon. Optical Materials Express, 1(5), pp.856–865.

Spaepen, F., 2000. Interfaces and stresses in thin films. Acta Materialia, 48(1), pp.31–42.

Stoney, G.G., 1909. The tension of metallic films deposited by electrolysis. Proceedings Of The Royal Society Of London Series A-containing Papers Of A Mathematical And Physical Character, 82(553), pp.172–175.

Vineyard, G.H., 1982. Grazing-Incidence Diffraction And The Distorted-Wave Approximation For The Study Of Surfaces. Physical Review B, 26(8), pp.4146–4159.

Wang, Z.L., 2000. Characterizing the Structure and Properties of Individual Wire-Like Nanoentities. Advanced Materials, 12(17), pp.1295–1298.

Wortman, J.J. & Evans, R.A., 1965. Young's Modulus, Shear Modulus, and Poisson's Ratio in Silicon and Germanium. Journal of Applied Physics, 36(1), p.153.

Wu, B., Heidelberg, A. & Boland, J.J., 2005. Mechanical properties of ultrahigh-strength gold nanowires. Nature materials, 4(7), pp.525–9.

Zhu, Y. et al., 2009. Mechanical properties of vapor-liquid-solid synthesized silicon nanowires. Nano letters, 9(11), pp.3934–9.

6. CONCLUSION AND OUTLOOK

In this work, we first set out to demonstrate *in situ* X-ray scattering as a viable tool for the study of Si and Ge NW growth. Morphological information of the NWs such as the diameter, length, spacing, orientation, facet configuration, cross-sectional area and tapering angle can be acquired during their growth, in a statistical manner, on a large area of the sample surface. Moreover, thanks to the fast acquisition of the GISAXS technique, we were able to follow in real time the rapid changes in the contact angle of the liquid alloy droplet. The result can then be used to calculate the evolution of the surface tension and of the supersaturation level in the very early stage of growth. With GIXD reciprocal space mapping, we have observed the existence of both the metastable β- and γ- phase AuGe, in addition to the more commonly occurring fcc Au, after annealing the catalysts at 500°C. The β phase eventually disappeared under the presence of digermane, together with part of the γ- phase AuGe that was not epitaxially connected to the substrate. Interestingly, our data strongly suggests that the remaining γ- phase AuGe resides at the interface between the catalyst and the Ge substrate and could hence be responsible for the different outcome of the VSS growth (straight NWs, crawling NWs).

We then went on to demonstrate, using anomalous scattering techniques, that the CVD Ge shell grown at 220°C is composed of a fully relaxed SiGe alloy with a uniform composition of $Si_{0.25}Ge_{0.75}$. The misfit stress in this case is probably released by Stranski-Krastanov growth and by defect formations. Annealing the sample or simply growing at higher temperatures (>280°C) destroys the uniformity with enhanced intermixing. The result is a varying Ge content that slowly increases from 0% to 60%-70% with increasing distance from the core-shell interface. The Ge shell meanwhile remains fully relaxed.

Finally, we have presented a new approach (dubbed the Displaced Bragg Method) for the *in situ* investigation of strain/stress evolution during NW bending using solely surface X-ray diffraction. The bending was induced, in our case, by depositing a second material on one side of the NWs. The strain, along the longitudinal and the transverse direction of the NWs, was obtained by analyzing the position shift of the displaced Bragg peaks whereas the total stress applied on the NWs was deduced by fitting the NW curvature, retrieved from the integrated intensities of the displaced Bragg peaks, with a model based on classic beam theory. Two cases were presented to illustrate the use of the Displaced Bragg Method. The bending induced by Ge deposition on Si NW sidewalls at 220°C is found to be mainly driven by the misfit stress, which scales linearly with Ge film thickness. On the other hand, the bending induced by Ge deposition on Si NW sidewalls at RT is found to be mainly driven by the surface stress, which evolves gradually from tensile to compressive for larger Ge film thickness. Additionally, the so-called Stationary Method is presented. The Stationary Method makes it possible to follow, though mostly qualitatively, the entire bending process in real time. The NWs were seen dancing back and forth with increasing amount of deposition as revealed by live stationary measurements with a 2D detector.

Future improvement involves extending the current experimental procedures to smaller and preferably monodisperse NWs. Growths with colloidal Au and with patterned substrates (Figure 6-1) have already shown promising results for the study of size effects on various aspects of growth, although their practical applications in quantitative analysis were hindered by the poor yield of straight [111] NWs specific to our growth conditions. The simple solution is to abandon completely the idea of growing smaller and monodisperse NWs with our setup and to focus instead on experimenting directly on as-grown NWs synthesized by other groups. The physical properties are completely

different for sub-50nm NWs and for NWs with considerably larger diameters. For instance, our Ge shell consists of fully relaxed 3D islands with a relatively high defect density. With smaller NWs, it is possible to grow a high quality 2D shell layer with coherent strain. Anomalous scattering can then be applied before and after annealing to study the effect of backend processes on the performance (strain) of coreshell NWs.

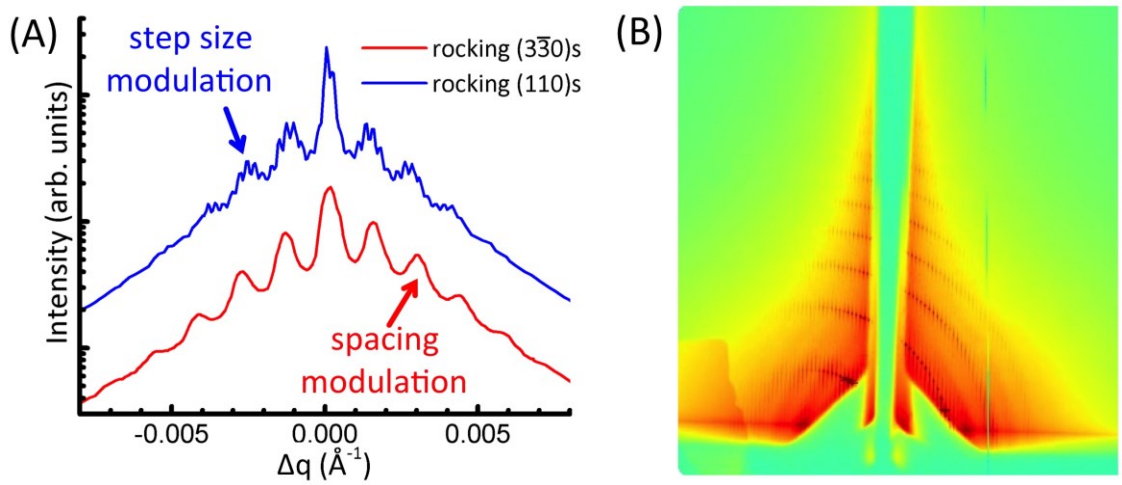

Figure 6-1 : (A) Rocking scans on a patterned sample revealing modulation related to the spacing between the patterned NWs and to the step size parameter. The step size is a user-defined length used in e-beam lithography beyond which a physical movement of the sample is performed instead of simply deflecting the electron beam. (B) GISAXS images of a patterned sample. The large form factor is modulated by the crystalline interference function of the ordered Au catalyst array as it intersects the Ewald's sphere.

[This Page Intentionally Left Blank]

APPENDIX I: WORKING WITH 2D DETECTORS AND PYROD

Surface X-ray Diffraction (SXRD) is a powerful technique for *in-situ* surface and interface structure determination (Feidenhans'l 1989; Robinson & Tweet 1992). Historically, point detectors have been used for data acquisition, but are gradually being replaced by the next generation two-dimensional (or area) detectors which come with much higher resolution, lower noise, better dynamic range and faster acquisition. However, the lack of knowledge of suitable data acquisition techniques or the absence of appropriate *ex post* data analysis method would not only cost the full advantage of using 2D detectors, but might also lead to misinterpretation of the experimental data.

This chapter will cover some established ways (Drnec et al. 2014) that we published earlier on data acquisition and data treatment which exploit the full potential of 2D detectors. These recipes have been used routinely on the two surface diffraction beamlines (ID03, BM32) at the ESRF. A brief introduction to PyRod, a software package dedicated to the visualization, analysis and simulation of surface diffraction data for 2D detectors will be given at the end.

PREREQUISITES

Unless otherwise specified, the diffraction geometry in this chapter is that of a Z-axis (six-circle) diffractometer (Vlieg 1997), but the measuring techniques are available for all kinds of geometries (though they might bear different names) and the analysis methods can be easily adjusted to yield similar results.

The convention for a six-circle diffractometer is the following (Figure I- 1): β_{in} is the incidence angle, β_{out} is the outgoing angle, γ is the out-of-(sample)-plane detector angle, δ is the in-(sample)-plane detector angle, and ω is the sample rotation around the axis perpendicular to the surface or sample azimuth. In the Z-axis mode, $\beta_{in} = \alpha$ and β_{out}

$=\gamma$, h and k are the in-plane diffraction indices and l is the out-of-plane diffraction index (often perpendicular to the surface). $\mathbf{Q}$ is the momentum transfer which is the difference between the outgoing and incoming wavevector $\mathbf{Q} = \mathbf{K}_f - \mathbf{K}_i$. In the case of surface X-ray diffraction, $\mathbf{Q}$ is often depicted as the combination of its in-plane and out-of-plane components $\mathbf{Q}_{\parallel} = \mathbf{Q}_X + \mathbf{Q}_Y$ and $\mathbf{Q}_{\perp} = \mathbf{Q}_Z$.

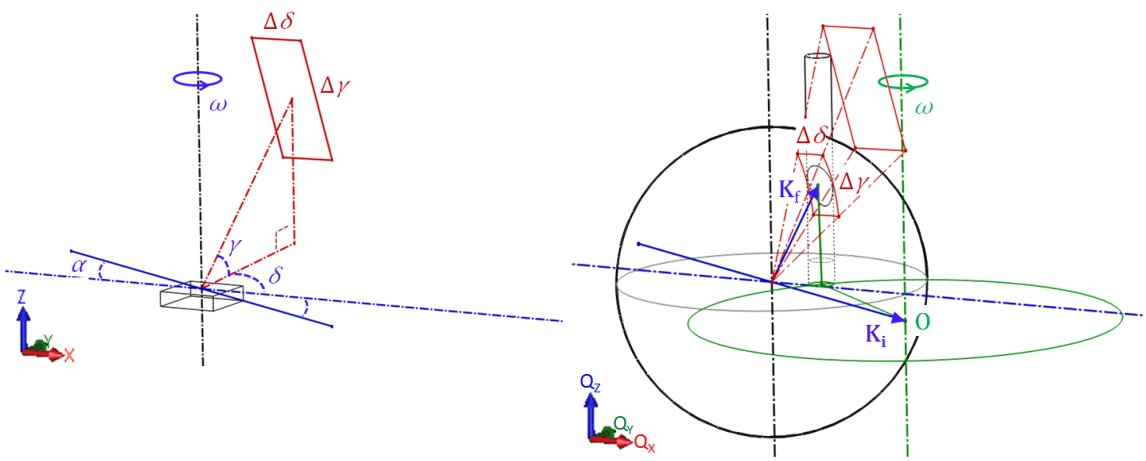

Figure I- 1: (left) Schematic representation of the angle convention in the real space (in the reference system of the diffractometer). The incident beam is confined in the XZ plane, while the sample surface is parallel to the XY plane. (right) Schematic representation of the angle convention in the reciprocal space. For elastic scattering we have $|\mathbf{K}_i| = |\mathbf{K}_f|$. The point **O** denotes the reciprocal space origin. A homogeneous crystal truncation rod is added (black cylinder); the intersection with the Ewald sphere is illustrated as a deformed ellipse. The sample surface plane is shown as a grey circle, while the green circle depicts the reciprocal plane $Q_{\perp} = 0$. Also shown is the projected detector acceptance onto the Ewald sphere, given by $K_f \Delta\gamma$ and $K_f \Delta\delta$.

The foremost difference between a 2D and a point detector is the extent of spatial information that can be obtained in a single acquisition. A point detector detects a small part of the reciprocal space defined by the post sample slits and/or by the detector size with no additional spatial resolution. Rocking scans are required in order to calculate the integrated intensity of a specific reflection. In general, 2D detectors have a much larger

angular acceptance, and their spatial resolution is defined by their pixel size. Therefore, it is possible to obtain an image of the intensity distribution around a given reflection in one single acquisition, provided that the detector acceptance is large enough to accept the full size of the reflection. In some cases sufficient information on the peak profile is stored in one image. As a result, structure factor determination is possible even without performing the rocking scans (Specht & Walker 1993; Vlieg 1997), which greatly reduces the acquisition time (by a factor of 10-100). Even when the use of rocking scans becomes inevitable (*e.g.* the acceptance of the 2D detector is not sufficiently large, which is often the case for small outgoing angles), a wide range of data along the rod can be extracted thanks to the large volume of Q space covered during the scans.

STATIONARY SCANS

Traditionally, a complete rod intensity profile is measured through a series of rocking scans at different l values along the rod. By using 2D detectors, it is possible to replace each rocking scan by one single stationary measurement, thus speeding up vastly the data acquisition. However, certain conditions must be fulfilled.

1. (Figure I- 2, left) The in-plane projection of the finite acceptance of the detector expanded by $K_{\mathrm{f}}\Delta\gamma\sin\gamma$ and $K_{\mathrm{f}}\Delta\delta$ should be sufficiently large to fully contain the cross section of the rod. This is not always true as $\sin\gamma$ vanishes at $\gamma = 0$. Hence, for low l values, one often has to perform a rocking scan or attempt to compensate for the missing intensity either analytically or numerically.

2. (Figure I- 2, right) $|F_{hkl}|$ should be approximately constant over the intersected l range Δl.

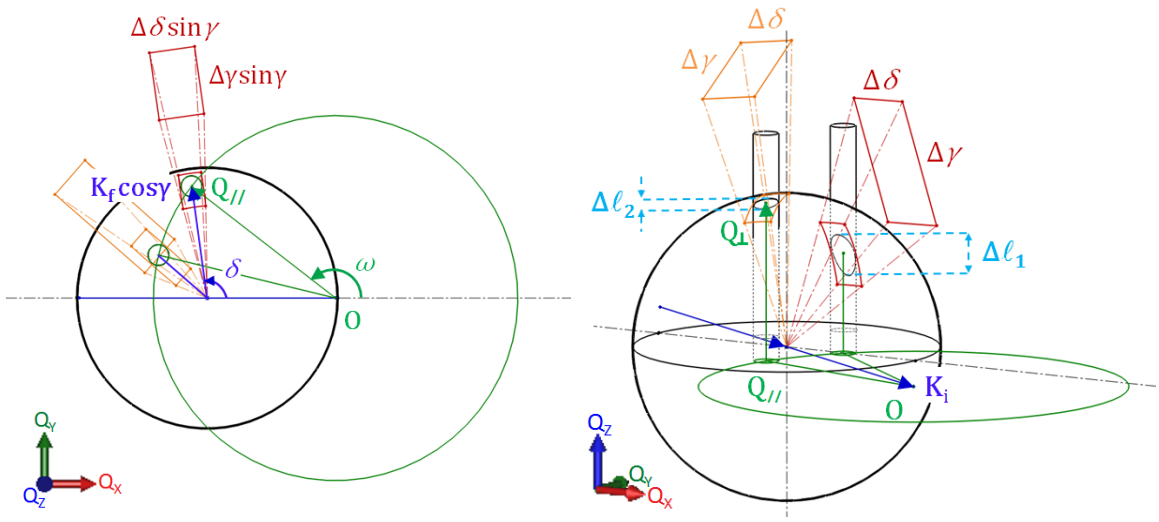

Figure I- 2: (left) Top view of two stationary measurements of the same rod at different l values. The in-plane projection of the finite acceptance of the detector is proportional to $\sin\gamma$ and thus is smaller for lower l values (red) than for higher l values (orange). The measurement is only valid if the projected rectangle is large enough to contain the rod cross section (small green circle). (right) Perspective view of the same measurements. Integration should be carried out only if the intensity distribution is approximately uniform along l within the intersected range Δl, which itself is proportional to $\cos\gamma$. The condition is thus generally easier to fulfill at higher l values (orange) than for lower l values (red).

The complete analysis procedure of stationary l scans, implemented in PyRod, and depicted schematically in Figure I- 3, is the following:

1. For a given (h,k) rod, raw data are collected by conducting stationary measurements at different l values. Note that the position of the measured peak remains fixed in the detector frame, while its width is stretched by the Lorentz factor $\sin^{-1}\gamma$.

2. For each image a peak search is performed in order to locate the peak area, which may be different for each image.

3. The background intensities within the peak area are estimated and subtracted.

4. The correction factors (Vlieg 1997) are applied to the integrated intensity. The entire data set is assembled to compute the $|F_{hkl}|$ profile of the rod.

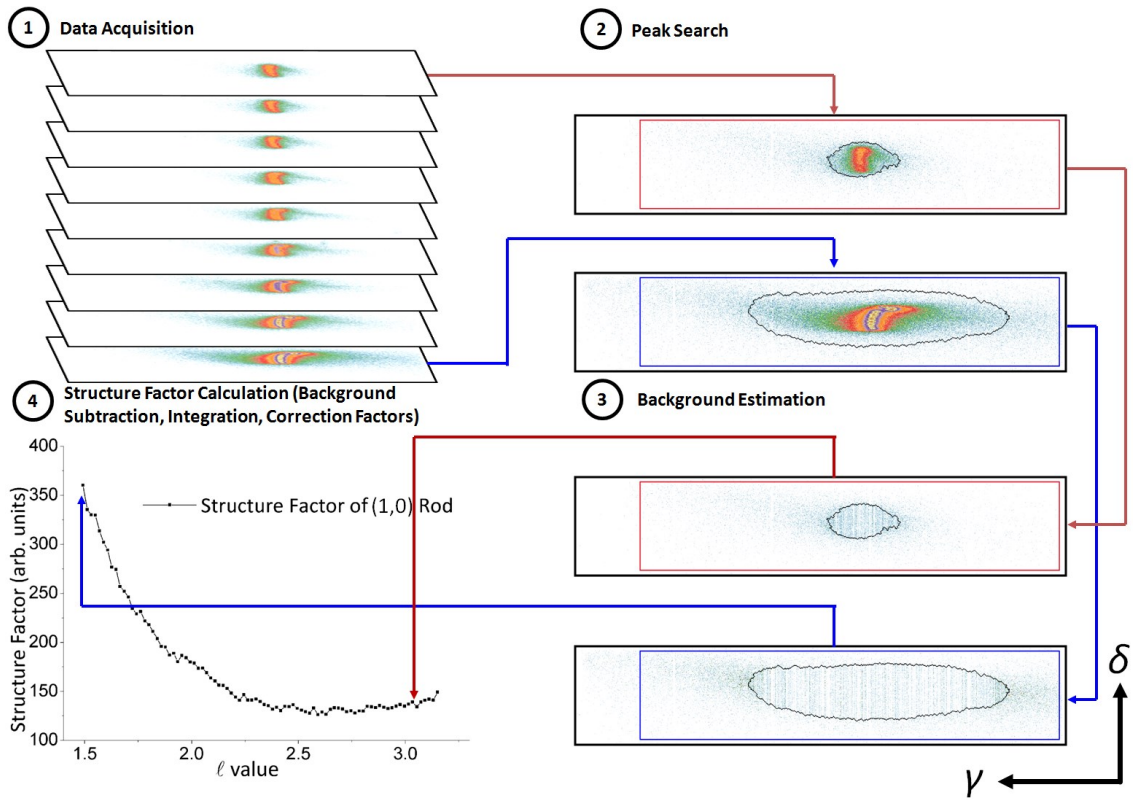

Figure I- 3: Complete analysis procedure of stationary *l* scans. The example used here is a (10*l*) scan of an Ir(111) sample.

ROCKING SCANS

A significant part of the rod is measured when performing a rocking scan, thanks to the nonzero out-of-plane acceptance of the 2D detector (Figure I- 4 right). The "height" Δl, of this intercepted volume in the l direction is given by $K_f \Delta\gamma \cos\gamma$, which is $K_f \Delta\gamma$ when the detector approaches the surface plane ($\cos\gamma \cong 1$). The classic approach of treating the entire rocking scan as a whole, yielding just one structure factor at the given l value is both inefficient and inaccurate, considering that $|F_{hkl}|$ might vary significantly within the integration volume for large Δl. A more appropriate approach consists of dividing the data into small groups. Each group contains pixel intensities from different images corresponding to approximately the same l value, $l \in [l - \frac{\delta l}{2}, l + \frac{\delta l}{2}]$. These data,

when regrouped, form new images of consecutive cross sections of the diffraction rod, allowing us to extract several structure factors at the same time (Figure I- 5).

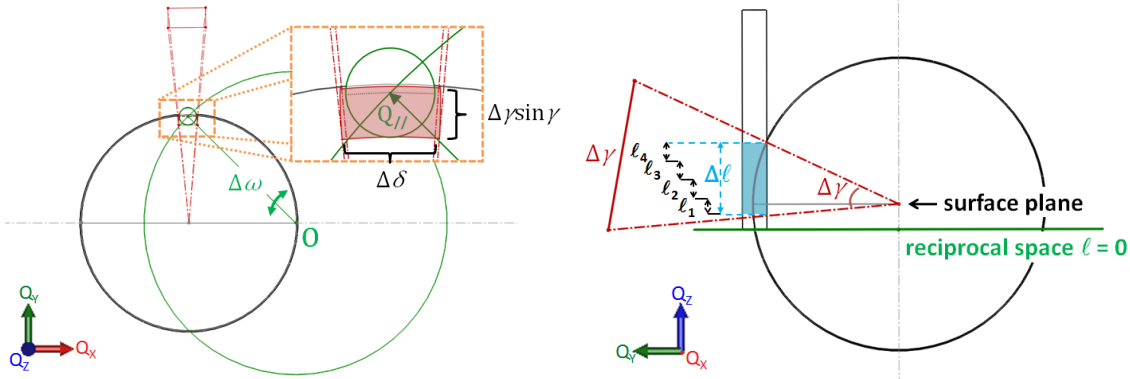

Figure I- 4: (left) Top view of one measuring point during a rocking scan at low outgoing angle γ. The in-plane projection of the detector acceptance (red filled rectangle), being proportional to $\sin\gamma$, no longer contains the entire cross section of the surface rod (small green circle). A full integration thus requires a series of measurements spread along $\Delta\omega$, so that $Q_{\parallel}\Delta\omega \gg$ FWHM of the rod. In reality $\Delta\omega$ should be much larger to take into account the inclination of the detector and to measure background intensities. (right) Side view of the same measuring point. To increase measurement efficiency, we take advantage of the large out-of-plane detector acceptance $\Delta\gamma$. By carefully rearranging the data acquired with the 2D detector and regrouping those that correspond to the same l values (l_1, l_2…), it is possible to reconstruct the rod intensity profile within the Δl range.

The complete analysis procedure of the rocking scans, implemented in PyRod and schematically depicted in Figure I- 5, is the following:

1. For a given (h,k) rod, raw data are collected by performing an ω scan(s) at one (or multiple) l value(s). Note that the size of the peak remains practically unchanged while its center drifts within the detector frame during the scan.

2. For each scan, pixel intensities with the same l values (l_1, l_2…) are regrouped to form a new image. This yields a series of cross-sectional views of the rod at different l values. Normally, instead of generating one new image for every possible l value, the 2D image data are divided into a number of slices with thickness Δl. A simple summation along the γ direction is then applied to the pixels that fall into $l \in [l - \frac{\delta l}{2}, l + \frac{\delta l}{2}]$ to

increase the statistical power of each slice. Note that the result of this operation is a series of newly formed images lying in the δ-ω plane.

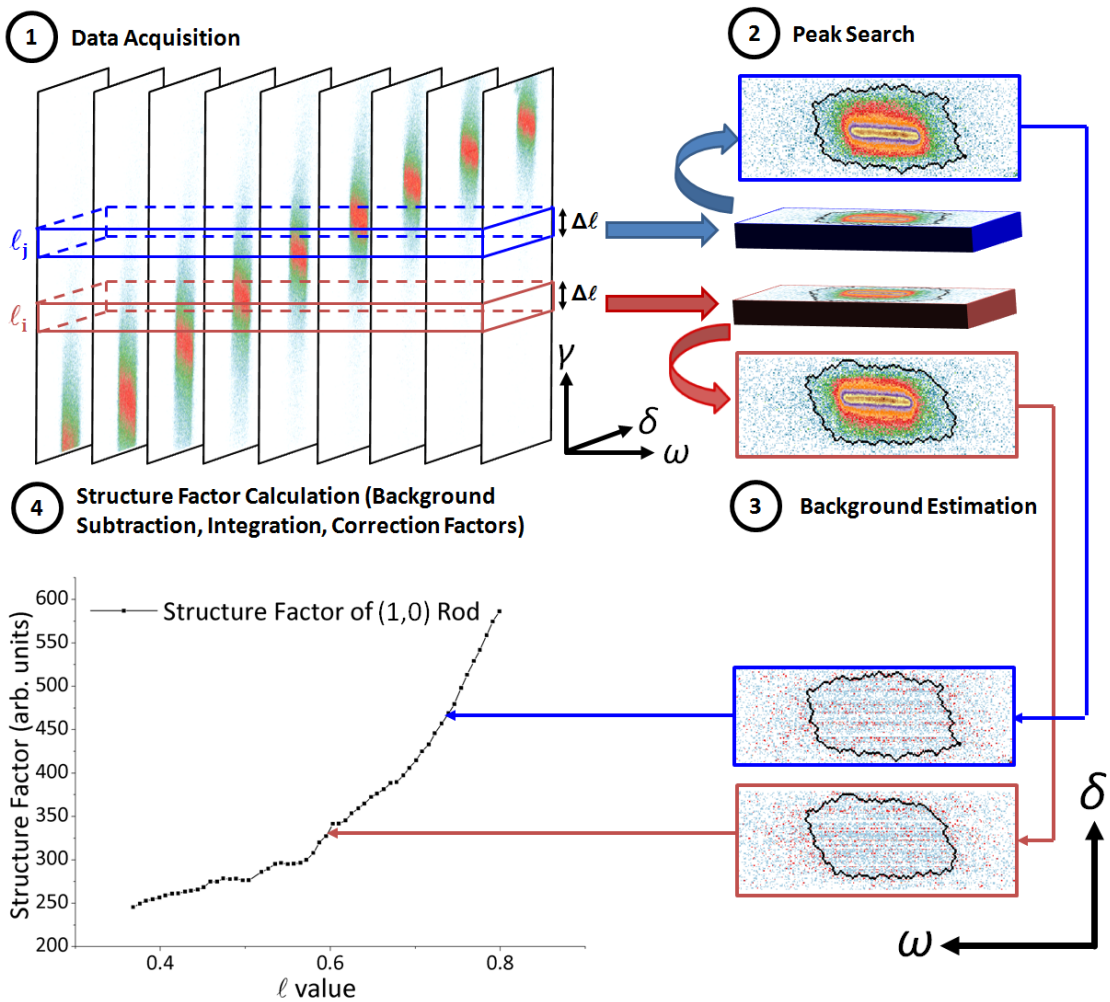

Figure I- 5: Complete analysis procedure of rocking scans using 2D detectors. The example used here is a rocking scan at $l = 0.6$ of the (1,0) rod of an Ir(111) sample.

3. A peak search is then performed on each newly created δ-ω image to locate the peak area. The background intensities within the peak area are estimated and subtracted same as in the case of stationary measurements.

4. The correction factors (Vlieg 1997) are applied to the integrated intensity. The entire data set is assembled to compute the $|F_{hkl}|$ profile of the rod.

COMBINING THE TWO APPROACHES

The measuring time can be greatly reduced by combining the two techniques together, using rocking scans for lower *l* values and stationary measurements for higher *l* values to cover complementary parts of the rod. Concordant structure factors can be found in the overlapped regions measured by the two techniques (Figure I- 6).

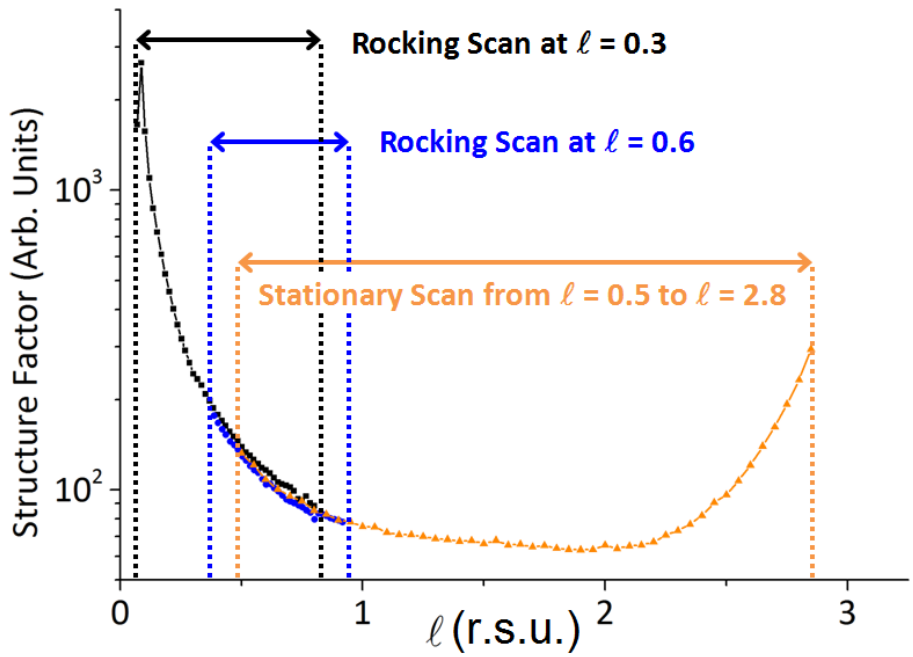

Figure I- 6: Demonstration of combining the two techniques, with two rocking scans covering *l* ranging from 0.03 to 0.9 and a stationary measurement covering *l* from 0.5 to 2.8. Subsequent analysis yields concordant results in the overlapping regions.

PyRod: Introduction

PyRod is a python based software developed on the BM32 (French CRG) beamline at the European Synchrotron Radiation Facility (ESRF) for the visualization, analysis and simulation of surface X-ray diffraction data acquired with 2D detectors. The objective is to offer the users a simple and easy to use toolkit to exploit the full capacity of the 2D detectors. The source code (requires Python 2.6+, GTK+2.0) as well as executable for Windows platform (no prerequisites required) can be downloaded from http://zhoutao.eu/pyrod.

PyRod: Visualization

The visualization mode (Figure I- 7) offers easy access to the scan results and to the associated 2D images. It also provides, with simple mouse clicks, comprehensive view (Figure I- 8ABC) of the 3D volume spanned by the 2D detector during a scan, as well as support for quick RoI integration and reciprocal space mapping (Figure I- 8D).

PyRod: Analysis

PyRod offers two data analysis routines as described in the previous sections. The Stationary Mode works under the assumption that a complete cross-section of the rod is captured in each of the images taken by the 2D detector. If the necessary conditions are met, the complete structure factor profile of (often the upper part of) the rod can be obtained with several mouse clicks (the correction factors are applied automatically). When the stationary scans are not applicable, multiple rocking scans are usually performed instead. The Rocking Mode takes advantage of the large (out-of-plane) detector acceptance of the 2D detectors by dividing it into a series of slices (Figure I- 9). A cross-sectional view of the rod is then reconstructed for each individual slice which is then used to calculate the structure factor profile.

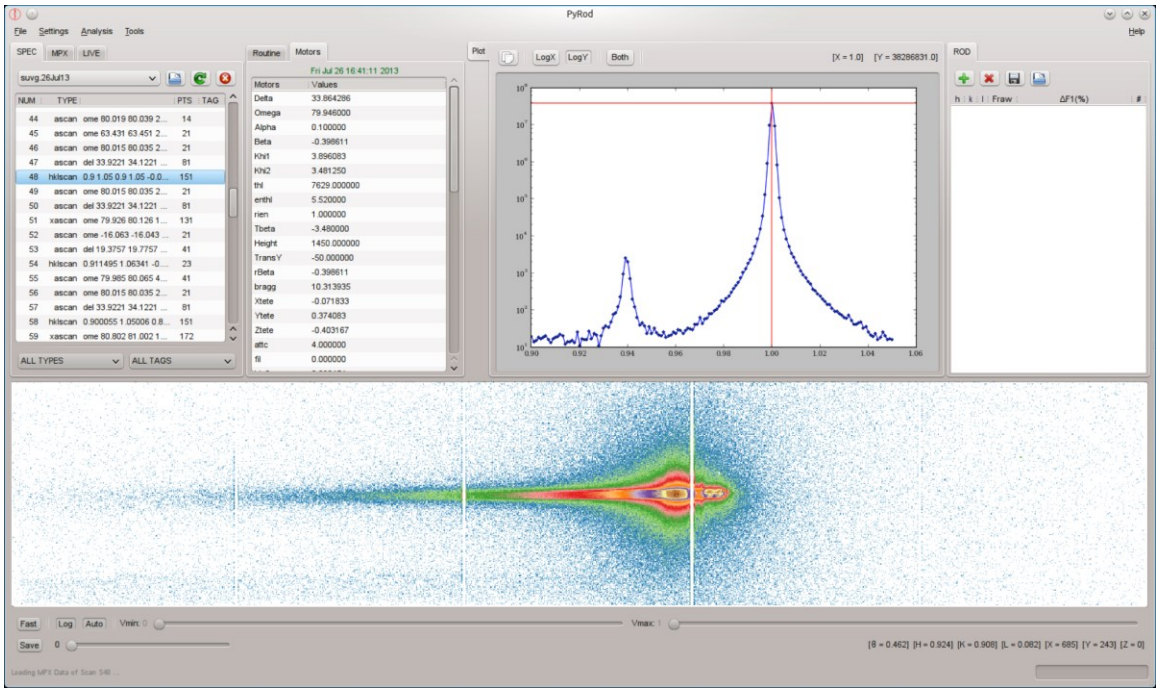

Figure I- 7: The GUI for the visualization mode of PyRod. For a given point of a scan, the correponding 2D image is displayed on the lower canvas while the integrated intensity within the RoI is plotted on the upper canvas.

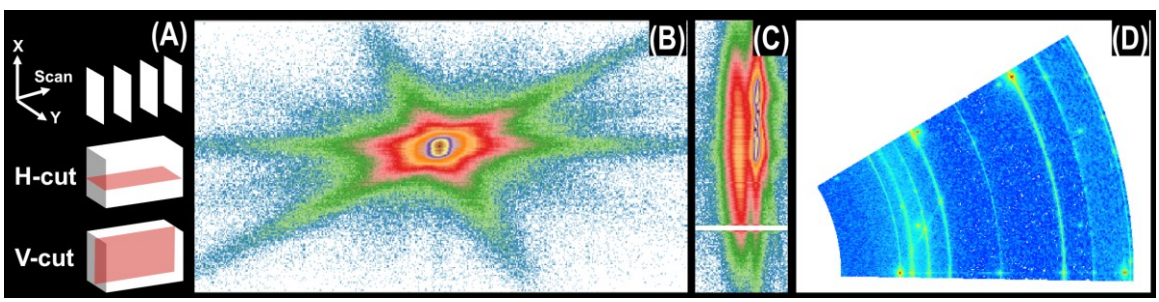

Figure I- 8: (A) A 3D volume is explored with each scan, thanks to the large acceptance of the 2D detectors. Instead of browsing through the data image by image, PyRod offers two different perspective view of the 3D volume, H-cut and V-cut. (B) A H-cut on a rocking scan in the vicinity of a Si Bragg peak reveals features of the dodecagon cross-section of the NWs, equivalent to what can be obtained by performing a reciprocal space mapping (RSM) with a point detector. (C) A V-cut on a radial scan in the vicinity of a out-of-plane Si Bragg peak reveals peaks from both the Si core and the Ge shell of the SiGe heterostructure NWs. The strain values can then be extracted immediately from the reconstructured image. (D) Results from Reciprocal Space Mapping are displayed by simply multi-selecting the scans.

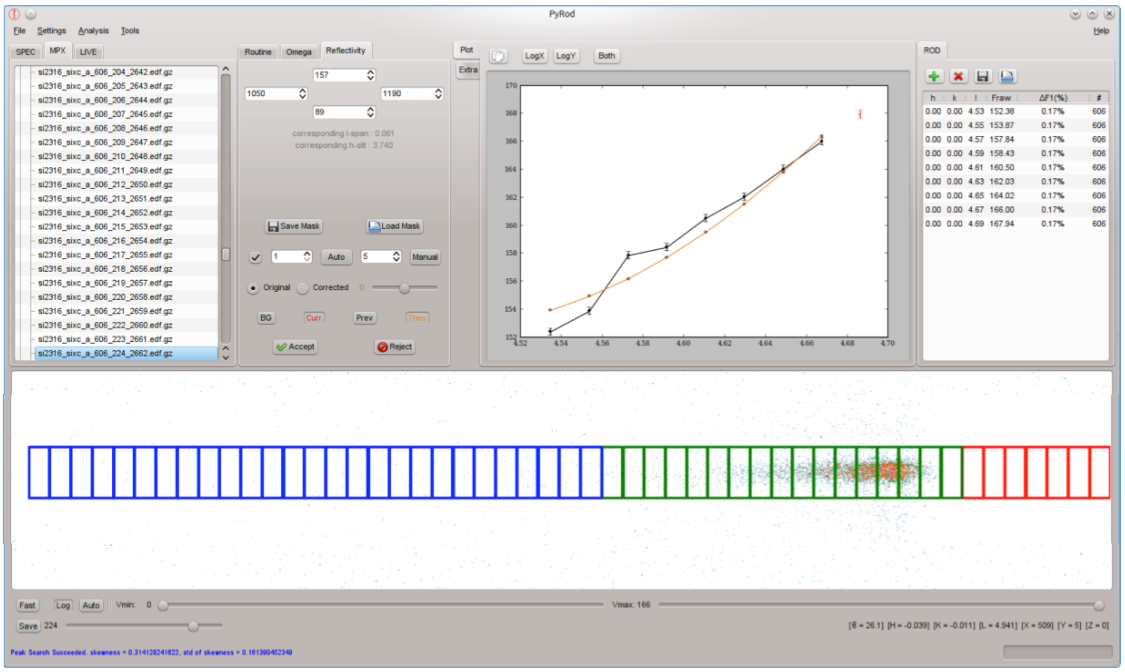

Figure I- 9: The Rocking Mode divides the 2D images into a series of slices. Each slice corresponds to a rod cross-section at a different *l* value. The structure factor of the already analyzed slices (green rectangles) are plotted on the upper canvas (black curve). Once finished, the results are exported to the upper right panel, where subsequent data reduction takes place. PyRod will also attempt to calculate the theoretical structure factors (yellow curve) for comparison if a unit cell model waas previously entered in the simulation panel.

PyRod: Simulation

The simulation mode works in a similar way as ROD (Vlieg 2000), but comes with a more user-friendly graphical interface. It also accepts functions as inputs for the atom displacements/occupations, which can reduce significantly the total number of fitting parameters when necessary.

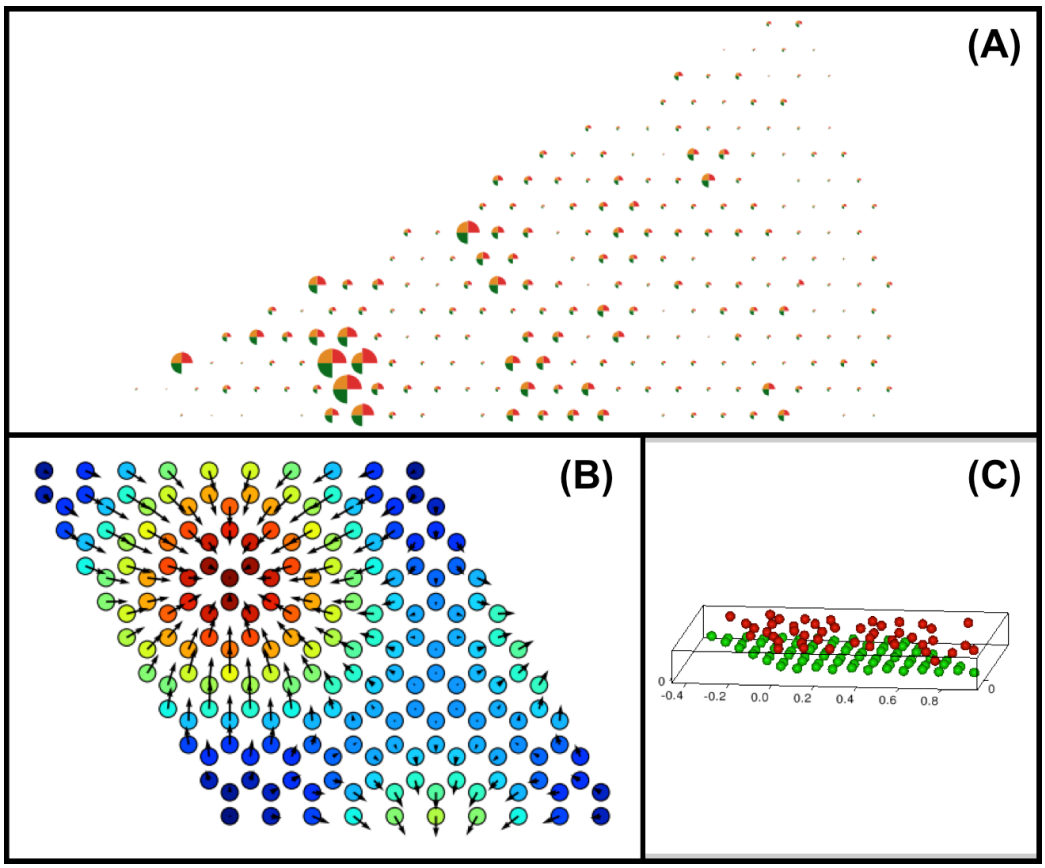

Figure I- 10: (A) Comparison between the in plane experimental structure factors (red) and the theoretical ones (orange and green). The orange wedges represent the total structure factor (surface+bulk) of the fitted model while the green wedges represent the contributions from only the surface layers. (B) The fitting result of a graphene layer. The in plane displacements of the atoms with regard to their original positions are shown in quivers while the out-of-plane displacements are shown in fake color scale. (C) The positions of the atoms can also be viewed in 3D.

References:

Drnec, J. et al., 2014. Integration techniques for surface X-ray diffraction data obtained with a two-dimensional detector. Journal of Applied Crystallography, 47(1), pp.365–377.

Feidenhans'l, R., 1989. Surface structure determination by X-ray diffraction. Surface Science Reports, 10(3), pp.105–188.

Robinson, I.K. & Tweet, D.J., 1992. Surface X-ray diffraction. Reports on Progress in Physics, 55(5), pp.599–651.

Specht, E. & Walker, F., 1993. Oxidation state of a buried interface: Near-edge x-ray fine structure of a crystal truncation rod. Physical Review B, 47(20), pp.13743–13751.

Vlieg, E., 1997. Integrated Intensities Using a Six-Circle Surface X-ray Diffractometer. Journal of Applied Crystallography, 30(5), pp.532–543.

Vlieg, E., 2000. ROD: A program for surface X-ray crystallography. Journal of Applied Crystallography, 33(2), pp.401–405.

[This Page Intentionally Left Blank]

APPENDIX II: ON CLASSICAL BEAM THEORY

This chapter will cover a brief introduction to the Euler-Bernoulli Beam Theory, followed by some simple derivations that lay the groundwork for the approach we used to solve the problems discussed in Chapter 5.

EULER-BERNOULLI BEAM THEORY

Euler-Bernoulli beam theory is a simplification of the linear theory of elasticity which describes the relationship between the beam's deflection and the applied load. It is a special case of Timoshenko beam theory (Timoshenko 1983), and is restricted only to small deflections of a beam subjected to lateral loads.

Considering the NW to be composed of infinitesimal elements with length d**l** along the axial direction, and let **K** be the external force applied on the NW per unit length, **M** be the moment of the internal stresses on its cross-section. The total moment acting on any of the elements must be zero in equilibrium:

$$d\mathbf{M} + d\mathbf{l} \times \mathbf{F} = 0 \qquad \text{(II- 1)}$$

Dividing the above equation by dl and keeping in mind that d**l**/dl=**t**, where **t** is the unit vector tangential to the NW, we have

$$d\mathbf{M}/dl = \mathbf{F}\times\mathbf{t} \qquad \text{(II- 2)}$$

Equations (II- 1) and (II- 2) form a complete set of equilibrium equations for a NW bent in any manner (Landau & Lifshitz 1986). These equations can be considerably simplified in the case of NWs with small deflections, which requires the radius of curvature of the bent NW to be everywhere larger than the length of the NW. Differentiating Equation (II- 2) we have

$$\frac{d^2\mathbf{M}}{dl^2} = \frac{d\mathbf{F}}{dl} \times \mathbf{t} + \mathbf{F} \times \frac{d\mathbf{t}}{dl} \qquad \text{(II- 3)}$$

The second term contains the small quantity d**t**/d*l* and can thus be neglected. Without going into any details, we give directly an alternative form of Equation (II- 3)

$$M_y = -EI_y \frac{d^2Y}{dZ^2} \qquad \text{(II- 4)}$$

where Z is parallel to the axial direction of the NW before bending. Y is in the surface plane of the sample, Y-Z forms the principal plane of bending (where the bending occurs). E is the Young's modulus of the NW, I_y is the area moment of inertia for the NW cross-section with respect to the Y-axis . EI is also called the stiffness of the NW.

AREA MOMENT OF INERTIA

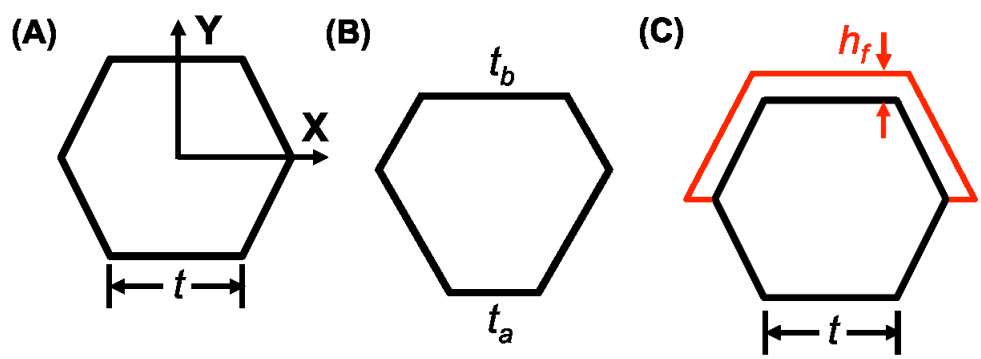

Figure II-1: Schematics of (A) a regular hexagon with side length t, (B) a trigonal hexagon with side length t_a, t_b, and (C) a regular hexagon with side length t and a uniform deposition of thickness h_f on one side.

The area moment of inertia (or second moment inertia) for an arbitrary shape with respect to the Y-axis in Cartesian coordinates is defined as

$$I_y = \iint x^2 dxdy \qquad \text{(II- 5)}$$

In the case of a regular hexagon with side length t (Figure II-1A), the area moment of inertia with respect to the Y-axis is the same as to the X-axis, and is given by

$$I_x = I_y = \frac{5\sqrt{3}}{16} t^4 \qquad (\text{ II- 6 })$$

For a trigonal hexagon such as the one described in Figure II-1B, we have

$$I'_y = \frac{\sqrt{3}[(t_a + t_b)^4 + 2t_a t_b (t_a^2 + t_b^2)]}{64} \qquad (\text{ II- 7 })$$

and

$$I'_x = \frac{\sqrt{3}[t_a(\frac{t_a}{2} + t_b)(t_a^2 + 2t_a t_b + 2t_b^2) + t_b(t_a + \frac{t_b}{2})(2t_a^2 + 2t_a t_b + t_b^2)]}{48} \qquad (\text{ II- 8 })$$

It can be easily demonstrated that there is little difference between the area moment of inertia for a trigonal hexagon and that for an equivalent regular hexagon with $t = (t_a + t_b)/2$. For a highly asymmetric hexagon, $t_b = 2t_a$, we have $I'_y = 0.9975\, I_y$ and $I'_x = 0.9547\, I_x$. Moreover, all the area moment of inertia concerned in Chapter 5 is the one with respect to the Y-axis, it is thus reasonable to simplify our NW model to one with a regular hexagonal cross-section since the difference is less than 0.25%.

We should also take into account the contribution from the Ge film of thickness h_f deposited on one side of the NW. The area moment of inertia of the Ge part is given by

$$I''_{Ge,y} = \frac{5}{4} t^3 h_f + \frac{5\sqrt{3}}{4} t^2 h_f^2 + \frac{5}{3} t h_f^3 + \frac{5\sqrt{3}}{18} h_f^4 \qquad (\text{ II- 9 })$$

Combining Equation (II- 6) and (II- 9), and knowing that

$$EI = E_{Si} I_{Si} + E_{Ge} I_{Ge} \qquad (\text{ II- 10 })$$

The effective stiffness of a Si NWs with Ge deposition is thus

$$EI = \frac{5\sqrt{3}}{16} t^4 E_{Si} + (\frac{5}{4} t^3 h_f + \frac{5\sqrt{3}}{4} t^2 h_f^2 + \frac{5}{3} t h_f^3 + \frac{5\sqrt{3}}{18} h_f^4) E_{Ge} \qquad (\text{ II- 11 })$$

STONEY'S FORMULA

The NWs remained attached to the substrate during the bending experiment, and have hence one of their ends free and the other one "clamped" at the sample surface.

The clamped end of the NW can neither move nor change its direction which leads to (the prime denotes differentiation with respect to Z)

$$Y = 0, \qquad Y' = 0 \qquad \text{for } Z = 0 \tag{II- 12}$$

At the free end, the force **F** and moment **M** must be zero, hence we have

$$Y'' = 0, \qquad Y''' = 0 \qquad \text{for } Z = L \tag{II- 13}$$

where L is the original length of the NW before bending. The solution to Equation (II- 4) depends on the force and moment applied to the NW. In the next page is listed the solutions to some of the most common cases.

Schematic	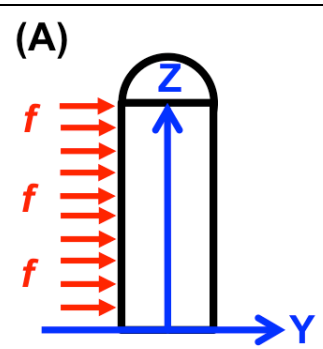	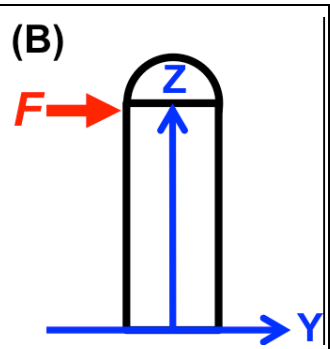	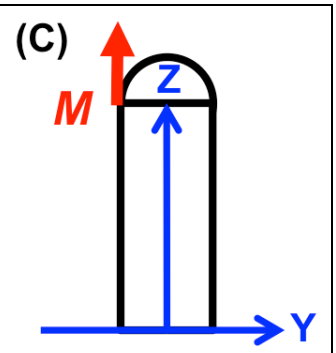
Y=	$\frac{fZ^2}{24EI}(Z^2 - 4ZL + 6L^2)$	$\frac{fZ^2}{6EI}(3L - Z)$	$Y = \frac{MZ^2}{2EI}$ (II- 14)
Force	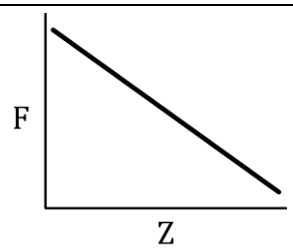	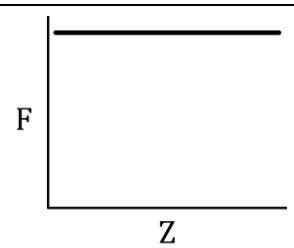	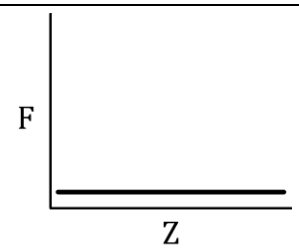
Moment	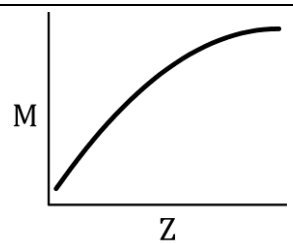	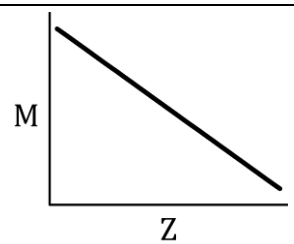	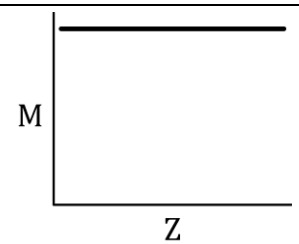
Y	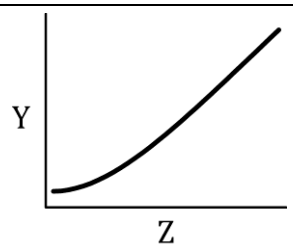	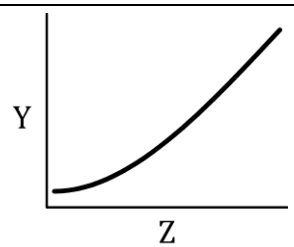	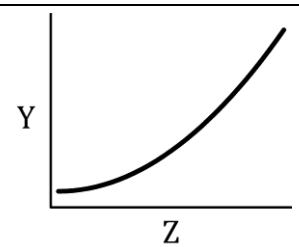

Table II- 1: Analytical solution, force, moment and displacment of a bent NW when (A) force **f** is applied uniformly on the NW sidewall (B) a concentrated force **F** is applied on the free end (C) a concentrated moment **M** is applied on the free end.

Let us consider a stress σ, created by a film of thickness h_f, deposited on one side of the NW with a square cross-section of side length h_s. The resulted moment is

$$M = \sigma h_f \cdot \frac{h_s^2}{2} \qquad \text{(II- 15)}$$

The area moment of inertia for a square cross-section is

$$I = \frac{h_s^4}{12} \qquad \text{(II- 16)}$$

Exchanging both Equation (II- 15) and (II- 16) into Equation (II- 14), we obtain Stoney's formula (Stoney 1909; Berry 1988).

$$\sigma = \frac{E h_s^2}{6 h_f (1 - \upsilon_s^2)} \cdot \frac{1}{R} \qquad \text{(II- 17)}$$

where R is the radius of curvature of the bent NW with $R = d^2Z/dY^2$. υ_s is the Poisson's ratio, $E/(1-\upsilon_s^2)$ is the plate modulus for elongated rectangular beams.

In order to calculate the curvature of the Si NWs bent by Au/Ge depositions, we consider the moment **M** to be the result of both the differential surface stress $\sigma_s = \sigma_{s1} - \sigma_{s2}$ and the misfit (interface) stress σ_m

$$M = \sqrt{3} t^2 \sigma = -\sqrt{3} t^2 (\sigma_s + \frac{3}{4} h_f \sigma_m) \qquad \text{(II- 18)}$$

The negative sign in the above equation stems from the fact that σ is applied on one side of the NW whereas σ_{s1} and σ_m are intrinsic stress in the film. Combining Equation (II- 4), (II- 11) and (II- 18), we have

$$\frac{d^2Y}{dZ^2} = \frac{-\sqrt{3} t^2 (\sigma_s + \frac{3}{4} h_f \sigma_m) \cdot (1 - \upsilon_s^2)}{\frac{5\sqrt{3}}{16} t^4 E_{Si} + (\frac{5}{4} t^3 h_f + \frac{5\sqrt{3}}{4} t^2 h_f^2 + \frac{5}{3} t h_f^3 + \frac{5\sqrt{3}}{18} h_f^4) E_{Ge}} \qquad \text{(II- 19)}$$

and hence

$$Y = \frac{-\sqrt{3} t^2 (\sigma_s + \frac{3}{4} h_f \sigma_m) \cdot (1 - \upsilon_s^2)}{\frac{5\sqrt{3}}{16} t^4 E_{Si} + (\frac{5}{4} t^3 h_f + \frac{5\sqrt{3}}{4} t^2 h_f^2 + \frac{5}{3} t h_f^3 + \frac{5\sqrt{3}}{18} h_f^4) E_{Ge}} \cdot \frac{Z^2}{2} \qquad \text{(II- 20)}$$

SOLUTIONS FOR TAPERED NWS

Solution to Equation (II- 19) becomes much more complicated in the case of tapered NWs, where the side length *t* itself is a function of *Z*.

$$t = t_0 - \frac{Z}{L}(t_0 - t_L) = t_0(1 - nZ) \qquad n = \frac{t_0 - t_L}{Lt_0} \qquad \text{(II- 21)}$$

Here, t_0 is the side length of the NW close to the sample surface and t_L is the side length close to the tip of the NW. Equation (II- 19) can be rewritten as follows:

$$\frac{d^2Y}{dZ^2} = \frac{-\sqrt{3}(\sigma_s + \frac{3}{4}h_f\sigma_m)\cdot(1 - v_s^2)\cdot t_0^2(1 - nZ)^2}{\frac{5\sqrt{3}}{16}t_0^4(1 - nZ)^4E_{Si} + \left(\frac{5}{4}t_0^3(1 - nZ)^3h_f + \frac{5\sqrt{3}}{4}t_0^2(1 - nZ)^2h_f^2 + \frac{5}{3}t_0(1 - nZ)h_f^3 + \frac{5\sqrt{3}}{18}h_f^4\right)E_{Ge}} \qquad \text{(II- 22)}$$

Finding the exact analytical solution to the above equation is almost impossible. A simplification can be made if the last two terms on the denominator can be neglected, in other words if

$$\frac{5\sqrt{3}}{16}t_0^4 > \frac{5}{4}t_0^3h_f > \frac{5\sqrt{3}}{4}t_0^2h_f^2 \gg \frac{5}{3}t_0h_f^3 > \frac{5\sqrt{3}}{18}h_f^4 \qquad \text{(II- 23)}$$

The above condition normally holds in our case, Equation (II- 22) thus becomes

$$\begin{aligned} \frac{d^2Y}{dZ^2} &= \frac{m_1}{m_2(1 - nZ)^2 + m_3(1 - nZ) + m_4} \\ m_1 &= -\sqrt{3}(\sigma_s + \frac{3}{4}h_f\sigma_m)\cdot(1 - v_s^2) \\ m_2 &= \frac{5\sqrt{3}}{16}t_0^2E_{Si} \\ m_3 &= \frac{5}{4}t_0h_fE_{Ge} \\ m_4 &= \frac{5\sqrt{3}}{4}h_f^2E_{Ge} \end{aligned} \qquad \text{(II- 24)}$$

Finally, by taking into account the boundary conditions described earlier in Equations (II- 12) (II- 13), we have

$$
\begin{aligned}
Y = -m_1 \cdot \Bigg(& \sqrt{4m_2m_4 - m_3^2} \cdot \ln(m_2(1-nZ)^2 - m_3nZ + m_3 + m_4) \\
& + 2(m_2(2-2nZ) + m_3) \cdot \tan^{-1}\left(\frac{2m_2(nZ-1) - m_3}{\sqrt{4m_2m_4 - m_3^2}}\right)\Bigg) \\
& /(2m_2n^2\sqrt{4m_2m_4 - m_3^2}) + C_1Z + C_0 \\
C_1 = {} & 2\tan^{-1}\left(\frac{-2m_2 - m_3}{\sqrt{4m_2m_4 - m_3^2}}\right)/(n\sqrt{4m_2m_4 - m_3^2}) \\
C_0 = {} & (\sqrt{4m_2m_4 - m_3^2}\ln(m_2 + m_3 + m_4) + 2(2m_2 + m_3) \\
& \cdot \tan^{-1}\left(-2m_2 - m_3/\sqrt{4m_2m_4 - m_3^2}\right))/(2m_2n^2\sqrt{4m_2m_4 - m_3^2})
\end{aligned}
\qquad \text{(II- 25)}
$$

References:

Berry, B.S., 1988. Anelastic Relaxation and Diffusion in Thin-Layer Materials. In D. Gupta & P. S. Ho, eds. Diffusion Phenomena in Thin Films and Microelectronic Materials. Park Ridge, New Jersey: Noyes Publications, pp. 73–145.

Landau, L.D. & Lifshitz, E.M., 1986. Theory of Elasticity,

Stoney, G.G., 1909. The tension of metallic films deposited by electrolysis. Proceedings Of The Royal Society Of London Series A-containing Papers Of A Mathematical And Physical Character, 82(553), pp.172–175.

Timoshenko, S., 1983. History of Strength of Materials: With a Brief Account of the History of Theory of Elasticity and Theory of Structures,

APPENDIX III: SAMPLE PREPARATIONS

The metal catalysts (Au or Al) were deposited using a MEGA2000 effusion cell. Typical deposition rate varies from 0.06 to 0.12 nm/min and was calibrated using a quartz microbalance (INFICON). We use Si_2H_6 (Linde Electronics) and Ge_2H_6 (70% He+30% Ge_2H_6, SAFC Hitech) as precursor gas for the growth of Si and Ge NWs, respectively. SiH_4 and GeH_4 were also available but were seldom used due to their relatively low reactivity. The maximum partial gas pressure that can be reached in the growth chamber is limited by the maximum flux (1sccm) of the mass flow controller, which corresponds to approximately 4×10^{-5}mbar as measured by a ceramic capacitance gauge (PFEIFFER CMR 375). Higher partial gas pressures (~10^{-2}mbar) are attainable by reducing the rotation speed of the turbo pump. The sample can be heated to ~600°C by radiative heating and up to ~1400°C by electron bombardment. The temperature was monitored by an infrared (IR) pyrometer (INFICON).

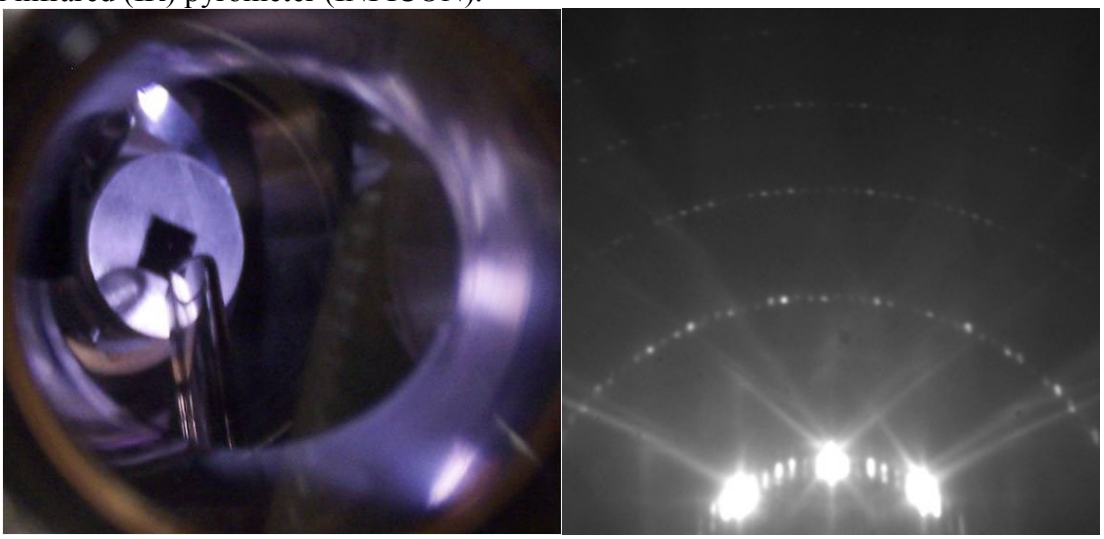

Figure III- 1 : (left) A Si sample of ~ 6mm×6mm mounted vertically on a Mo sample holder as seen from one the windows of the UHV chamber. A quartz tube was initially used to feed the precursor gases directly to the sample surface. (right) RHEED measurements were frequently employed to verify the surface quality of sample preparations. Up to five Laue zones of the Si(111)-(7×7) reconstruction were observed.

SAMPLE PREPARATION

Si(111) samples are prepared using a modified Shiraki Etch (Ishizaka 1986).

	Procedure and Notes
Solvent Degreasing	1. Ultrasonic bath in deionized water (DI-H_2O) for 10min
	2. Ultrasonic bath in methanol for 5min To ensure a smooth transit from H_2O to hydrophobic TCE
	3. Ultrasonic bath in trichloroethylene (TCE)
	4. Ultrasonic bath in acetone for 5min TCE residue removal
	5. Ultrasonic bath in methanol for 5min Acetone residue removal
	6. Ultrasonic bath in DI-H_2O for 10min Methanol residue removal
Standard Cleaning	7. H_2SO_4(98%):H_2O_2(30%) = 3:1 (known as SPM, Piranha solution, Caro's Acid) at 90°C for 10min, then rinse in DI-H_2O. Advantages: very effective way for organic residues removal Drawbacks: leave S residues, possible re-deposition of materials due to less favorable zeta potential (Karen Reinhardt 2008).
	8. NH_4F(40%):HF(49%) = 7:1 (BHF for Buffered HF or BOE for Buffered Oxide Etch) for 60 sec, then rinse in DI-H_2O. BHF may be ill advised in attempt to prepare atomically flat Si(001) surface, as it will develop the (111) facets upon etching, thus increasing the surface roughness (Ohmi et al. 1992). This turns out to be, however, very advantageous for preparing flattened Si(111) surface on an atomic scale. For the preparation of Si(001) surface, we use 2.5% HF solution 30 sec.
	9. NH_4OH(29%):H_2O_2(30%):H_2O = 0.25:1:5 (known as the SC-1 solution in RCA cleaning) at 90°C for 10min, then rinse in DI-H_2O. Effective for particle removal due to negative zeta potential, but will induce metallic contamination. The concentration of ammonium in the solution varies in the literature. A mixture of 1:1:5 is standard for RCA cleaning while 1:1:3 was used in (Ishizaka 1986). Much lower ammonium content was used in our case, as it was reported to have improved the particle removal capability by a factor of 2 without significant increase in surface roughness(Mishima et al. 1989).
	10. BHF for 60sec, then rinse in DI-H_2O.
	11. HCl(37%): H_2O_2(30%):H_2O = 3:1:1 (SC-2 solution in RCA cleaning) at 90°C for 10min. Metallic contamination removal and formation of protective oxide (~1-1.2nm thick (Grundner & Jacob 1986)).
	12. Rinse in overflowing DI-H_2O. Samples are then stored in DI-H_2O.

Table III- 1 : Cleaning procedures and notes for Si(111) samples.

The samples (Si or Ge) were mounted vertically during the experiments as the polarization factor for scattering is maximized (equals to 1) in a vertical scattering plane (Als-Nielsen & McMorrow 2011). A thick film of liquid Indium (capillary adhesion) was used to maintain the sample on the Molybdenum sample holder (Figure III- 1, left).

For the removal of the protective chemical oxide formed during step 11 and for the preparation of a nicely reconstructed surface, the sample was slowly ramped up to 760°C in the UHV chamber (the temperature at which no SiC was formed even after hours at 1×10^{-8}mbar, as established with our experiments). The sample then underwent a 5min-flash at 830°C once the pressure dropped below 1×10^{-9}mbar. Our RHEED and X-ray observations seem to confirm that longer annealing time (>5min) and/or higher annealing temperatures (>830°C) only slightly improve the surface quality while increasing significantly the risk of forming SiC and of sample detachment (by Indium evaporation) from the Mo holder. Finally, RHEED (Figure III- 1, right) and X-ray measurements were used to verify that the oxide desorption process was complete and that the surface was fully reconstructed.

The degreasing steps for Ge(111) follow the same as what was described for Si(111) preparations. The standard cleaning is different and consists of multiple (often 2 to 4) cycles of alternating 30-sec-dip in 10% H_2O_2 and in 2.5% HF solution, which respectively reforms and strips the GeO_x oxide at the sample surface. Unlike Si, Ge oxide cannot be used as a protective layer owing to its high solubility in water. As a result, no protective chemical oxide layer was preserved during the last step of Ge preparation, although a thermal oxide layer was inevitably formed at the sample surface after it was exposed to air for ~10min at 220°C during the mounting procedure (Indium glue).

The oxide desorption and surface preparation of Ge(111) samples under UHV were carried out at much lower temperatures, for three reasons. First of all, Ge oxide has

a low sublimation temperature of merely 700°C. Secondly, a reaction based desorption process is known to occur well below the sublimation temperature, typically around 400°C-550°C (Wang et al. 2010). Lastly, Ge has a relatively low melting point of 938.2°C (T_{melt}=1414°C for Si), not to mention the various alloys that it risks forming with Mo at even lower temperatures (ASM 1992). The heating process should thus be limited to ~700°C to ensure the complete removal of the oxide layer while avoiding any potential damage to the sample. In practice, the samples were slowly ramped up to 650°C, during which the pressure of the UHV chamber did not exceed 5×10^{-9}mbar. This was followed by a 5min-flash at 725°C once the pressure dropped below 10^{-9} mbar.

References:

Als-Nielsen, J. & McMorrow, D., 2011. Elements of Modern X-ray Physics, Second Edition. Wiley Online Library. Available at: http://onlinelibrary.wiley.com/book/10.1002/9781119998365.

ASM, 1992. ASM Metals Handbook VOLUME 3 Alloy Phase Diagrams,

Grundner, M. & Jacob, H., 1986. Investigations On Hydrophilic And Hydrophobic Silicon (100) Wafer Surfaces By X-Ray Photoelectron And High-Resolution Electron-Energy Loss-Spectroscopy. Applied Physics A: Materials Science & Processing, 39(2), pp.73–82.

Ishizaka, A., 1986. Low Temperature Surface Cleaning of Silicon and Its Application to Silicon MBE. Journal of The Electrochemical Society, 133(4), p.666.

Karen Reinhardt, W.K. ed., 2008. Handbook of Silicon Wafer Cleaning Technology, 2nd Edition, William Andrew.

Mishima, H. et al., 1989. Particle-Free Wafer Cleaning And Drying Technology. IEEE Transaction On Semiconductor Manufacturing, 2(3), pp.69–75.

Ohmi, T. et al., 1992. Dependence Of Thin-Oxide Films Quality On Surface Microroughness. IEEE Transaction On Electron Devices, 39(3), pp.537–545.

Wang, S.K. et al., 2010. Desorption kinetics of GeO from GeO2/Ge structure. Journal of Applied Physics, 108(5), p.054104.

APPENDIX IV: LIST OF SAMPLES CONCERNED IN THIS WORK

Sample	Figure	Growth Condition
290811B	2-3B	Si, 540°C, 2ML Au under Ar, 0.15sccm, 3h
051211	2-4AB, 2-6C, 3-7, 3-8, 3-14A	Si, 540°C, 5ML Au, 0.9sccm, 2.5h
040213A	2-4C	Si, 4ML Au at RT, anneal 550°C 20min, 480°C, 0.6sccm, 30min
041211C	2-4D	Si, 440°C, 5ML Au, 0.9sccm, 30min
011211	2-6DEF, 3-14C	Si, 520°C, 5ML Au, 0.6sccm, 2h
040811	2-6G	Si, 600°C, 2ML Au under Ar, 0.3sccm, 3h
251112	2-7A, 3-18 to 3-21	Ge, 5ML Au, anneal 500°C 35min, 340°C, 0.5sccm static, 2h
061112B	2-7B	Ge, 5ML Au, anneal 500°C 25min, 285°C, 0.5sccm static, 40min
021112B	2-7C	Ge, 5ML Au, anneal 400°C 10min, 285°C, 0.5sccm static, 40min
231012B	2-7D	Ge, 5ML Au, anneal 400°C 10min, 385°C, 0.5sccm static, 1.5h
061112D	2-7E	Ge, 5ML Au, anneal 500°C 25min, 200°C, 285°C, 0.5sccm sta., 40min
061112C	2-7F	Ge, 5ML Au, anneal 500°C 25min, 285°C, 0.03sccm static, 1.5h
130513C	2-9AB	Si, 540°C, 7ML Au, 0.9sccm static, 2h, 300°C, 48min CVD Ge shell
160213	2-9C	Si, 530°C, 6ML Au, 0.9sccm, 1h, 290°C, 70min CVD Ge shell
231013	2-9D	Si, 380°C, 3ML Au, 0.9sccm, 2h, 220°C, 32nm MBE Ge bending
010213A	2-10A	Si, 5ML Au, anneal 500°C 25min, 280°C, 0.5sccm static Ge_2H_6, 40min
311012C	2-10B	Si, 520°C, 5ML Au, 200°C, 290°C, 0.5sccm static Ge_2H_6, 20min
221112F	2-10C	Si, 5ML Au, anneal 450°C 50min, 300°C, 0.8sccm static Ge_2H_6, 40min
221112E	2-10D	Si, 5ML Au, anneal 450°C 15min, 300°C, 0.8sccm static Ge_2H_6, 40min
141212A	2-11A	Si, 500°C, 3ML Au, 0.9sccm static 20min, 285°C 0.8sccm Ge_2H_6 40min
171212A	2-11BCD	Si, BI, 450°C, 3ML Au, 0.9sccm, 40min, 285°C, 0.8sccm Ge_2H_6, 80min
061112E	2-12A	Ge, 550°C, 5ML Au, 0.9sccm static Si_2H_6 20min
110213A	2-12B	Ge 5ML anneal 500°C 35min, 300°C 0.5sccm static 1h, 500°C 0.6sccm Si_2H_6 40min
200213	2-12C	Ge 5ML anneal 500°C 35min, 300°C 0.5sccm static 1h, 400°C 0.9sccm Si_2H_6 1h
130313A	2-12D	Ge 500°C 5ML, 300°C 0.8sccm 1h, 380°C 0.9sccm Si_2H_6 110min
151212C	2-13C	Si, 50nm colloid Au, anneal 475°C 25min, 0.9sccm, 20min
021112C	2-13D	Ge, 50nm colloid Au, anneal 400°C 10min, 285°C 0.5sccm static 40min
041211B	2-14A	Si, lift-off 25nm Au, 480°c, 70min
021211	3-1 to 3-5, 3-9	Si, 525°C, 5ML Au, 0.1sccm for 1h, then 0.9sccm for 2h
280612	3-6	Si, 4ML Au, anneal 530°C 50min under Ar, 0.1sccm, 3h20 with break
280912B	3-10, 3-11, 3-12	Si, 530°C, 5ML Au, 0.1sccm, 70min
290912B	3-13	Si, 540°C, 5ML Au, 0.1sccm 30min, 1.5nm MBE Ge, 0.1sccm 30min
241112	3-14B	Si, 480°C, 5ML Au, 0.9sccm, 1h
040313	3-15, 3-16	Ge, 5ML Au, anneal 500°C 35min, 200°C, 300°C, 0.8sccm, 40min
260713	4-2A, 4-3, 4-5, 4-7 to 4-10	Si, 570°C, 7ML Au, 0.9sccm, 1h, 100min CVD Ge shell
310713	4-2B, 4-4, 4-6	Si, 550°C, 0.9ML Au, 0.9sccm, 1h, 80min CVD Ge shell
290713	4-12	Si, 455°C, 3ML Au, 0.9sccm, 1h, 40min CVD Ge shell
100513	4-13	Si, 550°C, 7ML Au, 0.9sccm static, 2h, 300°C, 96min CVD Ge shell
031013C	4-15	Si, 560°C, 7ML Au, 0.9sccm, 1h, 220°C, 8nm MBE Ge shell
231013	5-3 to 5-8	Si, 480°C, 3ML Au, 0.9sccm, 2h, 220°C, 32nm MBE Ge bending
160514	5-9, 5-10, 5-11	Si, 480°C, 3ML Au, 0.9sccm, 2h, RT, 117nm MBE Ge bending
291013	5-12, 5-13, 5-14	Si, 480°C, 3ML Au, 0.9sccm, 2h, RT, 18nm MBE Au bending
311013A	5-15	Si, 480°C, 3ML Au, 0.9sccm, 2h, RT, 2nm MBE Au opposite side
171213A	5-16, 5-17	Si, 560°C, 5ML Au, 0.9sccm, 2h, RT, 50nm MBE Au bending
011113B	5-18	Si, 480°C, 3ML Au, 0.9sccm, 2h, RT, 2.3nm MBE Co bending

[This Page Intentionally Left Blank]